Laser Surface Texturing for High Friction and Other Surface Engineering Applications

Andrew Dunn

A dissertation submitted for the degree of Doctor of Philosophy

Heriot-Watt University

School of Engineering and Physical Sciences

June 2016

Abstract

The use of laser surface texturing (LST) for surface engineering, in particular the generation of high static friction surfaces, has been investigated. The niche nature of high friction surfaces has meant that the field has largely been discarded and forgotten, leaving an opening for novel and innovative research as a result.

Several regimes for generating high friction surfaces were considered: exclusive use of LST on a single surface (as in a shim configuration), use of LST on both surfaces of a contact and LST of a single surface in conjunction with additional surface engineering processes. Each of these three regimes was found to operate by a different mechanism of high friction, namely adhesion, interlocking and embedding.

The laser surface texturing was performed using a self-built, commercially available laser processing workstation encompassing a pulsed nanosecond fibre laser and galvanometric scanner. Analysis of the surface textures was performed using optical microscopy and profilometry with further investigations performed by cross-section, SEM and EDX analysis. Friction testing of the textured samples was performed by a custom made testing rig, with direct measurement of the applied normal force via an in-line load cell, and real-time measurement of the load force by a 100kN hydraulic press.

A wide range of laser texturing parameters and material properties were investigated, with each of the three regimes exhibiting different optimal parameters. High friction coefficients (μ_s>0.8) can be repeatedly obtained at normal pressures of up to 100MPa when LST has been used in conjunction with additional surface engineering (hardening) processes and when both surfaces of the contact have been treated with laser surface texturing. In the latter case, static friction coefficients of μ_s~1 with processing rates of greater than 1cm^2/s have been achieved. Several relevant applications for such high friction surfaces have also been discussed.

The feasibility of integrating beam shaping optics into an industrial style laser processing workstation has also been demonstrated and possible applications for such shaped beams discussed.

Acknowledgements

A PhD project, and the resulting thesis, is not something which can be undertaken entirely independently. As such, there are a number of people who I would like to acknowledge for their input in making this thesis a reality.

First and foremost, I would like to thank Professor Duncan Hand and Dr Jonathan Shephard for giving me the opportunity to work within the Applied Optics and Photonics group and supervising me over the last three years. I would also like to thank Dr Krystian Wlodarczyk for his assistance, ideas and opinions. Without their input, this project would not have progressed nearly as quickly or smoothly as it did.

Special thanks go to both of my industrial collaborators, SPI Lasers and MAN Diesel & Turbo, particularly Paul Harrison, Jack Gabzdyl, Jesper Carstensen and Erica Hansen. Their support, through loans of equipment, use of facilities and invaluable expertise, was vital for many aspects of the project.

I would also like to thank the workshop staff here at Heriot-Watt, particularly Alistair Blyth and Richard Kinsella, for tolerating my endless requests for grinding of samples and related tasks in a jovial manner.

Finally, I would like to thank my friends, family and officemates for putting up with my ranting and rambling over the last three years and keeping me on track.

ACADEMIC REGISTRY

Research Thesis Submission

Name*:*	Andrew Dunn		
School/PGI:	School of Engineering and Physical Sciences		
Version: *(i.e. First, Resubmission, Final)*	Final	Degree Sought (Award **and** Subject area)	Doctor of Philosophy in Physics

Declaration

In accordance with the appropriate regulations I hereby submit my thesis and I declare that:

1) the thesis embodies the results of my own work and has been composed by myself
2) where appropriate, I have made acknowledgement of the work of others and have made reference to work carried out in collaboration with other persons
3) the thesis is the correct version of the thesis for submission and is the same version as any electronic versions submitted*.
4) my thesis for the award referred to, deposited in the Heriot-Watt University Library, should be made available for loan or photocopying and be available via the Institutional Repository, subject to such conditions as the Librarian may require
5) I understand that as a student of the University I am required to abide by the Regulations of the University and to conform to its discipline.

* *Please note that it is the responsibility of the candidate to ensure that the correct version of the thesis is submitted.*

Signature of Candidate*:*		Date:	

Submission

Submitted By *(name in capitals):*	Andrew Dunn
Signature of Individual Submitting:	
Date Submitted:	

For Completion in the Student Service Centre (SSC)

Received in the SSC by *(name in capitals):*			
Method of Submission *(Handed in to SSC; posted through internal/external mail):*			
E-thesis Submitted (mandatory for final theses)			
Signature:		Date:	

Table of Contents

List of Symbols & Abbreviations

BEC(/BET)	- Beam Expansion Collimator (/Telescope)
CP	- Counterpart
cw	- Continuous wave
d	- Nominal Focal Spot Diameter
EDX	- Energy Dispersive X-ray spectroscopy
EP	- Extended Profile (laser models)
IR	- Infrared
HRC	- Rockwell Hardness C
HV	- Vickers Hardness
HVOF	- High Velocity Oxy-Fuel
MDT	- MAN Diesel & Turbo SE
NIR	- Near-Infrared
ns	- Nanosecond
PRF	- Pulse Repetition Frequency
R_a	- Linear Surface Roughness (arithmetic)
s	- Pulse Separation
S_a	- Areal Surface Roughness (arithmetic)
SAI	- Surface Area Index
SCAPS	- SCanner APplication Software
SEM	- Scanning Electron Microscopy
SPI	- SPI Lasers UK Ltd.
SS	- Stainless Steel
μ_s	- Static Friction Coefficient
Φ	- Crater Diameter

List of Publications & Awards

Journal Publications:

Dunn, A., Carstensen, J.V., Wlodarczyk, K.L., Hansen, E.B., Gabzdyl, J., Harrison, P.M., Shephard, J.D., Hand, D.P., *Laser surface texturing for high friction contacts*, Applied Surface Science, Volume 357 Part B, December 2015, Pages 2313-2319 doi:10.1016/j.apsusc.2015.09.233

Ta, D.V., **Dunn, A.**, Wasley, T.J., Kay, R.W., Stringer, J., Smith, P.J., Connaughton, C., Shephard, J.D., *Nanosecond laser textured superhydrophobic metallic surfaces and their chemical sensing applications*, Applied Surface Science, Volume 357 Part A, December 2015, Pages 248-254, doi:10.1016/j.apsusc.2015.09.027

Wlodarczyk, K.L., Ardron M., Waddie, A.J., **Dunn, A.**, Kidd, M.D., Weston, N.J., Hand, D.P., *Laser microsculpting for the generation of robust diffractive security markings on the surface of metals*, Journal of Materials Processing Technology, Volume 222, August 2015, Pages 206-218, doi:10.1016/j.jmatprotec.2015.03.001

Dunn, A., Carstensen, J.V., Wlodarczyk, K.L., Hansen, E.B, Gabzdyl, J., Harrison, P.M., Shephard, J.D., Hand, D.P., *Nanosecond laser texturing for high friction applications*, Optics and Lasers in Engineering, Volume 62, November 2014, Pages 9-16, doi:10.1016/j.optlaseng.2014.05.003

Conference Contributions:

Dunn, A., Carstensen, J.V., Wlodarczyk, K.L., Hansen, E.B., Gabzdyl, J., Harrison, P.M., Shephard, J.D., Hand, D.P., *Laser Texturing for High Friction Applications (1403)*, Proceedings and invited talk presented at ICALEO (International Congress on Applications of Lasers & Electro-Optics) 2014, San Diego, USA

Dunn, A., Wlodarczyk, K.L., Shephard, J.D., Hand, D.P., *Surface Engineering with Lasers*, Poster presented at Manufacturing The Future (MTF) Conference 2014, Glasgow, UK

Dunn, A., Wlodarczyk, K.L., Shephard, J.D., Hand, D.P., *Surface Engineering with Lasers*, Poster presented at EPSRC Centre for Innovative Manufacturing in Laser-Based Production Processes, Edinburgh, UK

Other Publications

Dunn A, *Laser Texturing to Generate High Friction Surfaces*, LIA Today, Vol.23 No.3, May/June 2015

Dunn A, Carstensen JV, Wlodarczyk KL, Hansen EB, Gabzdyl J, Harrison PM, Shephard JD and Hand DP. *Nanosecond laser texturing for high friction applications*. The Laser User Magazine, Issue 073, Spring 2014

Awards:

IPaQS Postgraduate Research Prize – Second Year

Chapter 1 – Introduction

1.1 Rationale

1.1.1 Surface Modification

Surface modification can be used to change and improve many different surface properties of a material including, but not limited to, friction, wettability, hardness, and corrosion resistance. The ability to tailor one, or more, of these properties controllably is of great interest for a large number of engineering applications, where even small improvements to the surface properties can improve the performance or efficiency of a system significantly.

As a result, there are a number of techniques which have been developed in order to modify surface properties, including electron beam treatments, lithography, chemical treatments, plasma treatments, electric discharge, sand blasting and laser processing. All of these techniques have their own advantages and disadvantages, making them more or less suitable for different applications. For the work detailed in this thesis, laser processing in the form of surface texturing is used as the primary modification technique.

1.1.2 Increasing Friction

At first consideration, deliberately attempting to increase the friction coefficient of a surface sounds counterproductive. As a result, there has been very little scientific research performed in this area, with even less published. However, despite this initial perception of the idea, there are a number of applications where high friction coefficients are useful, or even essential. The first of these which comes to mind are the brake discs and pads fitted to every vehicle on the road.

In addition to this type of application which makes use of kinetic friction, there are others for which high *static* friction coefficients are beneficial. For example, friction surfaces are useful for reducing the tightening forces required for a joint or to secure precision fittings easily. It is primarily for the latter reason that industrial collaborator MAN Diesel & Turbo (MDT) has significant interest in high friction surfaces – for use

in components in their marine diesel engines. Individual applications for these surfaces are discussed in detail at the end of their appropriate chapters (Chapter 5 and Chapter 6).

1.2 Aims & Objectives

The aim of the project reported in this thesis was to develop and understand the processes which allow the friction properties of a surface to be controllably modified, primarily by the application of high power lasers. In contrast to the bulk of scientific literature in the field of laser surface texturing, the aim here is to increase the friction coefficients of engineering materials.

The use of high power lasers to modify the friction properties may allow significant improvements in these applications when compared to traditional techniques. Such improvements may be in the results achieved, the reliability and precision of the modifications or in the speed of the process. For certain applications, it is also possible that the use of high power lasers for surface engineering is the only possible technique which is practically viable.

This project received financial and technical support from an industrial sponsor, SPI Lasers UK Ltd, who made equipment – including pulsed fibre lasers and relevant optics – available to the project. As mentioned in Section 1.1.2, an industrial collaboration was also set up with MDT – the primary driver interested in the generation of surfaces with high static friction coefficients. MDT provided materials, access to testing facilities and technical advice.

In order to achieve the desired high friction surfaces, several different methods were considered. Using previous knowledge from MDT, laser texturing of a single surface with the intention of embedding the asperities into the counterpart in order to achieve high friction was considered first, as discussed in Chapter 4. Due to the limited friction coefficients obtained in this regime, two secondary processes, plasma nitriding and conventional heat treatment, were then used in addition to the laser texturing process with the understanding that harder asperities would be better able to embed into the counter surface. The results and outcomes of the tests on these samples are presented in Chapter 5. At the same time as the work with externally hardened samples, another regime for achieving high friction was considered involving laser texturing of both

surfaces of the contact in order to enable interlocking of the surface features generated. The interlocking process and the parameter space pertaining to this regime are covered in significant detail in Chapter 6. Finally, the introduction of bespoke, commercial beam shaping optics into the laser processing workstation was considered. Although a shaped beam was not anticipated to improve the high friction surfaces, it was considered a proof-of-principle with possible applications within other surface engineering applications, such as laser polishing.

1.3 Summary of Chapters

- Chapter 1 provides an introduction to the thesis, including the primary motivation and key ambitions for the work presented.

- Chapter 2 introduces background information on laser processing and surface engineering in general, with an extended focus on the literature surrounding the use of lasers for performing a wide variety of surface modifications for engineering applications. Laser surface texturing for applications requiring friction reduction is also discussed before the requirements for high friction contacts are reviewed, as well as currently available literature in the field.

- Chapter 3 covers the preliminary experimental work performed in order to characterise the laser processing workstation. The design of the experimental laser processing set-up and the interaction between the laser pulses and sample material are discussed at this stage, as well as some experimental results concerning the effect of pulse duration on laser processing. Based on the results obtained, some assumptions are made as to the best parameters to use for the following laser texturing.

- Chapter 4 provides some details of the method used to test such surfaces prior to detailing the initial textures and test results. A wide range of the parameter space is also explored here, as well as significant analysis of the sample properties, including surface roughness parameters, and results in order to determine the most important properties and parameters to achieve high friction

coefficients. The effect of increasing repetition rate on the friction and material properties is also explored at this stage.

- Chapter 5 details the progression of the work discussed in Chapter 4, primarily concerning the influence of material hardness on the friction coefficient. Methods of material hardening are compared, followed by friction test results based on plasma nitrided and heat treated tool steel samples. Specific examples of applications for this type of process are discussed, including findings from tests performed with real components.

- Chapter 6 examines a slightly different approach to increasing friction, whereby both contacting surfaces are laser textured rather than just one, as previously considered. The effect of changing normal pressure on the friction coefficient is studied in detail, as is the presence of the 'micro-slips' observed in a number of the friction test results. Another application for high friction surfaces is also presented, for which the texturing of both contacting surfaces is an appropriate solution.

- Chapter 7, departing somewhat from the other work discussed in this thesis, looks at the preliminary characterisation of beam shaping optics. Two beam shaping optical set-ups are investigated with possible applications in surface engineering considered.

- Chapter 8 presents the outcomes of the investigations discussed in this thesis, as well as summarising their usefulness for industrial applications. Possible areas of future research are also suggested.

Chapter 2 – Background & Review

This chapter aims to give some basic background information on laser material processing, surface engineering and friction as well as an overview of the existing literature available on these and related subjects. Several applications for surface engineering are also discussed, with particular attention paid to friction surfaces.

2.1 Laser Materials Processing

The advent of the laser, theorised by Albert Einstein and first realised by Theodore Maiman in 1960, enabled a wide range of applications, including those which, until that point, had not even been considered [1]. Applications facilitated by the unique properties of lasers include: spectroscopy (Raman spectroscopy, LIBS, etc. [2-4]), precision measurement (through time-of-flight and interferometric techniques [1, 5]), laser cooling of solids [6], nuclear fusion (National Ignition Facility, HiPER) [1], defence (object tracking, directed energy weapons, etc. [1]) and medical (dental, laser scalpel, etc. [7, 8]).

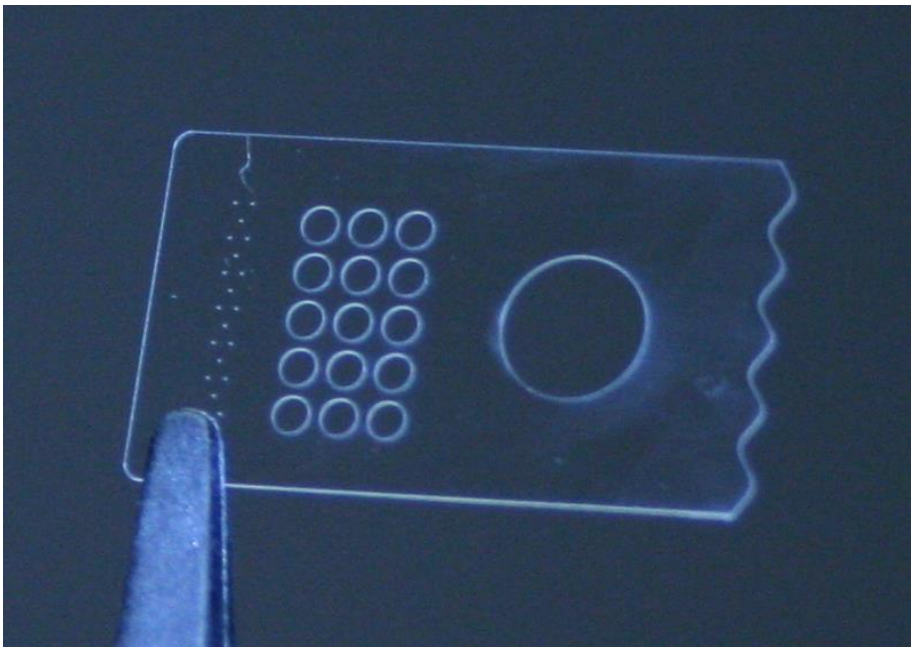

Figure 2.1. Thin flex glass (100µm thick) cut with a picosecond laser with a wavelength of 532nm [9]

In addition, a huge industrial and commercial field of lasers for materials processing has evolved, with a significant amount of research still taking place in this area. Laser applications within material processing include cutting (see Figure 2.1), drilling, welding, engraving, additive manufacturing and surface modification [10]. It is this last

sub-category of laser materials processing, surface modification, or surface engineering, which is the focus of the work detailed in this thesis. Figure 2.2 shows several different laser induced surface modifications generated on a tool steel substrate.

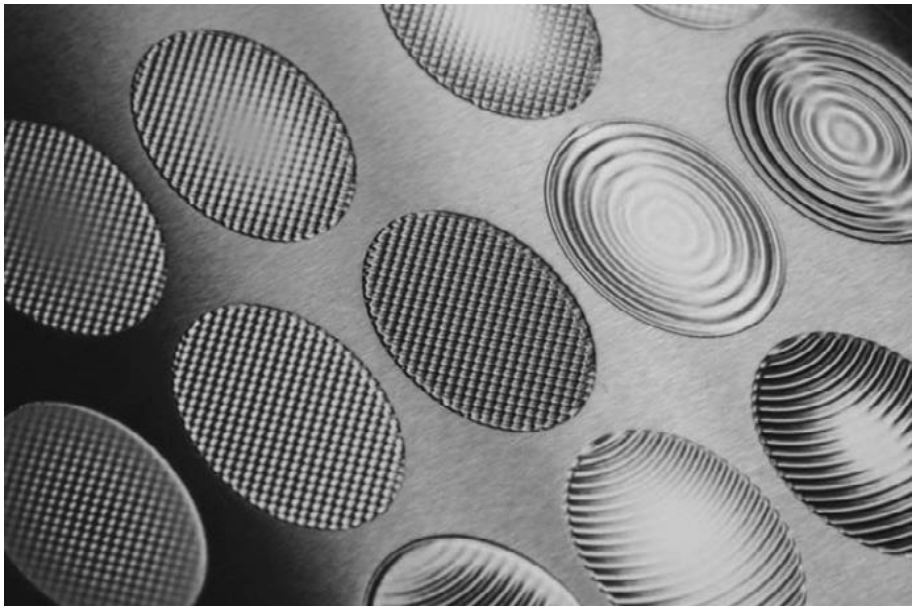

Figure 2.2. Several periodic and aperiodic surface structures generated by laser re-melting techniques on tool steel 1.2343 [11]

2.1.1 Laser Properties

As previously discussed, there are a wide range of laser applications, most of which are only possible due to the unique properties of laser radiation. Lasers tend to share several properties which differentiate them from other light sources [1, 12], namely:

- Directionality,
- High spatial/temporal coherence,
- Narrow spectral width (near monochromatic), and
- High fluence/power.

Despite this commonality, there are a wide range of lasers available with many different parameters, such as wavelength and pulse duration (or continuous wave (cw)). A selection of laser types typically used for materials processing and their properties are shown in Table 2.1.

Laser Type	Pulse Duration	Repetition Frequency	Wavelength Range (μm)	Fluence	Intensity
Fibre laser oscillators	CW-1ps	CW-MHz	1.07-2.1	Modest	High
Amplified fibre lasers	ns-fs	kHz-MHz	1.07-2.1	High	High
Diode lasers	CW-μs	CW-kHz	0.8-1.2	Modest	Low
Excimer oscillators	10-20ns	200Hz	0.308, 0.248, 0.193	High	Modest
Excimer amplifiers	1-10ps	10Hz	0.248	High	High
Nd:YAG oscillators	5-20ns	20Hz	1.06, 0.532, 0.355, 0.266	High	Modest
Nd:YVO_4 oscillators	5-10ns	20kHz	1.06, 0.532, 0.355, 0.266	Modest	Modest
Yb:YAG amplifiers	0.5-20ps	20mHz	1.06, 0.532, 0.355, 0.266	Modest	High
Ti:Sapphire oscillators	10-100fs	100MHz	0.7-1.0	Low	High
Ti:Sapphire amplifiers	100-150fs	5kHz	0.7-1.0	High	High

Table 2.1. Properties of lasers commonly used for laser material processing [13]

Laser-material interactions are highly dependent on the laser parameters, particularly the wavelength, pulse duration and fluence. However, as a result of the wide range of laser sources and parameters available, see Table 2.1, it is typically possible to select an appropriate source for a given application.

2.1.2 Light-Matter Interaction

As well as the laser (light) properties, the interaction of light with matter depends on many material properties, such as the absorption and thermal conductivity [14]. When light is absorbed by a material, the photon's electromagnetic field causes the excitation of the free electrons (and possibly band electrons) in metals, vibrations in insulators (or even excitation out of bands, resulting in breaking of bonds), or both (in semiconductors) [15]. This process is dependent on the materials' reflectivity and absorption coefficient, both of which are related to the refractive index and dielectric function. As the electrons in metals have no resonance frequency with the lattice, their interaction with the lattice is determined entirely by collisions [16]. The dielectric function of metals can therefore be written as:

$$\varepsilon = 1 + \omega_p^2 \frac{-\tau_e^2 + i\frac{\tau_e}{\omega}}{1 + \omega^2 \tau_e^2} \quad (2\text{-}1)$$

where $\omega_p = \sqrt{\frac{N_e e^2}{m_e \varepsilon_0}}$ is the electron plasma frequency, N_e is the number of electrons, m_e is the mass of an electron, ε_0 is the permittivity of free space and τ_e is the electron collision time. Due to the dependence on the refractive index, the reflectivity and absorption of a material also vary with the wavelength of the incident radiation, as shown in Figure 2.3, and the temperature of the material.

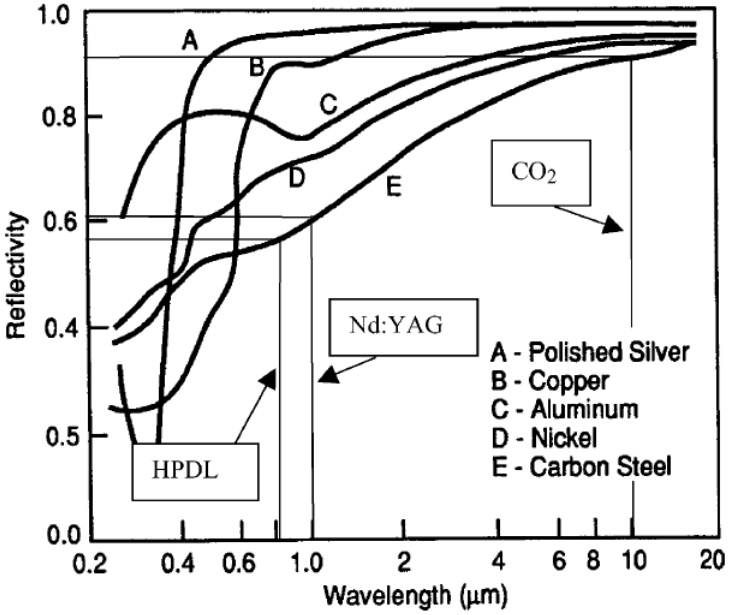

Figure 2.3. Typical reflectivities as a function of wavelength for various metals and alloys [7]

When the incident light is from a high intensity source, such as a laser, the optical properties of the material can change considerably, by one of three mechanisms [16]:

- The production of heat by the beam can change the density of the material or its electronic characteristics, possibly leading to thermal self-focussing (an effect caused by a change in refractive index of the material due to the heating action of the incident light) or 'thermal runaway'
- Optical generation of free electrons by inter-band transitions in metals, or impact ionisation in semiconductors and insulators, leading to a significant increase in the absorption coefficient
- A non-linear distortion of electron orbitals, or whole molecules, by the electric field of the intense beam can lead to changes in reactivity, structural order and therefore refractive index [16, 17].

The reflectance of metals usually decreases when irradiated with high enough intensity light. This is a thermal effect, which makes them vulnerable to thermal runaway (a snowball effect), particularly in the IR region due to the high initial reflectance. This is caused by the shortening of the electron-lattice collision time [16], which is typically ~10^{-13}s for metals (and 10^{-12}-10^{-6}s for non-metals) [15]. As a result of this, ultrashort pulses (~10^{-12} - 10^{-15}s) tend to produce more sharply defined features, with very little change to the surrounding material [18]. Longer pulses, on the other hand, tend to generate relatively large 'heat affected zones' around the incident pulse, due to the heating effect caused by the 'long' pulse duration. Depending on the fluence of the incident beam, the absorption can lead to atoms near the surface rearranging to alter the surface structure (as can be used for surface hardening [19]), localised melting and/or ablation of the material surface, as depicted in Figure 2.4.

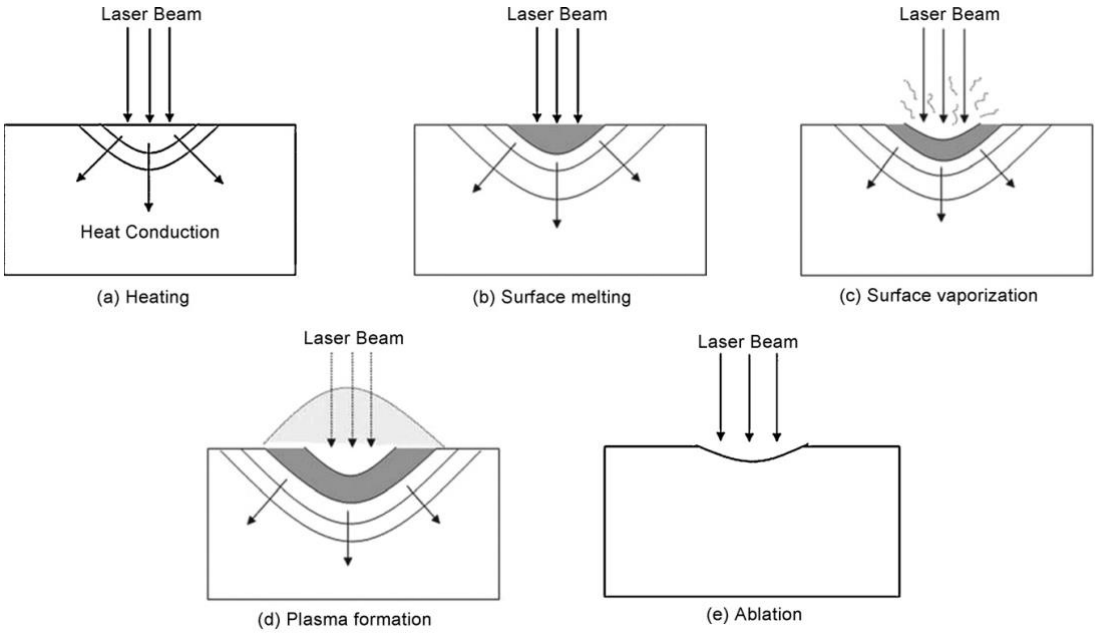

Figure 2.4. Effect of an incident beam on a material surface, for varying laser fluence [20]

The heat produced by the laser beam on the material surface is also transferred, primarily through conduction, through the material. This can be described by the heat equation:

$$\rho c \frac{\partial T}{\partial t} = k_T \nabla^2 \mathrm{T} \qquad (2\text{-}2)$$

where T is the temperature, ρ is the density, c is the heat capacity and k_T is the thermal conductivity of the material. In the simplest model, these parameters can be assumed to be constant. For more accurate calculations, however, their temperature dependence

must also be considered [21]. The thermal penetration depth, on the other hand, can be approximated easily with a much simpler equation:

$$l_{th} = (\kappa \tau_p)^{\frac{1}{2}} \quad \text{(2-3)}$$

where κ is the thermal diffusivity and τ_p is the duration of the laser pulse [21]. Whilst analytical solutions to Eq. (2-2) are not easily available (especially when combined with a moving laser heat source), it is possible to solve some scenarios numerically. However, the complexity increases significantly when melting and ablation of the material are also considered.

The optical properties of the material can also be modified by both melting and ablation. Figure 2.5 shows a diffraction grating generated on stainless steel by a laser induced melting process. This can occur either by mechanical deformation of the surface or by plasma effects. When the laser fluence is above the ablation threshold, an increase in irradiance (>10^6Wcm^{-2}) can lead to the produced vapour becoming 'supersaturated' resulting in micron sized droplets condensing – absorbing and scattering a portion of the incident beam [16]. The vapour cloud is also likely to have a different refractive index from the surrounding atmosphere and, as a result, distort the wavefront of the incident beam. For even greater laser fluences (~10^7-10^{10}Wcm^{-2}), the vapour can become ionised (plasma) and absorb a significant portion of the laser beam. This plasma can also reradiate light as a blackbody, which may actually increase the absorption at the surface for infra-red beams [16]. If heated to a suitably high temperature, the plasma may become transparent to the laser wavelength and therefore allow transmission of the beam through to the surface without absorption or scattering.

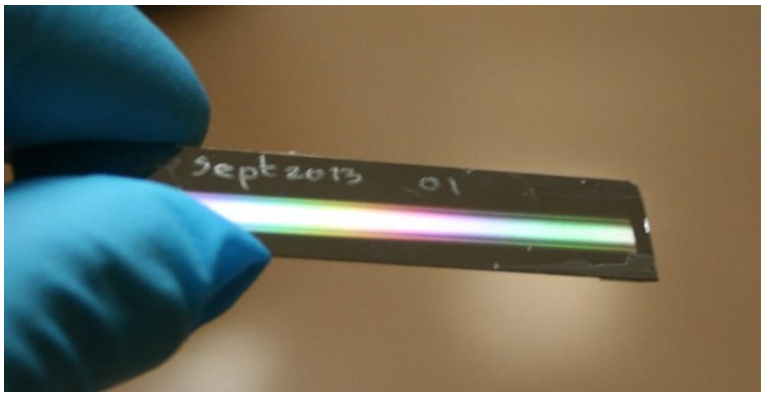

Figure 2.5. Diffraction grating generated on a stainless steel substrate with a UV, nanosecond laser by surface melting

The process parameters can also have a significant effect – a high pulse overlap, for example, can result in residual heat from the previous pulses affecting the absorption and effect of later pulses – a process which is directly related to the previously described thermal runaway. This has been witnessed experimentally on the ablation rates of Yttria-stabilised tetragonal zirconia polycrystal (Y-TZP) [22] where a very high pulse overlap was found to give deep but inconsistent grooves, whilst low pulse overlap generated discrete craters at the bottom of the cut, with the optimal overlap found to lie in between. In this case, the effect was emphasised by the very low thermal diffusivity ($D \sim 0.0053 cm^2/s$) of Y-TZP.

In addition, the minimum feature size which is possible to obtain with a laser is dependent on the wavelength, as described by the diffraction limit. This typically limits the feature size to approximately the wavelength of the light source [15]. However, techniques such as phase-shifting can facilitate the fabrication of sub-wavelength features [10].

2.2 Surface Engineering

Surface engineering, the act of modifying the surface properties of a solid material, has many applications within mechanical engineering, chemistry and electrical engineering. Many material properties, such as hardness, wear resistance, wettability and electrical resistance, are all at least partially dependent on surface properties. As a result, surface engineering is very attractive for many industries and therefore a lot of scientific research is being performed in this field for a wide range of applications.

2.2.1 Surface Engineering Techniques

In addition to the large number of surface properties which can be modified and resulting applications, there are also many techniques available in order to achieve such modifications. Some of the most common techniques include:

- Electroplating [23, 24],
- Thermal spraying [25, 26] (see Figure 2.6),
- Electron beam treatment [27, 28],
- Chemical treatment [29],
- Electric discharge [30, 31],
- Sand blasting [32], and
- Laser treatment.

Figure 2.6. Photograph of a robotic arm HVOF spraying of steel shims for MDT

Although each of the competing techniques used for surface engineering applications has its own advantages and disadvantages, laser treatment has several characteristics which are particularly advantageous. These include high flexibility, repeatability, accuracy and speed as well as lack of tool wear and negligible effect on the bulk material properties to name a few. As a result, laser treatment is a near ideal technique for applications which can obtain acceptable absorption at a suitable wavelength [10, 33]. For metallic substrates, which are the concern of the experimental work presented in this thesis, this is a fairly easy condition to satisfy.

2.3 Methods of Laser Surface Engineering

Even within the sub-category of laser surface engineering, there are several methods of modifying various surface properties. The most common of these methods are discussed prior to considering the applications for laser surface engineering.

2.3.1 Melting

Melting and ablation are two of the most commonly used regimes for laser surface engineering and laser micro-machining in general. Melting of the material surface occurs when the incident beam intensity is high enough such that enough energy is absorbed by the material to raise the temperature of the surface above the melting point. Melting can be used to generate several different surface structures such as dimples, grooves and hatches (see Figure 2.7), and so can be used for several applications such as

friction reduction and optical modifications. These types of structures are typically no more than a few microns deep.

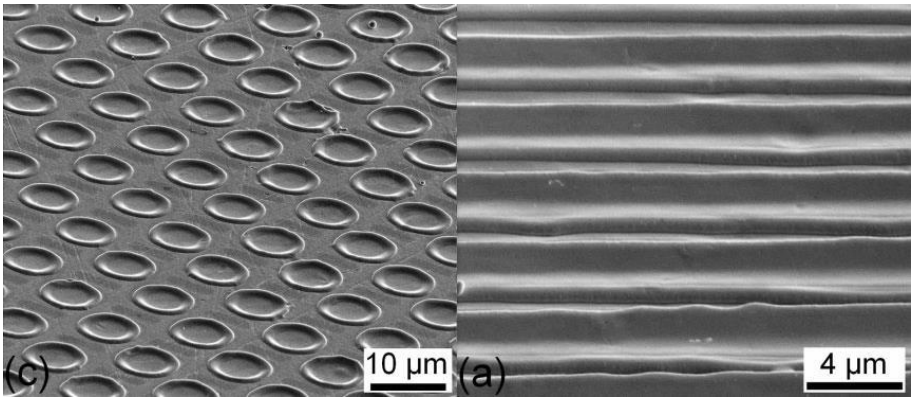

Figure 2.7. Simple surface structures made by laser melting, with dimples on the left and grooves/trenches on the right [34]

More advanced structures can be generated through the combination of laser melting with other techniques, such as laser interference metallurgy [34]. In addition, the flow of the melt, which generates the surface features, can be controlled by modulating the laser power, resulting in highly precise surface structures [11]. Laser melting has also been shown to remove features from a surface, in the field of laser polishing which is attracting a lot of attention [35-39]. Unlike the fabrication of dimples, in this case it is desirable to maintain a relatively flat surface on the melt pool, thus allowing pre-existing surface features to be smoothed out. However, issues have arisen due to the inherent properties of laser induced melt pools, i.e. thermal gradients, which lead to thermo-capillary (Marangoni) flow and result in surface waviness.

Several additive manufacturing (AM) techniques also make use of laser melting in order to build three dimensional parts from powder [40-42]. The powder is typically deposited on the surface into a flat and relatively thin layer (~40µm) and then selectively melted (Selective Laser Melting, SLM) with a laser beam. The molten powder then solidifies and another powder layer is added and the process repeated. This process allows the fabrication of complex three dimensional components, an example of which is shown in Figure 2.8. Research into additive manufacturing of different materials and alloys, as well as improving the physical properties of the manufactured parts is still ongoing [43].

Figure 2.8. Additive manufactured hip endoprosthesis fabricated by a selective laser melting process [44]

2.3.2 Ablation

Ablation occurs when an even higher intensity beam is used, increasing the temperature of the material surface above the boiling point of the material, causing it to vaporise and be ejected from the surface. Similar to melting, ablation can produce the same kinds of features but with a greater depth, albeit not as smooth. For longer pulse durations (>ns), this is primarily due to two mechanisms. First, some of the ablated material which leaves the surface is redeposited on the surface near the location of the laser pulse, resulting in, mostly spherical, loosely attached debris (see Figure 2.9 (E)). Second, the vaporisation of material within the dimple/crater generates a recoil pressure (due to the change in volume), resulting in significant melt flow outwards from the crater, as observed in Figure 2.9 (C).

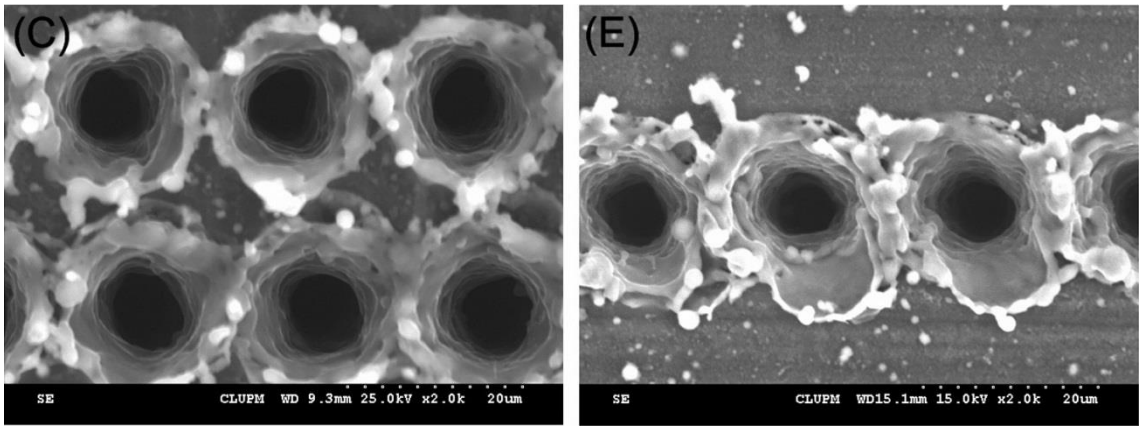

Figure 2.9. SEM images for microholes fabricated with a nanosecond laser of 355nm wavelength on an aluminium substrate [45]

Ablation is frequently used in laser cutting [46-48] and milling/engraving [49, 50] applications where material removal is required.

2.3.3 Drilling

Drilling involves the creation of a relatively deep hole in the material by ablation and melt ejection. This is achieved through the same thermal process as described in Section 2.3.1 but, in order to obtain the greater depth, the incident beam may be repeated several times at the same lateral position (percussion drilling) [51, 52] or in a circular geometry (trepan drilling). This allows ablation to take place multiple times on the same area, allowing deeper holes or dimples to be made, such as the hole shown in Figure 2.10. Whilst the number of surface structures possible with drilling is limited, several different properties of the surface can be altered using this technique. Applications for laser drilling include drag reduction in aircraft wings [51] and increased cell adhesion in biological implants (see Section 2.4.3).

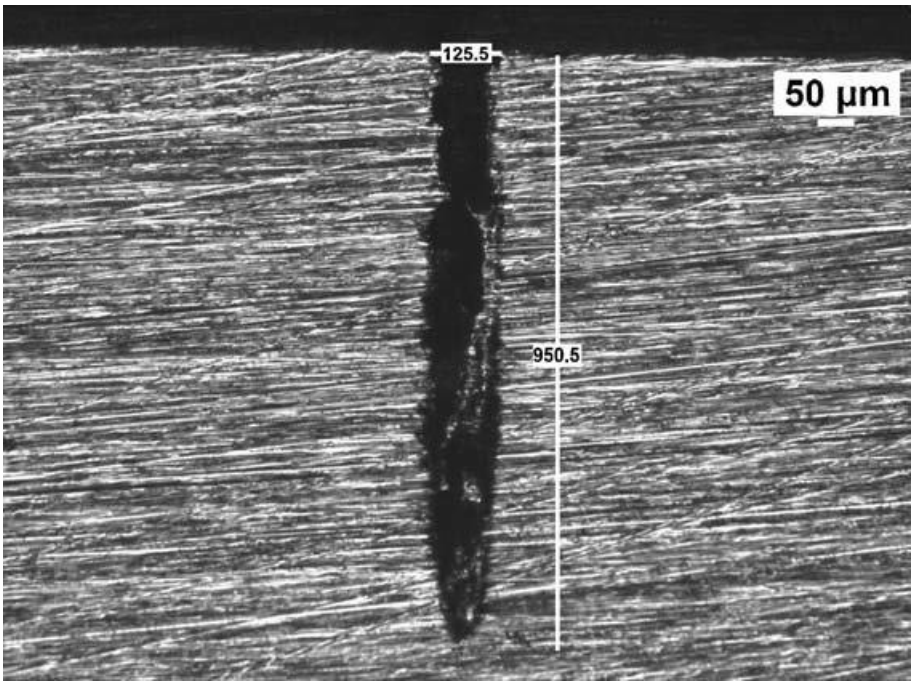

Figure 2.10. Example blind hole in mild steel fabricated by laser drilling [53]

2.3.4 Alloying

There are several methods of producing surface alloys with lasers. One of these involves melting an area of the surface and then adding the alloying material into the molten pool [54]. It is also possible to pre-place powder on the material surface and melt both materials with the incident laser beam [55]. Schematics of these two

techniques are shown in Figure 2.11. Another method involves dipping the material into a large pool of molten alloy which creates a serrated interface between the two materials. Subsequent laser processing melts the material leading to a continuous interface, as well as the possibility of altering the chemical structure near the surface of the material [54]. Laser surface alloying can also be used to alter the surface microstructure of the material.

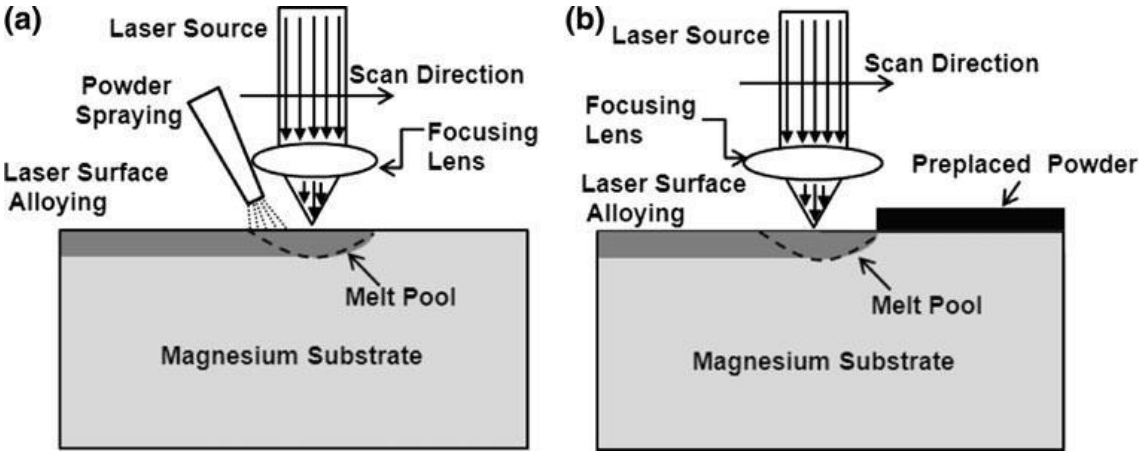

Figure 2.11. Two example set-ups showing different methods of adding alloying material to a surface [55]

2.3.5 Cladding

Laser surface cladding is a process by which a layer of material is added to the surface of the substrate by the use of laser beams. The added layer which is bonded to the surface of the substrate, is usually rather thick (normally >500μm) [55]. The process uses the laser beam to melt the material which is being added which is usually in powder form – either sprayed or pre-placed, see Figure 2.12. At the same time, a small amount of the substrate is also melted to allow the two materials to fuse together without the two mixing significantly (unlike alloying) [55].

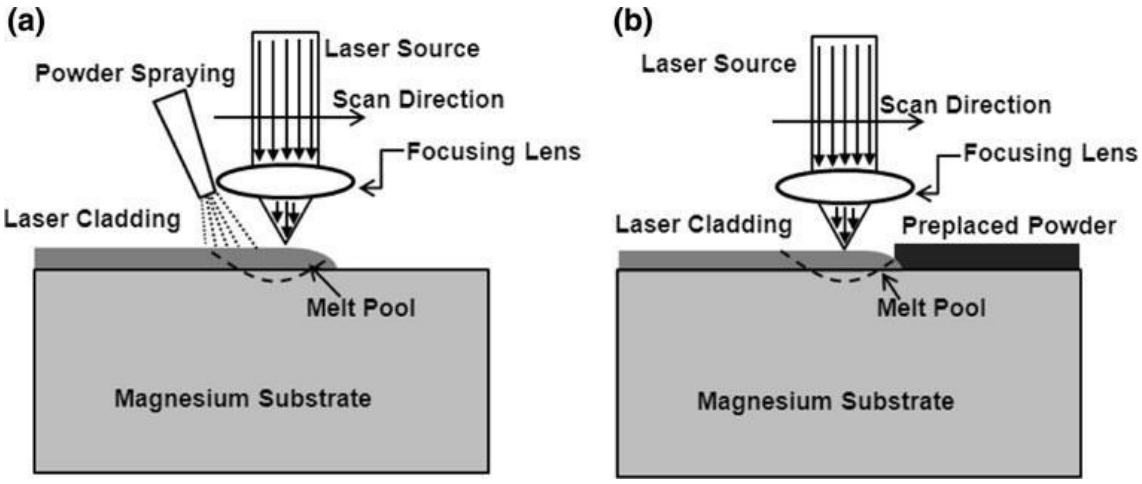

Figure 2.12. Schematics of the two primary powder application methods for laser surface cladding [55]

2.3.6 Hardening

There are two primary procedures through which lasers are used to induce surface hardening. When a high intensity laser beam heats the surface of the material rapidly, large temperature gradients are formed in the material. As a result, there is a swift transfer of energy through the material by conduction and so the material cools rapidly. In steel, for example, this can lead to the formation of martensite without requiring external quenching [19]. In addition, the sample undergoing laser treatment can be placed below a confinement medium (usually water). This confines the shock wave (resulting from the rapid thermal expansion of both sample and confinement medium) which generates compressive stress in the surface, a process known as laser shock hardening or 'shock peening' [10, 56]. Laser shot peening has several advantages over conventional hardening methods, such as less surface roughening, no embedded particles and it is flexible in surface geometry. However, short pulses (usually <100ns) with high pulse energy (>5J) are required in order to provide substantial increases to the hardness [57].

2.4 Applications of Laser Surface Engineering

Each of the methods of laser surface engineering can be used to alter a variety of different surface properties and, therefore, can be used for a range of applications. Some of the most successful applications for laser surface texturing are discussed briefly before friction and its applications are reviewed in detail.

2.4.1 Wettability

Controlled modification to the wettability, the surface property which defines the contact angle between the solid surface and contacting liquid, allows for many

interesting applications, such as self-cleaning surfaces, corrosion resistance and drag reduction [58]. Laser texturing is a prominent method used for modifying the wettability properties, with a significant amount of work published in this field, particularly on metallic substrates. In particular, super-hydrophobic surfaces, defined as having a solid-liquid contact angle greater than 150° (as shown in Figure 2.13), have received a lot of attention.

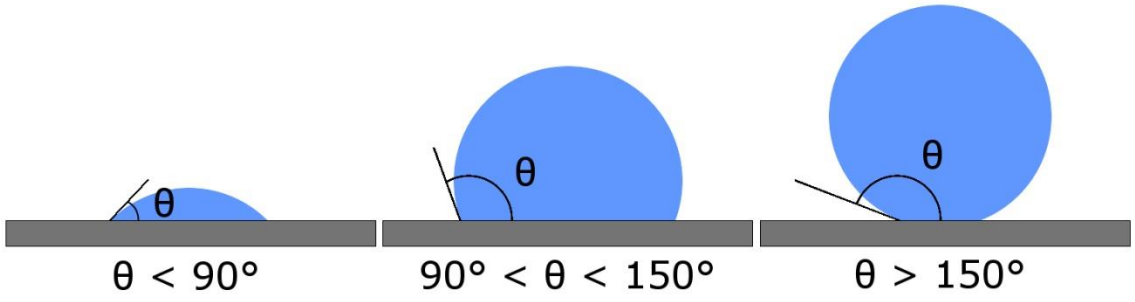

Figure 2.13. Schematic of contact angles depicting hydrophilic, hydrophobic and super-hydrophobic regimes

The wettability property of a material is related to the average surface roughness of the material, but it has also been found to depend on the surface oxygen content as well as the surface energy [59]. As a result of this, however, most research into wettability properties of a surface focuses on roughening the surface to enhance wettability [60]. This is based on two theories of wettability, namely Wenzel's model and Cassie-Baxter's model. Both of these define the contact angle of liquid on a rough surface, with Wenzel's model assuming that the liquid is in full contact with the surface and the Cassie-Baxter model assuming that there are air pockets between the liquid and the rough surface [60]. Schematics of the two wettability theories are depicted in Figure 2.14. The contact angle is usually measured optically, with a set volume of water placed on the sample surface.

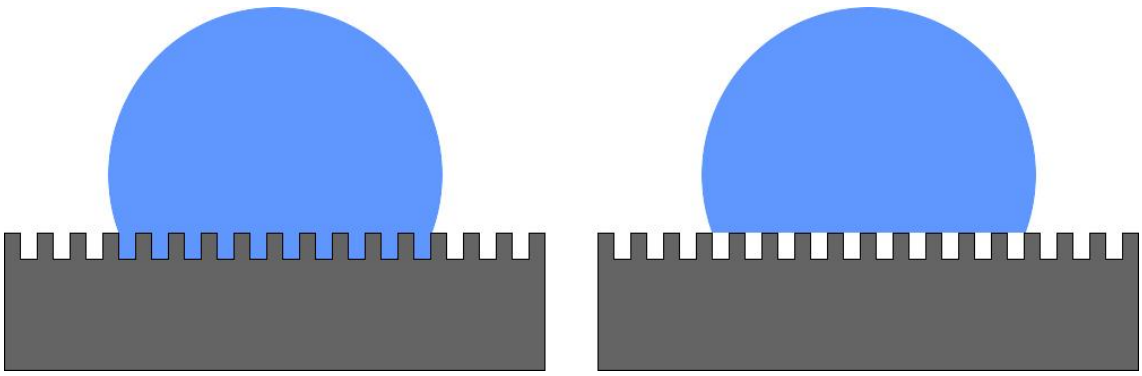

Figure 2.14. Schematics of the Wenzel (left) and Cassie-Baxter (right) for wetting of rough surfaces

Literature regarding laser texturing for wettability modification has typically concerned the use of ultrafast (pico-/femto-second) lasers [61-63]. Martínez-Calderon et al., for example, have shown super-hydrophobic behaviour (contact angle of 156°, compared to 75° for the untreated surface) on stainless steel grade 304 (AISI304) with both micro- and nano-scale features generated by irradiating the surface with a femto-second laser [64]. An example of such multi-scale surface structuring is shown in Figure 2.15.

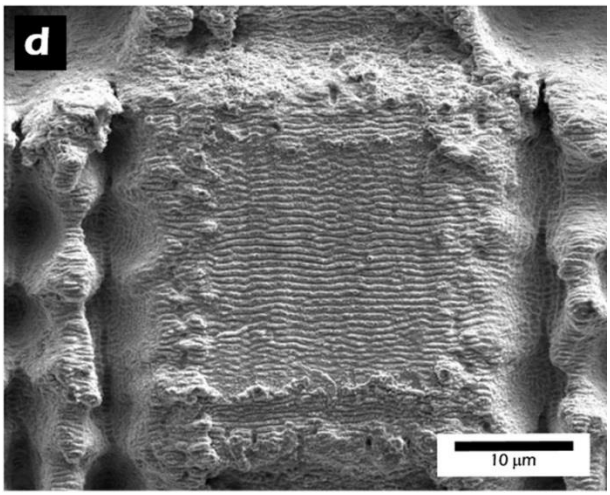

Figure 2.15. SEM micrograph of hydrophobic surface structure with both micro and nanoscale roughness [64]

Similar surfaces, generated on the same material, but without the nano-scale LIPSS (Laser Induced Periodic Surface Structures) features exhibited a significantly lower contact angle of 144°, indicating that multi-scale roughness is beneficial for generating super-hydrophobic surfaces, hence the focus on the use of ultra-fast laser systems for this application.

Despite these results, it has been shown that super-hydrophobic surfaces can be fabricated without the use of ultra-fast lasers [58]. In this case, contact angles of up to 152° have been demonstrated on nanosecond laser textured brass and copper substrates as well as the self-cleaning property of these superhydrophobic surfaces. However, the wettability was found to change over time, see Figure 2.16, with the surface observed to be hydrophilic immediately after fabrication and super-hydrophobic after 11-30 days (depending on the substrate and laser parameters).

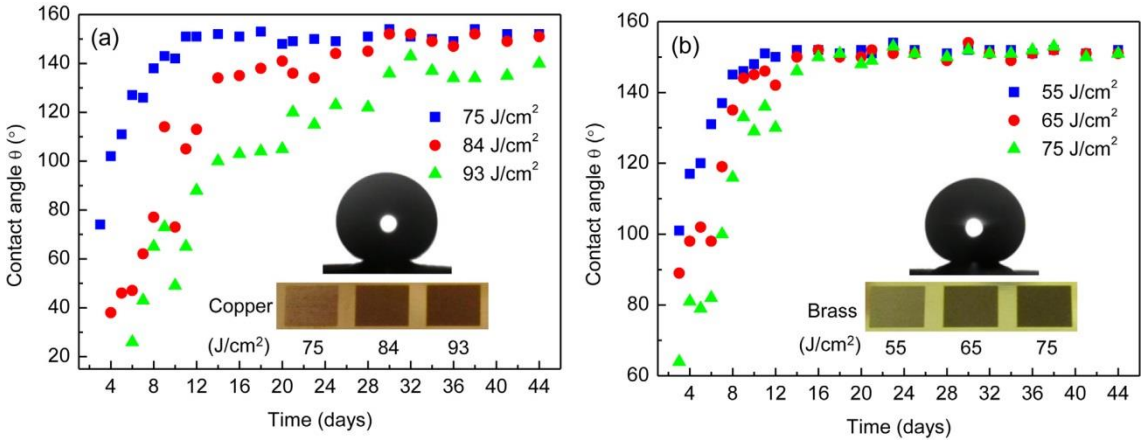

Figure 2.16. Contact angle (wettability) as a function of time for a) copper and b) brass substrates exposed to nanosecond laser texturing with various energy densities, with inset images showing side-on views of water droplets on superhydrophobic textures [58]

As there is no change in the surface morphology over time, the change in wettability is attributed to changes in the surface chemistry, namely in the form of de-oxidation processes [58, 65].

2.4.2 Optical Surfaces

Laser marking is an increasingly common alternative to traditional printing and engraving. There are two main types of laser marking – high contrast laser marking, which has applications in labelling, barcoding and other identification [66], and colour marking, which is desirable for jewellery [67], company logo marking, anti-counterfeiting [68] and others. Conventional laser marking is generally attained by engraving the material surface by ablation. Colour laser marking, however, can be achieved by several different mechanisms including oxide layer formation [69], thermo-chemical reactions [70], annealing and laser induced periodic surface structures (LIPSS) [68]. In addition, lasers can also be used to fabricate other structures on the surface which exploit the properties of light, such as holograms.

Although conventional laser marking is relatively well understood and has been used in industry for long time, research is still taking place in order to find new applications for this process and enhance the capabilities of these laser marking systems [50]. Chen et al., for example, have studied the feasibility of using a laser system to mark eggshells with great success, as can be seen in Figure 2.17 [66].

Figure 2.17. Example identification characters laser marked directly the shell of an egg [66]

Research has been conducted into the marking of plants and fruits with varying degrees of success. Marx et al., for example, have shown successful laser marking of both apples and rhododendron at low laser power levels (5-10W) [71]. In addition, previous studies into laser marking of various other food produce, including avocados and oranges, are mentioned.

Colour marking, on the other hand, is more complex. Most laser colour marking in the literature makes use of ultra-short pulse lasers to generate micro- or nano-gratings (LIPSS), which then exhibit different colours through diffraction [68, 72, 73]. Whilst these gratings can produce a range of vivid colours on most metal surfaces, they cannot produce a uniform colour suitable for logo marking, for example. They do still have their applications, though, with anti-counterfeiting being most suitable. For this application, Yao et al. have demonstrated that two perpendicular gratings can be generated on the same surface area, providing a changing appearance – both colour and geometrically – depending on the orientation of the incident light, as shown in Figure 2.18 [68].

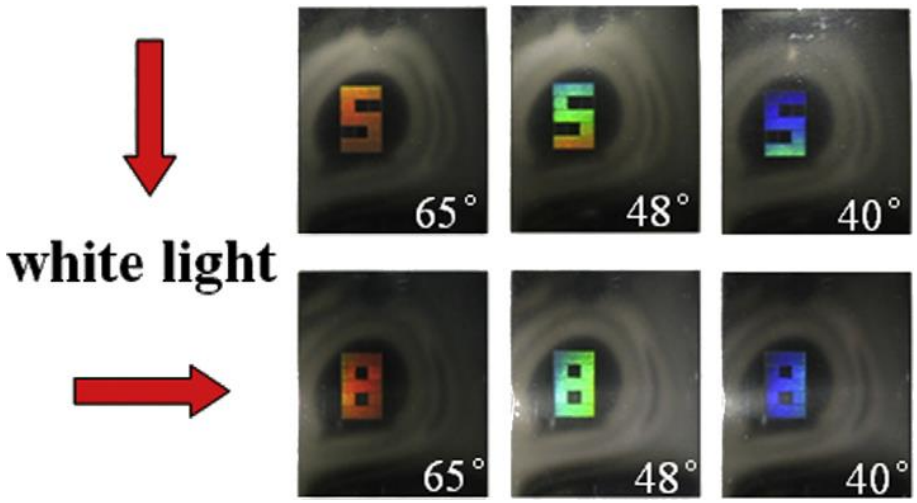

Figure 2.18. Altered appearance of the perpendicular LIPSS markings depending on the direction and angle of the incident light source [68]

The formation of an oxide layer is another method of generating colour markings on a metal surface. The incident laser beam is used to heat the surface of the material such that it undergoes a chemical reaction with the oxygen in the air, producing a transparent oxide on the surface [69]. Provided that the depth of the oxide layer can be kept constant, this allows a uniform colour mark to be viewed due to thin film interference. Li et al. have performed analysis of the oxide layer formed on stainless steel by the irradiation of an Nd:YVO4 laser with wavelength of 355nm, pulse width of 25ns and 7-10W power. The results show that a range of colours can be generated on stainless steel, but also that the process is very sensitive to the laser parameters used to generate the mark [69]. In addition, Antonczak et al. have generated an impressive colour palette on grade 304 stainless steel with a commercially available 20W fibre laser [74]. Although the marks were found to be sensitive to several laser processing parameters, primarily the power, scan speed and spot size (energy density), the obtained marks were highly reproducible as shown in Figure 2.19.

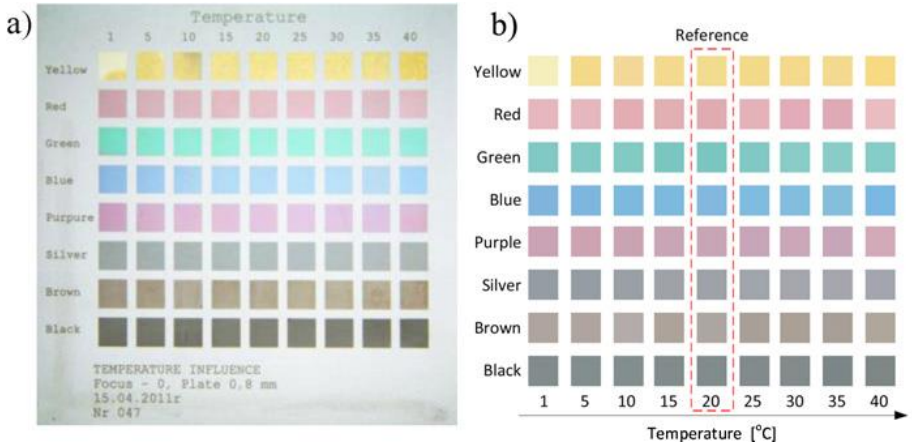

Figure 2.19. Range of colour marks generated on stainless steel 304 at various ambient temperatures [74]

In addition to simple surface marks, information can also be encoded in a surface by generating a diffractive optical element. Wlodarczyk et al., for example, have shown that it is possible to fabricate optically smooth surface features with ultra-violet nanosecond laser pulses, facilitating the generation of holographic structures which can be used as security/anti-counterfeiting marks [75]. In this case, the encoded information becomes visible by illuminating the marked area with a coherent light source and imaging the reflection.

Laser polishing is also receiving increased research attention as an alternative to conventional polishing methods [35-37]. In contrast to the other applications discussed, the aim of laser polishing is to remove surface features leaving an, ideally, optically smooth surface.

Surface roughness can be significantly reduced by laser polishing, as shown by Ukar et al. By using a 1kW fibre laser with 100µm focal spot size, the surface roughness of cast iron (GGG70L) was reduced by 88% to R_a=0.5µm [76]. Similar results have also been observed on AISI H13 tool steel, with a 78% reduction in S_a witnessed after laser polishing with a 550W fibre laser with 1mm spot size, see Figure 2.20 [77]. Use of multiple beams in an attempt to improve results further by pre-heating the surface has also been investigated. Although the micro-roughness was found to increase in martensitic tool steel compared to single beam processing, a smoother surface was obtained for TiAl6V4 (up to 36% lower roughness depending on the spatial wavelength). This was achieved due to the increased melt duration facilitated by the pre-heating beam [78].

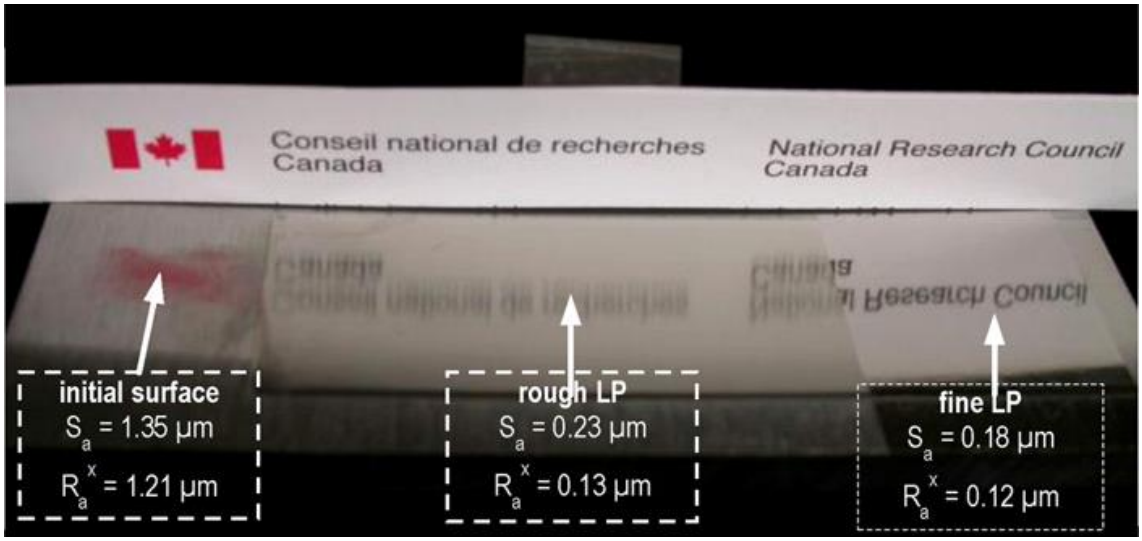

Figure 2.20. H13 tool steel sample showing the initial surface alongside two laser polished surface areas with text printed on paper reflected from the laser polished sample [77]

Although significant improvements in the surface roughness of the laser polished samples have been achieved, there are still issues of waviness of the resulting surface caused by thermo-capillary flow which need to be addressed [37]. Use of a homogenised beam profile may improve the resulting waviness by minimising the thermal gradients within the laser spot.

2.4.3 Adhesion Properties

The adhesion properties of a material surface can also be improved by laser processing [79]. With the use of an intermediate adhesive layer, these improved adhesion properties can be achieved by the generation of dimples or grooves on the material surface to increase the roughness, or holes can be drilled into the material [53]. The use of adhesion instead of welding or mechanical fastening has several advantages, including the prevention of local stress concentrations generated by welding and a reduction in weight compared to the use of screws or bolts [53]. Recently, however, the increase in activity related to improving adhesion properties of metals has been driven by the medical field and, in particular, biomedical implants [69]. As a result, nearly all of the work in this area has been carried out on titanium, or a titanium alloy, due to its inherent properties (strength, corrosion resistance and bio-inertness) [53].

Erdogan et al. have shown that the use of a picosecond laser to generate micro-grooves on the surface of titanium-based alloy, Ti6Al4V, does not improve the cell attachment and proliferation compared to the other surface modification techniques (acid etching and sand-blasting) [79]. It is noted, however, that this kind of laser texturing does have

advantages over the others in terms of spatial selectivity and so may still be useful for certain applications.

Zimmerman et al. also found that laser surface treatment did not provide substantial improvements over other texturing techniques. In this study the surface texturing was performed on titanium using an Nd:YAG laser with wavelength of 1064nm and 80ns pulse length [80]. However, it was noted that the adhesion characteristics of the laser textured sample improved significantly after hydrothermal ageing, with a lap shear strength of ~18MPa compared to ~2MPa and ~4MPa for the untextured and chemically etched samples respectively. This is assumed to be caused by the formation of an oxide layer on the surface which, along with increased roughness and some modification to the underlying layers, leads to a highly stable surface. The possibility of using laser texturing to improve the efficiency of catalytic process is also mentioned, however there appear to have been no studies into this possible application [80].

It has been hypothesised that using the laser to drill holes instead of (or as well as) texturing the surface could improve adhesion properties. Man et al., for example, have compared the fracture load of mild steel after three different treatments – sand blasting, 60 grit grinding and laser hole drilling at various densities (using a 100W SPI fibre laser). The results show that the fracture load increases logarithmically with hole density and, for hole densities greater than $10/cm^2$, the sample with laser hole drilling showed improved adhesion compared to the sand-blasted and grit grinded samples [53]. Two methods of improving the drilling are then suggested. Initially, drilling at an angle to the normal is considered, with the idea that the roots of the angled drill holes will meet creating a form of tunnel to allow cells which grow there to gain access to nutrients more easily, thus allowing stronger bonding. The second suggested method uses the same principle but, rather than angling the drill holes, chemical etching is used to join the roots of the holes. Both of these ideas were achieved experimentally but neither of them were studied in terms of their adhesion properties or for cell attachment [53, 81].

2.5 Friction

Contacting surfaces, and the resulting friction phenomena, are integral to an endless number of applications, many of which are immediately obvious, such as clutches, brakes and ball bearings. However, other applications rely on friction in less obvious

ways, such as mechanical machining, nails and wheels/tyres. From an early level, students are taught about friction in a very simplistic manner, typically involving a basic free body diagram like that shown in Figure 2.21 [82].

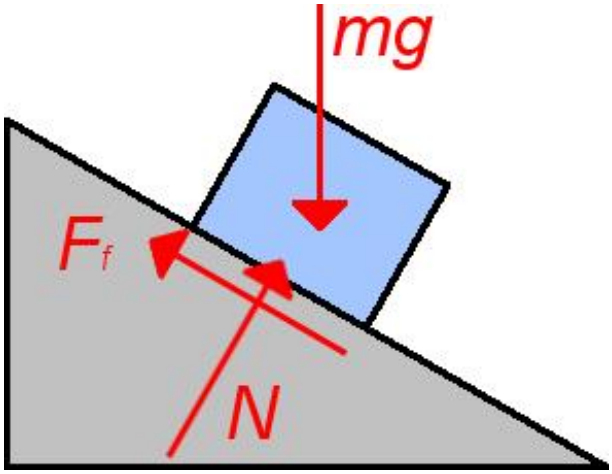

Figure 2.21. Basic free body diagram for a simple friction problem with block of mass *m* on an angled surface and the resulting forces shown in red

The resulting friction coefficient, μ, of the block-slope contact can then be calculated, very simply, as:

$$\mu = \frac{F_f}{N} \tag{2-4}$$

where F_f is the friction force and N is the normal force acting on the block. Two key conclusions can be taken from this simple equation: the friction force is proportional to the applied normal force and the friction force is independent of the contact area [83, 84]. Generally, friction can be grouped into two different types, namely static and kinetic, denoted μ_s and μ_k respectively. As the names imply, the type of friction depends on whether there is relative movement between the two surfaces in question. In addition, the static friction coefficient is generally assumed to be a material constant although this has been shown to not be the case [85].

Although this simplistic view of friction holds true for a surprising number of situations, the technicalities are somewhat more complicated. As such, a number of contact models have been proposed and developed in an attempt to understand the finer details of the mechanics providing the foundation for friction, including the Chang-Etsion-Bogy (CEB) friction model and Derjaguin-Muller-Toporov (DMT) adhesion model [86, 87]. Calculations based on these models typically consider a small

number asperities and relatively simple contact geometries, such as a spherical asperity contacting a plane surface, although scaling of the friction modelling from microscopic level to macroscopic level is currently being undertaken [88, 89]. In addition, the models are based on elastic-plastic contacts and, as such, the normal load, mechanical properties, nominal contact area and surface roughness have been shown to have a large impact on the calculated static friction coefficients [87]. This is due to the deformation of the asperities as the surfaces are brought into contact under the influence of an external normal force, resulting in adhesion forces and material plasticity contributing to the friction coefficient [90].

Although there are several different contact regimes, such as point contact and rolling contact, it is primarily the flat-on-flat contact friction regime which is of interest for the work presented in this thesis [84].

2.5.1 Reducing Friction

In most cases, friction only becomes a major concern where relative movement is desired and therefore friction is unwanted, reducing the system efficiency and increasing wear. Static friction, or 'stiction', can also be a concern; however this is typically limited to a few applications, particularly valves and N/MEMS (nano-/micro-electromechanical systems) [91-94]. As a result, a significant amount of research has taken place with regards to decreasing the kinetic friction coefficient of contacts, including a considerable focus of the use of laser surface engineering for this application. Typically, the friction coefficient of a contact can be reduced by the application of a lubricant, either solid or liquid. However, the surfaces themselves can also be modified in order to reduce the friction coefficient, particularly when combined with lubrication.

2.5.1.1 Laser Surface Texturing for Reducing Friction

The majority of the work in this area has concentrated on the generation of arrays of dimples on one of the contacting surfaces in order to reduce the friction coefficient of lubricated contacts. As depicted in Figure 2.22, there are three primary methods by which these laser-induced dimples act in order to reduce the kinetic friction coefficient [95, 96].

1. The dimples act as lubricant reservoirs, allowing replenishment of lost lubricant.
2. The lubricant held within the dimples can act as hydrodynamic bearings, applying a force perpendicular to the contacting surface.
3. The dimples can act as traps for wear debris, reducing the wear of the surfaces.

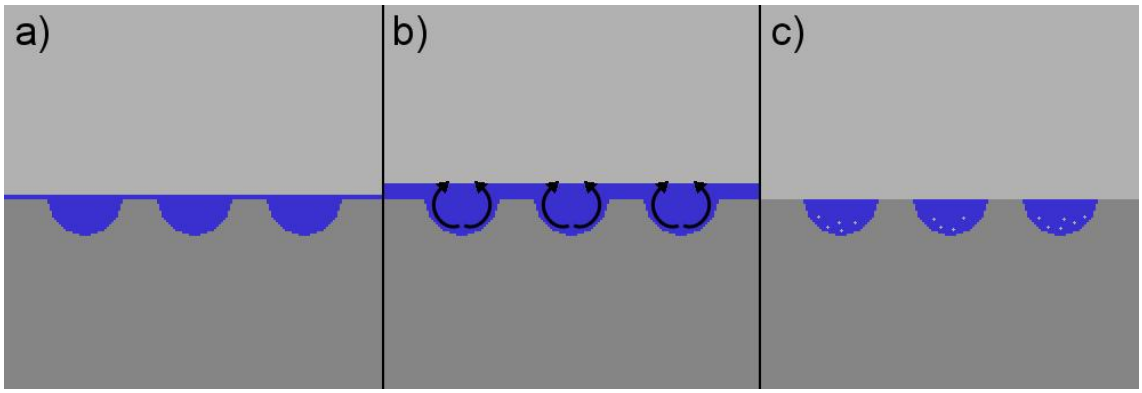

Figure 2.22. Schematic depicting the three methods by which dimples act to reduce friction; a) lubricant reservoirs, b) hydrodynamic bearings and c) debris traps

Dimensions for these dimples typically vary between 50-300µm diameter with 5-80µm depth [97, 98] for a range of dimple area coverage. As well as the large range of laser processing parameters, there are many other variables to consider for this application including the sample materials, contact type, contact pressure, sliding speed, lubricant type and ambient temperature. Therefore, despite the publication of many positive results for a range of applications, it is difficult to make a single conclusion from the literature in this field [96]. However, a selection of results is discussed in order to understand the present state of research in this area.

It has been shown, by Ze et al., that laser surface texturing can be used to successfully decrease the friction coefficient of a contact [99]. In this study, both dimples and grooves were generated on cemented carbide prior to reciprocating ball-on-flat tests with Ti-6Al-4V balls using Molybdenum disulphide (MoS_2) solid lubricant. Friction coefficients were reduced by 15-20% for dimpled samples and 30-35% for grooved samples compared to untextured samples. Wear rates were also found to decrease, although this was found to be dependent on the sliding speed [99].

Laser surface texturing has also been used to reduce the friction coefficient of Si_3N_4/TiC in reciprocating sliding contact with a stainless steel ball (AISI 440C) [100]. In this case, laser texturing was performed in order to generate arrays of grooves on the

surface, both linear and 'wavy' (see Figure 2.23), with separation varied between 100µm and 400µm. The wavy grooved sample with 100µm separation proved to provide the largest decrease in average friction coefficient, with a drop of 22.1% from μ_k~0.65 (for untextured) to μ_k~0.5. In addition, the wear rates of all laser textured samples were found to be lower than that of the untextured sample. It is expected that the capture of wear debris by the grooves is responsible for the observed improvements.

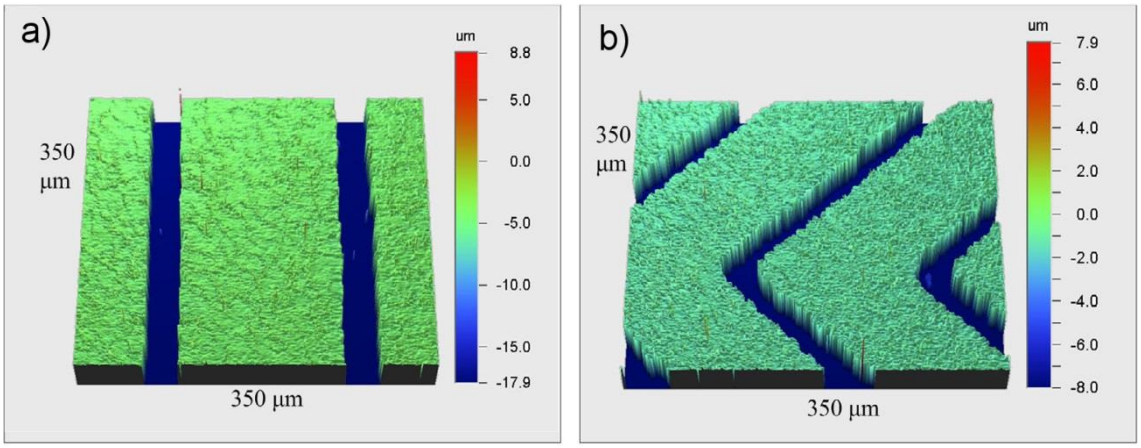

Figure 2.23. WLI measurements of a) linear and b) wavy grooves fabricated into Si3N4/TiC for friction reduction [100]

For dimples, the depth and aspect ratio have been shown to be important parameters. Scaraggi et al. have shown that the optimal dimple depth for friction reduction changes with dimple diameter from 3.7µm at 50µm diameter to 3.9µm at 100µm diameter, regardless of the lubrication regime [101]. The results presented also highlighted the sensitivity to the dimple depth, with dimples slightly deeper or shallower resulting in higher friction coefficients than the untextured surface. In this study, testing was performed with a pin-on-disk tribometer using textured AA6061 aluminium alloy substrates with a machined 100Cr6 ball bearing.

Braun et al. have also presented interesting results [102]. Laser texturing was performed on C85 steel, generating arrays of spherical dimples with diameters ranging from 15µm to 800µm, constant depth-to-diameter ratio of 0.1 and dimple area coverage of 10%. Friction tests were performed under mixed lubrication (using poly-alpha-olefin) against 100Cr6 bearing steel. Results showed that the depth, or depth-to-diameter ratio, is not the only important parameter but that the friction coefficient is also highly dependent on the dimple diameter. In addition, friction testing at different temperatures resulted in different optimal texturing parameters, 200µm dimple diameter at 50°C compared to 40µm dimple diameter at 100°C. This is

primarily due to the change in lubricant viscosity with temperature, resulting in a shift in the friction regime.

Dimple density was also found to be an important parameter, with 5-10% being deemed the most efficient dimple density – Ze et al. indicated that a density of 7.1% resulted in the lowest coefficient of friction value [103] whilst Voevodin et al. suggests a density of approximately 10% [104]. Although it has not been thoroughly investigated, dimple depth can also have an effect on the friction coefficient with Podgornik et al. suggesting that increasing depth leads to lower friction values, when using an Nd:YAG laser with a wavelength of 1064nm on AISI 52100 steel [95].

More complex techniques for laser texturing have also been reported. Laser interference metallurgy, for example, has been used to fabricate dimples, grooves and 'cross' patterns on grade 304 stainless steel [34]. Testing was performed using a pin-on-disk tribometer with typical engine oil (20W/50). Whilst lower friction coefficients were obtained for all of the laser textured samples compared to untextured, the lifetime of the grooved samples was found to decrease compared to untextured, indicating that the groove structure allows the lubricant to drain away easier than on flat surfaces. Both dimple and cross patterns, shown in Figure 2.24, were found to decrease the friction coefficient and increase the lifetime of the lubricating film by 150% and 1500%, respectively [34]. This was attributed to a greater structural density and depth which allows a larger volume of lubricant to be stored in the 'reservoirs' without exhibiting a draining effect.

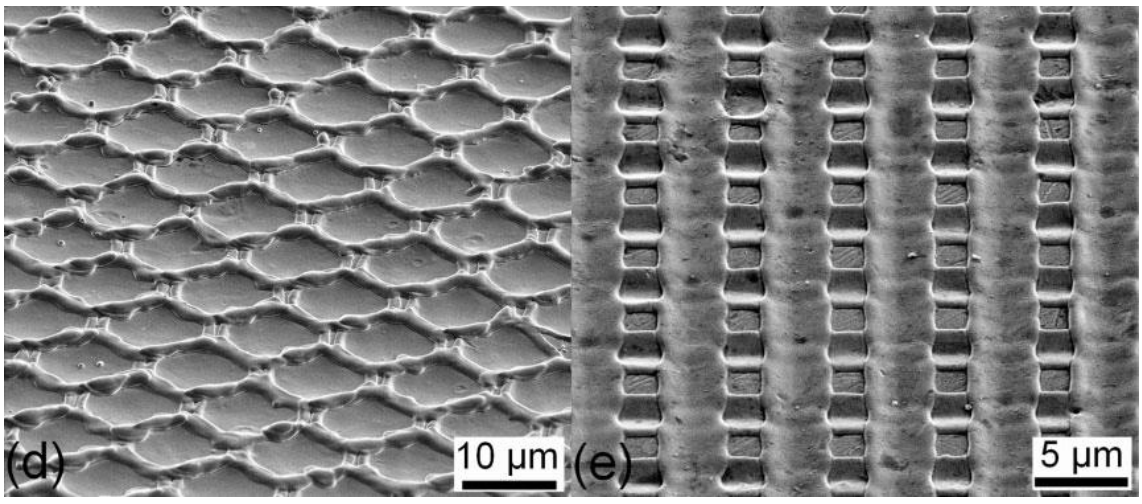

Figure 2.24. SEM micrographs of dimple and cross patterns on SS304 generated by laser interference metallurgy [34]

In addition to this substantial improvement, Etsion states that, with appropriate laser surface texturing, the lifetime of mechanical seals can be increased by a factor of three [105]. This testing was performed by Gadiv Petrochemical Industries Ltd., one of the largest petrochemical companies in Israel. The seal treated with LST performed for more than 10,000h over 38 months, compared to an untextured seal which required replacement four times within the same period.

Interestingly, it has also been shown that the use of multiple different shapes within the same surface texture can result in friction reduction [106]. In this case, a Q-switched Nd:YAG laser was used to fabricate three different textures on hardened (~60HRC) AISI 52100 steel and tested with a pin-on-disc tribometer. All textures contained circular dimples in addition to elliptical, square or triangular dimples. Friction was found to decrease compared to an untextured sample under both dry and lubricated conditions, with significant wear debris trapping by the dimples observed.

The effect of the resulting bulges generated at the circumference of laser induced dimples has also been studied for lubricated friction applications [107]. Testing was performed on a laser textured copper based alloy using a reciprocating pin-on-disk tribometer with a Cr-coated steel pin. All dimpled samples were found to have lower friction coefficients and wear rates compared to that of the polished samples. In addition, whilst the bulges around the dimples were not found to be detrimental to the friction, samples with smaller bulges resulted in lower friction coefficients [107].

Contrary to the majority of the literature, Olofinjana et al. have reported that, under certain conditions, laser surface texturing can actually increase the friction coefficient of a surface [108]. The resulting surfaces tested in this case are shown in Figure 2.25. In the absence of lubricant additives, samples subject to LST exhibited reduced friction coefficients compared to polished samples. On the other hand, when low friction additives were present, the LST was observed to disrupt the stable tribochemical flows, resulting in higher friction coefficients than for the polished samples. In addition, laser surface texturing of both contacting surfaces has been found to be detrimental to the friction coefficients and wear rates, with an increase of 100% in friction coefficient being reported by Hoppermann and Kordt [109].

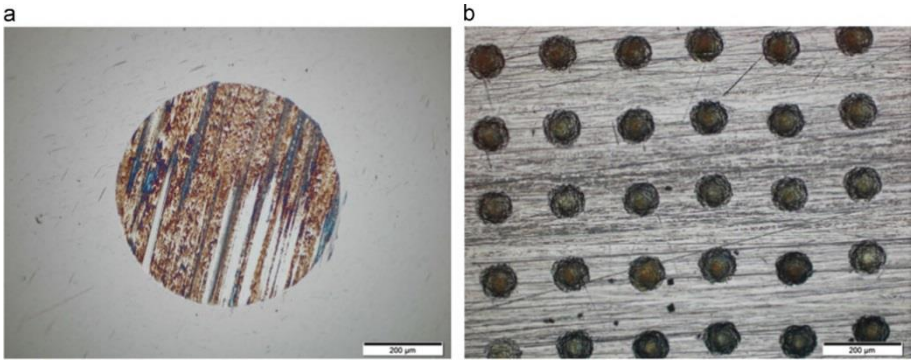

Figure 2.25. Optical micrograph of wear track on (a) ball and (b) LST flats tested with additised oil [108]

Therefore, it is clear that laser surface texturing, in the form of dimples, grooves or more complex features, can be used to reduce the friction coefficient and wear rate of a contact if an appropriate texture is chosen. The optimal texture is dependent on many variables and, as a result, a trial and error process is typically used in order to determine the best parameters. In addition, inappropriate choice of texture parameters can not only lead to sub-optimal performance, but may also increase the friction coefficient compared to an untextured surface. Whilst this increase in friction is clearly undesirable in the cases mentioned here, in certain cases it can be beneficial.

2.5.2 Increasing Friction

With the exception of a handful of applications such as brakes, kinetic friction is typically deemed detrimental. However, for many applications it can be beneficial to have high static friction, particularly in cases where relative movement is unwanted or transfer of force/torque through an interface is desired. Examples include the handbrakes and clutches in cars. It should also be noted that, in these types of applications, the contact is typically unlubricated.

2.5.2.1 High Friction Regimes

Therefore, research into the generation of high friction surfaces is substantiated by the existence of applications requiring such surfaces. Intuitively from everyday life, we associate rough surfaces with high friction. However, surface roughness is not the only property which can impact the static friction coefficient. In order to create a metal-metal contact with a high static friction coefficient at least one of the following regimes must play a significant role: embedding, interlocking and adhesion. Without a significant contribution from any of these three possibilities, any contact will maintain a relatively low friction coefficient.

2.5.2.1.1 Embedding

Embedding occurs when the normal force applied to a contact is large enough that some of the asperities on at least one of the surfaces are pushed into the counter surface material. This requires one of the surfaces to be substantially harder than the other for noticeable embedding to occur. Figure 2.26 shows a simplified schematic of exaggerated embedding.

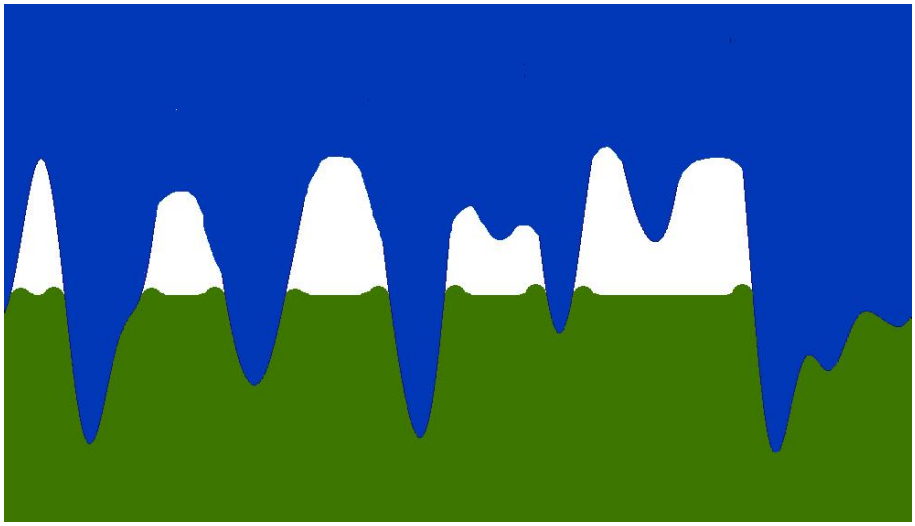

Figure 2.26. Schematic showing embedding of asperities of rough upper (blue) surface into flat lower (green) surface; white areas indicate air gaps between the two surfaces

When a load force is applied to such a contact, slippage is only observed when either the embedded asperities break due to the shear force or when the substrate in which they are embedded yields and thus the asperities plough through the surface. Therefore high static friction coefficients can be obtained.

2.5.2.1.2 Interlocking

Two surfaces can interlock effectively when both surfaces have similar topographical features, such as the perfect case shown in Figure 2.27. Unlike embedding, interlocking does not inherently require application of a high normal force to enable good interlocking. However, for a pair of surfaces which do not inherently interlock perfectly, a large normal force can facilitate some surface deformation resulting in improved interlocking and increased real contact area. In the perfect case, the friction force would be required to break all asperities from one or both of the surfaces in order for the surfaces to move laterally relative to one another.

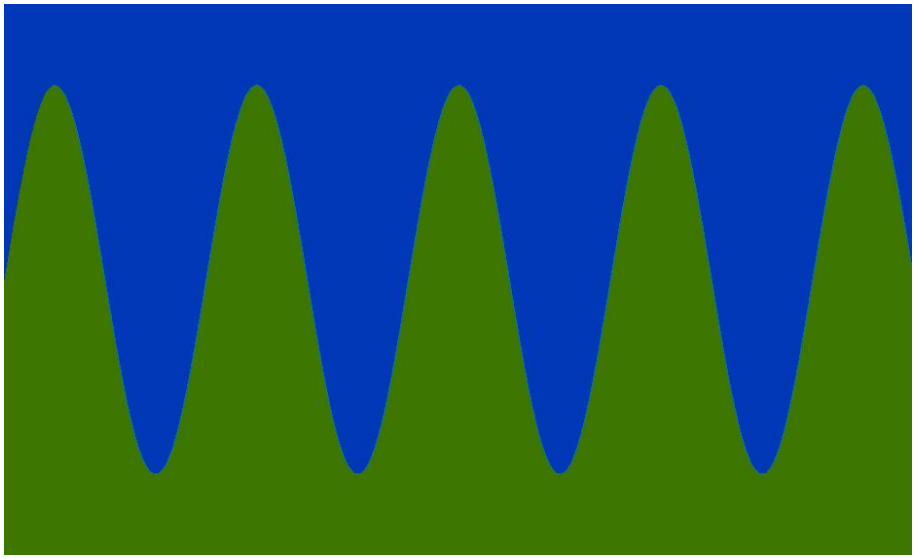

Figure 2.27. Schematic showing perfect interlocking of two surfaces

2.5.2.1.3 Adhesion

Adhesion can also contribute to the friction coefficient of an interface, particularly when one of the contacting materials is soft or smooth [83]. Adhesion arises from intermolecular forces which generate an attraction between the atoms and molecules from the two surfaces when they are in close proximity. This is the same process which occurs during cold pressure welding. In this case it is the plastic deformation caused by the large normal force which causes any surface oxide or contaminants to be pressed out and direct metal-metal contact to be made [110]. In order to produce lateral movement between the two substrates, all of the chemical bonds formed are required to be broken in addition to any possible embedding and interlocking of the asperities.

2.5.2.2 Techniques for Increasing Static Friction

Several different techniques have been reported to result in relatively high friction surfaces, although typically the focus is towards increased hardness for wear reduction in these cases.

HVOF (high velocity oxygen fuel) and HVAF (high velocity air fuel) spray coatings of WC–10Co4Cr, for example, have been shown to give friction coefficients of around 0.6 at room temperature, and greater than 1 at elevated temperatures of 400°C [111]. In these tests, coatings were sprayed onto low-carbon Domex 355 steel substrates with thicknesses of 250-300µm. Friction and wear testing was performed with Al_2O_3 spheres on a ball on disk tribometer. It should also be noted that the micro-hardness of the spray coating was measured to be in the range of 800-1750HV for all samples tested.

Electrolytic hard chrome (EHC) plating has also shown promise with friction coefficients of 0.52±0.07 reported at room temperature [112]. Friction tests here were performed with a grade 304 stainless steel (~227HV) ball-on-flat reciprocating tribometer and compared to samples coated with WC-CrC-Ni by HVOF. All samples were polished to R_a=1-1.4µm prior to testing. In these tests the HVOF sprayed samples exhibited a friction coefficient of 0.35±0.05 at 25°C.

Some more creative techniques have also been investigated, such as the generation of nano-textures on aluminium substrates by anodic aluminium oxidation [113]. The nano-texture, consisting of a hexagonal array of dimples with ~250nm diameter (see Figure 2.28a), resulted in friction coefficients >4 under dry conditions when measured with a PDMS ball on flat test.

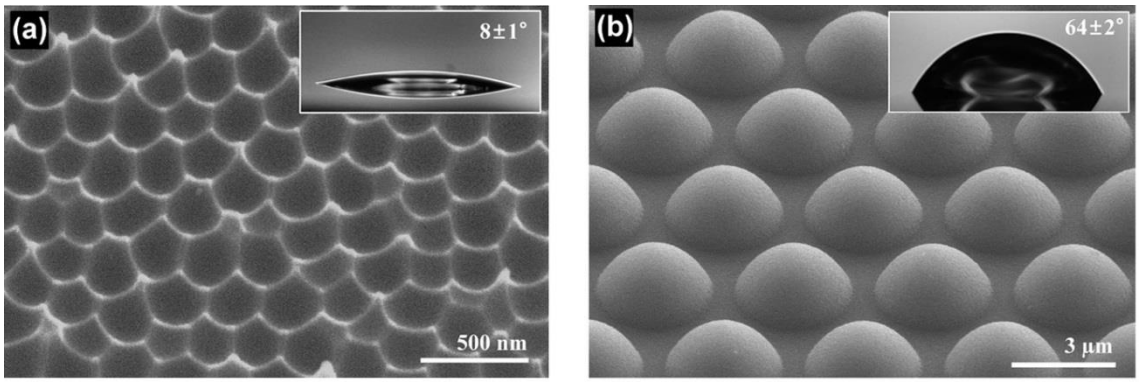

Figure 2.28. SEM images of a) nano-textured and b) micro-textured aluminium surface generated with anodic aluminium oxidation, inset images show wettability measurements for these textures [113]

Each of the techniques that have been mentioned thus far have been tested under sliding conditions; as a result, the friction coefficients quoted are kinetic, rather than static, however they give an indication of the coefficients which are achievable.

An interesting idea to intentionally increase the static friction coefficient of a surface has been put forward and tested by Hammerström and Jacobson [114]. By using a combination of photolithography, etching and CVD (Chemical Vapour Deposition) of diamond, regular arrays of diamond pyramids have been successfully generated with area densities of 2% and 22%. SEM micrographs of the 22% area density surface are shown in Figure 2.29. The diamond textures were tested in flat on flat tests against both steel and silver substrates at normal pressures up to 20MPa, with the resulting static friction coefficients consistently >1.2. Such high friction coefficients were obtained due

to embedding of the diamond pyramids into the metal substrates, which then require a large force to plough through during the friction tests. Despite the impressive friction coefficients obtained, the intricate and environmentally unfriendly process required to generate such textures make this technique unappealing for industrial processes.

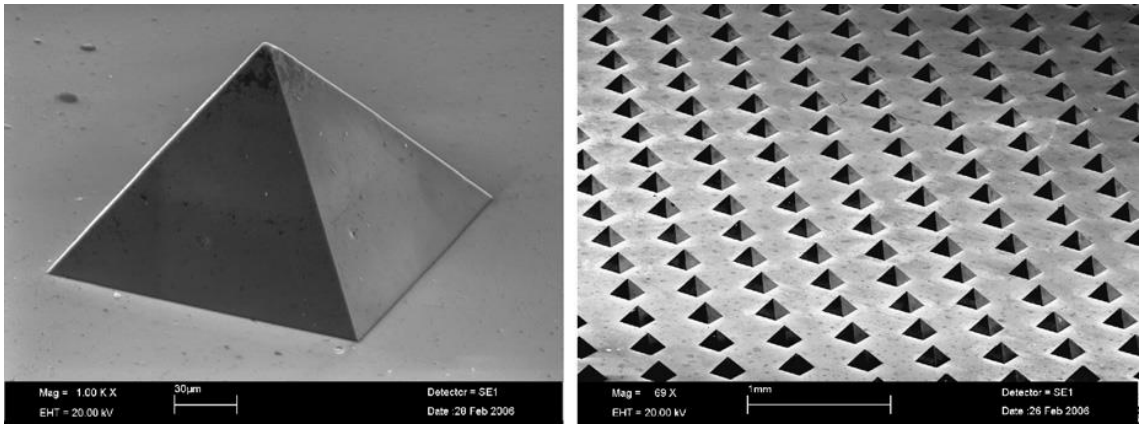

Figure 2.29. SEM images of surface with 22% area fraction covered with diamond pyramids [114]

As mentioned in Section 2.5.1.1, LST has been reported to increase the friction coefficient under sliding conditions [108, 109], albeit unintentional and undesirable in these cases. In addition, Vilhena et al. have also shown that laser texturing can increase friction, when the contact width is in the same range as the diameter of the generated dimples. For these tests, textures were generated with dimples of 150µm diameter and 10µm depth and tested in both point and flat contact regimes. The friction coefficient was found to decrease in the flat contact regime but increase in the case of point contact [115].

Contrary to the previously discussed literature, Varenberg et al. have shown that the trapping of wear debris in the laser induced dimples can also increase the friction coefficient [116]. Unlike the case of lubricated contact where removal of wear debris from the contact zone decreases friction, in particular dry contacts, the presence of wear debris can act to prevent adhesion. For the steel-on-steel (hardened 4140 steel) results presented, the friction contribution from adhesion was larger than the contribution of the debris in the contact zone, resulting in a friction increase upon trapping of the debris.

More recently, a novel approach has also been considered where raised bumps on the surface are generated by deep penetration welds [117]. In this case, the friction coefficient was found to increase significantly compared to the untextured sample (up to

~0.82 compared to ~0.3); however the torque-angle curves indicate that this is kinetic friction rather than static friction.

2.5.2.3 Applications of MDT

As previously mentioned, MDT has interest in high friction surfaces, with several possible applications suggested appropriate for work performed as part of this project. These applications were within the main bearing, drive shaft and piston rod assemblies in their diesel marine engines. A diagram of a 'small' two-stroke MDT is shown in Figure 2.30.

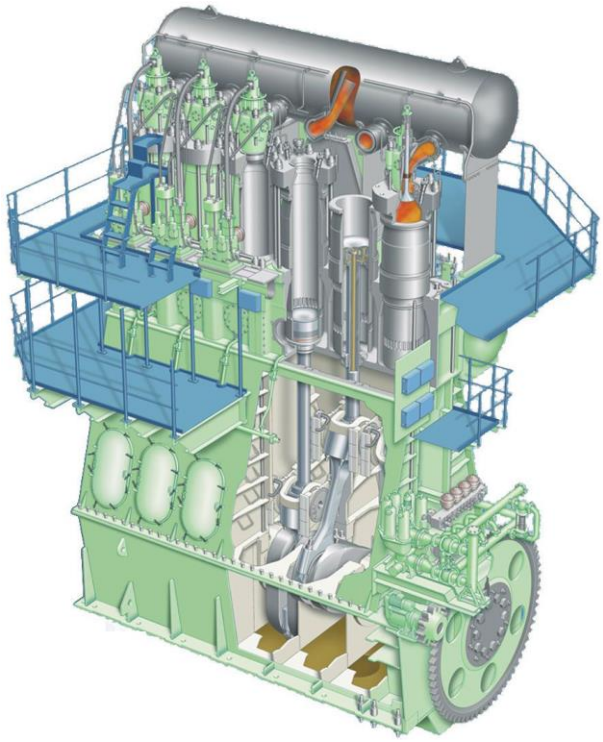

Figure 2.30. Diagram of MDT two-stroke diesel engine from which the high friction applications are based

These applications are discussed in detail at the end of the relevant chapters. However, the initial application considered, the main bearing assembly, required a minimum static friction coefficient of μ_s=0.6. For this case, an intermediate shim with high friction was required to be placed between the two components of the engine. Therefore, initial trials were set up to emulate this arrangement, with the application requirement set at 0.6. Initial studies performed by MDT and SPI Lasers gave promising results, with friction coefficients of up to μ_s=0.79 being achieved [118]. This positive outcome led to the continuation of this work, enabling the results presented in this thesis.

2.6 Summary & Conclusion

Surface engineering is a very broad field, which has only very briefly been covered here. Through a variety of techniques, significant research is currently taking place in order to satisfy the huge range of applications requiring tailored surface properties. Laser surface texturing has been shown to be an extremely competent and versatile technique for surface engineering applications, particularly in the field of friction reduction. Despite a number of applications requiring high friction surfaces, little research has been presented thus far on surface modification for increasing friction coefficients. With this in mind, the work presented in this thesis aims to address this gap by using laser surface texturing in order to achieve high static friction surfaces.

Chapter 3 – Characterisation of Laser-Material Interaction

This chapter concerns the generation and characterisation of various surface features on stainless steel substrates by the use of near-infrared long (>200ns) nano-second laser pulses. These tests were performed in order to get an experimental understanding of the surface feature types able to be generated in this processing regime. Studied features include individual craters, lines (generated by overlapping pulses) and area textures (generated by overlapping lines) created by different laser types. Results from each of the feature types studied were also considered from the perspective of the high friction application requirements (directionality etc.).

3.1 Experimental Set-up

An experimental set-up was designed and made for laser processing; making use of several different models of SPI fibre lasers and a galvanometric scan head for scanning the laser beam across the surface of the samples. A basic schematic and photograph of the workstation are shown in Figure 3.1.

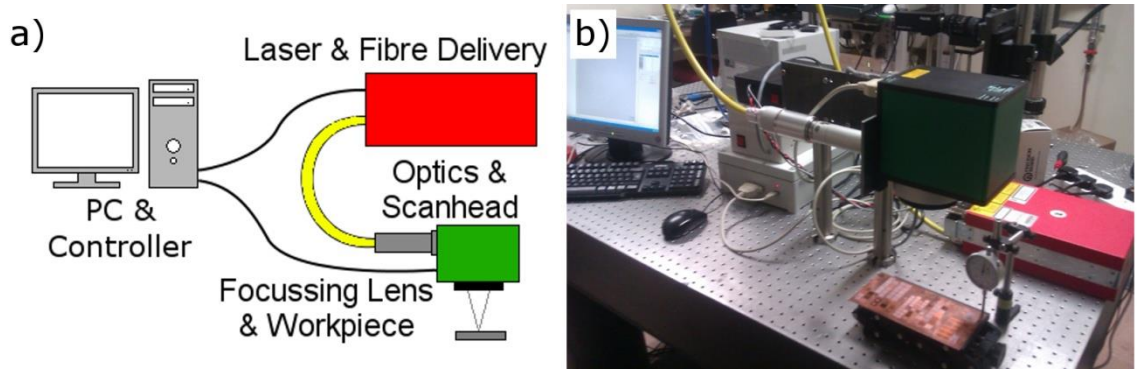

Figure 3.1. Schematic (a) and photograph (b) of laser processing workstation

Several different SPI lasers were used throughout the project, primarily the 20W HS-L, 50W HS-S and 20W EP-S, with different beam qualities, available power and pulse durations. Initial characterisation and testing was performed with a 20W HS-L laser. Table 3.1 gives a comparison of the different laser parameters available from each model used (from the SPI specifications).

Laser Model	20W HS-L	50W HS-S	20W EP-S	20W EP-Z	70W RM-Z
Wavelength	1064nm	1064nm	1064nm	1064nm	1064nm
Max. Avg. Power	20W	50W	20W	20W	70W
PRF0 (for WF0)	25kHz	70kHz	28kHz (WF32)	20kHz (WF32)	70kHz
Max. Pulse Energy	0.8mJ	0.71mJ	0.71mJ	1mJ	1mJ
Beam Quality (M^2)	$1.6<M^2<2$	<1.3	<1.3	<1.6	<1.6
Pulse Duration	9-200ns	15-220ns	3-490ns	3-500ns	35/250ns
Available Spot Sizes	~35, ~50µm	~25, ~35µm	~25, ~35µm	~32, ~43µm	~30, ~41µm

Table 3.1. Comparison of notable laser parameters for the different SPI laser models used, specifications from SPI (further waveform information available in Appendix A – SPI Laser Waveform Tables)

Here, the PRF0 (Pulse Repetition Frequency 0) is the highest repetition rate which gives the largest pulse energy for a given waveform (WF, tuneable pulse duration). The laser beam is delivered through the in-built optical fibre to the beam expander optics, which expand and collimate the beam prior to entering the galvo scan head. Two different beam expansion collimators (BEC) were used, giving nominal collimated output beams of 8mm and 11mm. The galvo-scanner then deflects the beam as required before an F-Theta lens (160mm FL) focusses the beam onto the work piece. Both the laser and scan head are controlled by a SCAPS hardware controller (USC-1) and computer software (SAMLight 2D).

3.1.1 Measurement & Analysis

Subsequent to laser processing, samples were measured and analysed with an optical microscope (Leica DM6000M). By using this microscope's depth measurement capability along with software dedicated to processing and exporting the 3D data (Leica Map), both lateral and depth information was acquired, allowing analysis in three dimensions. For the initial characterisation, this facilitated the measurement and analysis of crater depth and diameter, as well as 2D roughness information when looking at area textures. The data acquired was typically exported for analysis in Matlab, with custom written scripts to handle the particular data formats. Whilst not used for the results generated in this initial characterisation chapter, an Alicona InfiniteFocus 4G surface profilometer was also used to calculate a range of roughness parameters and measure various surface profiles of high friction textures presented in Chapter 6.

3.2 SPI 20W HS-L

Characterisation of the laser output was performed prior to any material processing. By using the same set-up as shown in Figure 3.1, but replacing the work piece with a thermopile power meter (Ophir FL-250A-LP1-SH-V1), the laser power and pulse energy were characterised. Using this set-up, with the power meter after the scan head, the power which is incident on the work piece during machining can be accurately measured. Figure 3.2 shows the dependence of the average power and pulse energy characteristics of the 20W HS-L laser on the pulse repetition rate, when using a simmer current of 85% (as advised by SPI), compared to the expected values from the manufacturer's specification. The simmer current facilitates a continuous state of population inversion within the laser, allowing laser pulses to be generated on demand. At low values of simmer current, full population inversion is not achieved and therefore the output pulse energy is lower than desired. However, if the simmer current is set too high, spontaneous emission is likely to occur, resulting in unwanted and possibly untimely beam leakage.

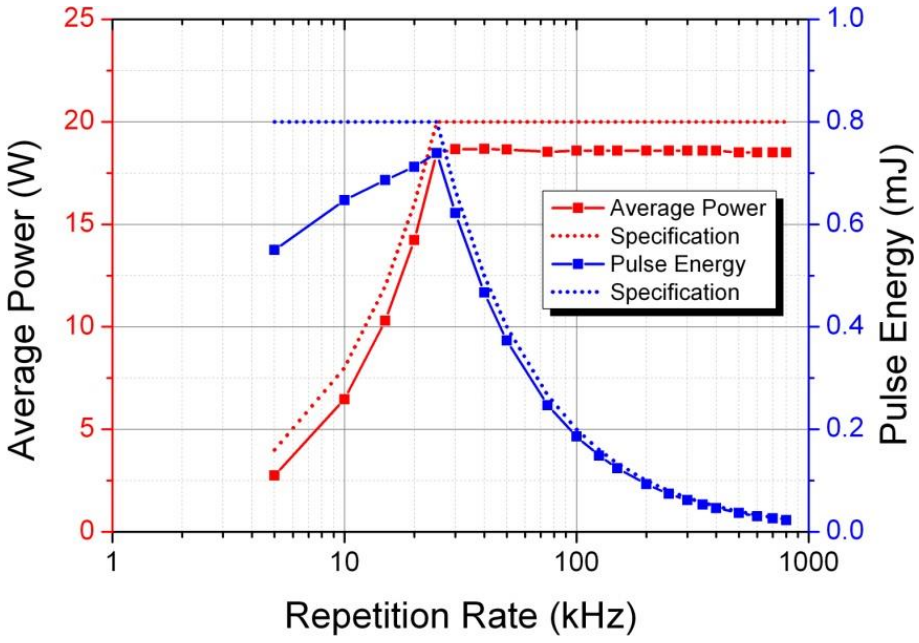

Figure 3.2. Average power and pulse energy as function of repetition rate for waveform 0 (~200ns pulse width) at maximum power and 85% simmer current, with the corresponding specification curves plotted as dotted lines

As can be seen in Figure 3.2, the average power is consistently below the specification value throughout the range of repetition rates by about 1.5W. This can, in part, be attributed to unavoidable losses in the collimating optics, galvo scan head and focussing optics. The pulse energy can also be found to tail off at low repetition rates, likely

caused by reduced population inversion at such low pump rates. This effect can be mitigated by increasing the simmer current, at the risk of increased beam leakage. A simmer current of 85% was used in these tests, and all future tests, as the output is close to the expected value for useful repetition rates with no noticeable beam leakage.

As a result of the laser properties observed in these measurements, the following laser-material interaction characterisation was performed using WF0 at 25kHz repetition rate in order to give the maximum pulse energy and power. A nominal beam diameter of 8mm was chosen at entry to the scan head, giving a theoretical focussed spot size of ~50µm. Initial characterisation was conducted on grade 304 stainless steel (SS304) with following tests on low alloy 'nitriding' steel (Cr-Mo-Al) and grade 316 stainless steel (SS316). All laser powers and pulse energies referred to are the expected, specification values, rather than measured/calculated values from these results, for simplification.

3.2.1 Individual Craters

First, the effect of increasing number of pulses on individual craters was studied. The number of pulses per crater was varied between one and five for each array of 25 craters generated, with each crater separated by 1mm. For crater arrays requiring more than one pulse, all 25 craters are generated with a single pulse before repeating for as many times as required. As a result, the laser beam is never stationary on a single crater and the time between consecutive pulses at a given crater location is >1ms.

Crater depth was found to increase linearly with number of pulses for pulse energies greater than the ablation threshold for SS304 (~0.2mJ, ~10Jcm-2), as shown in Figure 3.3.

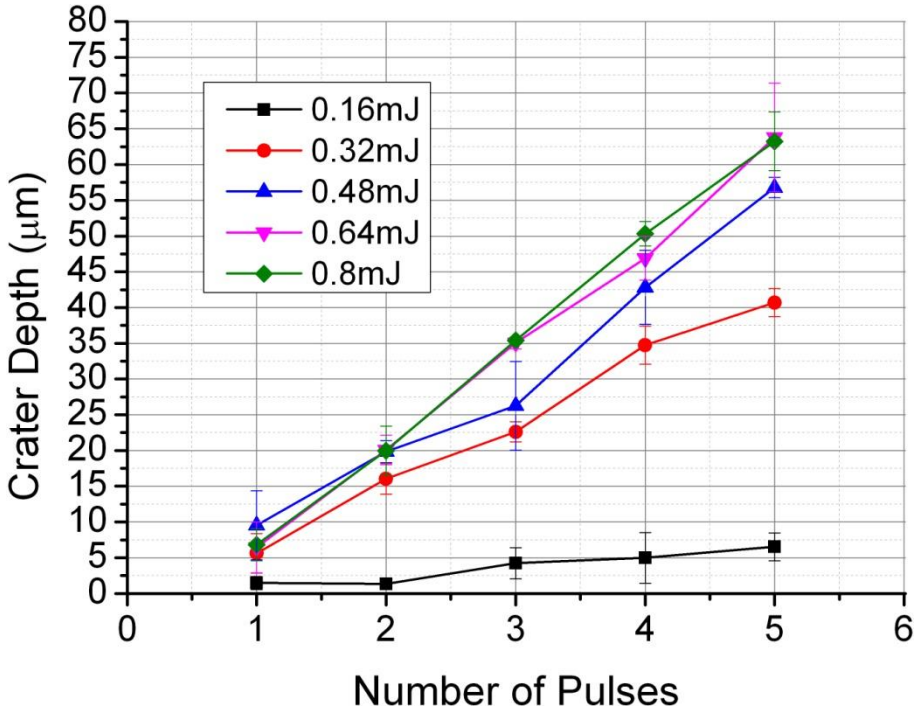

Figure 3.3. Crater depth as a function of number of pulses, for different pulse energies; 20W HS-L

The results show an approximately linear trend which confirms that each pulse (with energy above the ablation threshold) removes approximately the same depth of material from the crater. Given that the temporal pulse spacing (~1ms) is sufficient to allow the sample to reach close to thermal equilibrium between consecutive pulses and the change in depth being significantly less than the Rayleigh range (~1.8mm) of the focussed laser beam, this was the expected result. The diameters of the craters were then measured.

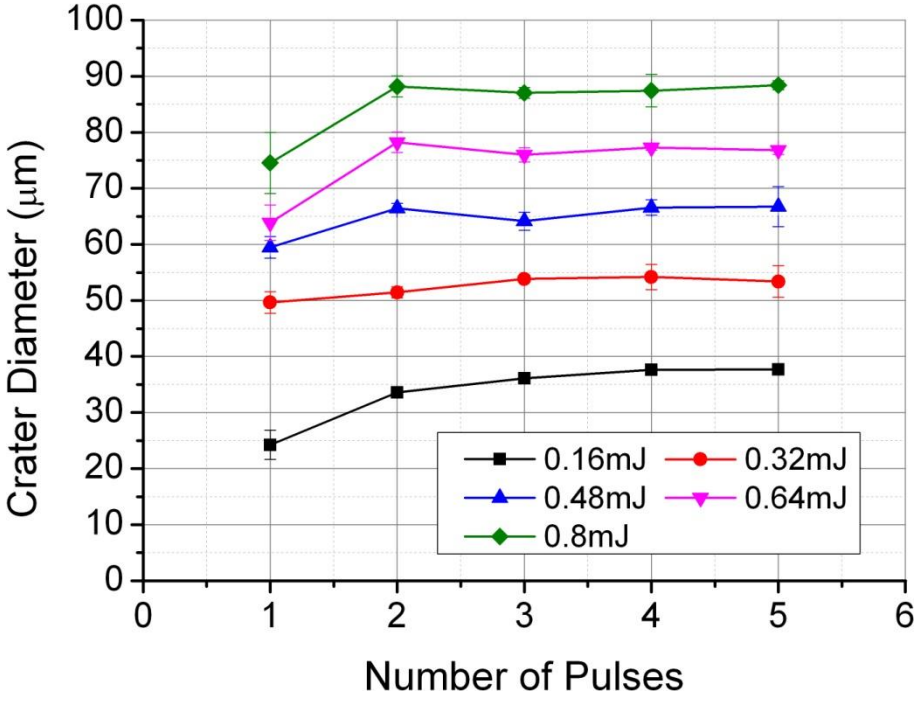

Figure 3.4. Crater diameter as a function of number of pulses, for different pulse energies

Figure 3.4 shows that the diameter of the crater is independent of the number of pulses used. Since the laser pulses are repeated at the same point on the sample, the area of the crater where the laser fluence is above the ablation threshold remains constant and so the diameter of the crater remains constant, regardless of the number of pulses. This is highlighted in Figure 3.5 which shows micrographs of two individual craters.

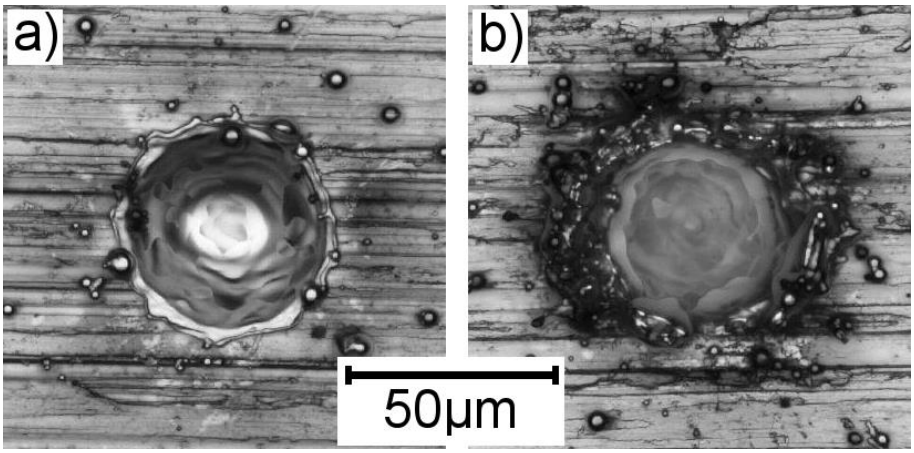

Figure 3.5. Comparison of single pulse (a) and five pulses in the same position (b) using the same laser parameters; ~0.4mJ

Figure 3.5a shows a crater generated by a single laser pulse, whilst Figure 3.5b shows a crater generated by five individual pulses using the same laser parameters. It is clear that the crater does not change shape or size significantly (<<5µm change), indicating that the scan head and controller system are performing as expected. However, more debris can be observed after five pulses, due to the increased depth of the crater reducing the ability of the pulse to eject the melt effectively.

By replotting the data shown in Figure 3.3 and Figure 3.4, the dependence of the crater depth and diameter on the pulse energy can be clearly observed, as shown in Figure 3.6.

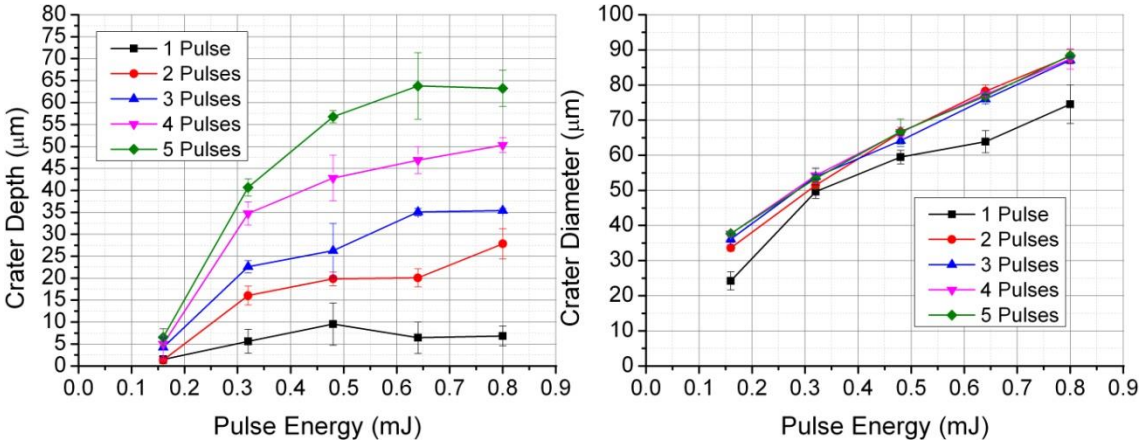

Figure 3.6. Crater depth (left) and diameter (right) as a function of pulse energy, for different numbers of pulses

In contrast to the results where the number of pulses was varied, the crater depth was found to increase only slightly by increasing the pulse energy when above the ablation threshold, whilst the diameter increased linearly with pulse energy. The crater diameter is likely to be highly dependent on the area of the central part of the beam for which the fluence exceeds the ablation threshold, explaining the dependence on pulse energy.

The results shown in Figure 3.3, Figure 3.4 and Figure 3.6 are the averages of 3 separate measurements obtained from the optical microscope mentioned in Section 3.1.1. The error bars plotted on these graphs are the standard deviations of the measurements and, as can be seen from the figures, is typically <<5µm, indicating that the features formed by the laser pulses are very uniform. This is in agreement with what was seen by visually inspecting the sample after laser processing.

3.2.2 Lines – Overlapping Pulses

Prior to generating area textures, the effect of overlapping pulses was studied on Cr-Mo-Al nitriding steel. The overlapping of pulses can be calculated as follows:

$$Pulse\ Overlap = \left(1 - \frac{v}{d \times PRF}\right) \times 100\% \qquad (3\text{-}1)$$

where v is the scanning speed of the laser beam across the surface and d is the nominal (calculated) $1/e^2$ focussed spot diameter of 50µm (see Figure 3.7, where $s=v/PRF$). By using a laser repetition rate of 25kHz and varying the beam scan speed between 62.5mm/s and 1250mm/s, pulse overlaps in the range of 0-95% (pulse separation 50µm-2.5µm) were achieved and used to machine single lines.

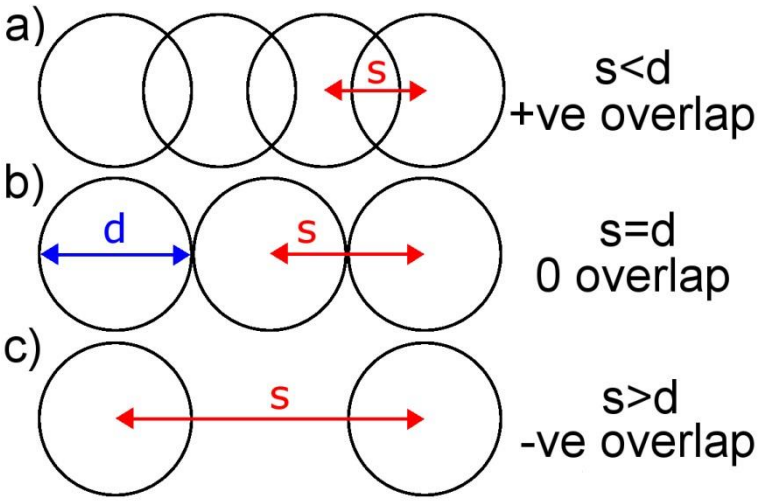

Figure 3.7. Schematic of three different pulse overlap configurations including positive overlap (a), zero overlap (b) and negative overlap (c)

It should also be noted that negative pulse overlaps are possible, as shown in Figure 3.7c, and correspond to pulse separations greater than the nominal spot diameter.

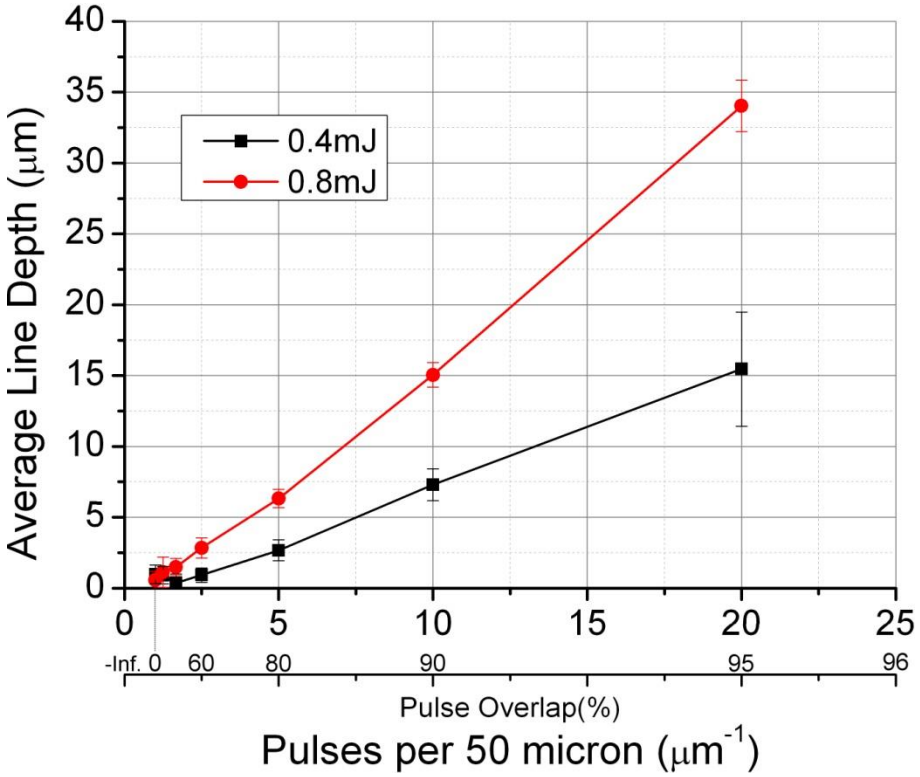

Figure 3.8. Average trough depth as function of linear pulse density

Figure 3.8 shows that the depth of the trough generated increased linearly with the number of pulses per distance; here 50μm was chosen as this corresponds to the nominal spot diameter. The values plotted are the minimum average values for each line, with the error calculated as the standard deviation of the depths along the line.

This is in agreement with the individual crater results which showed a linear increase with number of pulses. The observed difference between the two pulse energies is likely due to the difference in area which is ablated with each pulse; clearly the area for 0.4mJ pulses is smaller. As a result, the effective pulse overlap is decreased and so the depth per pulse achieved is significantly lower. The widths of the troughs were also measured, as shown in Figure 3.9.

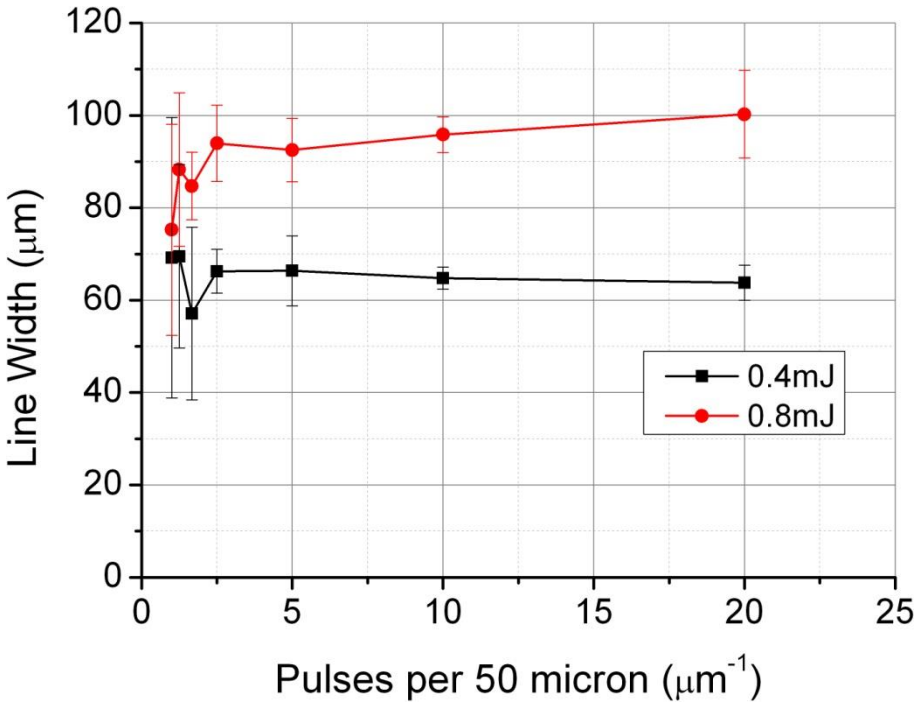

Figure 3.9. Trough width as a function of pulse overlap

For simplicity, the widths of the troughs were calculated as the separation of the ridges found at either side of the trough due to the melt eject, with the error bars indicating the standard deviation of these values within each data set. The trough widths were found to be independent of the pulse overlap, in agreement with the independence of the crater diameter from the number of pulses. The trough generated with pulses of 0.8mJ was also found to be wider than the 0.4mJ trough, as predicted from the individual crater results.

3.3 SPI 50W HS-S/20W EP-S

As in section 3.2 for the 20W HS-L laser, the laser power and pulse energy were characterised for the 20W EP-S. The 50W HS-S and 20W EP-S lasers have similar optical and pulse characteristics, with the differences being higher average power being achievable from the 50W HS-S through higher repetition rates and a wider range of

pulse durations ('waveforms') available from the 20W EP-S – complete tables of available waveforms for each laser used throughout this thesis can be found in Appendix A. The power and pulse energy characteristics for waveform 32 of the 20W EP-S are shown in Figure 3.10.

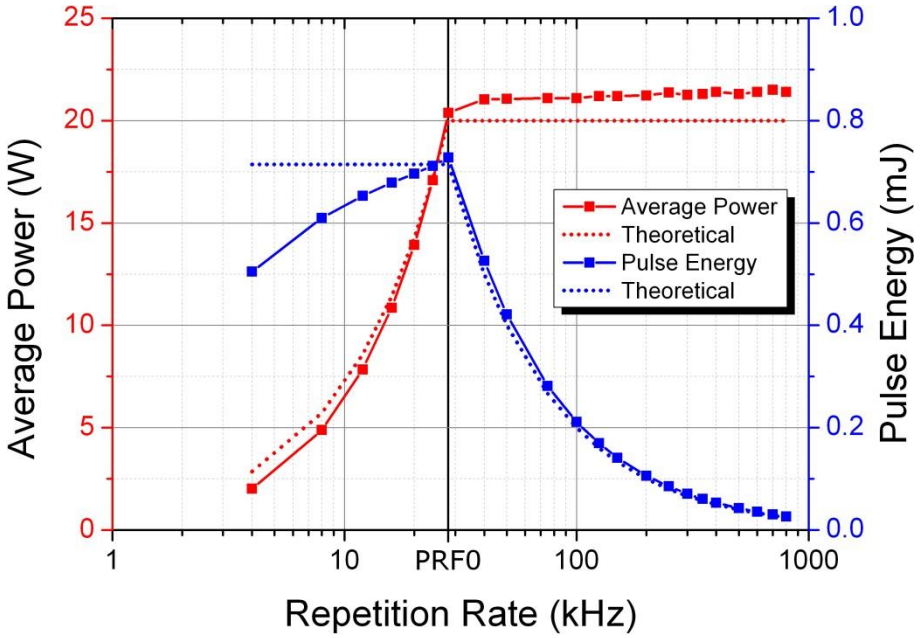

Figure 3.10. Average power and pulse energy as function of repetition rate for the 20W EP-S waveform 32 (~220ns pulse width) at 85% simmer current, with the corresponding specification curves plotted as dotted lines

In contrast to the trend for the 20W HS-L (Figure 3.2), the experimentally observed power is higher than the expected value. Again, the pulse energy tails off at low repetition rates but, as mentioned previously, this effect can be reduced by increasing the laser simmer current. This waveform, 20W EP-S WF32, is identical to WF0 of the 50W HS-S laser in terms of pulse duration and energy, with the only difference coming in the corresponding PRF0's (28 kHz vs 70 kHz) and average power.

3.3.1 Individual Craters

As in Section 3.2.1, individual craters were generated on stainless steel substrates (SS316 in this case) with a range of pulse energies and number of pulses. Figure 3.11a and b show the crater depth dependence on number of pulses and pulse energy, respectively.

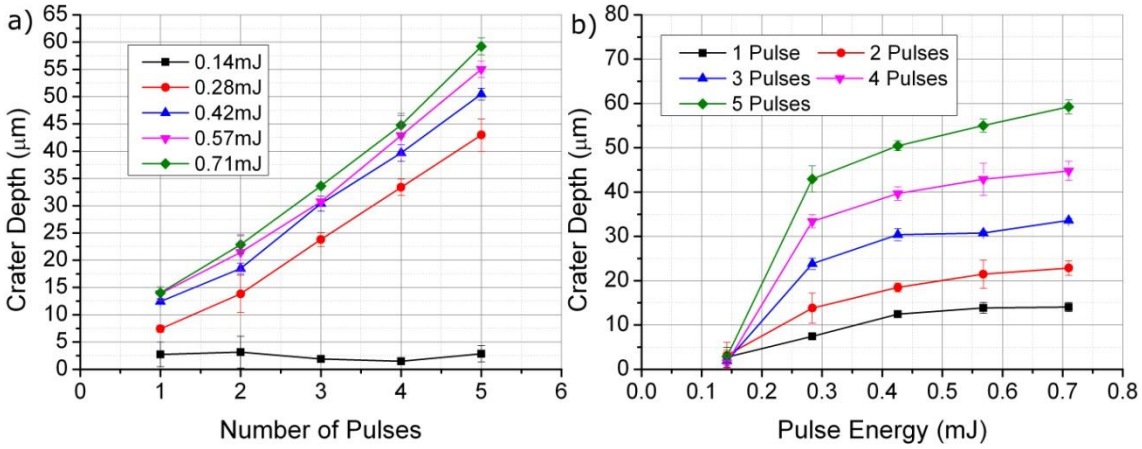

Figure 3.11. Crater depth as a function of number of pulses, for various pulse energies (a) and crater depth as a function of pulse energy, for different numbers of pulses (b); 20W EP-S

As observed previously for the 20W HS-L laser in Figure 3.3, the crater depth is found to increase approximately linearly with increasing number of pulses (Figure 3.11a); showing again that each pulse above the ablation threshold removes a consistent depth of material from the surface. Meanwhile, once above the ablation threshold, crater depth remains relatively constant with pulse energy – only slight increases in crater depths are observed for significant changes in pulse energy. As discussed further in Appendix C, the minimal effect of increasing pulse energy on the crater depth is likely due to the method of material removal. In this case, material is removed from the crater site primarily by melt ejection caused by the pressure exerted on the surrounding molten material by vaporisation. Due to the fixed pulse duration in these tests, increasing the pulse energy is not likely to greatly change the depth of the melt pool (given that the pulse duration is constant at ~220ns) prior to the material vaporisation, therefore it has little effect on the experimental crater depths. The dependence of crater diameter on number of pulses and pulse energy is shown in Figure 3.12.

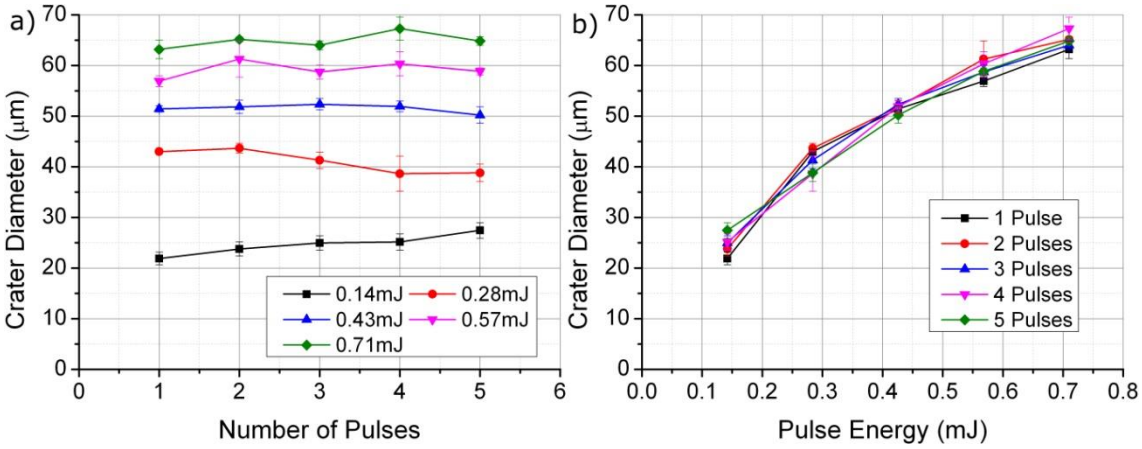

Figure 3.12. Crater diameter as a function of number of pulses, for various pulse energies (a) and crater diameter as a function of pulse energy, for different numbers of pulses (b); 20W EP-S

The crater diameter was found to be approximately linearly dependent on pulse energy whilst independent of the number of pulses, as shown in Figure 3.12. Again, this was as expected and agrees with the results obtained for the 20W HS-L laser (Figure 3.4 and Figure 3.6b). In addition, these trends are in agreement with the results presented by Vilhena et al. [115].

Following these findings, it is clear that it is possible to independently control both crater depth and diameter. Thus, by using the correct number of pulses and pulse energy to generate the crater, the required crater dimensions can be easily obtained.

3.3.2 Textures – Overlapping Lines

In order to create a texture on a material surface, it is necessary to generate arrays of lines in close proximity to each other, thus modifying a two dimensional area. Typically, these lines and the pulses within a single line will be similarly spaced; however this is not always a requirement.

3.3.2.1 Pulse Layout Design

Two different pulse layout strategies were considered and, in order reduce the available parameter space as much as possible, line-line separation was chosen to scale linearly with pulse-pulse separation in both cases. As a result, the first texture proposed was a simple square array, as shown in Figure 3.13.

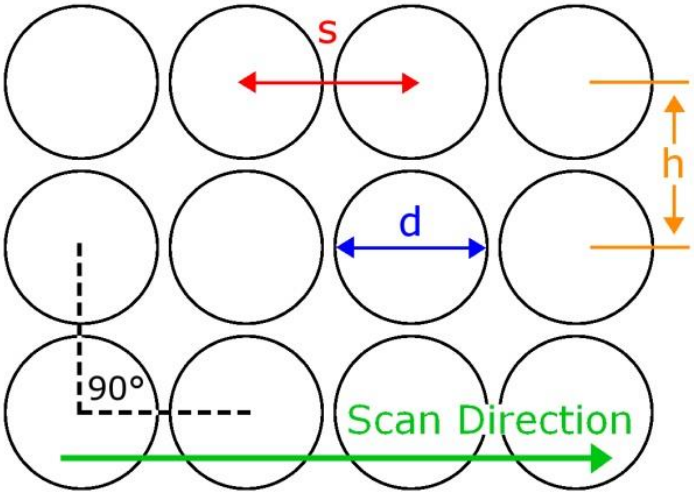

Figure 3.13. Schematic of 'square' pulse layout

This array is generated by producing a row of parallel lines with a line to line spacing (hatch), h, equal to the pulse to pulse spacing, s. This is the simplest two dimensional array which can be created, and is easily programmed on the computer software with the built in 'hatch' function. Due to the large degree of freedom available in choosing layout parameters, the pulse-pulse spacing and line-line spacing were chosen to be equal to each other by adjusting the hatch distance for each pulse-pulse spacing resulting in a consistently 'square' layout, regardless of the laser parameters. The second proposed pulse layout was a 'hexagonal' design, akin to the hexagonal close packed structure in crystallography. The way such a layout is composed is shown in Figure 3.14.

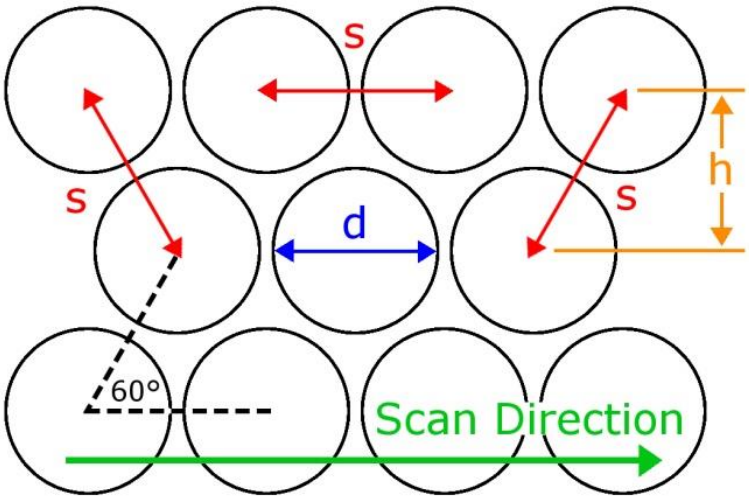

Figure 3.14. Schematic of 'hexagonal' pulse layout

In this case, there is an angle of 60° between adjacent pulses in neighbouring lines. As a result, the line to line spacing and pulse to pulse spacing are related as follows:

$$h = s \times \sin(60°) = \frac{\sqrt{3}}{2} \times s. \quad \text{(3-2)}$$

This arrangement results in each pulse maintaining the same pulse-pulse separation with each of its six nearest neighbours, at the cost of recalculating h for each pulse-pulse separation. Whilst the scan head software did not have a built-in feature for generating such arrays, they are fairly easy to generate by array copying individual lines with the required spacing and offset.

3.3.2.2 Pulse Layout Comparison

The square pulse layout was considered first. Figure 3.15 shows how changing pulse overlap affects the overall structure of the texture.

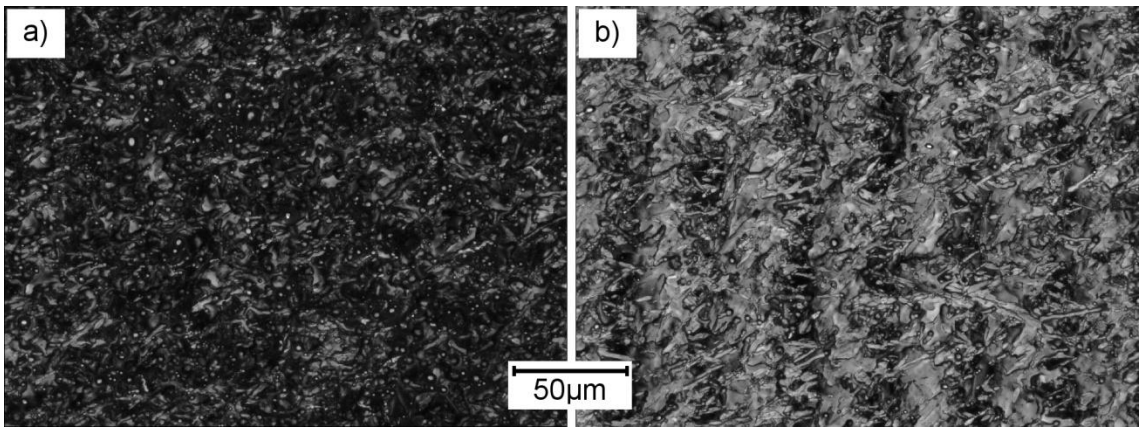

Figure 3.15. Optical micrographs of the square pulse layout with (a) 0% pulse overlap and (b) -50% pulse overlap; 20W EP-S, 20kHz, 25µm Ø 0.71mJ

At higher pulse overlaps, as shown in Figure 3.15a, the resulting surface texture exhibits a very homogeneous, random structure which masks the square pulse layout which generated it. As the pulse overlap is decreased, however, this pulse layout becomes more evident, exemplified by the very clear vertical structure in Figure 3.15b. As the MDT application requires an omnidirectional high friction coefficient, these types of structures are undesirable as they are likely to induce directionality to the resulting friction coefficient. This is especially the case for parallel, linear structures, which are guaranteed at very low pulse overlaps when using a square pulse layout. The textures were then repeated with the hexagonal pulse layout.

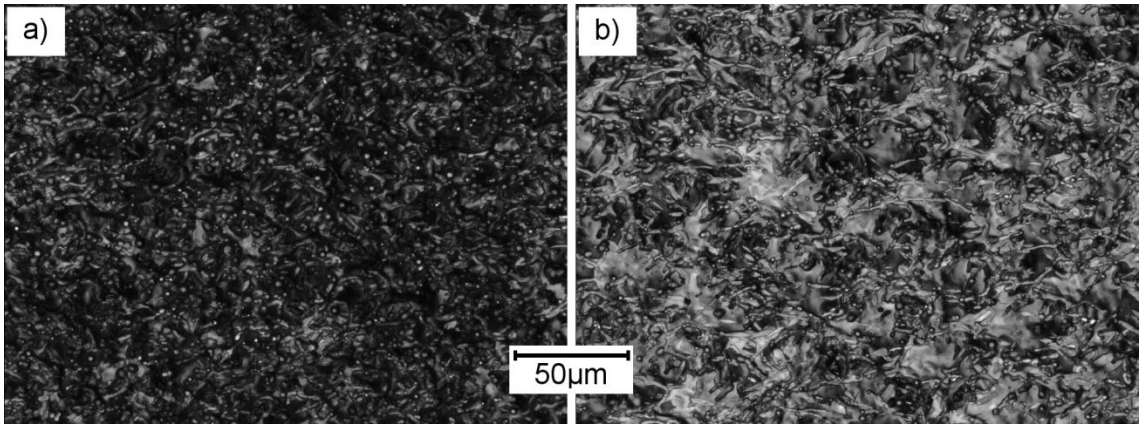

Figure 3.16. Optical micrographs of the hexagonal pulse layout with (a) 0% pulse overlap and (b) -50% pulse overlap; 20W EP-S, 20kHz, 25µm Ø 0.71mJ

As in Figure 3.15a, Figure 3.16a shows a very homogeneous, random structure which shows no signs of the underlying pulse layout. Whilst the resulting texture may not be quite so random, lower pulse overlap textures generated with the hexagonal pulse layout also conceal the hexagonal pattern, as demonstrated in Figure 3.16b.

Therefore, given the similarity between the two layouts at higher pulse overlap and the hexagonal patterns lack of clear orthogonal structure at lower pulse overlaps, all laser generated friction textures were created using the hexagonal pulse layout.

3.4 Waveform Characterisation

Given the wide range of pulse durations, or waveforms, available with the use of these two SPI fibre lasers, both direct measurements and characterisation of the interaction of these different waveforms with the sample material were performed.

3.4.1 20W HS-L

The SPI 20W HS-L laser is a standard laser model which has 25 different waveforms available to choose from (full list is shown in Appendix A). Table 3.2 shows a range of the possible waveforms, as well as the corresponding PRF0 repetition rates and maximum pulse energies.

Waveform #	Pulse Duration (ns; 10% Width)	PRF0 (kHz)	Max. Pulse Energy (mJ)
0	200	20	0.80
1	65	65	0.31
2	30	125	0.16
3	15	250	0.08
4	12	375	0.05
5	9	500	0.04

Table 3.2. Selection of waveform parameters for 20W HS-L

The selection of waveforms presented in Table 3.2 include the pulses with maximum available pulse duration and pulse energy, waveform 0, as well as the waveform with shortest pulse duration available, waveform 5. It should be noted that the values quoted here are the specified values provided by SPI rather than experimentally measured values for the particular laser used. The 10% width refers to the calculation of the pulse duration, from the time at which the pulse intensity rises above 10% of the peak until the pulse intensity falls below 10% of the peak. Given the shape of the SPI waveforms (see Figure 3.17 for example), this definition is much more appropriate than the standard full-width half-maximum definition. In order to confirm the specified pulse durations, tests were performed with a fast photo-diode (FPD, Thorlabs DET210) and oscilloscope (LeCroy 9354AM 500MHz) to measure the temporal response for each available waveform, as shown in Figure 3.17.

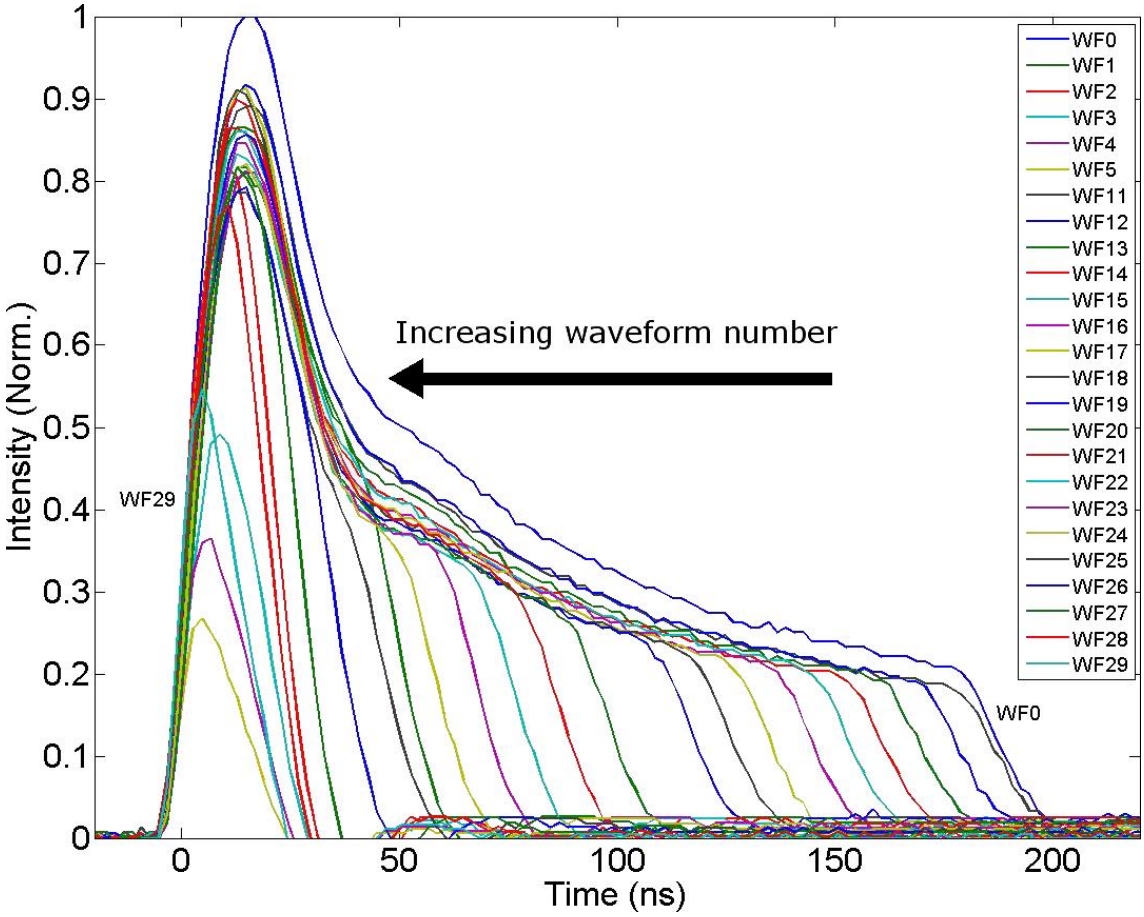

Figure 3.17. Temporal pulse shapes of the 20W HS-L waveforms, intensity normalised for PRF0 pulses

The measured temporal pulse shapes shown in Figure 3.17 are in agreement with the example shapes provided by SPI; the longer pulses show a large initial peak with a long, lower intensity 'tail' while shorter pulses exhibit a more Gaussian shape with no tail. From these measurements, the 10% pulse durations were calculated to be consistently longer (by ~10-20ns) than the values supplied by SPI. For the longer pulses, this discrepancy is primarily caused by the relatively poor signal-to-noise ratio due to running the laser being run at low average power to prevent damage to the FPD. For short pulses, however, the limited rise and fall time (>2ns) of the FPD and oscilloscope contribute more to the discrepancy than the SNR errors. Subsequent duration measurements performed with higher average power were found to be within 5ns of the nominal pulse duration for waveform 0. It should also be noted that waveforms 6-10 are duplicates of waveform 5 and therefore were not plotted individually.

3.4.2 20W EP-S

The 20W EP-S laser is part of the 'extended profile' (EP) range from SPI and, as a result, has a much wider range of waveforms available ranging from 3ns to 490ns pulse duration. Table 3.3 gives a selection of the waveforms available in this model.

Waveform #	Pulse Duration (ns; 10% Width)	PRF0 (kHz)	Max. Pulse Energy (mJ)
39	490	28	0.71
35	320	28	0.71
32	220	28	0.71
5	144	42	0.48
10	100	57	0.35
17	50	85	0.24
31	3	1000	0.02

Table 3.3. Selection of waveform parameters for 20W EP-S

As with the 20W HS-L laser in Section 3.4.1, the waveforms presented in Table 3.3 are specified values obtained from SPI which summarise the range of pulse durations available from the laser. All 40 waveforms (0-39) were also measured directly using the FPD, with the resulting temporal pulse shapes shown in Figure 3.18.

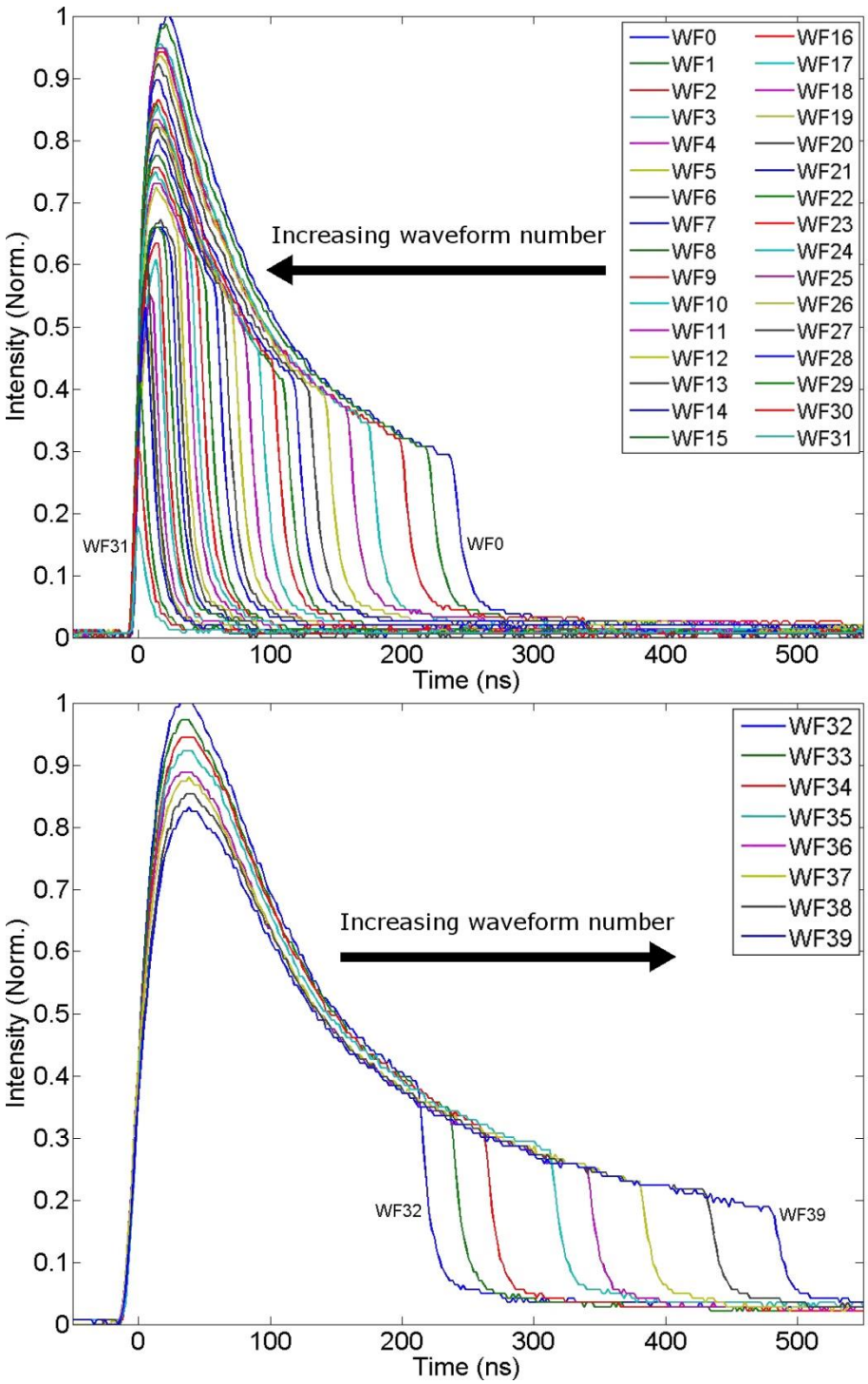

Figure 3.18. Temporal pulse shapes of the 20W EP-S waveforms, intensity normalised for PRF0 pulses

As with the measurements shown for the 20W HS-L, the shapes of the waveforms plotted in Figure 3.18 are as expected, although the durations were ~10-20ns longer than the theoretical, as discussed in 3.4.1 for the 20W HS-L measurements. Whilst the extended profile model increases the pulse duration range at both ends of the spectrum, the longer pulses (220-490ns) were of more interest as they can utilise the maximum pulse energy available from this laser.

3.4.2.1 Line Comparison

In order to determine the impact of the pulse duration on the laser-material interaction, a range of waveforms were selected and used to produce lines on a stainless steel substrate. For this comparison, the pulse energy was kept constant at 0.235mJ; corresponding to the maximum pulse energy available at waveform 17 (50ns), with the corresponding temporal pulse shapes shown in Figure 3.19.

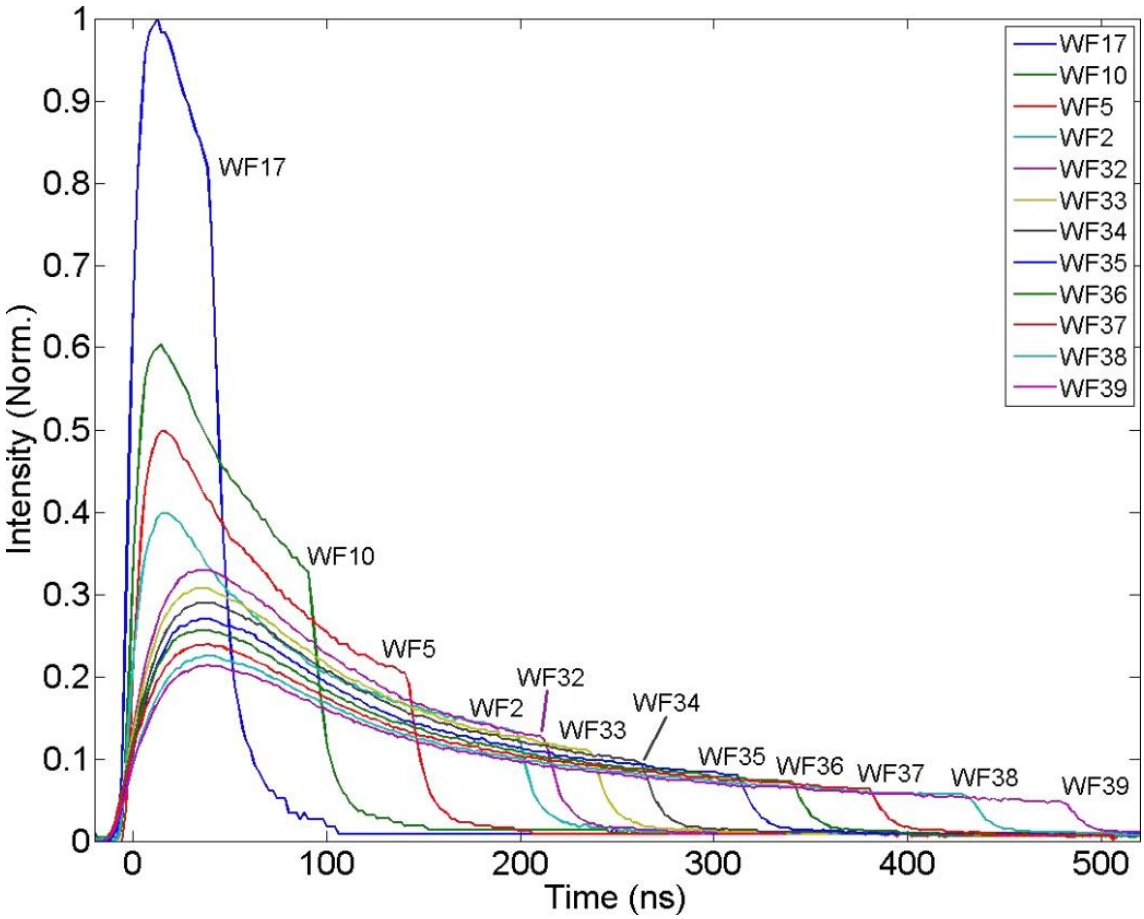

Figure 3.19. Temporal pulse shapes of waveforms selected for area texture comparison, intensity normalised for uniform energy per pulse

The difference in peak energy and pulse duration for the selected waveforms is clear from the curves presented in Figure 3.19; therefore a significant effect on the processing was expected. A constant repetition rate of 20kHz and 75% pulse overlap (6.25µm pulse separation) were also maintained throughout. Example micrographs are shown in Figure 3.20.

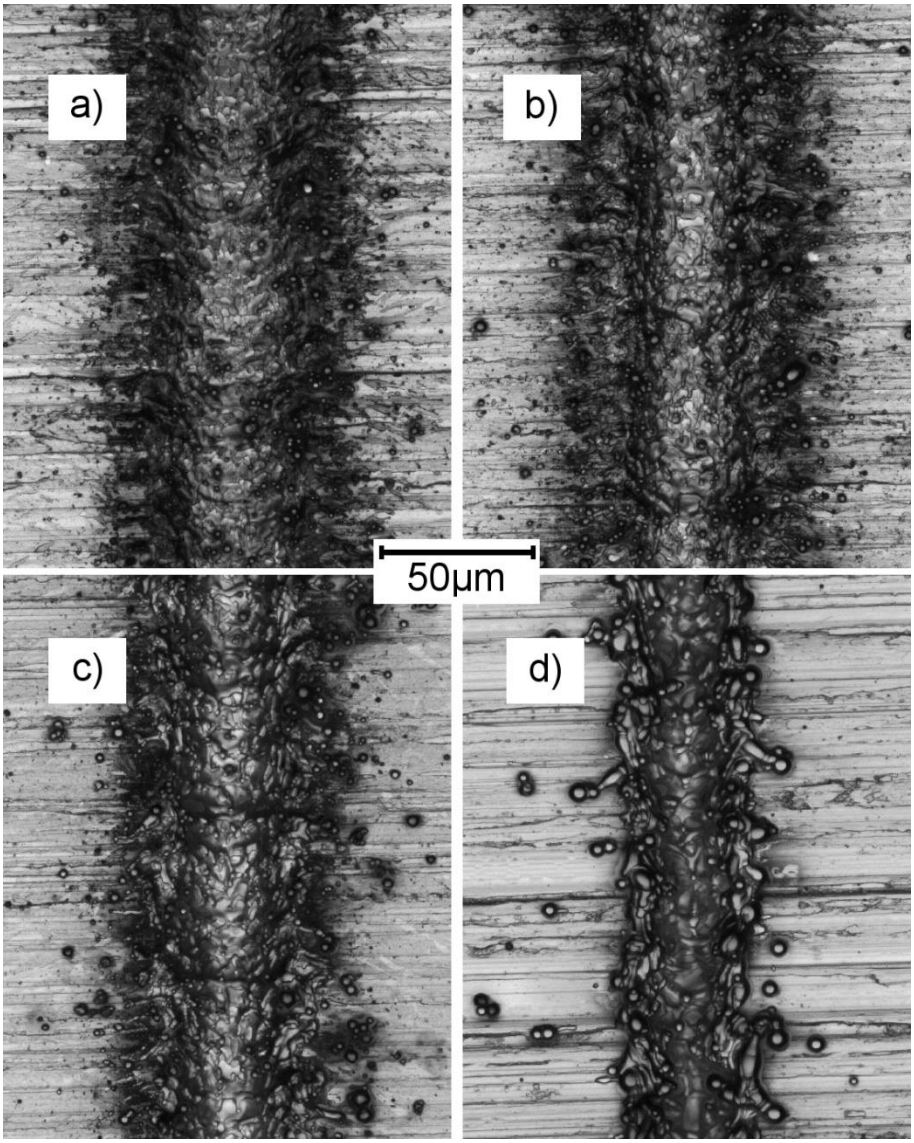

Figure 3.20. Micrographs of laser generated lines on SS316 using different pulse durations; 50ns (a), 100ns (b), 202ns (c), 490ns (d)

Figure 3.20 shows a marked difference in the resulting lines generated at different pulse durations. At shorter pulse durations (<100ns, Figure 3.20a, b), significant amounts of fine debris can be seen in a large (~20µm) area surrounding the line. As pulse duration is increased, the amount of this debris decreases and it remains closer to the machined line. The recast debris also forms larger globules as the pulse duration increases, exemplified by Figure 3.20d, due to the increased melt duration. These micrographs also serve to highlight the stability of the scanner and controller as little or no wobble can be observed on the generated lines. Figure 3.21 shows the average depth of the machined lines as a function of pulse duration.

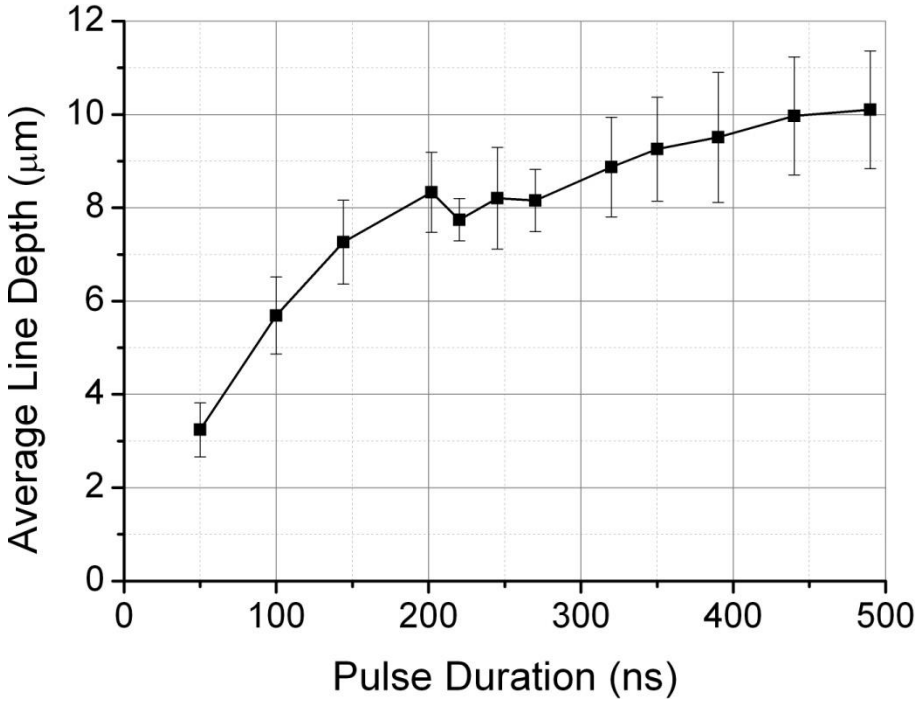

Figure 3.21. Average line depth as a function of pulse duration for selected waveforms; 20W EP-S, 0.235mJ

The average depth of the machined line can be seen to increase significantly, from ~3.3µm to >10µm, with increasing pulse duration in Figure 3.21. The error bars shown were calculated as the standard deviations of the depth along the length of the lines. With short pulses, the primary material removal mechanism is ablation/vaporisation eject, resulting in the significant debris seen in Figure 3.20a. Due to the short pulse duration, the material vaporisation occurs whilst the melt pool is relatively small resulting in the formation of many small droplets to form. The low volume of the droplets produced means that they are ejected from the site of the pulse before falling back onto the substrate and solidifying on the surface, contributing to the resulting debris seen in the micrographs. Despite the significant debris observed, the short pulse duration limits the total material moved due to the limited size of the melt pool which can be generated.

With longer pulses, less material is removed from the site of the pulse by ablation as the peak laser intensity is greatly reduced. However, a larger melt pool is generated and thus melt ejection becomes the primary material removal method. In this parameter space (with limited pulse energy), it is clear that melt ejection is a significantly more efficient material removal method than ablation for line depth, although the line width may be reduced if the melt is not ejected far from the trough.

3.4.2.2 Area Texture Comparison

Following the line comparison, the effect of pulse duration on area textures was also studied for various pulse waveforms. Using a 20kHz repetition rate and 12.5µm pulse separation (50% overlap), various surface roughness measurements were taken to examine the resulting textures, as shown in Figure 3.22.

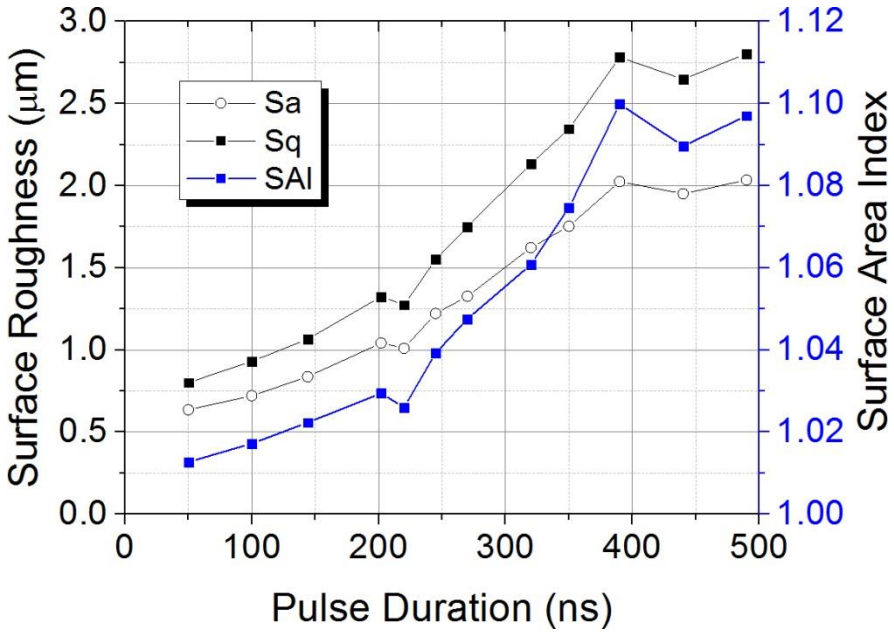

Figure 3.22. Surface roughness measurement comparison against pulse duration for selected waveforms

Where S_a is the arithmetic average roughness, S_q is the RMS roughness and SAI is the Surface Area Index – the ratio of the actual surface area to the nominal surface area. It is clear from the curves shown in Figure 3.22 that the pulse duration has a significant influence on the laser-material interaction. As expected, increasing the pulse duration increases the surface roughness of the resulting textures. This is due to the increased melt duration and therefore increased melt flow achieved with the longer pulses. It can also be seen that the roughness values appear to plateau in the region of 400-500ns. This is likely due to thermal dissipation effects where the increased pulse duration allows the thermal energy to spread and therefore the volume of molten material begins to decrease. This plateau, likely to actually be a turning point, is expected as in the extreme of a very long pulse with the same energy there will be no molten material at all due to the thermal dissipation of the substrate.

3.5 Summary & Conclusion

The work detailed in this chapter characterised the SPI fibre lasers used in this project, the laser processing workstation and the laser interaction with stainless steel substrates.

This allowed the system properties and resulting surface features which are possible with such a laser processing to be measured experimentally in order to determine the best way to approach the generation of high friction textures, as required by the MDT applications.

Both fibre laser systems tested performed close to their specification, although the pulse energy for both 20W HS-L and 20W EP-S tailed off when using pulse repetition frequencies below PRF0, as shown in Section 3.2 and Section 3.3. This effect can be minimised somewhat by increasing the laser simmer current, at the risk of increased beam leakage. As a compromise, a simmer current value of 85% was chosen and maintained throughout all characterisation and texturing processes.

The temporal pulse shape measurements in Section 3.4 were also found to be typically in agreement with the products specifications, although the pulse duration calculations consistently gave values 10-20ns longer than expected due to the poor signal-to-noise ratio, caused by the low average laser power used to prevent damage to the FPD, and limited rise/fall time of the FPD/oscilloscope (>2ns). In order to make use of the maximum pulse energy of these laser systems, longer pulse durations (~200ns+, WF0/32) were chosen for generating high friction textures.

Characterisation of the laser-material interaction also highlighted some interesting results. When studying individual craters, as in Section 3.2.1 and Section 3.3.1, the crater depth was found to be independent of pulse energy (above the ablation threshold of the substrate) but to increase linearly with number of pulses. Given that the depth of the craters generated was significantly smaller than the Rayleigh range of the focussed beam, it was expected that subsequent pulses would remove as much material as the initial pulse. The crater diameter, however, was found to be independent of number of pulses, but increased continuously with pulse energy. This is due to the crater diameter being dependent on the area of the beam for which the fluence exceeds the ablation threshold; therefore increasing the pulse energy increases the area of the beam which exceeds this threshold, resulting in increased crater sizes. These trends were consistent for both lasers on both SS304 and SS316 substrate materials. Following these results, it is clear that it is possible to independently control crater depth and diameter – craters of the desired dimensions can be achieved by choosing appropriate values for pulse energy and number of pulses.

The overlapping of pulses in order to generate lines on Cr-Mo-Al nitriding steel, presented in Section 3.2.2, showed similar trends to those observed for single pulses. The average line depth was found to increase linearly with number of pulses per distance whereas line width was independent of the pulse density, analogous to crater depth as a function of number of pulses and pulse energy. Increasing pulse energy increased the trough width as expected, however the average line depth also increased. This is likely due to the difference in area which is ablated with each pulse; clearly the area for higher pulse energy pulses is larger. As a result, the effective pulse overlap is increased and so the depth per pulse achieved is significantly higher.

Experimental comparisons of both square and hexagonal pulse layout designs shown in Section 3.3.2 clearly highlighted the difference between the two resulting structures. While both layouts result in highly homogeneous, random topographies when using high pulse overlaps; the underlying layout becomes very evident when the overlap is decreased. In this case, the square layout shows very clear lines in the final structure – a feature which is undesirable when omnidirectional properties are required. The hexagonal layout, on the other hand, showed no such linear structures and even the hexagonal shape was partially masked. This outcome makes the hexagonal layout significantly more appropriate for the MDT application and so all friction testing was carried out using this design.

Chapter 4 – Friction Textures – Initial Results & Investigations

This chapter concerns the generation, testing and subsequent investigations of the initial set of textured samples for high friction applications. The initial tests were designed to cover a wide range of the laser/processing parameter space in order to indicate the best parameters to use to achieve high friction coefficients, with the initial textures under test chosen as a result of the findings in Chapter 3. The tests undertaken and discussed in this chapter were performed with a sample textured on both faces contacting untextured counterpart surfaces. In addition to the testing of the textured surfaces, investigations into the testing set-up/procedure and process scalability, performed in order to identify possible sources of error and strategies for increasing industrial appeal, are presented and discussed.

4.1 Testing High Friction Surfaces

In order to determine the friction coefficient of the laser textured samples, it was necessary to design and build a custom testing rig. The set-up was required to be able to apply, and measure, a normal force (of up to 60kN) to the textured sample through two counter surface pieces whilst simultaneously facilitating the application of a load force directly to the textured sample. Figure 4.1 shows a photograph and schematic of the rig designed and made to do this.

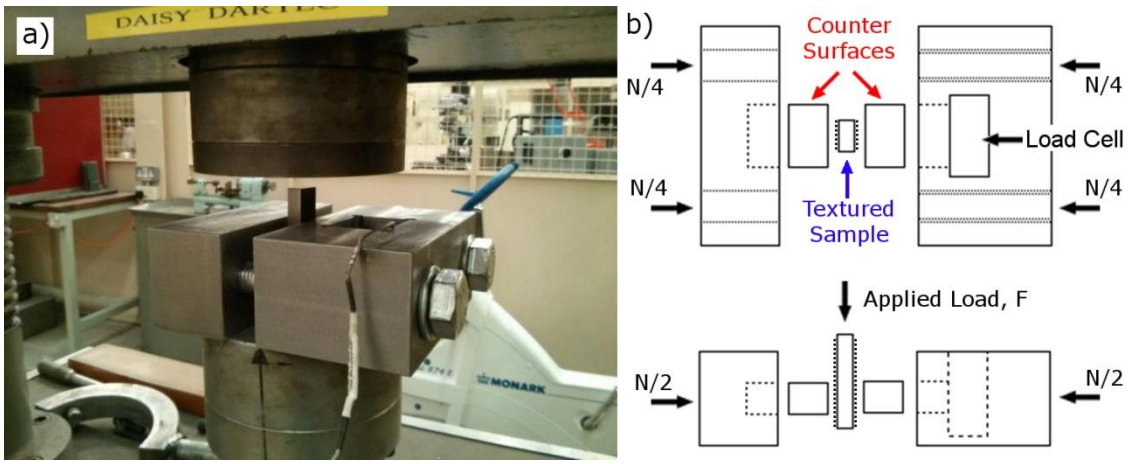

Figure 4.1. Photo of the complete friction testing set-up on a hydraulic press with a sample held by the normal force (a) and schematic of testing rig showing sample, counter surfaces and applied forces (N denotes Normal force) from top down view (top) and side on (bottom) views (b)

As shown in Figure 4.1b, set-up primarily consists of two steel blocks, which are held together by two high tensile steel bolts. These steel blocks were machined such that the

two counter pieces are held in place but protrude from the surfaces of the blocks, allowing the sample to contact the counter piece (nominal contact area of 20mm × 20mm) without touching anything else. The load force is applied through two counter surfaces and a miniature load cell (strain gauge), which is countersunk into the steel block such that it is able to measure the force on sample directly. The two bolts are manually tightened, evenly, until the read out from the load cell is at the desired value (to within ±1kN). At this point, the rig is disconnected from the load cell read-out and moved to a 100kN Dartec hydraulic press which is then used to apply the load force to the sample, as seen in Figure 4.1a. The computer controller connected to the Dartec allows real-time measurement and recording of the resulting force and displacement of the sample. The hydraulic ram was moved at a constant rate of 0.15mm/s and the load and extension data was acquired at a rate of 333Hz for 30 seconds for each test.

An example load-extension plot generated from data recorded by the computer connected to the Dartec is shown in Figure 4.2.

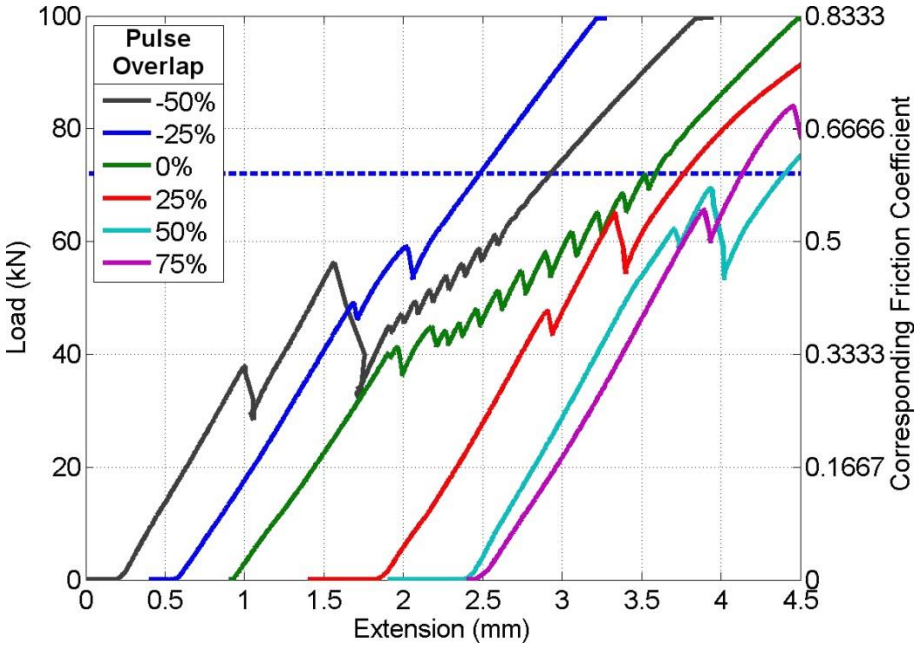

Figure 4.2. Example load-extension plot for six different friction tests with each plot offset to enhance readability

The six load-extension curves for the six friction tests, shown in Figure 4.2, all show a steady increase in 'extension' as the load force is increased; this can be attributed to the elastic deformation of the components in the system. Upon reaching a particular maximum load (F_{max}), the extension continued whilst the load force decreased

corresponding to the 'slipping' point of the sample. This slipping point can then be used to calculate the static friction coefficient of the sample texture, as follows:

$$\mu_s = \frac{F_{max}}{2 \times N} \quad (4\text{-}1)$$

where N is the normal force applied to the sample (60kN in these tests). The factor of two relates to the fact that both surfaces of the sample are under test. Upon slipping, the sample was deemed to have 'failed', as a real component would require replacement at this point, and so the remainder of the curves beyond this point were not analysed.

Whilst the design and use of this friction testing set-up was carefully thought through, it is impossible to ensure that there were no errors introduced. This is particularly the case when taking friction measurements at such high pressures and forces as are involved here. Prior to discussing the friction results, various possible sources of errors are investigated and discussed.

4.2 Sample Preparation

Each sample and counterpart was prepared in the same manner prior to each friction test. The test surface was initially ground to a surface finish with S_a<0.4µm and then cleaned with iso-propyl-alcohol (IPA) prior to laser texturing. No further cleaning or other process was performed on the textured samples before friction testing (unless explicitly stated otherwise). Between laser texturing and friction testing, the samples were carefully stored and transported in such a way that the textured surfaces did not contact any objects. After each friction test, both sample and counterpart were ground again in order to allow continued use of the same sample material.

4.3 Possible Friction Testing Issues

Issues, such as sample misalignment, loading speed and the tilting of counterparts were explored in order to determine the best practice for testing, whilst other possible issues acknowledged as plausible sources of errors and inconsistencies are recognised but not studied in detail in this thesis.

4.3.1 Sample Misalignment/Rotation

Great care was taken throughout testing to ensure that the samples were aligned in the test set up perpendicular to the counterparts (parallel to the direction of the applied load

force); however it is apparent that small misalignments are possible and quite likely to have a significant effect on the resulting load-extension curve and hence the calculated friction coefficient. Therefore, several tests were performed with deliberately misaligned samples (~5° misalignment angle) and compared to test results with well-aligned samples. All laser texturing parameters (50W HS-S, 12.5µm pulse separation, 20kHz on SS316) and testing parameters were kept constant for the comparison. Figure 4.3 compares the slipping point of the load-extension curves from these tests.

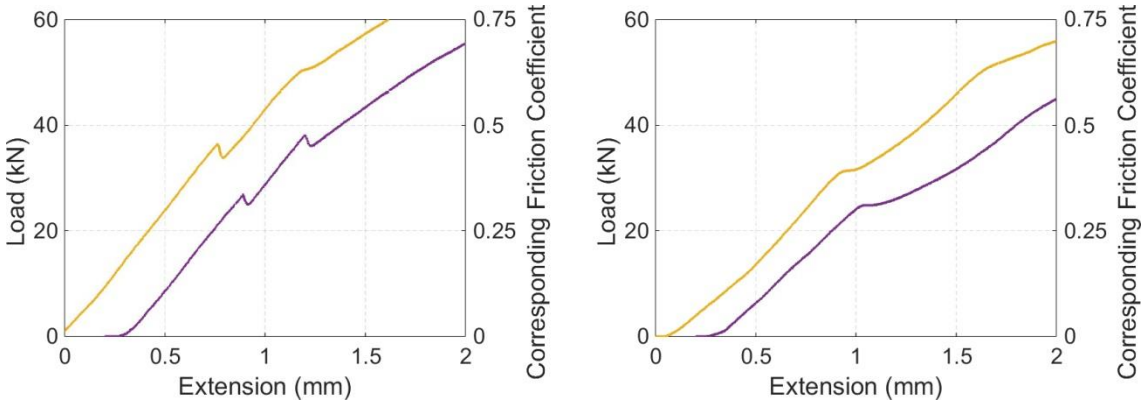

Figure 4.3. Close-up of the 'slipping' points on the load-extension curves for samples tested (left) with well-aligned samples and (right) samples misaligned by ≤5°; 50W HS-S, 12.5µm pulse separation, 20kHz on SS316

As highlighted by Figure 4.3, test results with well-aligned samples result in small but distinct slip points whereas the misaligned test results exhibit more continuous sliding, or points of inflection, on the load-extension curves. This is due to the rotational moment on the sample caused by the misaligned sample, the effect of which can easily be interpreted by the schematic shown in Figure 4.4.

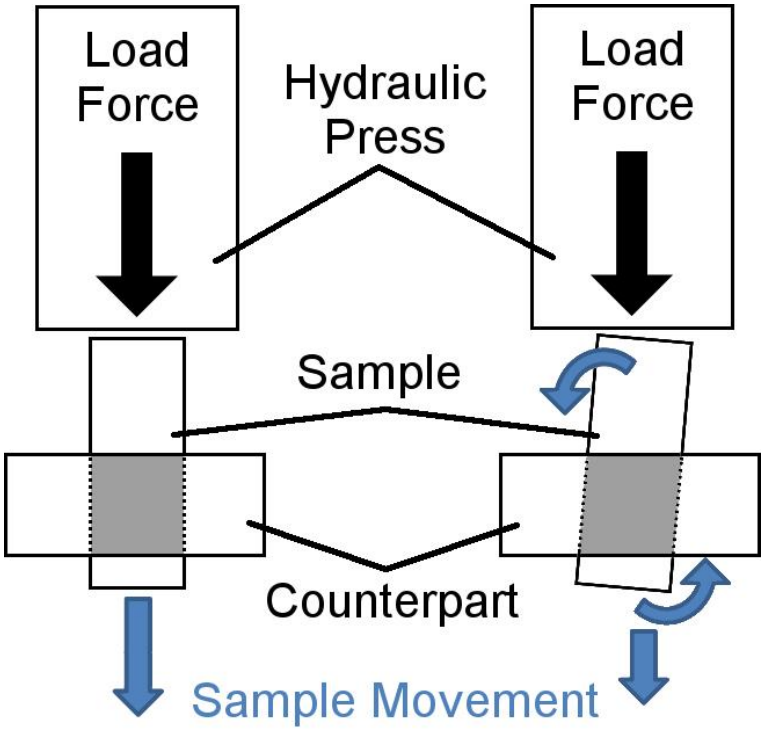

Figure 4.4. Schematic showing the resulting sample movement during friction tests with a well-aligned sample (left) and a misaligned (5°) sample

When the sample is well-aligned, the resulting movement is parallel to the direction of the applied load force as depicted on the left of Figure 4.4. When the sample is poorly aligned, however, the resulting movement of the sample is rotational around the contact area before the sample begins to move parallel to the load force, as shown on the right of Figure 4.4. If this rotational movement is large enough, then the sample will be in motion when the sample begins to slip parallel to the load force and therefore the contact will be in the kinetic friction regime rather than the static friction regime, as observed by the continuous sliding in Figure 4.3. Therefore, as previously noted, the samples were aligned as parallel as possible to the direction of the load force. This was typically achieved by ensuring that the sample and counterparts were perpendicular during the application of the normal force. This was achieved by using an additional block with a right angled edge to align the sample relative to the counterpart.

4.3.2 Test Loading Speed

While the loading speed was not expected to have a large impact on the friction coefficient, the effect of changing loading speed was examined experimentally. As mentioned in previously, the loading speed used for testing was 0.15mm/s, however loading speeds of up to 1.5mm/s were possible with the hydraulic press. Therefore, these two speeds (denoted fast and slow for 1.5mm/s and 0.15mm/s respectively) were

used for the comparison of loading speeds on the friction coefficient, with two typical load-extension curves shown in Figure 4.5. Laser texturing was performed on SS316 with the 50W HS-S laser with a pulse separation of 12.5µm and PRF of 20kHz.

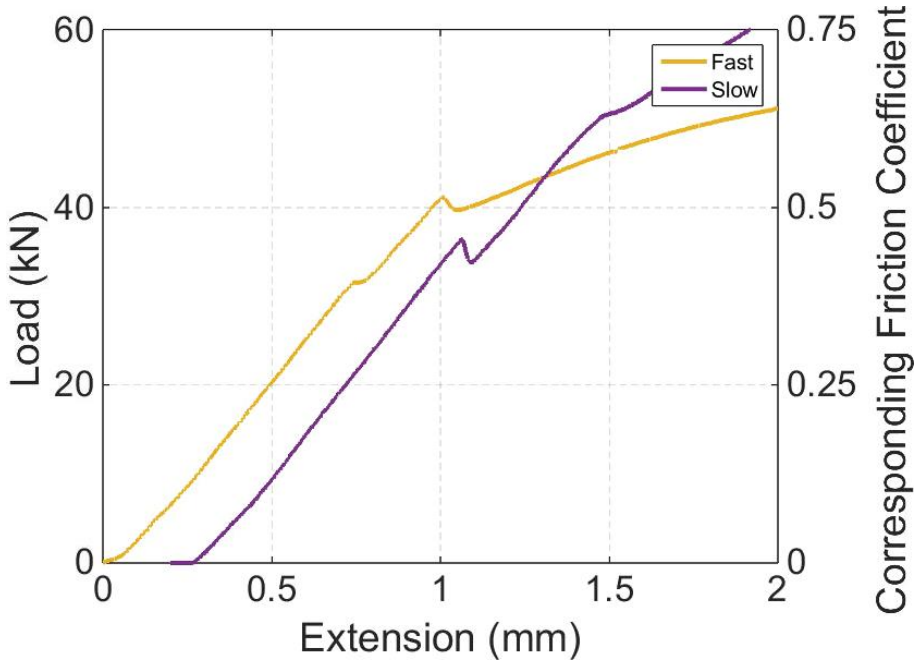

Figure 4.5. Comparison of load-extension curves at two different loading speeds; fast=1.5mm/s, slow=0.15mm/s

The slip points for these curves, shown in Figure 4.5, are observed to take place at approximately the same load value (36-41kN) as expected. The corresponding friction coefficients for these values are approximately μ_s=0.45 and μ_s=0.51 giving a difference of $\Delta\mu_s$=0.06, which is less than the typical standard deviation of $\Delta\mu_s$=0.1 for most of the friction tests performed. In conjunction with several results from tests performed with both surfaces textured (discussed in detail in Chapter 6), particularly the samples which exhibited no slipping up to 100kN load force, the speed of the application of the load force was determined to have an insignificant effect on the friction coefficient determination. As a result, despite increasing the time required for testing, the 'slow' loading speed was used as this enables higher resolution data acquisition of the load-extension curves.

4.3.3 Tilting of Counterparts

Another possible issue which was considered in detail was the tilting of the counterparts as a result of the applied load force during friction testing. Although the original design of the test rig was chosen in order to minimise the effect under normal testing

conditions (tolerance of <0.1mm, corresponding to a maximum tilting angle of <0.3°, on holes machined to hold counterparts), the wearing of the counterparts over time led to the modification of the rig such that an additional block was placed behind each counterpart in order to ensure the contacting surfaces protruded from the steel mounts. The schematic shown in Figure 4.6 shows three different cases for the counterpart tilting issue and highlights how the use of an additional block behind the counterpart exacerbates the effect.

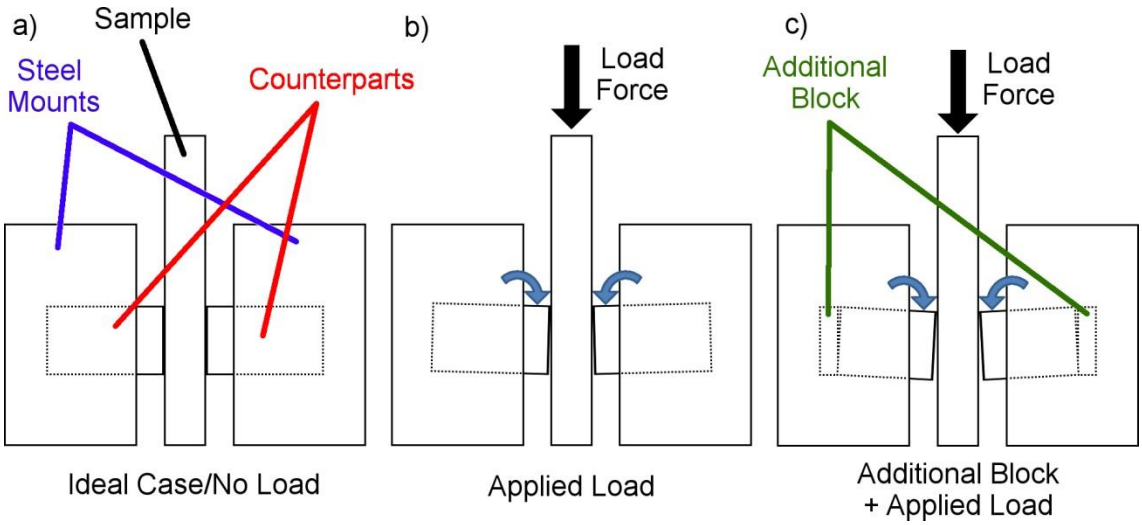

Figure 4.6. Schematic of the issue of counterpart tilting in three different cases concerning a) the ideal case with no tilting (as is the case with no load force), b) the small tilting angle observed in the standard testing configuration and c) the increased tilting angle observed in testing with additional blocks placed behind the counterpart blocks

From Figure 4.6a, the ideal case occurs where the counterpart remains perpendicular to the sample throughout the testing process, maintaining the same nominal contact area between the two surfaces. However, due to the geometry of the parts and testing rig (and material properties), it is impossible to avoid tilting of the counterparts entirely, as shown in Figure 4.6b, therefore reducing the nominal contact area. The additional blocks added behind the counterparts can be seen to exacerbate this effect in Figure 4.6c (by reducing the depth at which the counterparts are embedded from ~20mm to ~13mm) and subsequently further decreasing the nominal contact. Following the concerns raised on this issue, several experimental tests were performed in order to determine the effect of the additional block on the resulting friction coefficients. Testing was conducted on samples and counterparts both textured with the 20W EP-S laser with s=50µm, PRF=20kHz and pulse duration of 490ns (as in Chapter 6) with three different configurations for the testing rig: no additional blocks (standard testing configuration),

single additional block behind each counterpart and two additional blocks placed behind each counterpart (extreme case used purely for comparison). The laser texturing parameters and the testing normal load of 20kN was chosen in order to allow the greatest degree of counterpart tilting to take place (low normal force but high load force) whilst allowing the friction coefficients to be resolvable for all configurations. Results of five friction tests for each configuration are presented in Figure 4.7.

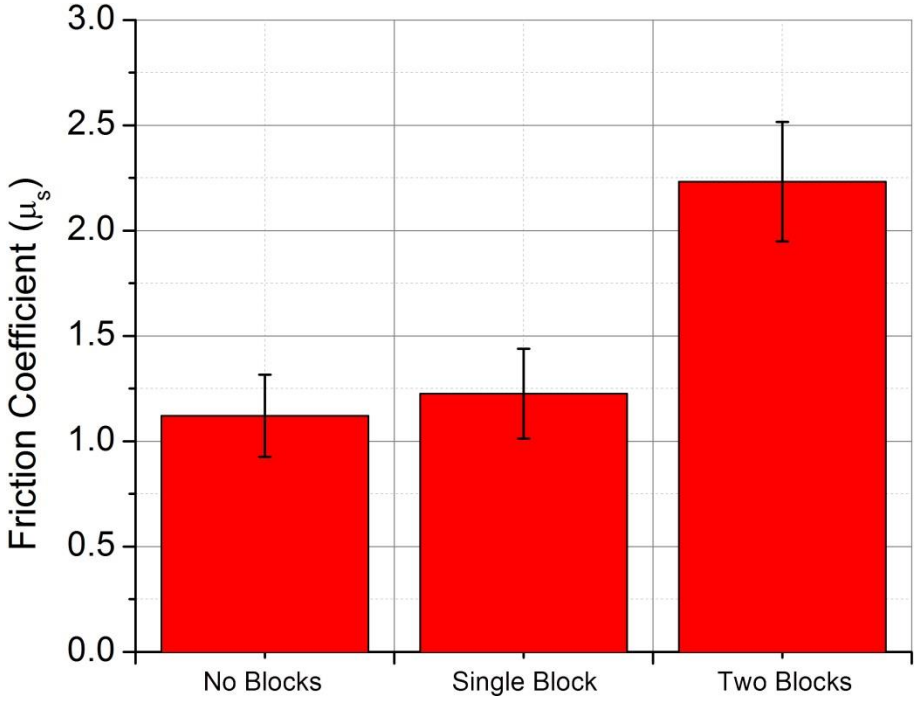

Figure 4.7. Friction coefficients obtained for three different testing configurations with none, one and two blocks placed behind the counterparts; texturing performed with the 20W EP-S laser using *s*=50µm, PRF=20kHz and 0.71mJ, 490ns pulses

Increased tilting of the counterpart was expected to increase the resulting friction coefficient measurement by deforming and pinching into the sample at high pressure along the top edge of the counterpart due to the reduced contact area. The friction results, from Figure 4.7, of the configuration with two blocks behind the counterpart clearly show that this increase is very large; with the average friction coefficient reaching μ_s~2.25 compared to μ_s~1.1 when no additional blocks were placed behind the counterparts. When a single block was placed behind each counterpart, the friction coefficients were found to increase only marginally to ~1.2; well within the experimental error for these tests (±0.2). The effect of the counterpart tilting can easily be observed by visually inspecting the nominal contact areas after friction testing, as shown in Figure 4.8.

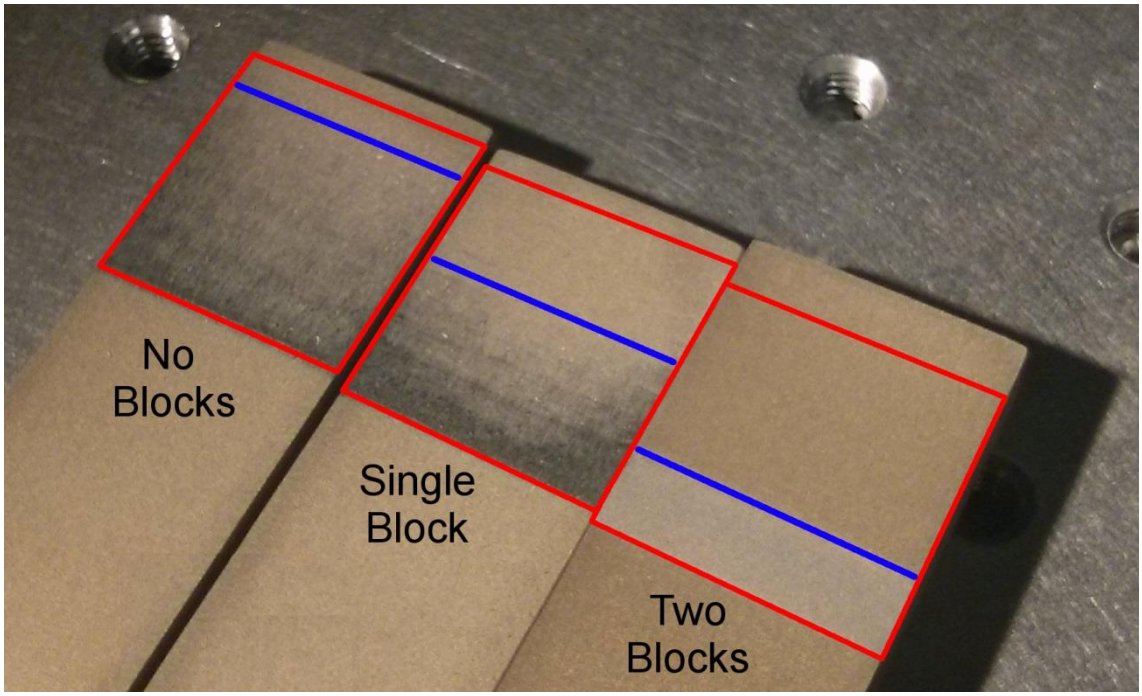

Figure 4.8. Photograph of three samples tested under the three configurations (none, one and two blocks placed behind the counterparts) with the nominal contact areas highlighted in red. Areas above the blue lines are not deformed; areas below the blue line are deformed. Texturing was performed with the 20W EP-S laser using *s*=50µm, PRF=20kHz and 0.71mJ, 490ns pulses

As can be seen in Figure 4.8, when the testing rig is used in the standard testing configuration (with no additional blocks), the deformed area of the sample (area below the blue line) covers a large percentage (>80%) of the nominal contact area indicating that good contact is maintained throughout the testing process. When testing is performed with single blocks behind the counterparts, this deformed area decreases to ~50% of the nominal contact area. This decreases even further, to <30%, when a second block is added to the testing rig. The decrease in contact area was expected and, ultimately, the tilting angle can have a significant impact on the resulting friction coefficient measurement. However, the two testing configurations used for all friction measurements in this thesis (no blocks and single additional block behind each counterpart) are consistent and appear to introduce no significant, avoidable errors to the friction coefficient measurement.

4.3.4 Other Issues

In addition to the possible issues previously mentioned, several other variables which may impact the friction coefficient measurement are acknowledged. However, due to limitations in both equipment set-up/design and time restraints, the full effect of these variables was not investigated. These variables include the room/atmosphere conditions

during testing (temperature, humidity etc.), surface contamination, sample age and statistical variations. The temperature and humidity of the atmosphere during testing are anticipated to have an effect on the resulting friction measurement, with an extreme case being presented by Sun et al. in which elevated temperatures of 500°C improved the wear resistance of laser textured TC11 alloy [119]. Given the location of the testing equipment, it was impossible to control these variables and no measurements were taken of them during testing. Surface contamination was kept to minimum by careful handling (holding sides of samples rather than contacting surfaces) and use of custom designed boxes for sample transportation; however some amount of contamination is expected to be unavoidable, especially when such surfaces are used in an industrial environment. For the results presented in this thesis, the age of the textured samples (time between laser texturing and friction testing) was typically <3 days and the sample age was expected to have an insignificant effect on the friction coefficient. However, results presented on LST for generating highly non-wetting surfaces [58] indicate that sample age can significantly change the surface chemistry, possibly also having an impact on the friction coefficient. Finally, there are a number of statistical variations which cannot be avoided [120], such as varying material properties (e.g. from composition variations) and a randomness to how the contacting surfaces meet (e.g. whether most peaks contact peaks or troughs from the opposite surface). As a result, the possible sources of error discussed were minimised throughout testing, with all friction experiments carried out as described in Section 4.1.

4.4 20W HS-L Textures for High Friction

As discussed in Section 3.3.2, a hexagonal pulse layout was used for the laser texturing. Initial friction tests were performed on Cr-Mo-Al alloy nitriding steel which was textured using a 20W HS-L laser. The effects of laser pulse energy and pulse overlap were considered first. Pulse energies of 0.4mJ and 0.8mJ were chosen for the initial study as these are both above the ablation threshold (~0.2mJ, ~10Jcm^{-2}), determined from the individual crater analysis in Section 3.2.1, whilst generating very different surface structures. Example textures are shown in Figure 4.9

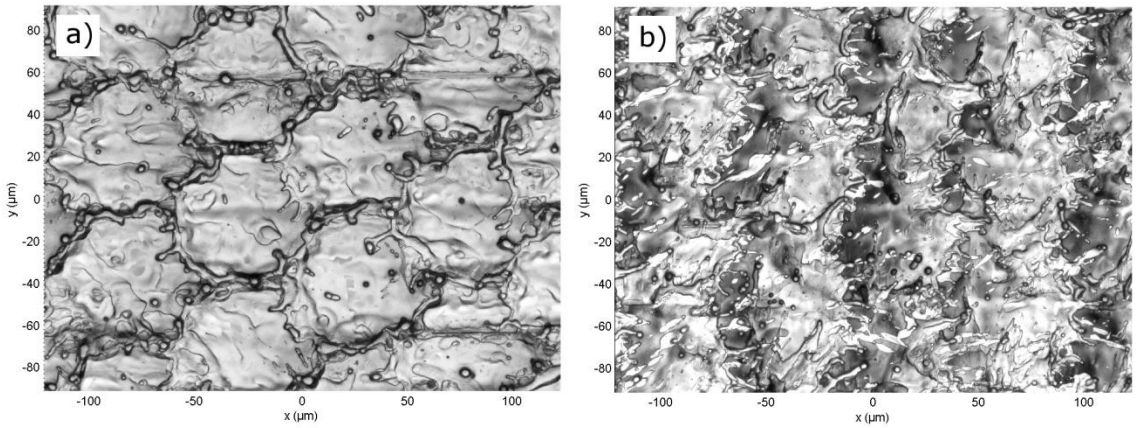

Figure 4.9. Micrograph of 0.4mJ (a) and 0.8mJ (b) pulse textures at -25% pulse overlap showing melt and ablation features, respectively.

For the 0.4mJ pulses, the surface features were dominated by melt effects, where molten material has been merely moved across the surface as shown in Figure 4.9a. For 0.8mJ pulses the effect of ablation is much more apparent, shown by the much larger molten splashes, some of which have clearly left the surface and resolidified elsewhere on the substrate in Figure 4.9b. As a result, the higher pulse energy texture has a fine-scale, rough surface (owing the smaller size of the recast molten material) whilst the texture obtained with the lower energy pulses has a smoother surface.

Pulse overlap was varied between -50% and 75% in order to achieve a range of surface roughness values. From the results shown in Section 3.2.2, a higher pulse overlap was expected to give larger peak-to-trough heights and result in higher surface roughness and friction coefficients.

4.5 Friction Measurements at 150MPa Normal Pressure

The load-extension data for the first set of friction tests performed at 150MPa (60kN) normal pressure is plotted in Figure 4.10.

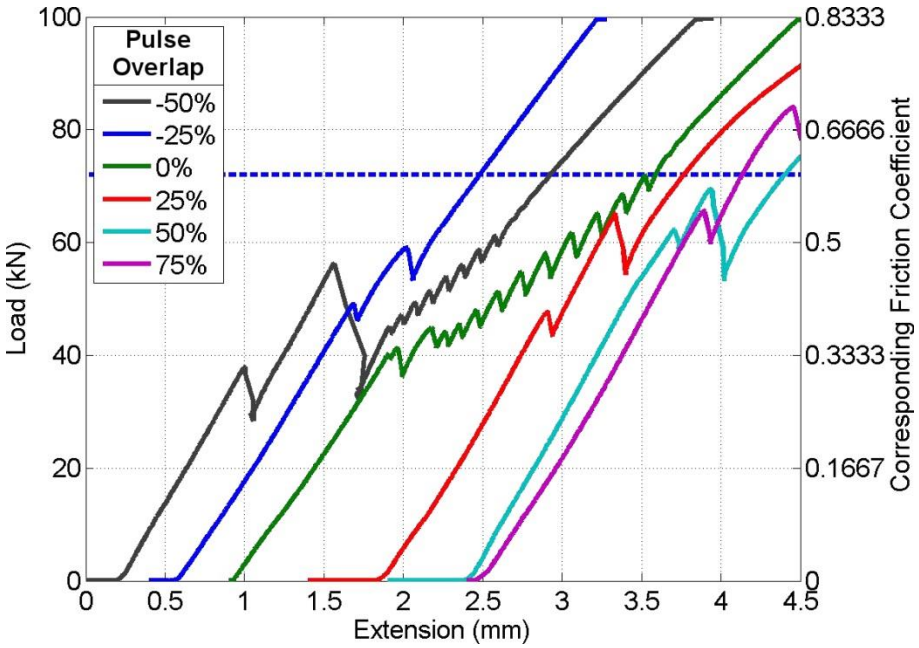

Figure 4.10. Load as a function of extension for initial set of friction tests using 0.4mJ textures with various pulse overlaps, with the corresponding friction coefficients for 60kN normal force shown; the dashed horizontal line indicates the desired friction coefficient of at least 0.6

By taking the F_{max} values from the load-extension curves and using Equation (4-1), the dependence of the friction coefficient on pulse overlap can be determined, as in Figure 4.11.

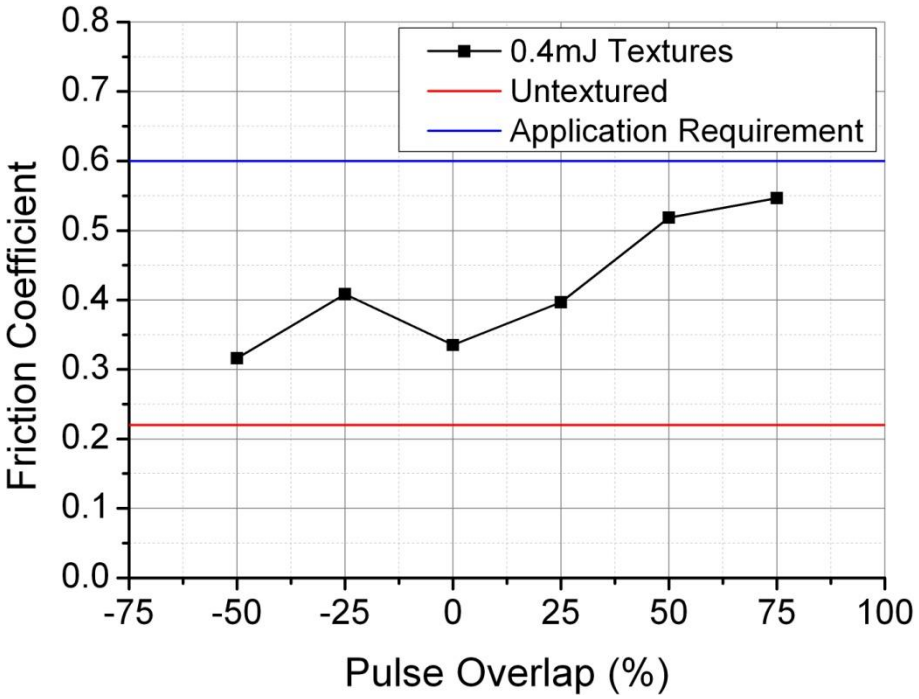

Figure 4.11. Friction coefficients as a function of pulse overlap for 0.4mJ textures. Untextured (μ_s~0.22) and application requirement (μ_s>0.6) shown as horizontal lines for comparison

With the exception of the slightly higher friction coefficient measured at -25% overlap, the general trend in Figure 4.11 shows that increasing the pulse overlap also increases

the resulting friction coefficient, with a maximum of μ_s=0.55 at 75% pulse overlap. This trend agrees with the expectations, as higher pulse overlap results in higher surface roughness. Although it should be noted that standard deviations of these values were not available, variations in these measurements of up to ±0.1 for the textured and ±0.04 for the untextured surface can be expected based on later findings. The textures generated using 0.8mJ were then tested, with the resulting load-extension curves shown in Figure 4.12.

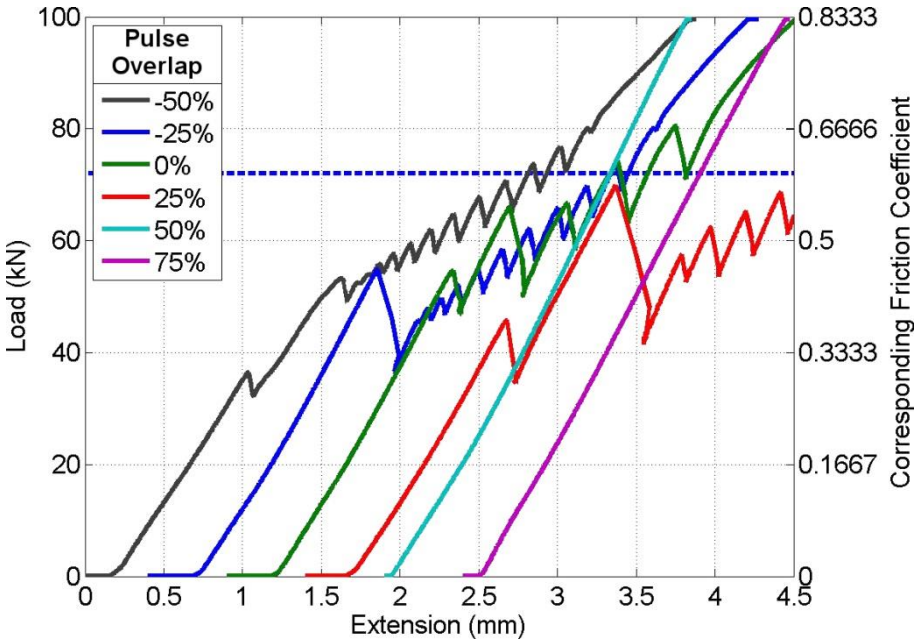

Figure 4.12. Load as a function of extension for initial set of friction tests using 0.8mJ textures with various pulse overlaps, with the corresponding friction coefficients for 60kN normal force shown; dashed horizontal line indicates the desired friction coefficient of at least 0.6

As with the 0.4mJ curves, most of the load-extension curves for the 0.8mJ textures, presented in Figure 4.12, show a steady increase in extension as the load force is increased before reaching a particular slipping point. However, two of the plotted curves, corresponding to the textures with 50% and 75% pulse overlap, show no such slipping point at all up to 100kN load force. For these textures, the load force required to cause the sample to slip exceeded the 100kN force available from the hydraulic press. As a result, the friction coefficients for these textures are at least 0.83. However, it was not possible to determine the exact value. Figure 4.13 shows the minimum friction coefficient as a function of pulse overlap for these textures.

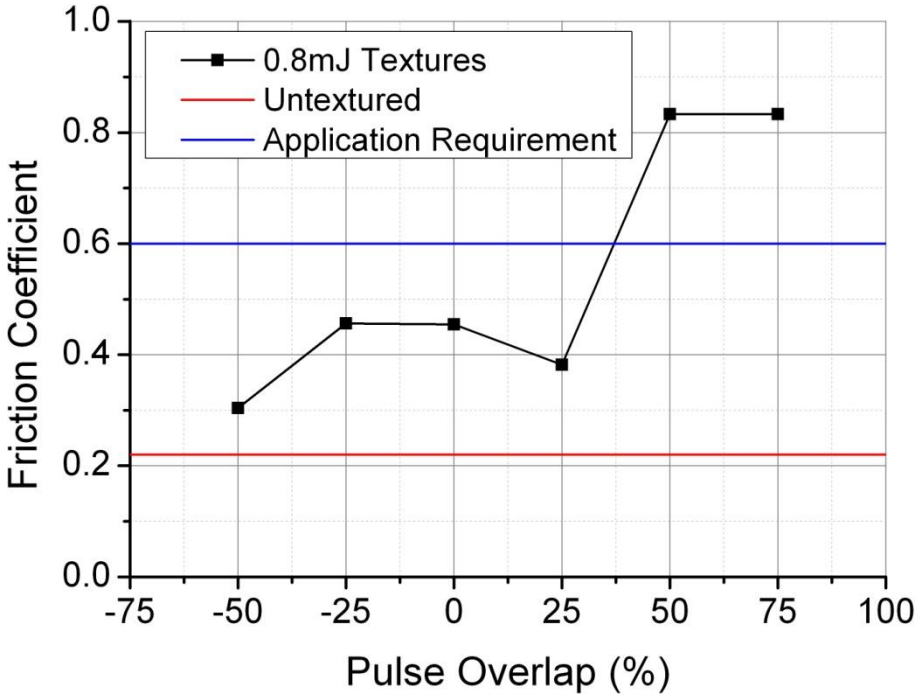

Figure 4.13. Friction coefficients as a function of pulse overlap for 0.4mJ textures. Untextured (μ_s~0.22) and application requirement (μ_s>0.6) shown as horizontal lines for comparison

As with the results of the 0.4mJ textures, the overall trend shown in Figure 4.13 indicates that increasing the pulse overlap increases the friction coefficient. This is highlighted by Figure 4.14 which directly compares two textures generated using the two different pulse energies.

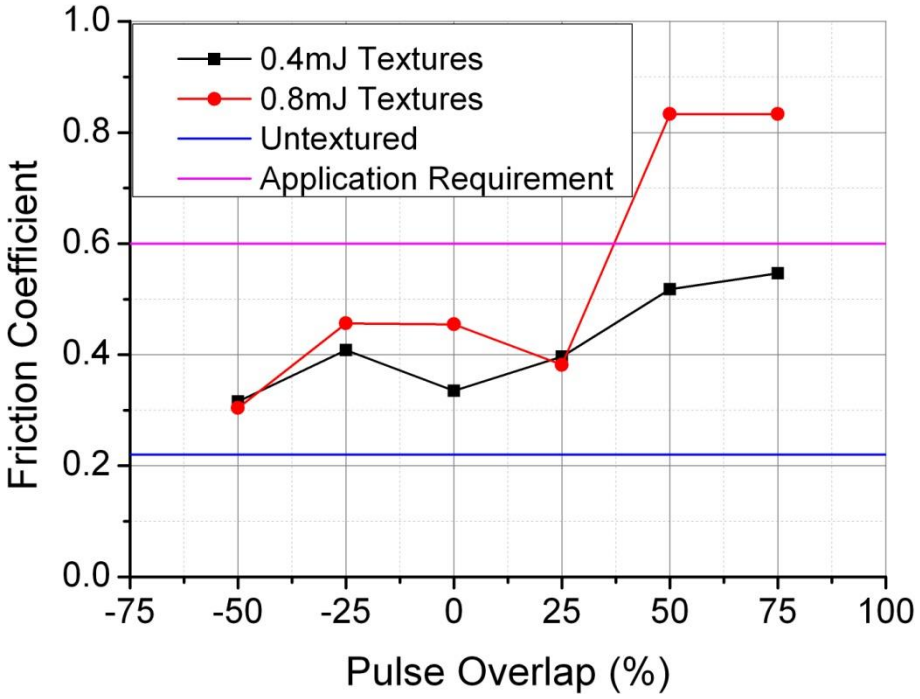

Figure 4.14. Friction coefficients as a function of pulse overlap for both 0.4mJ and 0.8mJ textures. Untextured (μ_s~0.22) and application requirement (μ_s>0.6) shown as horizontal lines for comparison

It is clear, from Figure 4.14, that using higher pulse energies consistently gives higher friction coefficients for the same value of pulse overlap. This is also in agreement with the results discussed in Section 3.2.2, where increasing the pulse energy increases the effective overlap, thus increasing the roughness of the texture.

4.6 Friction Measurements at 100MPa Normal Pressure

Following the results achieved at 150MPa normal pressure, which required >100kN load force in order to determine all of the friction coefficients, the normal pressure was reduced to 100MPa (40kN) for all following friction tests, unless stated otherwise.

4.6.1 Material Comparison

The 0.8mJ textures were then tested at the reduced normal pressure on three different sample materials, Cr-Mo-Al nitriding steel (quenched and tempered to ~355HB), low alloy carbon steel (hot rolled and normalised) and grade 316 stainless steel (cold rolled), with the results shown in Figure 4.15.

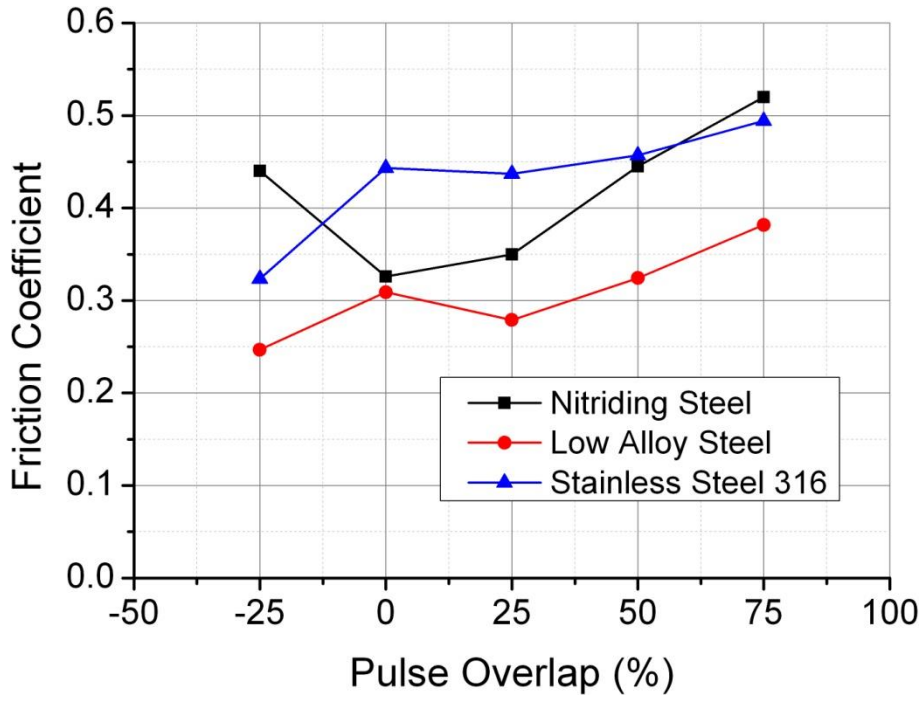

Figure 4.15. Friction coefficients as a function of pulse overlap for three different steel samples; tested at 100MPa (40kN) normal pressure

The friction coefficients observed in Figure 4.15 for the nitriding steel are clearly lower than those observed in Figure 4.13 and significantly so at pulse overlaps greater than 50%. This, contrary to the typical understanding of friction (where the friction coefficient is independent of the normal force), indicates that the applied normal force

has a significant impact on the resulting friction coefficient in this scenario. Due to the large normal pressures used during testing, the dependence of the friction coefficient on the normal pressure is understood to be a result of embedding where asperities of the textured sample are pushed into the counterpart by the normal pressure. Clearly, in this case, higher normal pressure results in more and deeper embedding of asperities, resulting in higher friction coefficients. Despite the decrease in friction coefficients compared to the 150MPa normal pressure, the general trend of friction increasing with pulse overlap is still observed.

There is also a clear difference in the friction coefficients achieved by the different materials, particularly in the case of the low alloy steel. This is most evident at higher overlaps, where the low alloy steel samples consistently provide ~0.1-0.15 lower friction coefficient compared to the other two sample materials. Unprocessed samples were found to give friction coefficients in the region of 0.2-0.25 for each of the three materials.

4.6.2 Roughness Dependence

The physical reason for the dependence of the friction coefficient on the pulse overlap was then considered. The initial assumption was that the increasing surface roughness, induced by the increasing pulse overlap, was the primary factor. Therefore, various different measures of surface roughness were measured for each texture and material, two of which are shown in Figure 4.16.

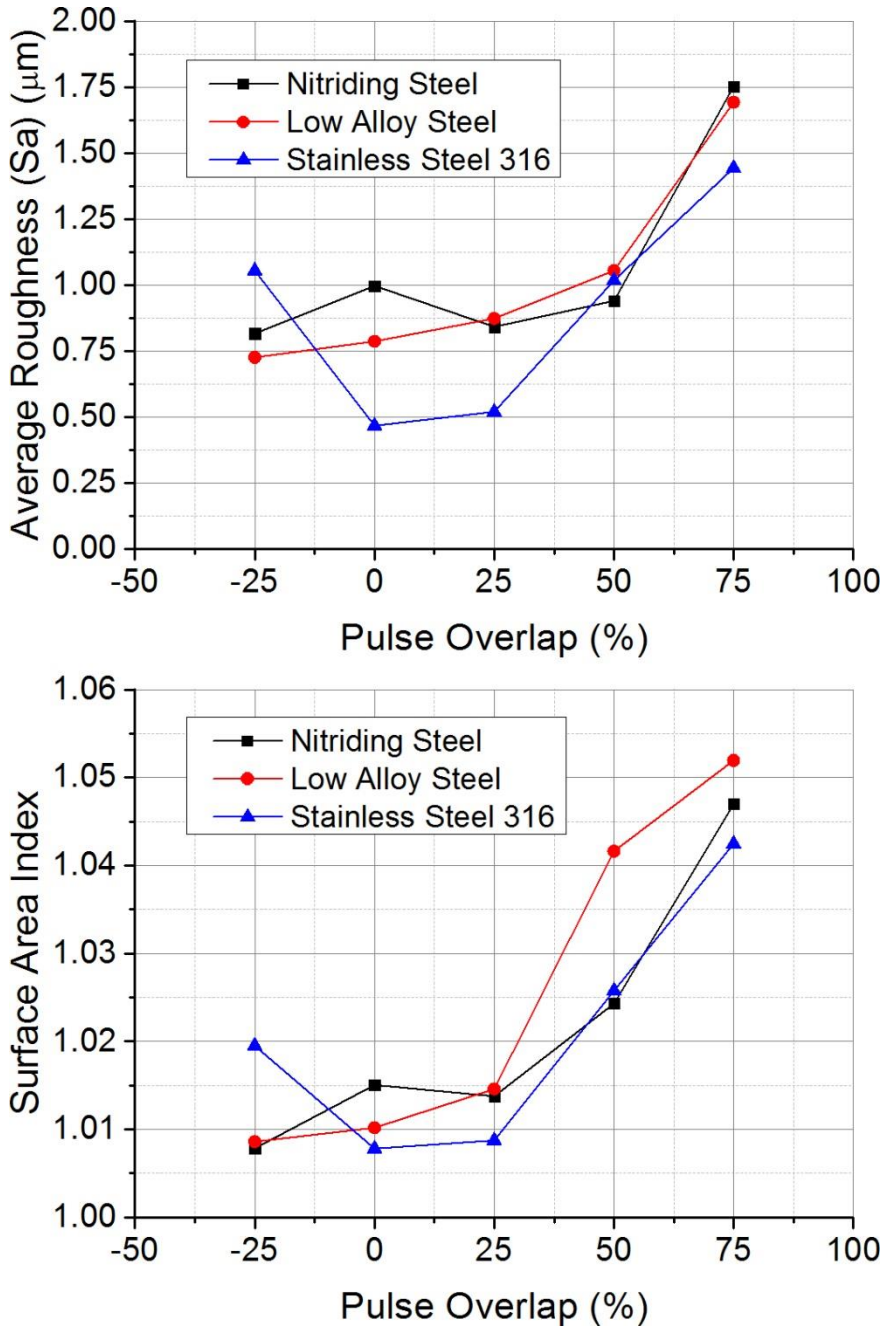

Figure 4.16. Average surface roughness and surface area index as a function of pulse overlap for three sample steels; textures generated using 0.8mJ pulses

S_a is the area arithmetic average surface roughness, equivalent to the line arithmetic average roughness value R_a. Surface area index, SAI, is another roughness measure determined as the ratio of the real surface area to the nominal surface area. Due to the insignificant differences observed between them, only two of the myriad of surface roughness measures are plotted here in order to observe the trends. The results shown in Figure 4.16, calculated over representative areas measuring ~250x180µm, indicate that increasing pulse overlap increases the surface roughness, as anticipated. However,

the variation with pulse overlap shows no strong correlation to the measured friction coefficients as highlighted in Figure 4.17.

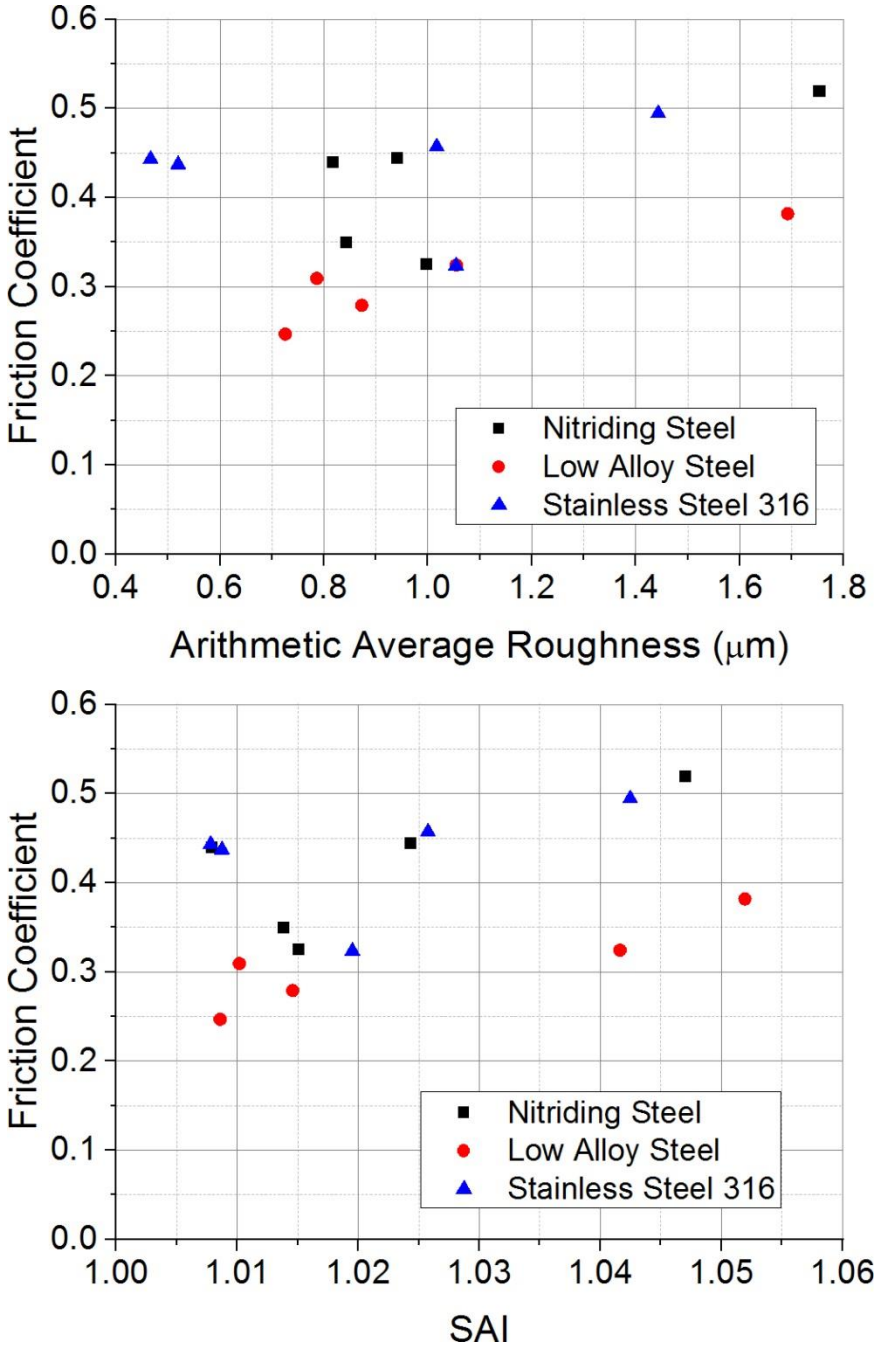

Figure 4.17. Friction coefficient as a function of arithmetic average roughness and surface area index for three sample steels; textures with various pulse overlaps generated using 0.8mJ pulses and tested at 100MPa normal pressure

A weak correlation between friction coefficient and the surface roughness can be observed in Figure 4.17, where increasing roughness leads to a small increase in the observed friction coefficient. However, there are a significant number of points in these plots which are anomalous to this trend, indicating that the roughness of the surface is

not solely responsible for the achieved friction coefficients. This analysis was performed for many other surface roughness parameters including S_q, S_t, S_{sk} and S_{ku}, all of which had weak correlations to the friction coefficient at best.

4.6.3 Hardness Dependence

Following the weak correlation between the friction coefficient and the surface roughness, the hardness of the sample material was considered as a possible cause of the observed increase in friction. Hardness testing was performed on the laser textured surfaces using a diamond tipped Vickers hardness macro indenter using a load of 30kgf for ~10s. The resulting indents were then measured optically, with the Vickers hardness HV, calculated as follows:

$$HV = \frac{2 \times F \times \sin\left(\frac{136°}{2}\right)}{d^2} \quad (4\text{-}2)$$

where F is the load (in kgf) applied to the sample by the indenter, *d* is the length of the diagonal of the resulting indentation and the 136° relates to the geometry of the Vickers indenter. Hardness values are written in the form of xxHVYY, where xx is the hardness value obtained with a load force of YYkgf. Results of the hardness measurements are shown in Figure 4.18.

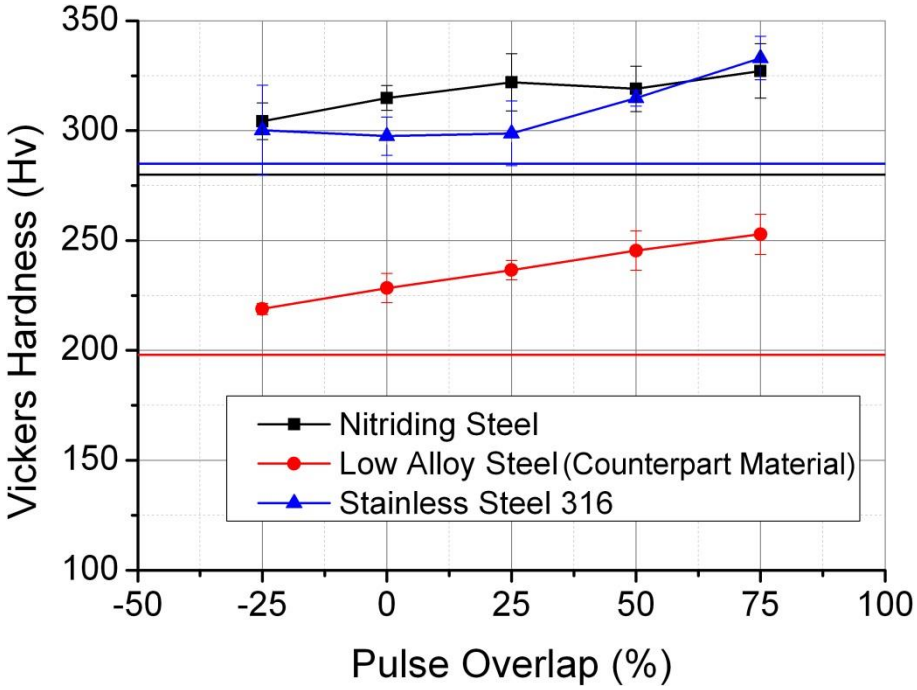

Figure 4.18. Material hardness as a function of laser pulse overlap for the three different steels textured with 0.8mJ pulses. The straight horizontal lines indicate the hardness of untextured samples of the corresponding steels

The results, shown in Figure 4.18, show that the laser texturing process increases the surface hardness compared to the as-received sample material in all three cases. The error bars plotted in this case are the standard deviation of the measurements five hardness indents on each sample. There is also a clear trend of the surface hardness increasing with pulse overlap. The increase in hardness is assumed to facilitate the embedding of the rough sample into the comparatively soft (low alloy) counter surface when the normal force is applied, increasing the ploughing forces required to move the sample relative to the counter surfaces. This assumption is also in agreement with the increased friction coefficients observed when testing at higher normal pressures, which would facilitate better, deeper embedding of the hardened asperities of the sample into the counter surface. It should be noted that, due to the indenter used, the size of the indents were of the order of 450µm across (diagonal) and 60um deep. As a result, the hardness measurements give an average over the surface texture features but are also significantly affected by the bulk material hardness. The measurements for both friction and hardness for each sample were therefore plotted against each other, as shown in Figure 4.19.

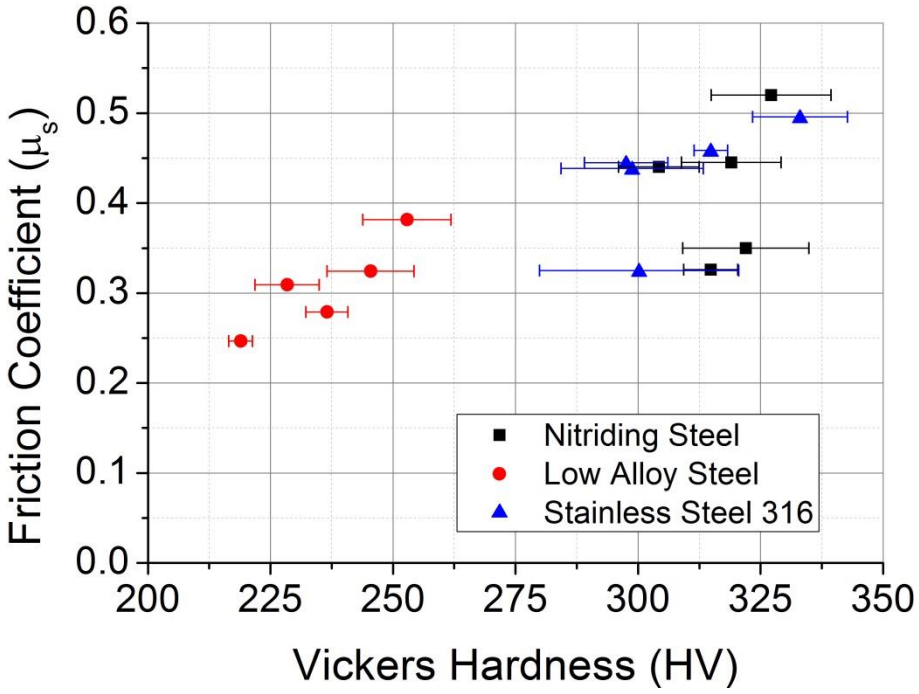

Figure 4.19. Relationship between friction coefficient and hardness for 3 different materials at a range of pulse overlaps. Textures generated using 0.8mJ pulses and tested at 100MPa normal pressure

Even with this limited sample size, there appears to be an approximately linear correlation between the surface hardness of the sample and the friction coefficient which can be achieved, albeit with a few outlying points. Therefore, it was assumed that hardness is the primary factor in determining the friction coefficient of a surface with the surface roughness playing a secondary role. In order to confirm this assumption conclusively, further tests were carried out with high hardness samples including laser hardened samples, nitrided steel alloys and heat treated tool steels. The materials used and the results of this work are detailed in Chapter 5.

4.6.4 SEM & EDX Spectroscopy Analysis

In order to determine the process through which the surface hardens by laser texturing, scanning electron microscope (SEM) and energy dispersive X-ray (EDX) spectroscopy analysis were performed on a cross-sectioned SS316 sample with a high pulse overlap texture, as shown in Figure 4.20.

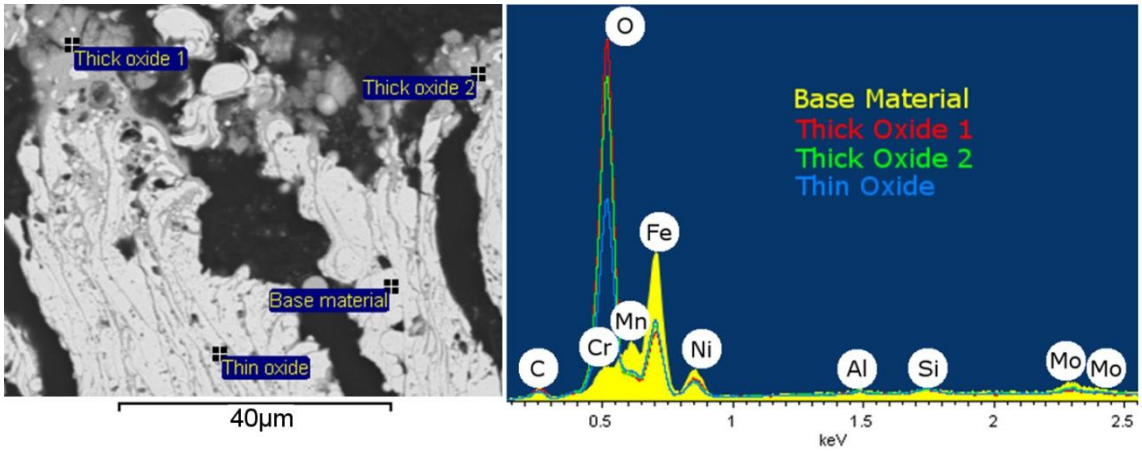

Figure 4.20. SEM and EDX analysis of SS316 with high pulse overlap (80%) laser texturing

By performing the laser texturing with such high pulse overlap (80%), it can be seen from the SEM cross-section in Figure 4.20a that the surface texture generated becomes highly porous and complex. Several different material regions can also be observed, as indicated by the different labels: base material, thick oxide and thin oxide. The base material in this case is the SS316 material which has been molten and recast, but without any significant chemical changes to the bulk SS316 material. The thick oxide is the darkened areas of material at the very top of the SEM image. As a result of the location of this material and the thermal energy present during laser processing, this region reacts significantly with the oxygen present in the air, thus generating a large area of heavily oxidised SS316 material at the very surface of the texture. This thick oxide layer is clearly visible on the surface of the sample by the change in surface colour, as seen in Figure 4.21. This colour ranges from a silvery/steel colour for untextured and very low pulse overlap to very dark brown/black for very high pulse overlap (caused by a combination of the dark oxide layer and light trapping caused by the enhanced surface roughness). Finally, fine lines of thin oxide can be observed in between large areas of base material. Due to the pulse-by-pulse and line-by-line nature of the laser texturing process, these lines of thin oxide are formed after each pulse where the surface of the molten steel oxidises slightly before being recast on the surface of the sample. As the pulse overlap is high in this case, these lines of thin oxide are both closely spaced and almost vertical in the resulting texture.

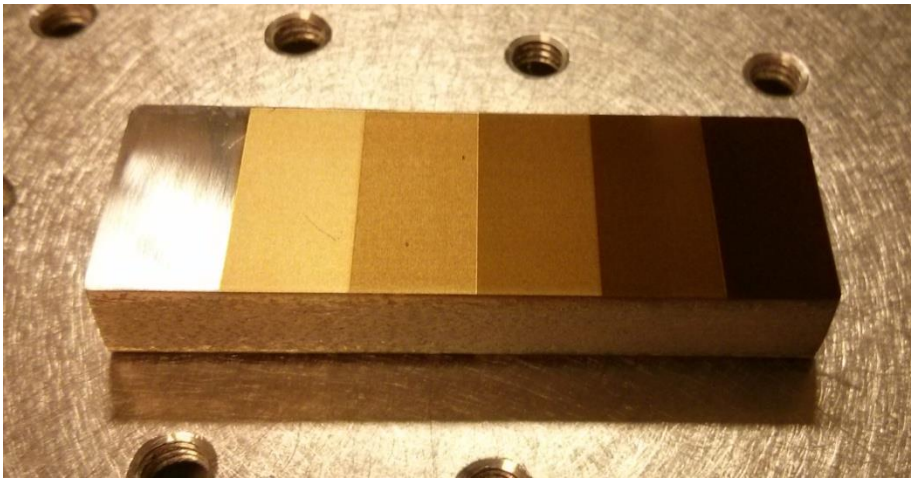

Figure 4.21. SS316 sample with different laser texturing pulse overlaps for comparison; from left to right: unprocessed, -25%, 0%, 25%, 50% and 75%

EDX analysis of the highlighted areas is shown in Figure 4.20b, where very large oxygen peaks can clearly be seen. Therefore, the increase in hardness observed in Figure 4.18 is assumed to be due phase changes and the formation of hard oxides with several of the alloying elements in the steels – primarily chromium oxide in SS316 and both chromium oxide and aluminium oxide in the case of the Cr-Mo-Al nitriding steel. The low alloy carbon steel, on the other hand, has neither of these alloying elements and therefore the textured samples do not reach the same hardness level of the other steel alloys tested. The hardness increase observed in this case is likely due entirely to phase changes in the steel structure caused by the heating and subsequent rapid cooling during the laser texturing process.

4.7 Effect of Laser & Processing Parameters

A wide range of the laser and processing parameters were then studied in order to determine the best laser properties and process settings to use in order to achieve the largest friction coefficient. In order to cover as much of the extremely large parameter space for this process, only one friction test was performed for each pulse overlap (pulse separation) and laser/process parameter combination. Therefore, the results discussed in the remainder of this chapter should not be considered as absolute and final, but rather act as an indication of the process parameters which should be studied in further detail.

4.7.1 Spot Size & Beam Quality (M^2)

The first of the parameters which were considered were the nominal focus spot size of the laser beam and the laser beam quality. By changing the beam expander optics, two different spot sizes of ~50µm (using a 75mm BEC) and ~35µm (using a 100mm BEC)

were attained and compared. Figure 4.22 shows a comparison of the friction coefficients obtained with these spot sizes.

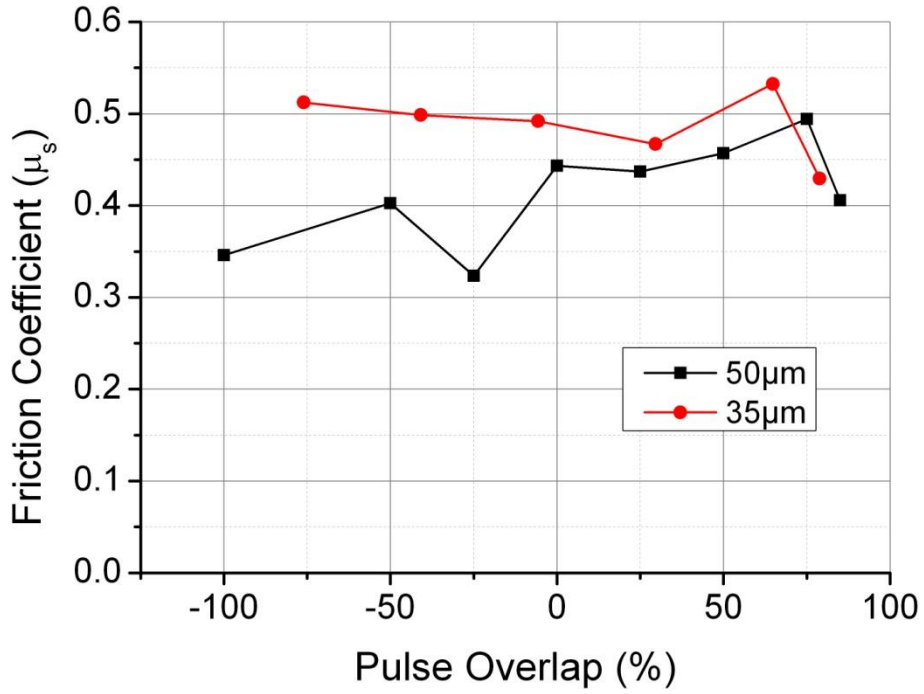

Figure 4.22. Friction as a function of pulse overlap for two different spot sizes on SS316. 20W HS-L (M^2~1.8), 0.8mJ @ 25kHz

As can easily be seen from Figure 4.22, the use of a smaller focal spot consistently results in slightly (~0.05) higher friction coefficients, with the exception of very high overlap (>75%) where the increased roughness is likely to have become detrimental to the friction coefficient by limiting the real contact area. However, as the spot sizes are different in this case, pulse overlap may not give the best comparison of the textures generated. As a result, the friction results were also plotted against the separation of the pulses used in the generation of the texture, thus eliminating the dependence on nominal spot size and allowing more direct comparisons in other aspects (such as processing time). With this in mind, all future friction results are presented in this way. Figure 4.23 shows the same friction results from Figure 4.22 plotted against pulse separation.

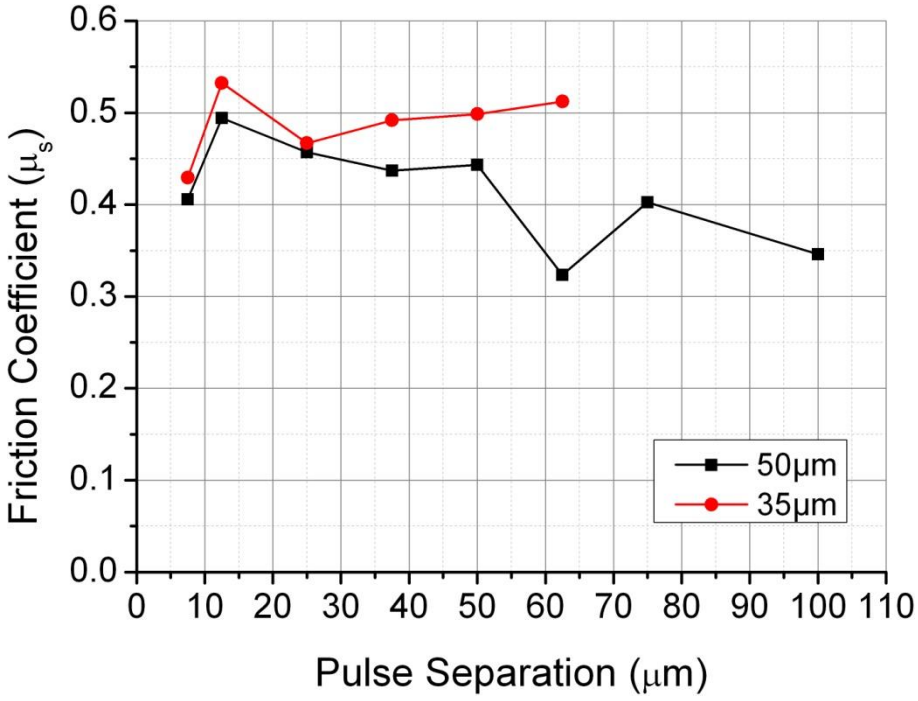

Figure 4.23. Friction as a function of pulse separation for two different spot sizes on SS316. 20W HS-L (M^2~1.8), 0.8mJ @ 25kHz

When plotted against pulse separation, friction coefficients of textures generated with the smaller spot size are found to be slightly higher than those obtained with the larger spot size. This is likely to be due to the increased energy density of the pulse (as pulse energy was kept constant) resulting in higher temperatures at the surface during the laser processing and therefore more oxide formation. The friction coefficients of textures generated by two beam qualities were then compared, as shown in Figure 4.24.

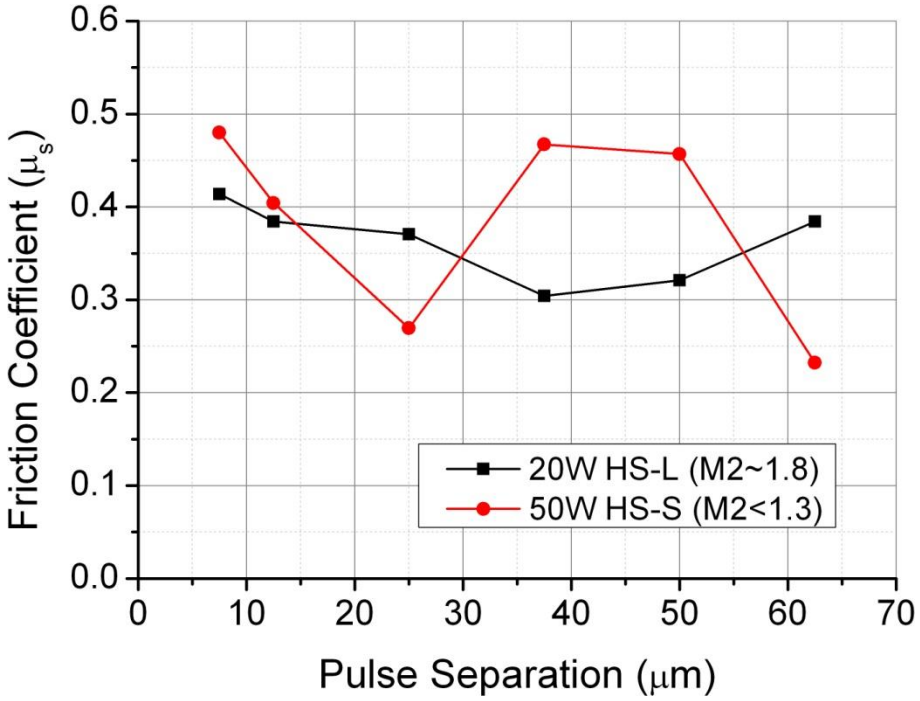

Figure 4.24. Friction as a function of pulse separation for two beam qualities (M^2) on SS316; Φ~35µm, 0.71mJ

By using a 75mm BEC with the 50W HS-S and a 100mm BEC with the 20W HS-L, nominal focal spot sizes of <35.2µm and ~36.1µm, respectively, were obtained, thus allowing an almost direct comparison of the beam qualities. The friction coefficients seen in Figure 4.24 show more variance than was expected, as the points plotted are single values rather than averages. However, there is no overall trend, suggesting that beam quality does not have a large impact on the resulting friction coefficient of the texture. This is not surprising as the effect of the lateral intensity of the pulse is likely to have minimal effect when melting and ablating, as is the case here, especially when the pulses are close together.

4.7.2 Multiple passes

The laser scanning strategy was then considered, in particular the use of multiple passes (i.e. for each spot in the pulse layout diagram, Figure 3.14, multiple laser pulses could be used). In order to achieve this, two possible strategies were considered. First, each line of the texture could be repeated as many times as required before moving on to the next line. Second, the full texture could be generated as in single pass, before repeating the whole texture the desired number of times.

Whilst the preferred approach was to repeat each pulse before moving the beam, the laser scanning software was unable to perform this layout effectively – memory

requirements for such a large number of individual spots proved too excessive, especially when pulse separations were very low (and therefore the number of pulses was very high). Therefore, repeating each line before moving to the next was used as the method of processing multiple passes. Figure 4.25 shows the friction results of textures generated in this way, for up to three consecutive passes, as a function of pulse separation.

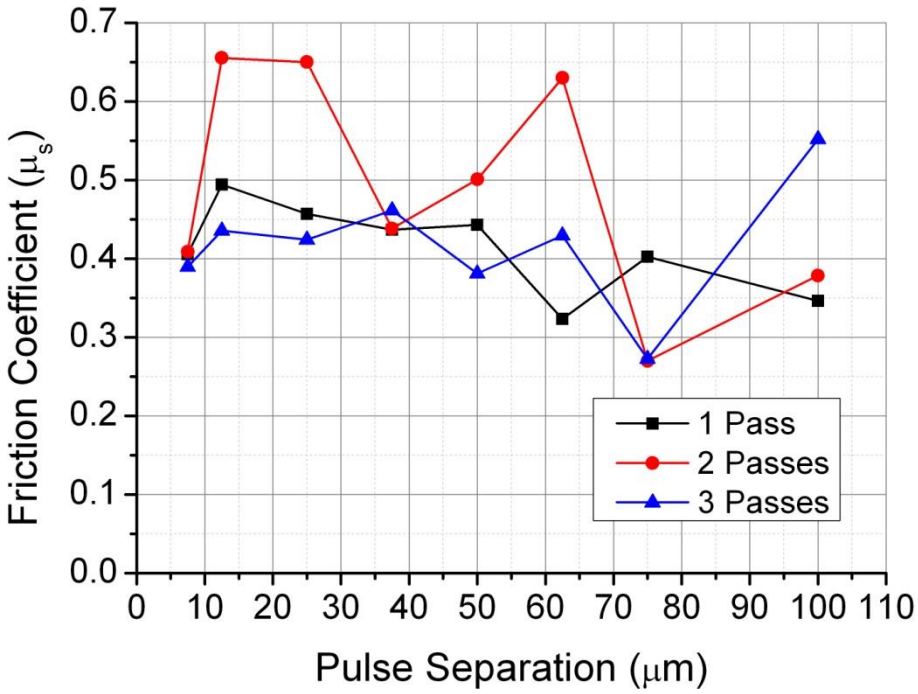

Figure 4.25. Friction coefficient as a function of pulse separation for different numbers of laser processing passes on SS316; 20W HS-L (M^2~1.8, Φ~50μm), 0.8mJ @ 25kHz

The curves observed in Figure 4.25 show no clear trend to indicate that using multiple passes are beneficial for increasing the friction coefficient of the texture. Coefficients obtained for two passes at several pulse separations (12.5, 25 and 62.5) are considerably higher than their counterparts for one and three passes; however, as these are single data points, it is likely that these are not consistently reliable values. Further to this, for each additional pass that is processed the total processing time increases by 100% of the original. Thus, in order to maintain industrial viability, single pass processes are much more desirable.

4.7.3 Processing Atmosphere

Following the SEM and EDX analysis discussed in Section 4.6.4, it was expected that performing the laser texturing process under an inert atmosphere would have a significant effect on the resulting friction coefficients of these textures. An argon

atmosphere was chosen for comparison to the processing in air, with the results shown in Figure 4.26.

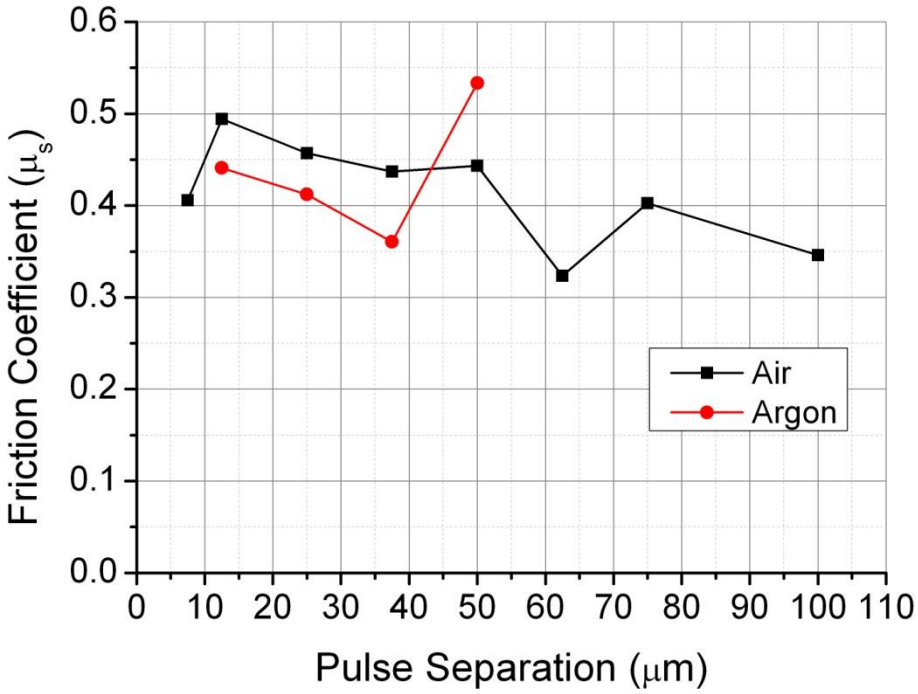

Figure 4.26. Friction coefficient as a function of pulse separation for laser processing under air and argon atmospheres; 20W HS-L (M^2~1.8, Φ~50μm), 0.8mJ @ 25kHz

With the exception of the friction coefficient obtained at 50μm pulse separation, the results shown in Figure 4.26 are in agreement with the expected outcome – performing the laser texturing process under an inert atmosphere reduces the resulting friction coefficient of the texture. As the inert atmosphere was achieved by placing the sample to be textured within a container before flushing argon gas through it, it is possible that a small percentage of oxygen was still present during texturing with the argon atmosphere. However, given the friction coefficients of the other three textures, it is likely that the high friction coefficient for the 50μm texture is due to the lack of a statistically significant number of tests.

4.7.4 Pulse Duration Comparison (20W EP-Z & 70W RM-Z)

Given the possibility to change the pulse duration of the laser easily through changing waveforms, the effect of the pulse duration on the friction coefficient was also considered. For this comparison, the 20W EP-Z and 70W RM-Z lasers were used, as the 20W EP-S was unavailable at the time. The 70W RM-Z laser (running at 20W average power) was used to generate textures with ~200ns pulses, whilst the 20W EP-Z

was used to generate textures with ~500ns pulses. Results of these tests are shown in Figure 4.27.

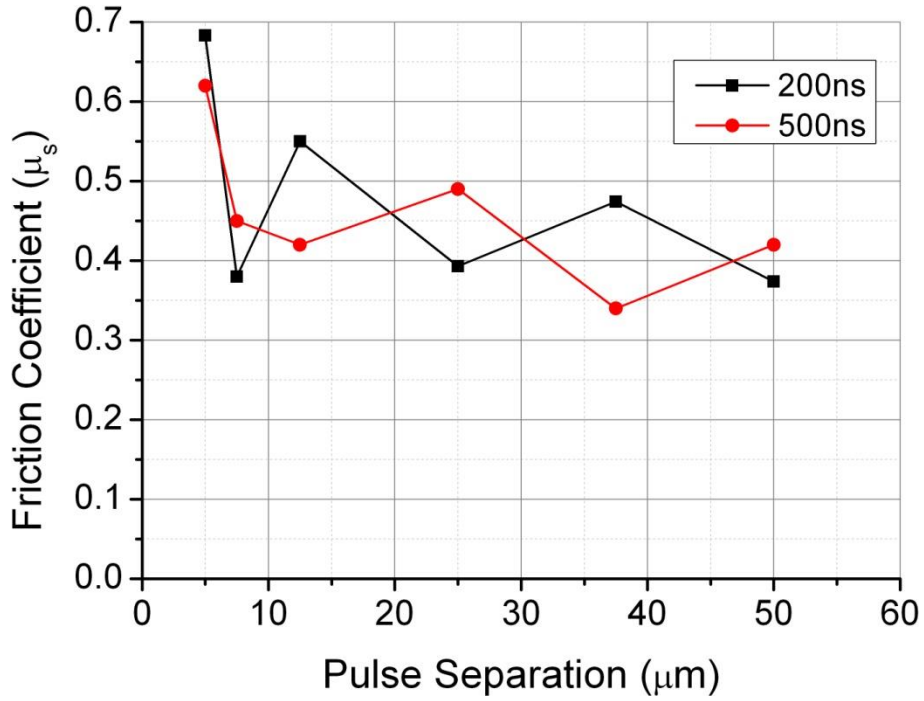

Figure 4.27. Friction coefficient as a function of pulse separation for different pulse durations on SS316; 20W EP-Z & 70W RM-Z (M^2~1.5, Φ~30μm), 1mJ @ 20kHz

From the results shown in Figure 4.27, there does not appear to be a large difference in achieved friction coefficients between textures generated with ~200ns pulses and ~500ns pulses, despite the increase in roughness observed in Section 3.4.2.2 for longer pulses. This is in agreement with the assumption that hardness, rather than roughness, is the main contributor to increased friction coefficients.

4.7.5 Repetition Rate

Finally, the effect of the laser repetition rate on the friction coefficients of the textured surfaces was investigated. The ability to increase the processing rate of the laser texturing is extremely valuable in industrial settings, where areas which require texturing can be very large – either due to the size of the components, as in the case of MDT, or due to sheer volume of components in mass production. Therefore, there is interest in utilising higher average power lasers with higher repetition rates to perform this surface texturing. The 70W RM-Z laser, used in the previous pulse duration comparison, was used to generate the textures for this initial study. Two repetition rates, 20kHz and 70kHz, were chosen for this comparison, with the results shown in Figure 4.28.

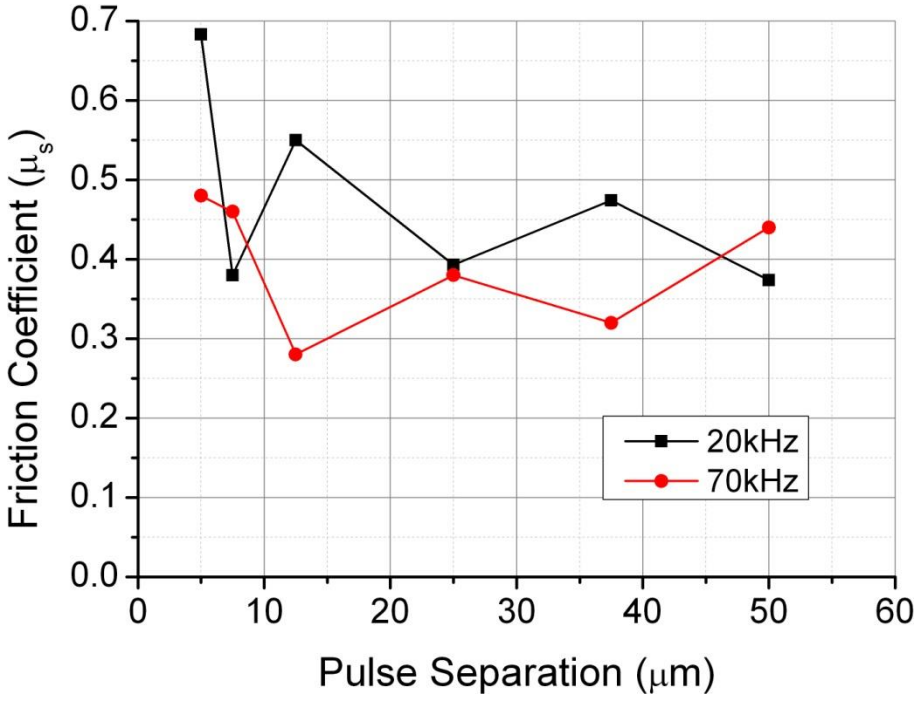

Figure 4.28. Friction coefficient as a function of pulse separation for different repetition rates; 70W RM-Z (M^2~1.5, Φ~30μm), 1mJ

The friction coefficients presented in Figure 4.28 indicate that the use of high pulse repetition rates for laser texturing is detrimental to the friction coefficient. It is assumed that the increased repetition rate, and therefore increased average power, changes the thermal profile of the surface. Thus, the chemical reactions (oxide formation) and possible phase changes at the surface of the steel are likely to be different, resulting in a poorer surface for high friction.

4.8 Increasing the Processing Rate for Industrial Processes

Given the results from Section 4.7.5, an investigation into the effect of the repetition rate on the friction, surface morphology and material properties was conducted, including alternate scanning strategies in an attempt to overcome the issues faced.

4.8.1 Friction of Textures generated with PRF's of 20kHz & 70kHz

4.8.1.1 20kHz Measurements

The 50W HS-S laser was used for this comparison, with textures generated with 12.5μm pulse separation at 20kHz and 70kHz repetition rates. All other parameters were kept constant: 0.71mJ pulse energy, 220ns pulse duration and ~25μm focal spot size. Figure 4.29 shows the friction curves obtained with the textures generated at 20kHz PRF.

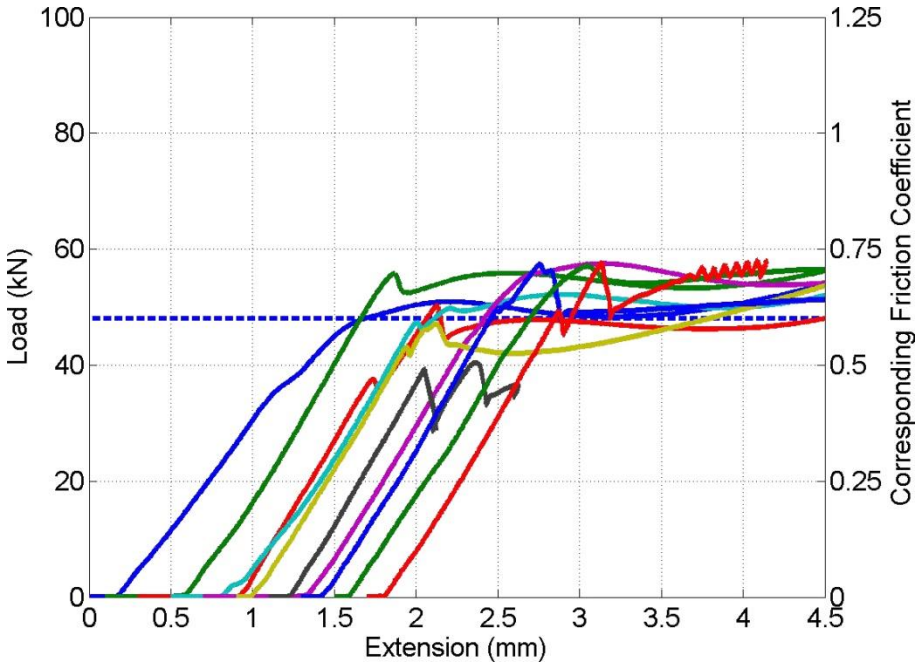

Figure 4.29. Load-extension curves for ten friction tests performed at 100MPa normal pressure on sample textures generated at 20kHz with 12.5µm pulse separation

For the 20kHz texture results, shown in Figure 4.29, the average static friction coefficient was determined to be 0.61 with a standard deviation of ±0.09, albeit one or two samples did not exhibit a particularly sharp slip point. This friction value, one of the highest averages achieved at 40kN (100MPa) normal force, was used as the baseline for the repetition rate scaling comparison. Figure 4.30 shows what a typical area of this texture looks like along with the corresponding z-profile data.

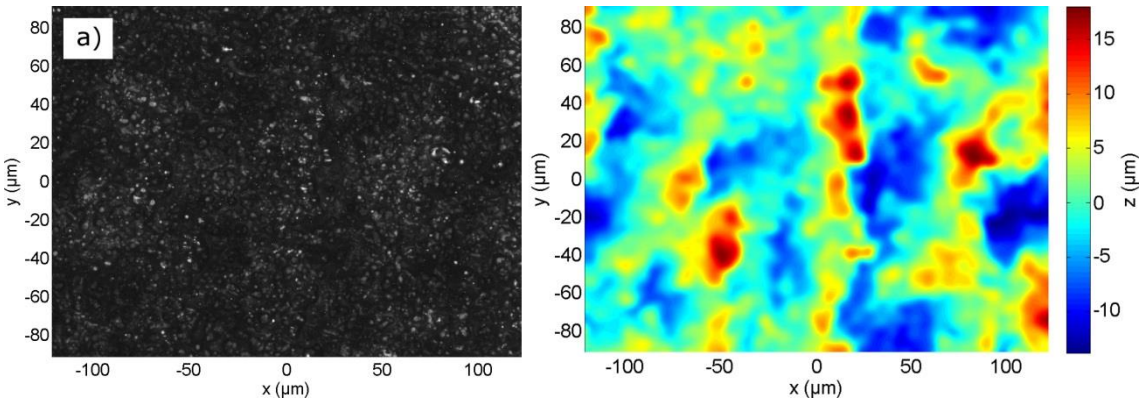

Figure 4.30. Optical micrograph (a) and z-profile (b) for the 12.5µm pulse separation texture generated at 20kHz; 50W HS-S, 0.71mJ, ~25µm spot size

As expected from the previous results, the low pulse separation leads to the generation of a highly random, homogeneous surface, as shown in Figure 4.30a. From the z-profile data shown in Figure 4.30b, the S_a value and peak-trough depth for this texture were calculated as 4.07µm and 31.8µm respectively.

4.8.1.2 70kHz Measurements

The friction tests were then repeated for the same texture generated with 70kHz repetition rate, with the resulting friction curves shown in Figure 4.31.

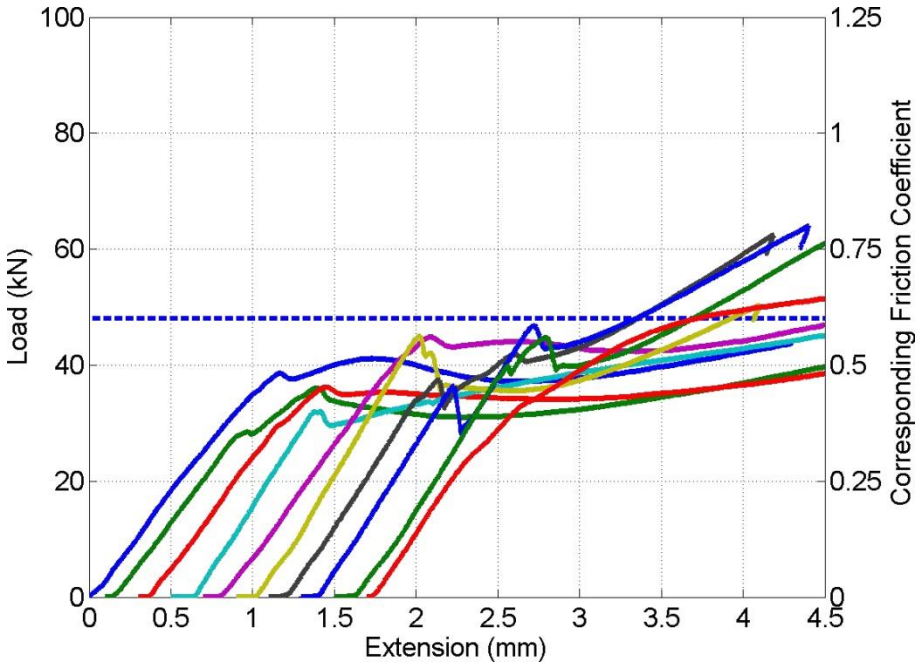

Figure 4.31. Load-extension curves for ten friction tests performed at 100MPa normal pressure on sample textures generated at 70kHz with 12.5µm pulse separation

For the 12.5µm pulse separation texture generated at 70kHz, the average friction coefficient was calculated as 0.48 with a standard deviation of ±0.07. As with the results observed at 20kHz, several of the curves in Figure 4.31 do not show sharp slip points, however it is clear that the friction coefficients are consistently lower for the 70kHz texture compared to the 20kHz texture. A micrograph and z-profile from a representative area of these samples are shown in Figure 4.32.

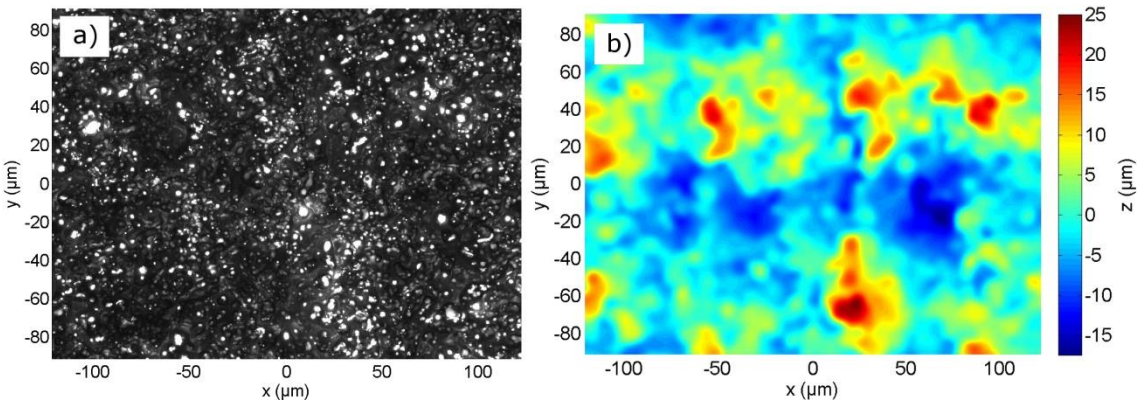

Figure 4.32. Optical micrograph (a) and z-profile (b) for the 12.5µm pulse separation texture generated at 70kHz; 50W HS-S, 0.71mJ, ~25µm spot size

Similar to the 20kHz texture, a homogeneous random structure can be observed in Figure 4.32, albeit with larger, deeper features. The S_a roughness and peak-trough depth were calculated as 4.72µm and 42.47µm respectively, notably higher than the values obtained for the 20kHz texture. It is possible that this increased roughness reduces the friction coefficient of the texture by limiting the contact area of the two surfaces. However, this is not the only possible explanation as the texturing process is clearly heavily dependent on the repetition rate and therefore thermal profile and cooling rate of the surface, which could have a significant impact on the surface chemistry, material properties (e.g. hardness) and, therefore, the friction coefficient.

4.8.2 70kHz Scanning Strategies

In an attempt to achieve friction coefficients of the 20kHz texture whilst maintaining the processing rate of the 70kHz repetition rate, two different scanning strategies were considered involving the interlacing of lines within the texture or interlacing of laser pulses within each line.

4.8.2.1 Interlacing Lines

The interlacing of lines was considered first, where the laser would 'skip' a certain number lines in the first pass before filling in the 'skipped' lines in the subsequent passes, the number of which would correspond to the number 'skipped'. For example, in a texture skipping 2 lines, the first pass would process lines 1, 4, 7, 10 etc., the second pass would process lines 2, 5, 8, 11 etc. and the third pass would process lines 3, 6, 9, 12 etc., as depicted in Figure 4.33c.

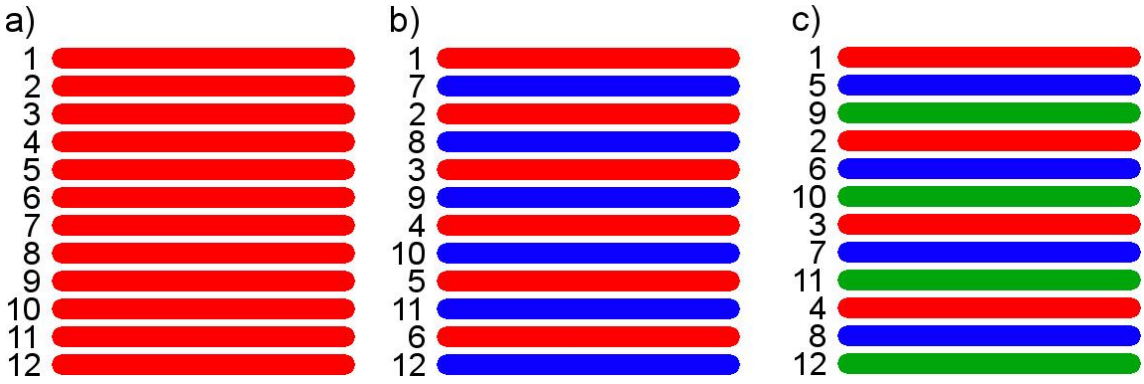

Figure 4.33. Schematic of the processing of interlacing lines for a) standard processing (no lines skipped), b) skipping one line and c) skipping two lines, with the order of the lines indicated to left of each schematic

The schematics shown in Figure 4.33 show the processing order pictorially, with the first pass in each case drawn in red, second pass in blue and the third pass in green. In this regime, a significant delay between adjacent lines is created, with the aim of

reducing the thermal build up in the material. However, two issues were found with this approach. First, the interlacing of lines does not help to reduce the thermal accumulation within each individual line and, second, the generation of the texture in this manner inherently generates non-isotropic structures on the surface which is not tolerable for the high friction application proposed by MDT.

4.8.2.2 Interlacing Pulses

As a result, the same principle of 'skipping' was then applied to the individual pulses within individual lines rather than to the full lines themselves. This technique delays the processing of adjacent pulses within a given line, reducing any thermal build up observed at 70kHz, whilst also producing the array of lines sequentially, thus preventing the generation of non-isotropic structures in the final texture. A schematic depicting the build-up of a single line using this strategy is shown in Figure 4.34.

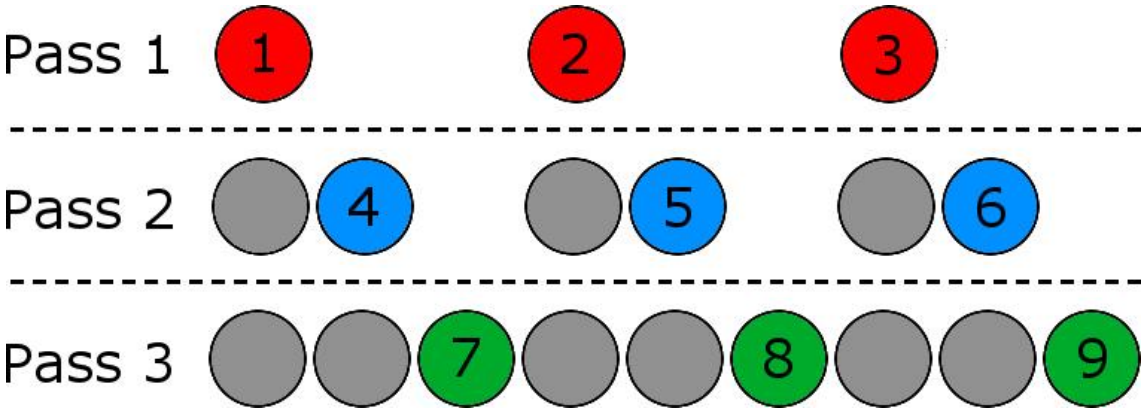

Figure 4.34. Schematic of the generation of a single line with interlaced pulses, by skipping two pulses. Each circle represents a single laser pulse, with coloured circles indicating pulses processed within the current pass and grey circles indicating the location of previous pulses (craters on the surface). For this short line, each pulse has also been numbered in chronological order for clarity.

Although the schematic shown in Figure 4.34 depicts the generation of an interlaced line by skipping two pulses, the process can be used for skipping any number of pulses. As a result, four interlaced textures were generated and analysed in order to select the texture which most closely represents that of the 20kHz texture observed in Section 4.8.1.1.

4.8.3 Surface Comparison of Standard & Interlaced Pulses Textures

Four textures were generated using interlacing of pulses at 70kHz from skipping just a single pulse to skipping four, denoted 70S1, 70S2, 70S3 and 70S4 respectively. The two textures generated by standard processing were also included in the comparison, denoted by 20S0 and 70S0 (skipping no pulses is equivalent to standard processing in this regime). Figure 4.35 shows optical micrographs for each of the six textures mentioned.

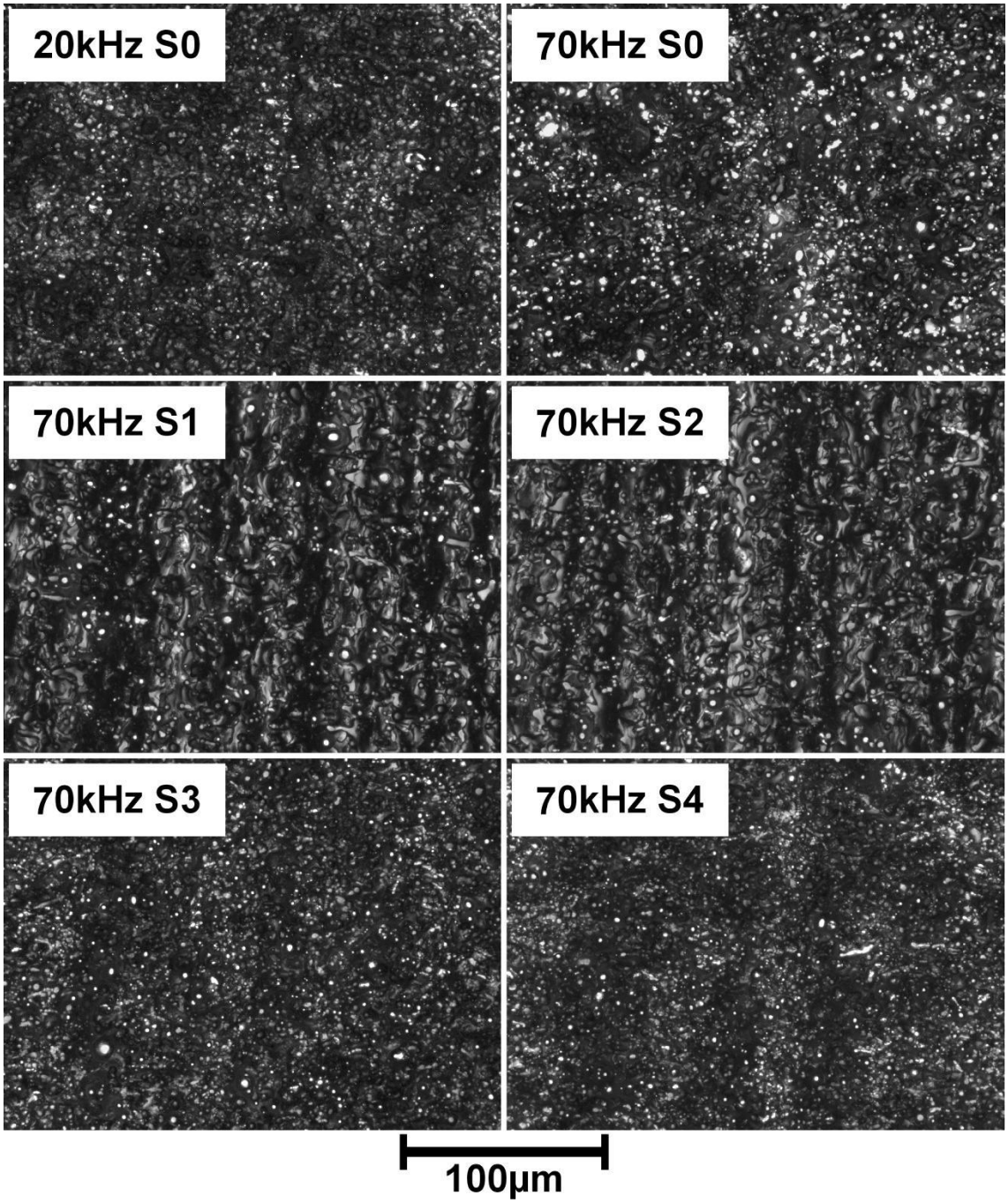

Figure 4.35. Optical micrographs comparing the surface textures observed with and without interlacing of pulses; labels denote the repetition rate at which the texture was fabricated and the number of pulses skipped in interlacing (0 is equivalent to standard processing)

By examining the 70kHz S1-S4 samples from Figure 4.35 visually, it is clear that both S1 and S2 textures exhibit distinct and undesirable linear structure whilst both S3 and S4 samples exhibit the homogeneous, random structure previously observed for the 20kHz texture. The z-profiles for the same textured were then considered, shown in Figure 4.36.

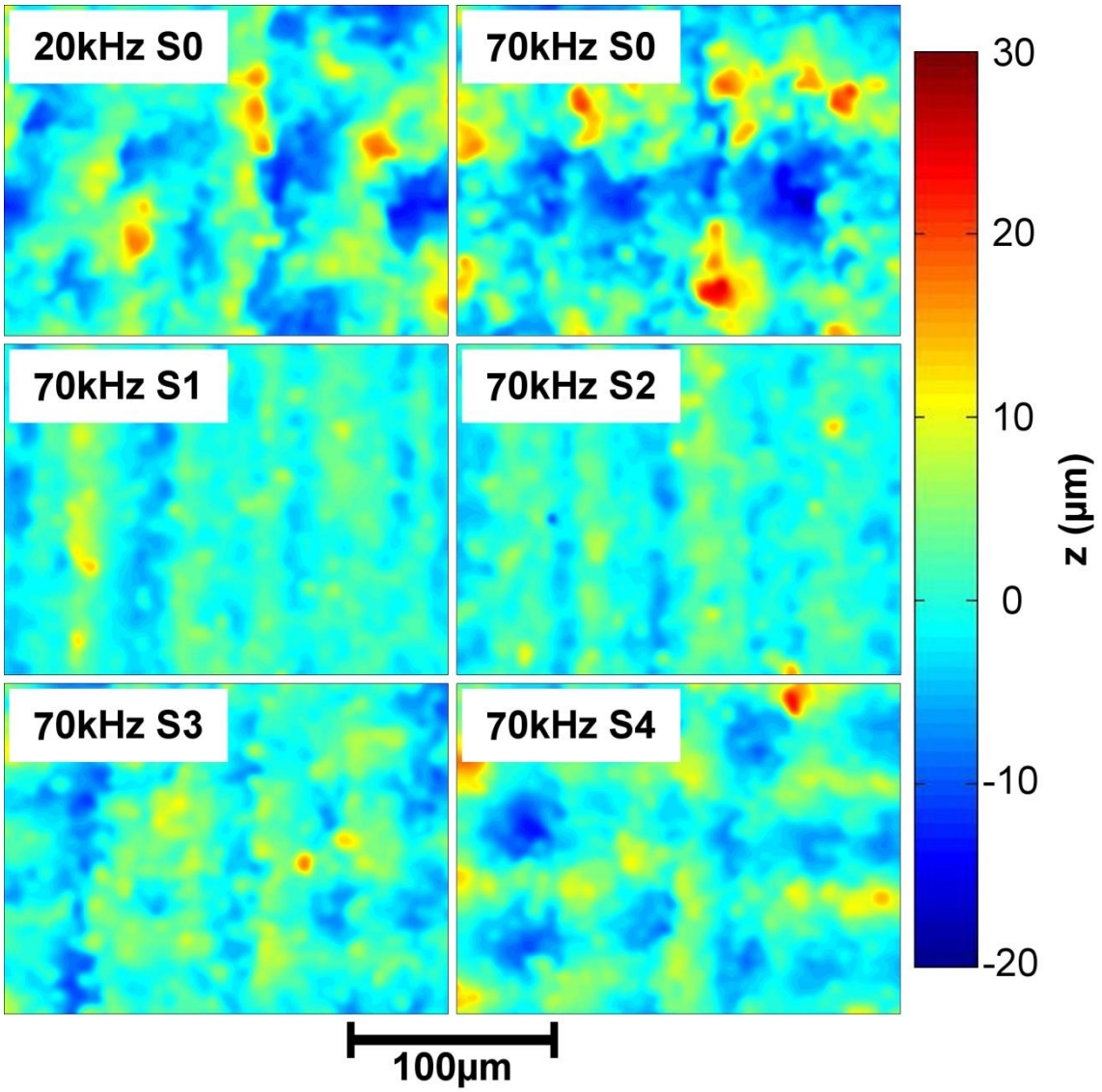

Figure 4.36. Z-profiles comparing the surfaces obtained with and without interlacing of pulses; labels denote the repetition rate at which the texture was fabricated and the number of pulses skipped in interlacing

The linear structure seen for the S1 and S2 textures in Figure 4.35 is even more evident in the z-profile data. As a result, these two textures were disregarded as possible alternatives. Both S3 and S4 exhibit similar z-profiles to the 20kHz texture, with little to choose between them from either z-profiles or optical micrographs. Therefore, given the fact that the S3 structure is slightly easier to design and set up within the scanner

software, the S3 scanning strategy was chosen for the friction testing comparison against the standard processing samples.

4.8.4 Friction Comparison of Standard & Interlaced Pulses Textures

Ten samples were then prepared using the 70S3 scanning strategy and subsequently friction tested, with the results shown in Figure 4.37.

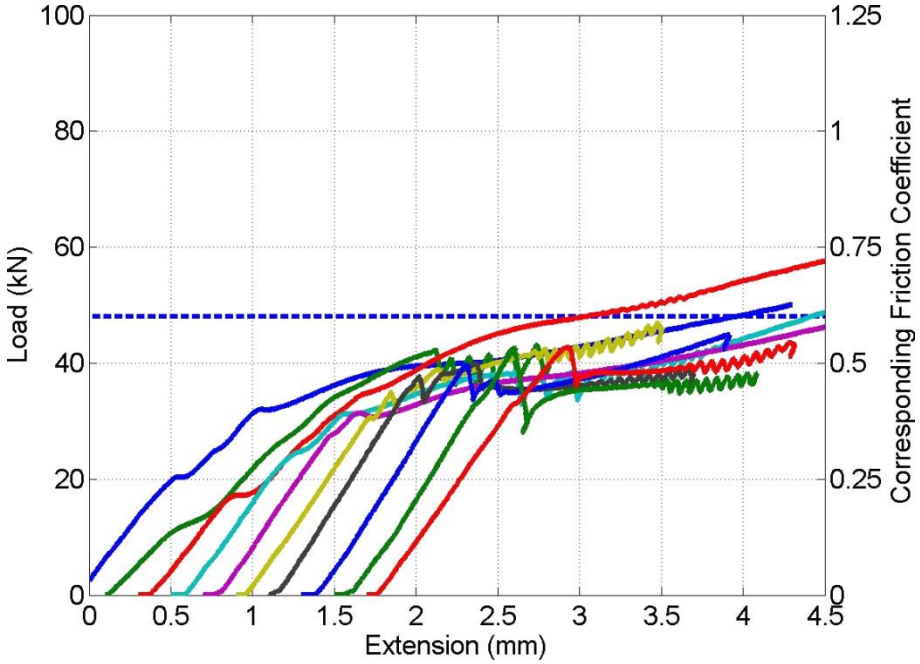

Figure 4.37. Load-extension curves for ten friction tests performed at 100MPa normal pressure on sample textures generated with 70kHz S3 scanning strategy and 12.5µm pulse separation

As with both previous textures discussed in Section 4.8.1, few of the load-extension curves in Figure 4.37 show sharp slip points, with several curves exhibiting no slip point at all. Despite this, the average friction coefficient was calculated to be 0.44 (for the 7 samples with a determinable slip point), lower than both 20S0 and 70S0, with a standard deviation of ±0.10.

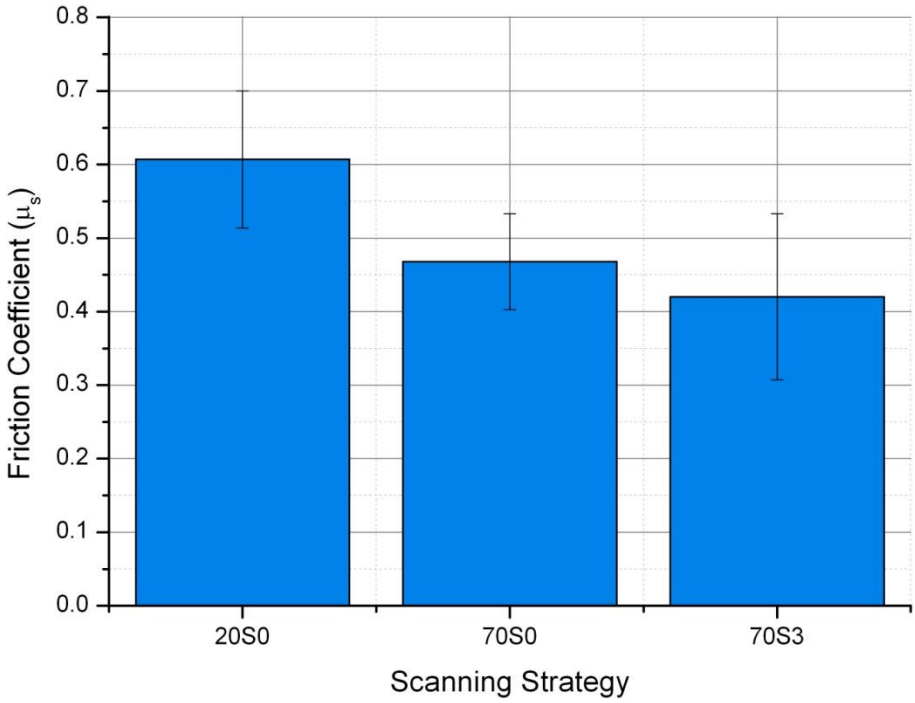

Figure 4.38. Comparison of friction coefficients for the various scanning strategies used

It is clear from the results of the three scanning strategies, shown in Figure 4.38, that the highest friction coefficients are still obtained when using the low repetition frequency of 20kHz. In fact, despite the change in scanning strategy to interlacing, the 70S3 texture resulted in lower average coefficients than the 70S0 texture. As the interlacing was designed to minimise any thermal accumulation effects, the process of building the texture up was analysed for potential issues, along with the 20S0 and 70S0 textures for comparison.

4.8.5 Possible Causes

4.8.5.1 Surface Hardness

As with the samples tested in Section 4.6, the three textures were hardness tested with the results shown in Figure 4.39.

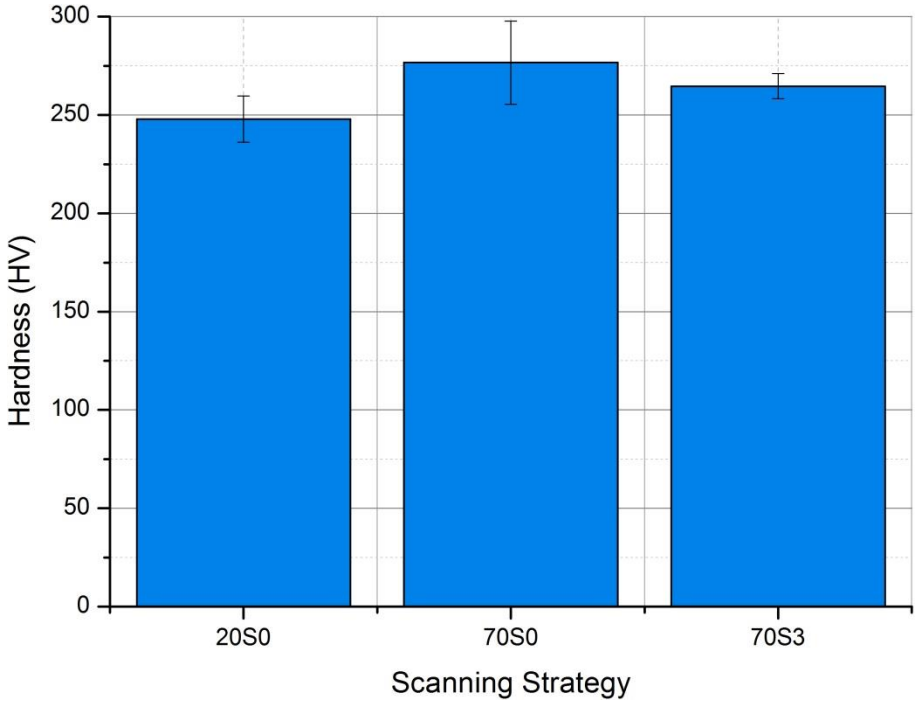

Figure 4.39. Comparison of Vickers hardness values for the various scanning strategies used

As shown in Figure 4.39, the measured hardness was found to increase when processing was performed at 70kHz, both sequential and interlaced, compared to 20kHz. However, the absolute hardness values are low in all three cases, with average hardness values ≤275HV. This explains the load-extension curves where no clear slip points are observed – the low hardness does not facilitate embedding and thus the friction is solely reliant on adhesion. In turn, this means that the hardness is not as important in this case as it was in Section 4.6 and other possible causes were then considered.

4.8.5.2 Line Build-Up

As the interlacing used reorders the pulses within individual lines, possible issues with the construction of single lines, shown in Figure 4.40, were then investigated.

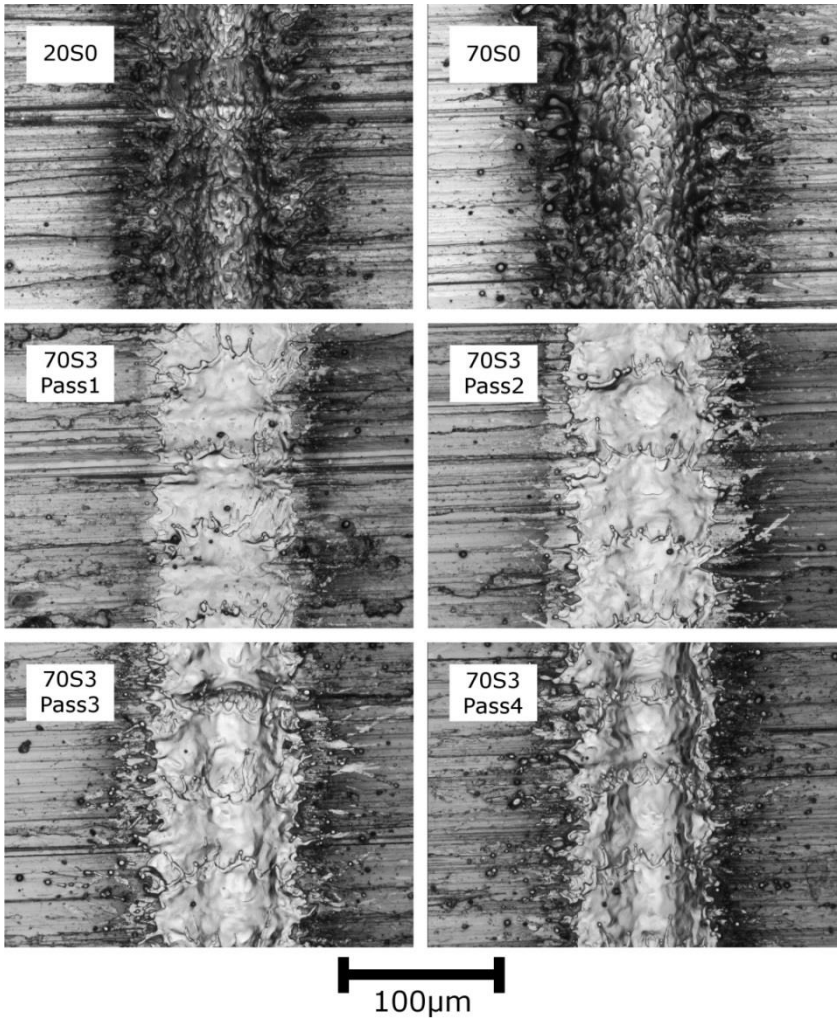

Figure 4.40. Optical micrographs comparing the construction and results of single lines for 20S0, 70S0 and 70S3 scanning strategies; lines generated on SS316 with 50W HS-S laser, 12.5µm pulse separation and 0.71mJ pulse energy

As can be seen from Figure 4.40, the two lines generated with the sequential scanning strategy, 20S0 and 70S0, have a similar appearance – a closely spaced periodic structure down the centre of the line (corresponding to the pulse separation) with a significant amount of recast material either side of the line. In contrast, the trough generated with interlacing (70S3 Pass4) appears much smoother down the centre of the line; with much less recast material at the sides. Despite this, the average trough depths for all three strategies, 20S0, 70S0 and 70S3, were similar, with depths calculated as 8.3µm, 8.7µm and 8.4µm, respectively. By considering the first three passes used in the generation of this line, the reason for the visual difference becomes evident. Due to the increased pulse-pulse separation and reduced thermal accumulation, much less material is ejected from the surface in the molten state, resulting in less recast material at the sides. Also, due to the increased pulse separation, consecutive craters overlap only slightly

(illustrated by 70S3 Pass1 in Figure 4.40) giving a smoother surface finish, which is not too dissimilar to pulsed laser polishing techniques.

The reduced thermal accumulation, due to the increased pulse spacing and the smooth/shiny surface generated acting to reduce the energy absorption from each laser pulse, will reduce the surface temperatures achieved (see Appendix C – Finite Element Model of Laser-Material Interaction) and therefore alter the surface chemistry. Both thermal and chemical changes are likely to have an impact on the resulting texture's friction coefficient.

4.8.5.3 Texture Build-Up

The construction of two dimensional textures was then investigated, with optical micrographs of three and six lines for each scanning strategy shown in Figure 4.41.

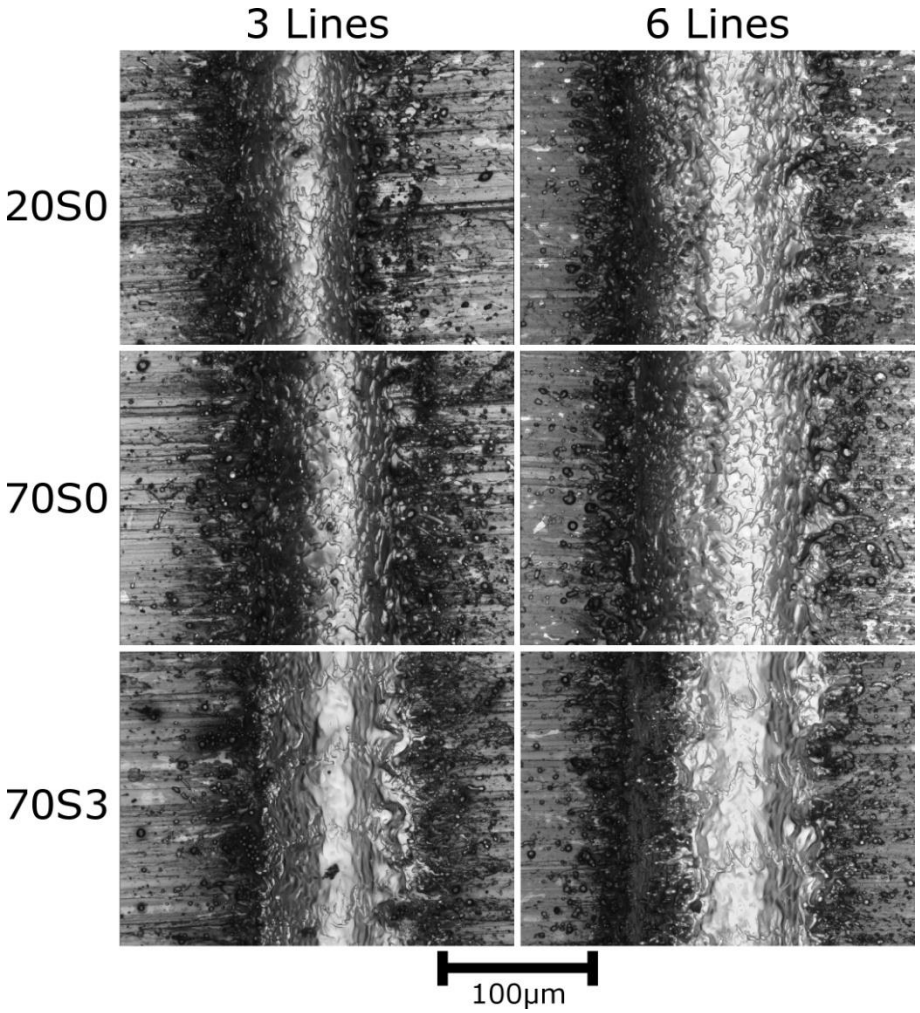

Figure 4.41. Optical micrographs comparing three and six lines for 20S0, 70S0 and 70S3 scanning strategies; generated on SS316 with 50W HS-S laser, 12.5µm pulse separation and 0.71mJ pulse energy

In each of the micrographs in Figure 4.41, each new line has been generated to the right of the previous lines. It is therefore clear to see that the resulting surface structure for each of the three textures is dominated by the small globules of recast melt (significantly darker areas to the left of the lines in these micrographs), whilst the larger scale structure is determined by the processing parameters. In other words, the peak-trough depths, S_a values etc. are dependent on the pulse separation and pulse energy whereas the surface structure observed via optical microscopy is primarily dependent on the formation of recast material. In the case of the interlacing pulses (70S3), the recast material appears finer in structure compared to 20S0 and 70S0, likely due to less melt being generated and therefore less material being recast with each pulse, possibly the cause of the observed difference in friction coefficients between the textures.

4.8.5.4 Cross-Sections

SEM micrographs were also taken of cross-sections of these three textures, with selected images shown in Figure 4.42.

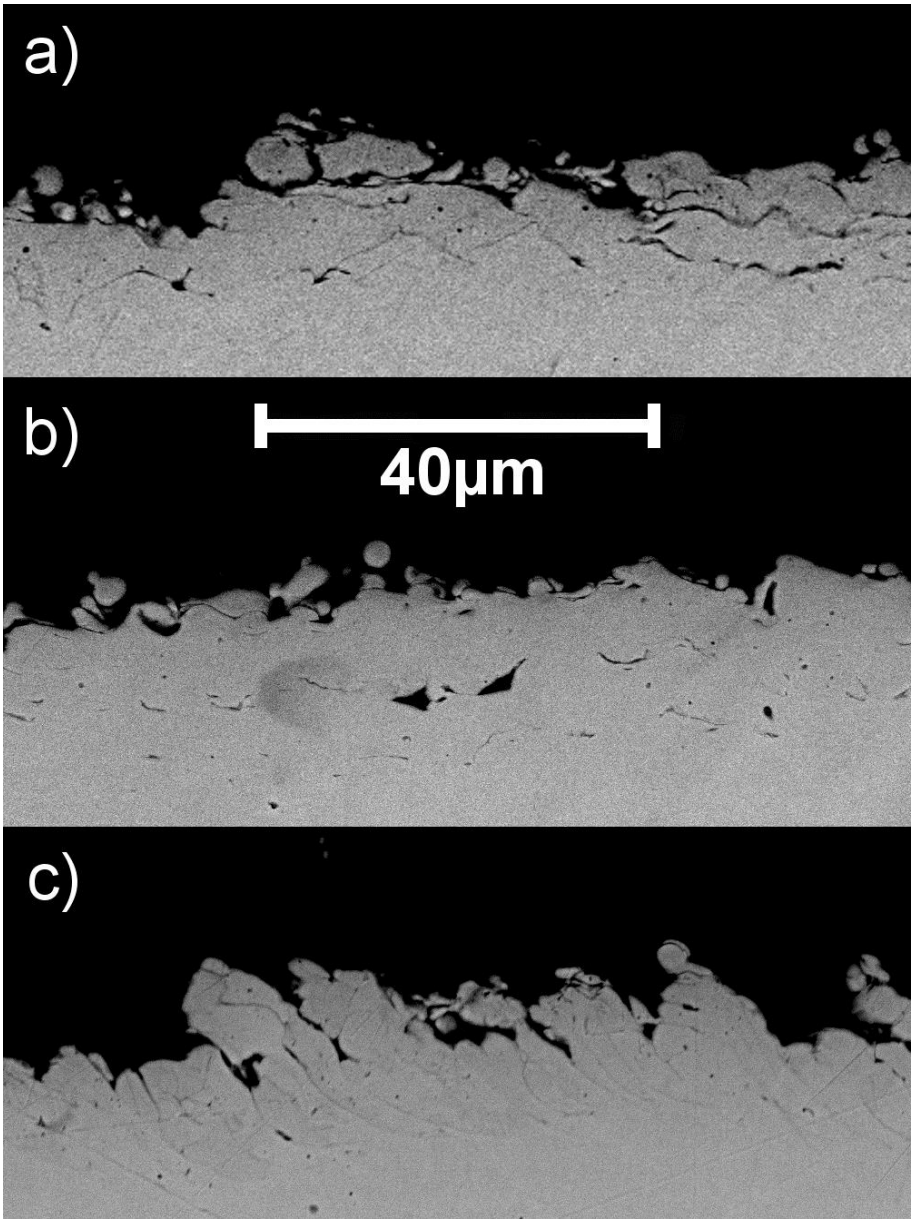

Figure 4.42. SEM images comparing cross-sections of the three textures: a) 20S0 b) 70S0 and c) 70S3

It is clear from all three of the cross-sections shown in Figure 4.42 (parallel to scanning line direction) that the structures generated by use of the 20S0 and 70S0 scanning strategies are similar (see Figure 4.42 a and b), with the formation of small voids, slightly deeper in the case of 70S0, below the surface and loosely attached material at the surface. Sub-surface features are fairly horizontal in formation, likely following the depth of the heat affected zone. In contrast, the structure generated by the 70S3 scanning strategy (Figure 4.42 c) shows no voids and little loosely attached material at the surface. In addition, the subsurface structure is closer to vertical in nature as a result of processing each line multiple times. Each dark line is likely a layer of thin oxide separating a layer of recast material from each line. This change in subsurface structure

may also contribute to the reduced friction coefficient observed using the interlacing scanning strategy.

4.9 Summary & Conclusion

This chapter aimed to provide a general background of the friction testing procedure, including any possible sources of error, and a broad understanding of the desirable physical properties of high friction textures following from the feature characterisation discussed in Chapter 3, in order to give an insight into the best laser and processing parameters. The possibility of increasing the processing rate in order to improve the industrial appeal of the process was also considered and discussed.

First, a number of possible issues with the friction testing rig were investigated and discussed. Rotational misalignment of the sample was found to significantly change the load-extension curve, removing the sharp slipping point and giving a curve indicative of continuous sliding. This can easily be overcome by ensuring that the sample is perpendicular to the counterpart as the normal force is being applied. On the other hand, the speed at which the load force was applied was found to have no significant impact on the measured friction coefficients.

Tilting of the counterparts, due to the geometry of the testing rig and application of the load force, was found to cause observable changes in the deformed contact area. This effect was exacerbated by the placement of additional blocks behind the counterparts by facilitating larger tilting angles. Observed friction coefficients were not significantly affected by a single block but showed a significant increase after a second block was added due to the decreased contact area and increased pressure.

Other issues, such as surface contamination, sample aging, variations in temperature and humidity and other statistical variables (e.g. material properties, etc.), were also discussed although not investigated. Ultimately, it is impossible to avoid all sources of error from tests entirely and, therefore, the best way to assess the performance of the textures predicted to be suitable for industry is testing of real components under normal working conditions.

The initial friction results, performed using a normal pressure of 150MPa, clearly highlighted several important outcomes. First, the fact that high static friction coefficients (μ_s>0.83) can be achieved solely by the use of laser texturing, giving reason and motivation for continued work on this application. The results also plainly indicated that use of higher pulse energies, at least up to ~0.8mJ, and increasing the pulse overlap are beneficial in order to increase the friction coefficient of a texture. The dependence of the obtained friction coefficients on the normal pressure applied during friction testing, contrary to the typical friction model, also proved insightful by implying the mechanism for achieving the observed high friction coefficients is embedding.

The material comparison and analysis also resulted in useful conclusions. Material composition was found to impact the obtained friction coefficient, despite using the same laser processing settings for each material. In particular, the low alloy carbon steel consistently gave lower friction coefficients than the SS316 and nitriding steel alloys. Despite the very general trends of both the surface roughness and the friction coefficient increasing with pulse overlap, analysis of these samples and results showed that there is, at best, a weak correlation between the two.

Following this, the hardness tests, which were performed on the textured samples, also indicated an increase with increasing pulse overlap, a result which was consistent across all three of the tested steel alloys. A stronger correlation was then observed between the hardness and friction coefficient of the texture, implying that the hardness of the texture plays a more significant role in determining the resulting friction coefficient. The surface hardening is likely to be due to phase transformations and the generation of thick oxides at the surface of the texture, in particular the formation of very hard oxides like chromium oxide and aluminium oxide as observed in the SEM and EDX analysis. In the case of the low alloy carbon steel, where such alloying elements are not present, the hardening observed is believed to be solely due to phase transformations caused by the heating and rapid cooling of the laser texturing process.

Despite the low number of samples tested for each laser and processing parameters comparison, several important conclusions could be made from the results. In general, use of a smaller focus spot, lower repetition rates and processing in an air atmosphere

resulted in higher friction coefficients. It is thought that the smaller spot, which provides a greater energy density; the lower repetition rate, which allows additional time for cooling of the substrate between pulses; and the oxygen in the air atmosphere all facilitate generation of these hard oxides in SS316 and the nitriding steel alloys. The pulse duration, on the other hand, was found to have little or no effect on the resulting friction coefficient whilst the comparison of multiple passes was inconclusive, the small gains observed for two passes was not felt to justify the increase in processing time.

Whilst the textures generated with a lower repetition rate, PRF=20kHz (μ_s~0.61), were found to result in higher friction coefficients than textures generated with a higher repetition rate, PRF=70kHz (μ_s~0.48), an investigation was performed into the repetition rate scaling in order to improve the industrial appeal of the process. In addition, various scanning strategies were considered in order to make use of the higher PRF available, while avoiding any possible issues relating to the increased PRF. However, testing of the interlacing texture which physically resembled the 20kHz texture most closely (70S3) resulted in even lower friction coefficients (μ_s~0.44).

Subsequent analysis of the three textures, 20S0, 70S0 and 70S3, indicated that there are three key differences between the textures; different thermal profiles during the texturing process possibly leading to different surface chemistry, changes in the size of the surface features (appears finer in the case of interlacing, 70S3) and variations in subsurface structures of the textures. These are all likely to contribute to the features on the textures generated at the higher repetition rate being unable to embed into the counterpart as effectively, resulting in the reduced friction coefficient.

As a result, it is evident that this particular process does not scale well with repetition rate for this application. However, if the material properties, surface chemistry and subsurface structure are not vital to the application, as is the case for many marking applications for example, then interlacing of pulses may still prove to be a beneficial strategy for increasing the rate of particular surface modification processes.

Following these outcomes, further friction tests were carried out using these inferred optimal conditions:

- Maximum pulse energy available from the laser (typically 0.7-1mJ)
- Low repetition rate, 20-25kHz, regardless of the laser PRF0
- Use of a small focus spot size (typically ~25-35µm)
- Processing in air atmosphere
- Hardened material surface
- A range of pulse separations were still used to provide comparisons between different processing settings, materials etc.

Further to this, primarily only the SS316 and nitriding steel alloys were textured, although the other materials were also used, including heat treated tool steel alloys and plasma nitrided steels, as discussed in Chapter 5.

Chapter 5 – Friction Textures – Hardened Material

This chapter discusses the static friction characteristics of hardened and/or laser textured materials, following the findings in Chapter 4 (Section 4.6.3) which indicate that high static friction coefficients can be obtained by increasing the hardness of the textured sample. Three different techniques were considered in order to increase the sample hardness, namely: laser treatment, plasma nitriding and conventional heat treatment. This increase in hardness was expected to change the friction regime from primarily adhesion based (as observed in Chapter 4) to an embedding based regime by enabling the laser generated asperities to embed into the counterpart without significant deformation. As a result, significantly higher friction coefficients were anticipated following the hardening process.

It should be noted at this stage that the geometry of the samples used for plasma nitriding and conventional heat treatment was changed to a cut-off circular shape (slices cut from a circular bar with a flat face for easier machining) and therefore the counterparts for testing of these were machined (into a 'T' shape) in order to maintain a nominal contact area of 20mm × 20mm. All friction testing discussed in this chapter was performed at 100MPa normal pressure (40kN normal force).

5.1 Material Hardening

5.1.1 Hardening by Laser Treatment only

As shown in Section 4.6.3, the laser texturing process was observed to increase the surface hardness of the material. As a result, a large range of texturing parameters was considered, primarily focussing on the high pulse overlap (low pulse separation) region as implied by the previous results in an attempt to generate the highest surface hardness possible only using the laser texturing system. Laser peening was not considered for hardening of the samples as the lasers available lacked the required pulse energy/power in order to perform this process.

5.1.2 Hardening by Plasma Nitriding

Following the limited results with laser texturing alone, plasma nitriding was considered as a secondary technique to be used alongside the laser texturing. Plasma nitriding is a case hardening technique, which can be used on a variety of metallic materials. The

process takes place over several hours in a low pressure environment in which nitrogen molecules are ionised at elevated temperature (typically 480-580°C). These ions react to form nitrides near the surface of the sample and penetrate into the sample, becoming interstitial components in the material lattice. The combination of these two processes leads to the generation of a hard surface layer. Under normal process conditions, a compound layer (nitride rich layer) is formed on the nitrided surface. This layer is very hard, making it desirable with respect to wear and corrosion resistance, but the compound layer is also very brittle and prone to peeling. In addition, it is known to reduce the friction coefficient [121]. Thus, the compound layer is undesirable for high friction application. By using a process gas with a high H_2/N_2-ratio the formation of compound layer can be supressed in the plasma nitriding process. In the case of the nitriding and grade 316 steels considered here, surface micro-hardness values of ~1100HV are achievable, with hardened layer thicknesses of up to ~200µm-1mm (depending on the material and process parameters chosen) [122, 123].

With regards to the generation of high friction surfaces, three cases involving plasma nitrided material were considered:

- Friction of samples plasma nitrided followed by laser texturing
- Friction of samples laser textured followed by plasma nitriding
- Friction of untextured samples after plasma nitriding

The impact of the laser texturing on the nitriding process, both before and after, was also considered, particularly in relation to the hardness and resulting friction properties. All plasma nitriding discussed in this thesis was performed by the Danish Technological Institute (DTI).

5.1.3 Hardening by Conventional Heat Treatment

In addition to the nitriding samples subject to surface hardening by the plasma nitriding process, several different tool steel samples were hardened by conventional heat treatment. Conventional heat treatment processes are used to increase the bulk and surface hardness of steel. In particular, quench hardening – a process which involves the heating of the material to a particular temperature prior to rapid cooling – can be

used. The quenching hardens the steel by forming martensite, a very hard and brittle crystalline steel structure, as a result of rapid cooling through its eutectoid point (temperature at which the phase structure would alter from austenite to ferrite/cementite under slower cooling conditions). Martensite is a metastable structure and therefore tempering, reheating the material to a particular temperature (below the critical point) before slowly cooling, is performed in order to stabilise the structure (by allowing partial phase changes and relieving stresses) and obtain the desired bulk hardness. Several different steels were considered for performing these tests, including Uddeholm Impax Supreme, Uddeholm Sleipner and Böhler S600 tool steels, with hardness ranging from 40 to 66HRC (~385-860HV).

Despite both plasma nitriding and conventional heat treatment increasing the surface hardness, the plasma nitriding was expected to result in higher friction coefficients by virtue of the higher surface hardness. Despite this, the expected interaction of the laser texturing and hardening processes was unknown, resulting in some uncertainty over which process order is optimal for generating high friction surfaces.

5.2 Laser Textured Material – Impact on Hardness

As discussed in Section 4.6.3, increasing pulse overlap (decreasing pulse separation) was found to increase the surface hardness of the textured samples. Therefore, the large range of textures and parameters friction tested in Section 4.7 were tested for hardness using the same procedure as in Section 4.6.3, with particular interest paid to textures generated with low pulse separation. The obtained hardness values for each set of processing parameters, as a function pulse separation, are plotted in Figure 5.1.

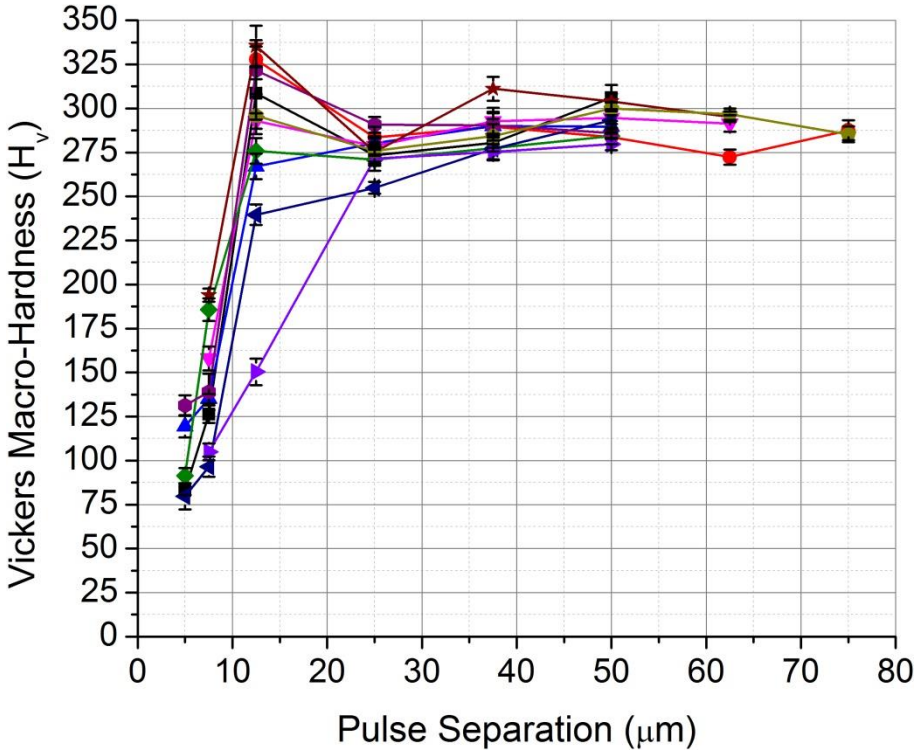

Figure 5.1. Vickers macro-hardness (using 30kgf) as a function of pulse separation of the laser texturing process. All results are on SS316 substrates with each curve representing slightly different laser texturing parameters (spot size, beam quality, repetition rate etc.)

The results presented in Figure 5.1 show that larger pulse separation textures (>40μm) have a surface hardness of ~275-300HV30. This is slightly lower than the results obtained previously, but not significantly so. As the pulse separation was decreased to 12.5μm, surface hardness was typically found to increase, up to ~325HV30 for certain textures, in line with the expectations. However, as the pulse separation was decreased further to 7.5μm and 5μm, the hardness values obtained decreased rapidly with results typically lying between 75HV30 and 150HV30. Despite seeming contradictory to the previous results shown in Figure 4.18, the very low pulse separations leads to a very high pulse density and, subsequently, very high roughness values. Consequently, the hard oxides generated in the laser texturing process, expected to result in a hard surface, are in the form of 'tall' asperities which are poorly attached to the substrate. In addition, these oxide structures are somewhat brittle due to the rapid cooling during the laser process. The combination of these two factors results in a surface structure which can deform and/or break easily under pressure (from either hardness indenter or counterpart). Therefore the hardness values obtained are lower than would be expected of fully annealed SS316 and the possible static friction coefficients are limited.

Following this conclusion, alternate methods of surface hardening were considered, starting with plasma nitriding.

5.3 Plasma Nitrided Material

Initial tests with plasma nitrided material were carried out on the 'nitriding' Cr-Mo-Al steel, which is particularly well suited to the process due to its structure and composition – the ~1% aluminium promotes high surface hardness values. For the first batch of tests, the samples were subject to plasma nitriding prior to laser texturing and friction testing. Texturing of the nitrided material was carried out with the 50W HS-S, 20W HS-L and 20W EP-S laser types

5.3.1 Plasma Nitriding followed by Laser Texturing

In order to understand the effect of the plasma nitriding on the friction coefficient, the initial tests looked to cover a range of texturing parameters. As a result, only a small number of tests (typ. 2-3) were performed for each texture/processing order. Figure 5.2 shows the average friction coefficients (standard deviation indicated as error) obtained for samples laser textured after plasma nitriding with both 50W HS-S (d~25µm, PRF=20kHz, 0.71mJ pulse energy) and 20W HS-L (d~50µm, PRF=20kHz, 0.8mJ pulse energy).

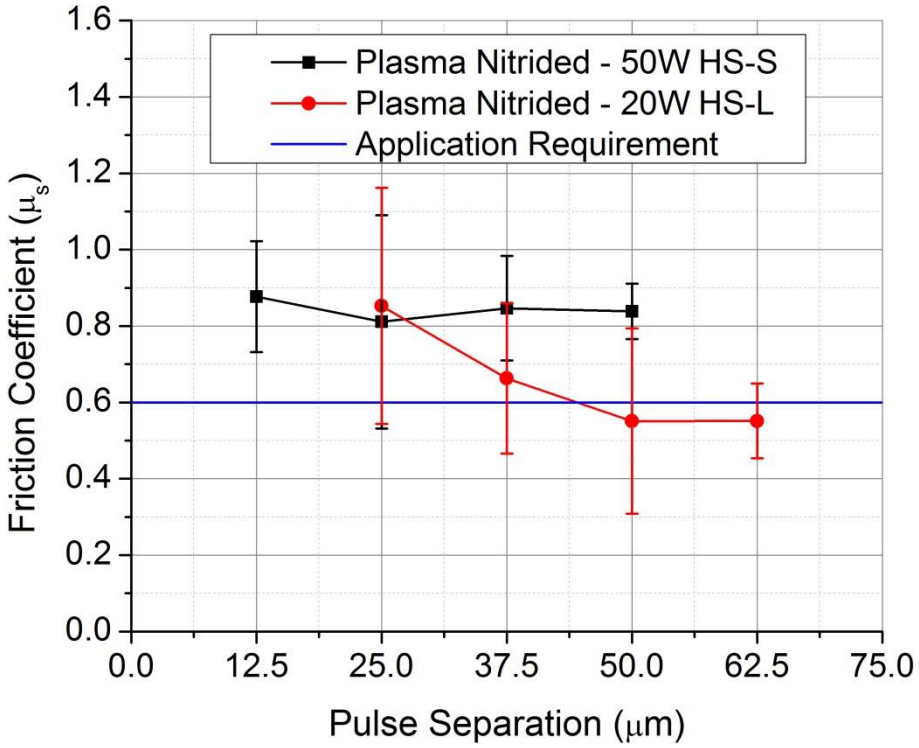

Figure 5.2. Friction coefficients as a function of pulse separation for plasma nitrided Cr-Mo-Al steel alloy samples both before laser texturing with 50W HS-S and 20W HS-L lasers

The friction results, shown in Figure 5.2, indicate that high friction coefficients of up to μ_s~0.9 are achievable with plasma nitrided samples. This was as expected, following from the results presented in Section 4.6. However, several sample textures processed with the 20W HS-L laser gave lower friction coefficients than anticipated (μ_s<0.6) when processed at higher pulse separations (>50μm).

5.3.1.1 Friction-Hardness Correlation

As with the previous (non-hardened) samples, macro Vickers hardness tests were performed on each of the plasma nitrided textures, with the results plotted in Figure 5.3.

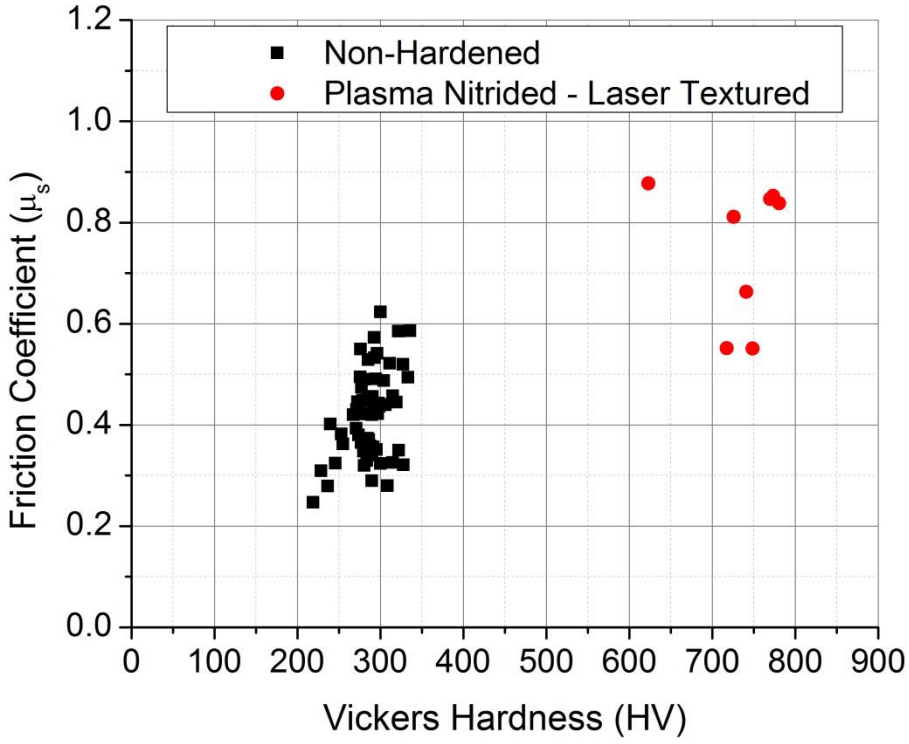

Figure 5.3. Friction coefficient as a function of surface hardness for a range of non-hardened samples (from Chapter 4) and the initial plasma nitrided samples

As can be seen from Figure 5.3, the macro Vickers hardness of the plasma nitrided samples was measured to be lower than expected (600-800HV30 compared to the expected ~1100HV). This is due to the applied load force (30kgf) and the fact that the hardness was measured on the surface rather than on a cross-section. As the plasma nitriding is a case hardening process, with hardened layer thickness dependent on the process parameters used, the indents made may have penetrated further than the depth of the hardened surface layer. There is a gradient to the hardness (with distance from the surface) which will also contribute to this effect. Despite this, the hardness is significantly higher than that of the non-hardened material (~300HV30) and several friction coefficients are also high, indicating that there is some correlation between hardness and friction as assumed. However, due to the limited number of samples tested, the exact correlation cannot be determined conclusively.

5.3.2 Laser Texturing followed by Plasma Nitriding

Following the initial plasma nitrided results, the same laser textures were tested but with plasma nitriding performed after the laser texturing process. The results of the friction tests with these samples are shown in Figure 5.4, with the values plotted being an average of 2-3 tests (as in Section 5.3.1).

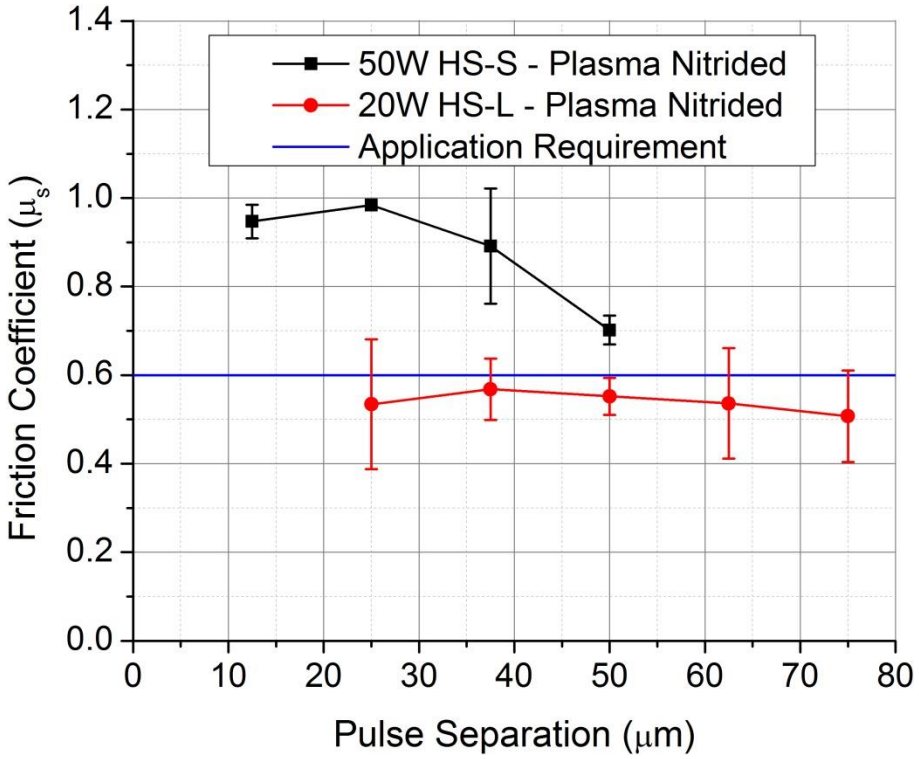

Figure 5.4. Friction coefficients as a function of pulse separation for plasma nitrided Cr-Mo-Al steel alloy samples both after laser texturing with 50W HS-S and 20W HS-L lasers

The results obtained for these tests, shown in Figure 5.4, were quite mixed and unexpected. Whilst high friction coefficients of up to μ_s~1 were obtained for the samples textured with the 50W HS-S laser, those textured by the 20W HS-L were significantly lower, with average values consistently less than 0.6. This was significantly lower than expected from plasma nitrided samples and, as a result, the interaction between the laser texturing and plasma nitriding processes was investigated in order to determine the cause of the unexpectedly low friction coefficients.

5.3.2.1 Interaction of Laser Texturing and Plasma Nitriding Processes

First, SEM images were taken of samples with identical laser texturing processing both before and after plasma nitriding process in order to determine any topological differences between the two processing orders. Two such images comparing a 12.5µm pulse separation (50W HS-S) texture with the two processing orders are shown in Figure 5.5.

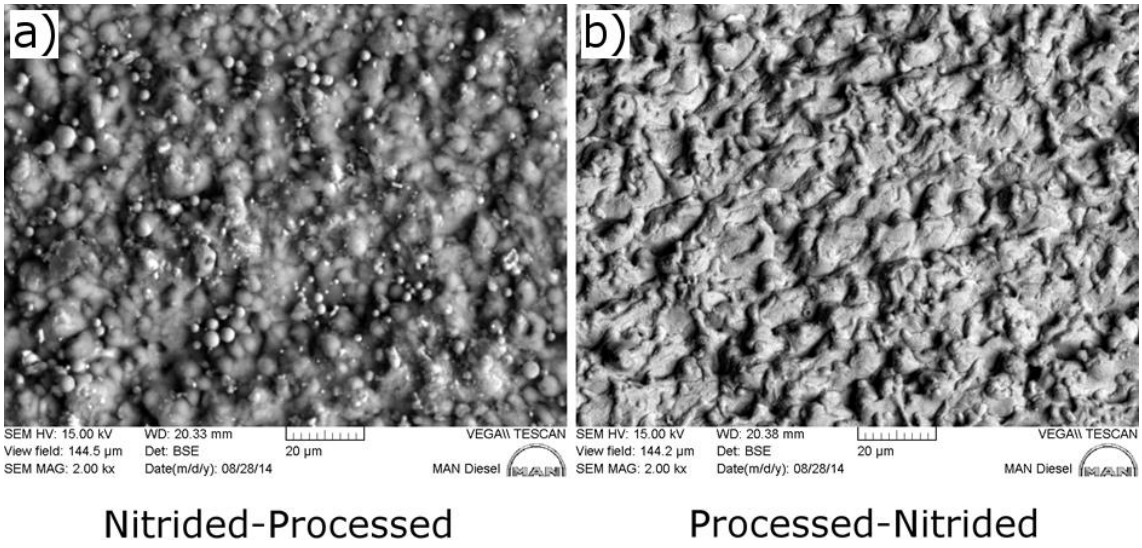

Figure 5.5. SEM micrographs comparing differences in surface structure with a) laser texturing after plasma nitriding and b) plasma nitriding after laser texturing

Laser texturing after plasma nitriding (Figure 5.5a) gives a surface structure which looks very similar to a non-nitrided, textured surface with spherical features and no clear underlying structure. When plasma nitriding is performed after laser texturing, as shown in Figure 5.5, the surface structure is changed dramatically. The appearance of the spherical features is greatly reduced and the structure looks more regular (direction of pulses, top to bottom, is determinable from the visible splash direction of the melt pool). This is believed to be due to the 'cleaning' effect of the plasma nitriding process which acts to remove the loose debris from the laser textured surface. These spherical features, formed as a result of the laser texturing process, are recast material which is only loosely attached to the surface, as discussed in Section 4.8.5.3. Therefore this may actually prevent good contact/embedding required for high friction. However this does not explain the poor results presented in Figure 5.4.

Hardness measurements were then performed on the samples that were laser textured prior to plasma nitriding. The results of these tests are shown in Figure 5.6, along with the results of the plasma nitrided-laser textured and non-hardened samples for comparison.

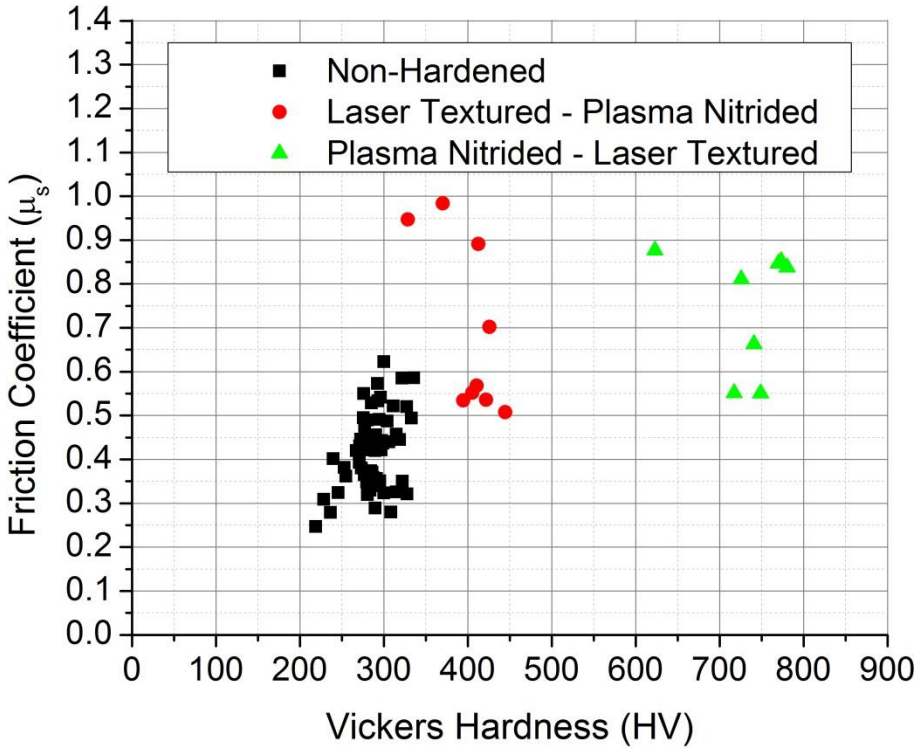

Figure 5.6. Friction coefficient as a function of surface hardness for samples plasma nitrided both before and after laser texturing

Unlike the initial batch of plasma nitrided samples, the laser textured-plasma nitrided samples were found to be comparatively soft, as shown in Figure 5.6, with hardness values between 300HV30 and 450HV30 rather than the ~700HV30 of the initial batch. This helps to explain why the 20W HS-L samples had significantly lower friction coefficients than expected; however the 50W HS-S results are somewhat higher than expected given the hardness. One plausible explanation is that the laser texturing and resulting remelting on the surface affects the plasma nitriding process. This may limit the diffusion of the nitrogen during plasma nitriding, affecting the generation of the hardened layer which will affect the hardness values measured by the macro-indenter. This difference between these two cases can be observed from the micrographs shown in Figure 5.7.

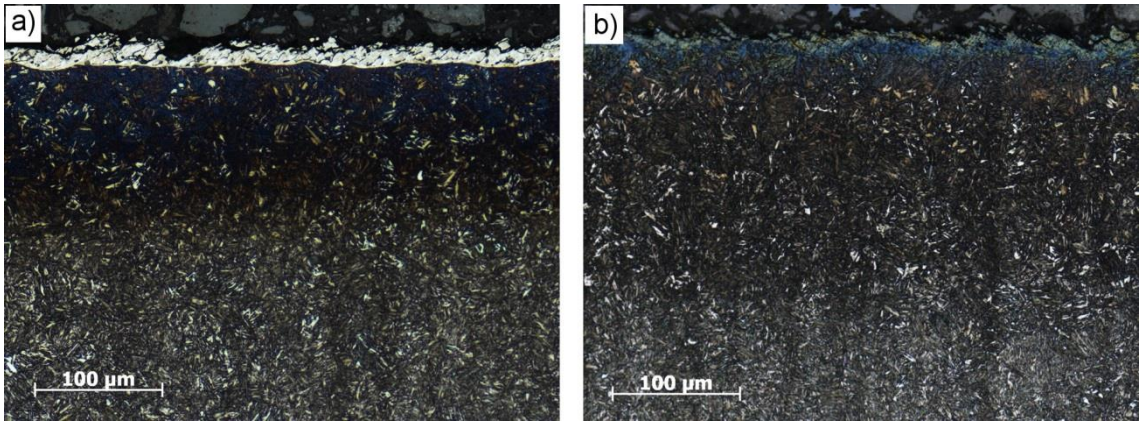

Figure 5.7. Cross section optical micrographs of samples with a) plasma nitriding prior to laser texturing and b) laser texturing prior to plasma nitriding chemically etched to show the difference in microstructure

From the structures visible in Figure 5.7, it can be seen that the nitrided layer is thinner for the nitrided-textured sample (Figure 5.7a) compared to the textured-nitrided sample (Figure 5.7b). However, the nitrogen concentration is also higher, as indicated by the darker layer, leading to a harder but thinner nitrided region. When laser textured prior to plasma nitriding, the changes to the surface appears to inhibit nitrogen entering the substrate, allowing deeper diffusion of the nitrogen into the steel due to the reduction in 'obstacles'. This reduced nitrogen concentration results in a lower hardness in the nitrided layer. In either case, the process of plasma nitriding these laser textured samples did not work as expected and so further testing and analysis was performed in this regime, particularly since the cleaning effect of the plasma nitriding was felt to be favourable for improved embedding and friction.

In addition to the SEM and macro-hardness measurements, cross-section analysis with micro-hardness measurements was also performed on the plasma nitrided samples. This analysis was undertaken at MAN Diesel & Turbo, Copenhagen using a LECO AMH43 automatic micro-hardness testing system. A micrograph of one of the plasma nitrided-laser textured samples (50W HS-S, s=12.5µm) with various micro-indents is shown in Figure 5.8.

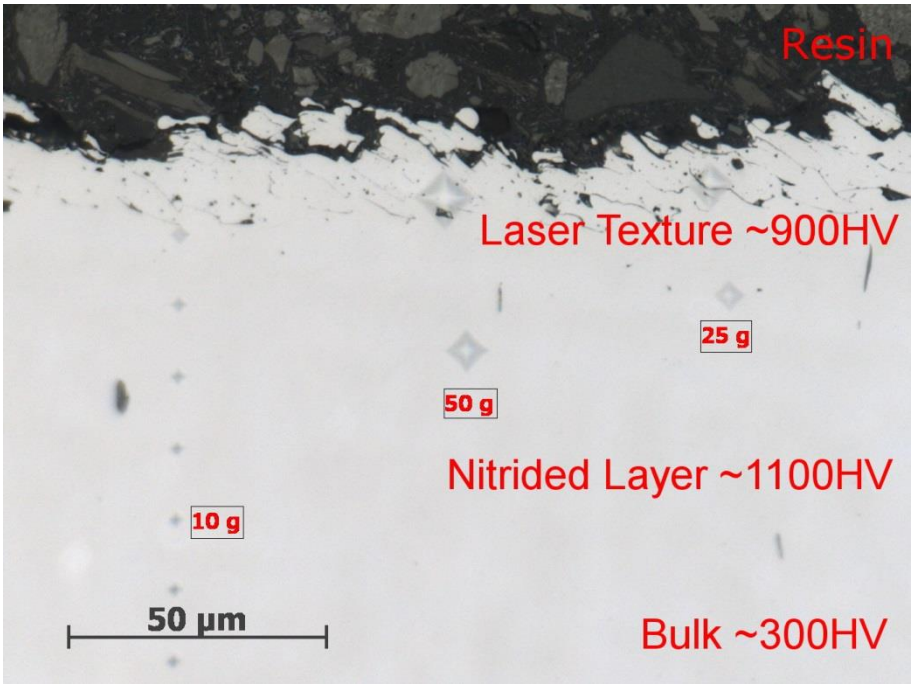

Figure 5.8. Cross-section micrograph of sample plasma nitrided prior to laser texturing with various Vickers micro-indents and different regions labelled

The micro-hardness indents in the plasma nitrided-laser textured sample, visible in Figure 5.8, show that the laser textured region (surface ~20µm) is softer than the untextured nitrided region by approximately 200HV0.025 (~18%). This is likely due to dissolution of the interstitial nitrogen and change in surface chemistry (oxidation) caused by the rapid heating, melting/ablation and cooling effects induced by the laser texturing process. Given this effect, the most effective way to process the samples appears to be to laser texture prior to plasma nitriding in order to obtain the full effect of the nitriding process, ideally resulting in a textured surface with a hardness of ~1100HV0.025. The same analysis was also performed on the laser textured-plasma nitrided sample with the same laser texturing parameters (50W HS-S, *s*=12.5µm), for which a cross-section micrograph is shown in Figure 5.9.

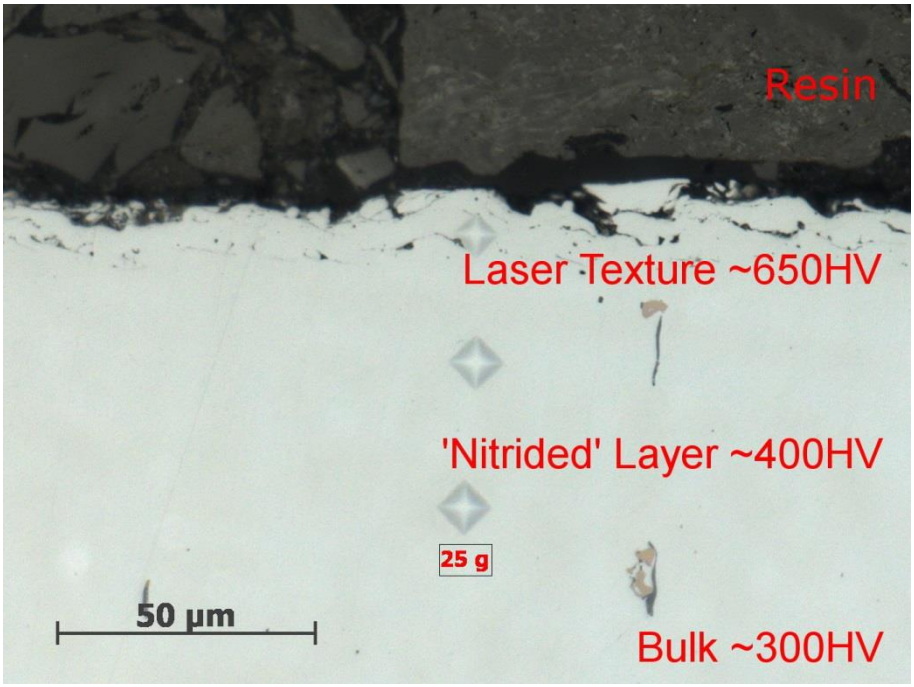

Figure 5.9. Cross-section micrograph of sample plasma nitrided after laser texturing with several Vickers micro-indents and different regions labelled

From the micro-indent measurements, shown in Figure 5.9, it is clear that the samples which were laser textured prior to plasma nitriding did not reach the same hardness as those laser textured afterwards. It is unclear from these results if this is a side-effect of the laser texturing process which cannot be avoided, or if the plasma nitriding process requires optimisation for this type of sample. However, the unexpected friction-hardness results presented in Figure 5.6 are more easily explained following this analysis. The low macro-hardness measurements are due to the formation of a much softer nitrided layer within the laser texture (of only ~650HV0.025) and, as a result, the macro-indenter easily penetrates this, thus giving a macro-hardness which is more representative of the bulk hardness. The high friction results obtained with the 50W HS-S laser textures are likely due to the increased number of asperities for embedding, due to the decreased pulse separation and increased energy density. Despite the lower surface hardness (which still appears to be high enough to enable some embedding into the counterpart) of these samples, the friction coefficients obtained are slightly (~0.05-0.1) higher than those obtained for the samples textured after plasma nitriding. This difference is within experimental error (given the limited number of samples tested); however, the cleaning effect of the plasma nitriding may also contribute to this.

The cross-sections and micro-hardness measurements presented in Figure 5.7, Figure 5.8 and Figure 5.9 go a long way to explain the apparently contradictory results from Figure 5.6. Despite the low macro-hardness of the textured-nitrided samples, it is clear from the micro-hardness results that the surface hardness is noticeably higher than the bulk (which is at least partially measured by the macro-indenter). The nitrided-textured samples, on the other hand, exhibited lower surface hardness than bulk hardness. The combination of these two results indicates that the hardness of the important parts of the samples – the asperities on the surface – is actually much more similar than the macro-hardness results suggested.

5.3.3 Plasma Nitriding Issues

Further tests were then planned, continuing from the results presented in Sections 5.3.1 and 5.3.2, focussing on samples laser textured prior to plasma nitriding as the cleaning effect and promise of higher surface hardness was expected to give the highest friction coefficients. Unfortunately, issues were encountered with several of the batches of nitrided material that were received from the DTI. This is highlighted by the batch of SS316 which was sent for nitriding. A cross-section of one such sample is shown in Figure 5.10.

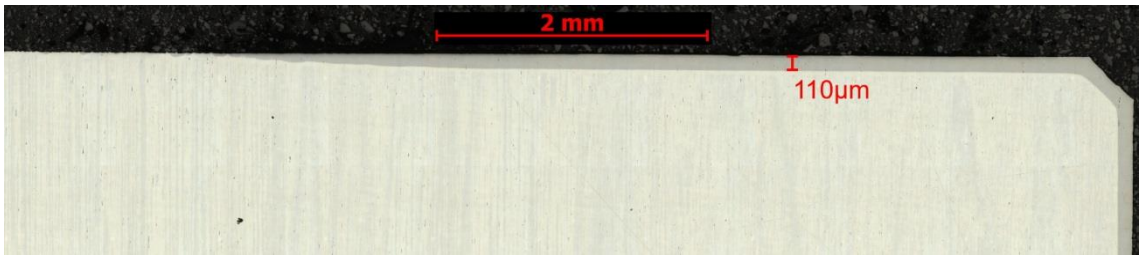

Figure 5.10. Optical micrograph of an untextured, plasma nitrided SS316 sample, with a nitrided layer clearly visible at the right hand side

The macro-hardness of the plasma nitrided SS316 samples (and others within the same batch of nitriding) were not as high as expected, even for those or parts of those which were untextured. Cross-sectional analysis of these samples, shown in Figure 5.10, clearly indicates that the reason for this is poor nitriding. The nitrided layer, which is approximately 110µm thick, can be seen at the right hand side of Figure 5.10 quickly gets thinner towards the centre of the sample (left of the micrograph) until it disappears entirely at around 5mm from the sample edge. It is suspected that the thinning of the nitrided layer was due to the arrangement of the samples within the furnace during the nitriding process. Due to the variance observed in nitriding layer thickness and

geometry of the samples, it is assumed that the samples were placed very closely together in the furnace, limiting the exposure of the surface to the nitrogen plasma to the edges, as depicted in Figure 5.11.

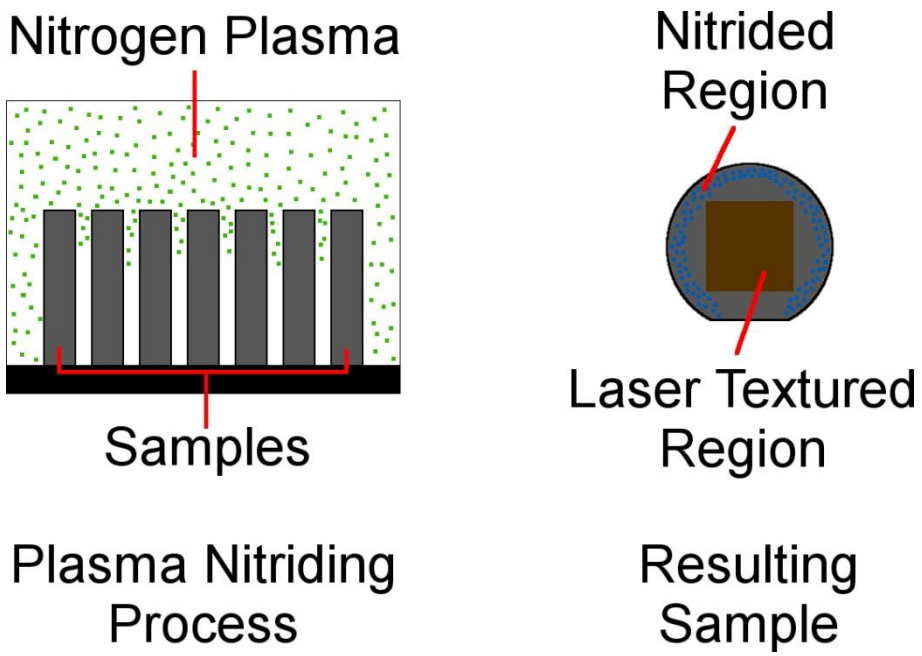

Figure 5.11. Schematic of plasma nitriding process with insufficient gaps between adjacent samples, limiting the surface area exposed to the plasma

If the samples were placed in the furnace with insufficient spacing, as illustrated in Figure 5.11, then the samples would be expected to exhibit a nitrided layer around the outside with minimal evidence of the nitriding process towards the centre, as was observed in Figure 5.10. In addition, micro-hardness measurements of the bulk and nitrided layer, shown in Figure 5.12, indicate hardness values of 350-400HV and 1100-1200HV respectively, as expected.

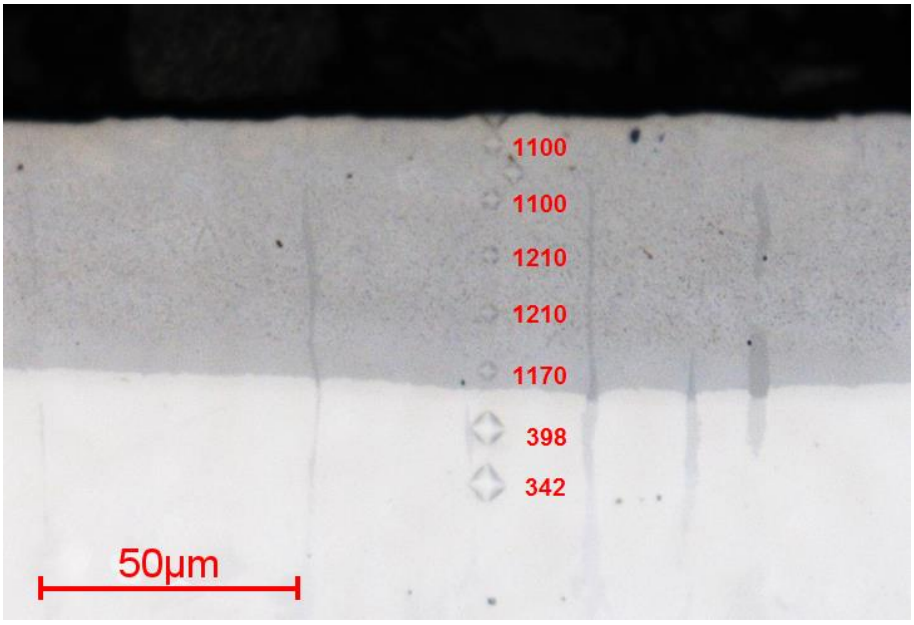

Figure 5.12. Cross-section optical micrograph of plasma nitrided SS316 sample with micro-indents shown in both the bulk and nitrided layer

The friction results of the samples found to be poorly or non-uniformly nitrided were disregarded due to the variability in the material properties, making any conclusions based on the samples highly unreliable.

5.3.4 Subsequent Tests

Fortunately, another batch of material was successfully nitrided after modification of the plasma nitriding process parameters, including placing the samples on one of the flat surface and nitriding before flipping the samples over and nitriding again, in order to improve the hardness, depth and homogeneity of the nitrided layer.

For the tests on these subsequent samples, laser texturing was performed with a 20W EP-S laser (d~25µm, PRF=20kHz, 0.71mJ pulse energy) at three different texture pulse separations (s=12.5µm, 25µm and 100µm) and two pulse durations (220ns and 490ns). A number of samples were also left untextured prior to both plasma nitriding and friction testing in order to determine the importance of the laser texturing in the case of plasma nitrided samples. Between 8 and 10 samples were tested for each texture (with the exception of the untextured for which only three were tested), with the average values plotted in Figure 5.13.

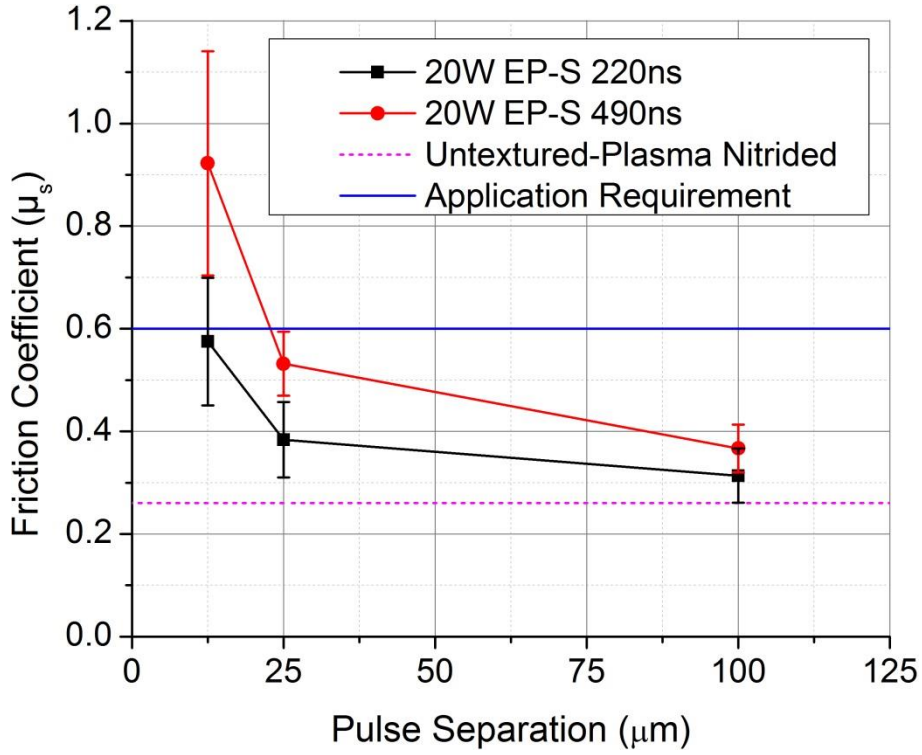

Figure 5.13. Friction coefficient as a function of pulse separation for samples laser textured prior to plasma nitriding. Texturing performed with 20W EP-S laser with 220ns and 490ns pulses with the dashed and solid horizontal lines indicating the average untextured-nitrided friction coefficient and the application requirement, respectively

Unlike the results presented in Figure 5.2 and Figure 5.4, the friction results of the subsequent tests, shown in Figure 5.13, exhibit a much stronger dependence on the pulse separation of the laser texturing. In this case, use of smaller pulse separation textures clearly results in higher friction coefficients (up to μ_s~0.9 at s=12.5μm) than larger pulse separation textures (μ_s~0.35 at s=100μm). While this somewhat contradicts the previous results (although there is an indication of this trend in the 50W HS-S results in Figure 5.4), it can be easily explained as the lower pulse separation will generate more surface features and asperities for embedding into the counterpart surface. Thus increasing the amount of embedding and requiring a larger force in order to shear an increased volume of counterpart material. In agreement with these results, it is also interesting to note that the untextured, plasma nitrided samples resulted in low friction coefficients of <0.3 despite being hardened sufficiently. This is most likely due to the lack of asperities available for embedding, limiting the effectiveness of the hardening process for high friction applications and therefore implying that the achieved friction coefficient is still dependent on the surface roughness despite being hardened.

5.3.4.1 Hardness Dependence

For completeness, and to provide a comparison with the previous tests, hardness measurements were performed on each of the sample textures discussed in Section 5.3.4, with the results plotted in Figure 5.14.

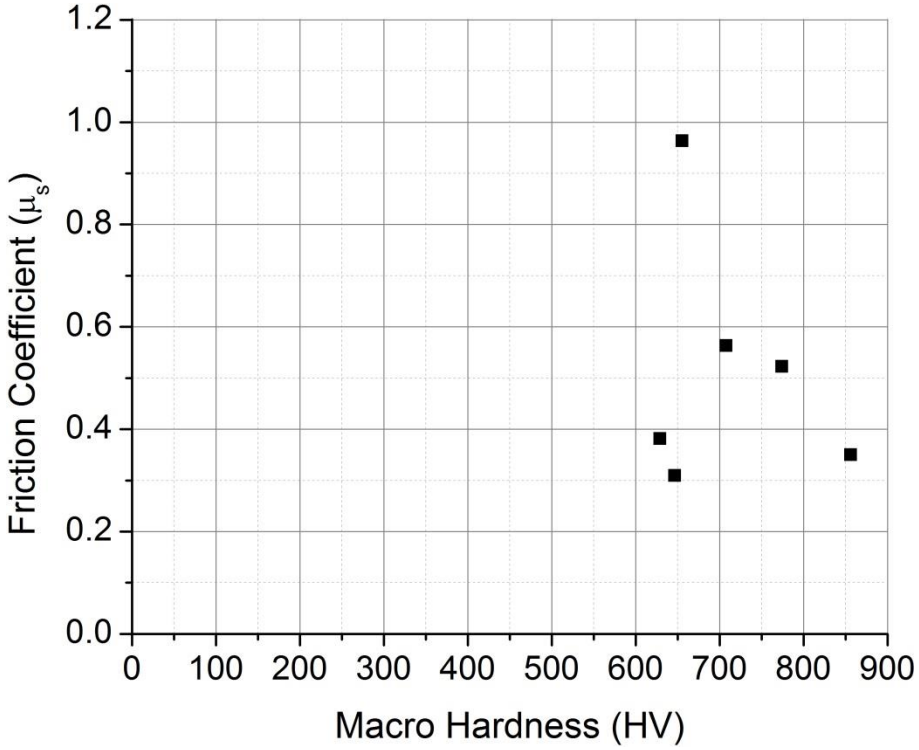

Figure 5.14. Friction coefficient as a function of macro-hardness for the batch of samples plasma nitrided after laser texturing with the 20W EP-S laser

As with the first nitrided samples (plasma nitrided prior to laser texturing), hardness values for this batch are consistently >600HV; however the friction coefficients are more varied. These results therefore imply that although high hardness values can facilitate high friction coefficients, it is not the only factor required in order to achieve these high values.

5.3.4.2 Roughness Dependence

Using the Alicona surface profiler, the average surface roughness for each of the samples was measured and the friction coefficients plotted against the resulting roughnesses, as shown in Figure 5.15.

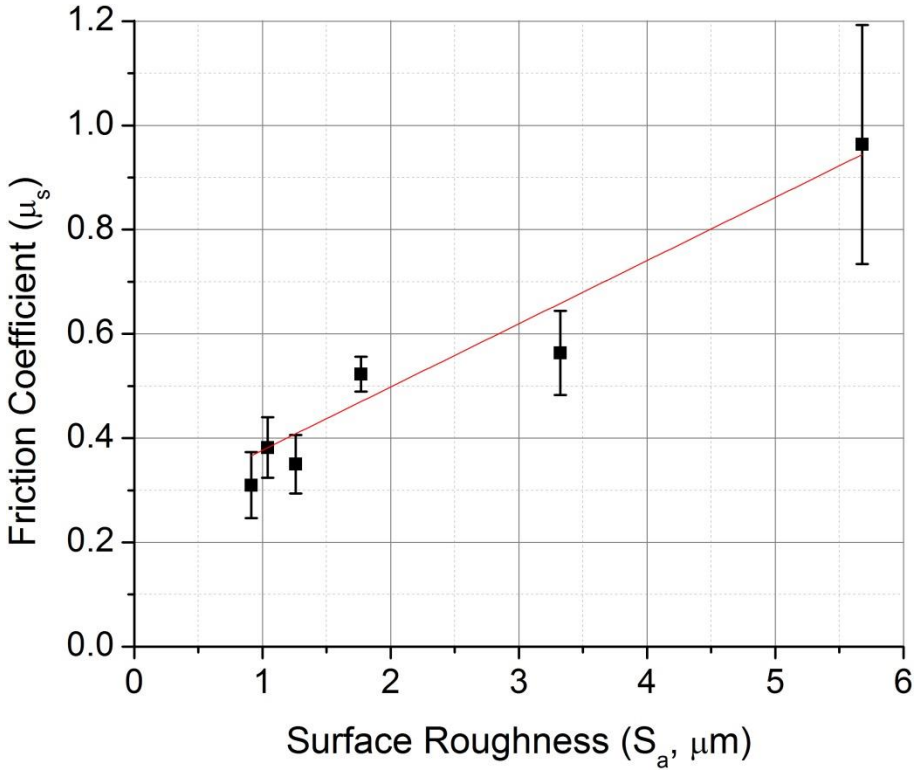

Figure 5.15. Friction coefficient as a function of average surface roughness, with a best fit straight line, for the batch of samples plasma nitrided after laser texturing with the 20W EP-S laser

The surface roughness results, presented in Figure 5.15, indicate that there is an approximately linear correlation between the static friction coefficient and the surface roughness for these samples. As discussed in Section 5.3.4, this is most likely due to the increase in number and size of the features and asperities available for embedding into the counterpart surface. Whilst this result appears contradictory to the early results, presented in Section 4.6, this is not necessarily the case. In order to achieve increased hardness in that case, low pulse separation (high pulse overlap) was required, thus also increasing the surface roughness. Only with the introduction of an external hardening process was it possible to decouple the effect of the hardness and roughness. Following the results obtained with the samples treated only with the laser and these results with the plasma nitrided material, it appears evident that both high hardness and high roughness required in order to achieve consistently high friction coefficients.

Although these results tend to conform to this conclusion and there is a well-founded explanation as to why this could be the case, due to the limited number of samples tested in this regime, further tests are really necessary in order to confirm this conclusion.

5.4 Heat Treated Material (Tool Steel)

Following the results on the plasma nitrided material, several tool steel alloys were considered with laser texturing performed prior to conventional heat treatment. Initial tool steel tests were performed on Uddeholm Impax Supreme tool steel with nominal heat treatment hardness values ranging from 41HRC to 52HRC (~375HV to ~525HV). Texturing of all tool steel samples was performed with the 20W EP-S laser, using a PRF of 20kHz, 0.71mJ pulse energy and nominal spot size of d=25µm.

5.4.1 Uddeholm Impax Supreme

The Uddeholm Impax Supreme tool steel samples were textured with 220ns pulses for a range of pulse separations between *s*=12.5µm and *s*=50µm. The results of the friction coefficient measurements are shown in Figure 5.16.

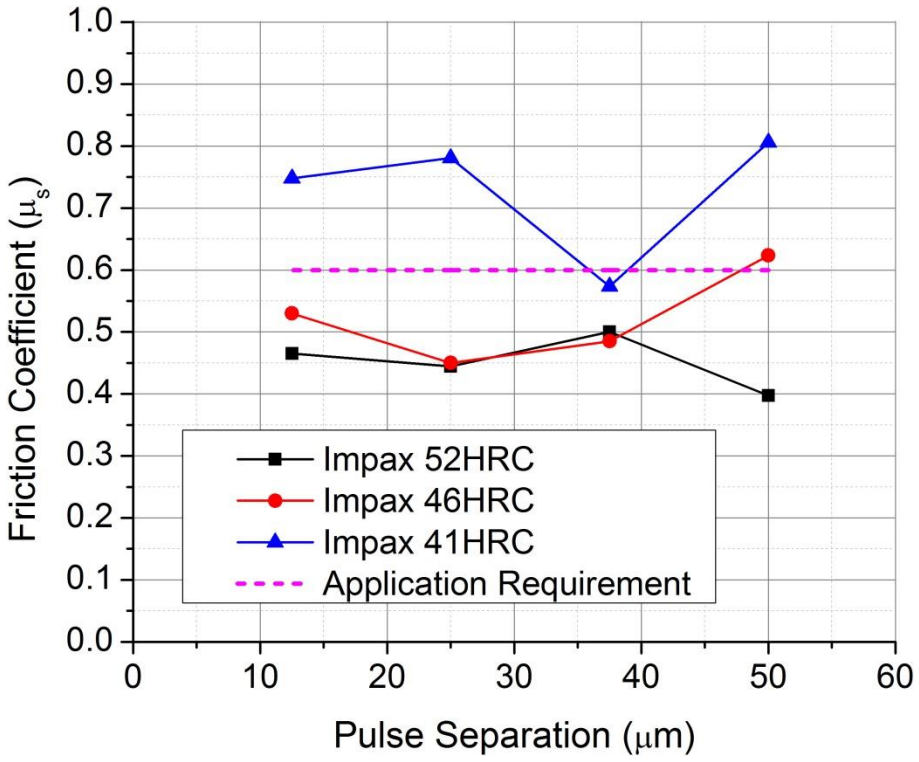

Figure 5.16. Friction coefficient as a function of pulse separation for Uddeholm Impax Supreme samples laser textured prior to heat treatment to three different nominal hardness values; the dashed horizontal line indicates the application requirement of μ_s=0.6

Contrary to expectations, the samples heat treated to the lowest hardness (41HRC) were found to result in the highest friction coefficients, as can be seen in Figure 5.16. Due to the limited number of samples available for texturing and testing, only 1-2 samples were friction tested for each texture/hardness combination and therefore no estimate of

the associated errors are given. It should also be noted that the 52HRC samples were tested first, without any cleaning processes. Following the poor friction results obtained with these samples, a cleaning process involving rape seed oil, soapy water and iso-propyl-alcohol (IPA) was used in order to remove any surface contaminants from the remaining Impax samples. As can be seen in Figure 5.16, this process was found to have no significant effect on the resulting friction coefficients. Further to the unexpectedly low friction measurements, hardness measurements were performed on each sample, with the results shown in Figure 5.17.

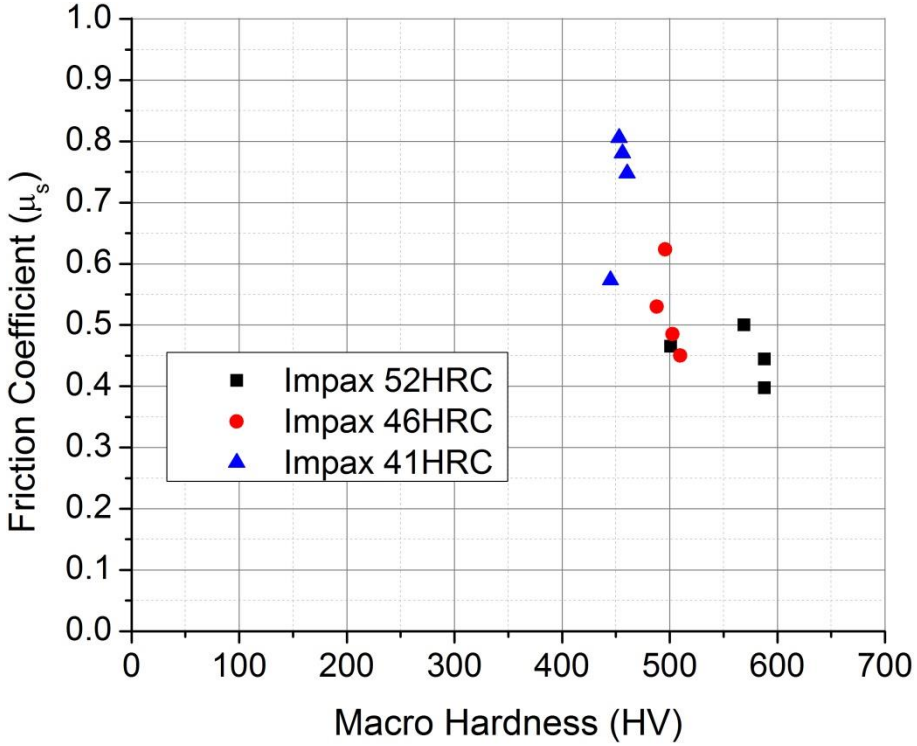

Figure 5.17. Friction coefficient as a function of Vickers macro-hardness for the range of tested Impax tool steel samples

Despite the cleaning process applied to the 41HRC and 46HRC samples, the general trend observed in Figure 5.17 indicates that increasing hardness leads to a decrease in friction coefficient, contradicting the expectations and previously observed results. One possible explanation for this inverse relationship is that the laser texturing process dissolves the carbides and forms martensite in the surface layer. During the tempering process, the bulk hardness decreases with increasing tempering temperature, but secondary carbides may form in the depleted zone to regain some surface hardness. In addition, the tendency to form secondary carbides increases with increasing tempering temperature. Therefore, it is possible that the samples with the lowest bulk hardness (highest tempering temperature) have the highest surface hardness due to the formation

of secondary carbides. As the macro-hardness tests measure both bulk and surface hardness simultaneously but the friction process is primarily reliant on surface hardness, this could explain the discrepancy in the observed results. Unfortunately, the limited number of samples and lack of access to micro-hardness testing facilities did not allow further investigation into this theory, however further testing was performed on two other tool steel alloys.

5.4.2 Böhler S600 & Uddeholm Sleipner

Following the tests on the Impax tool steel, two different tool steel alloys, Böhler S600 ("Böhler") and Uddeholm Sleipner ("Sleipner"), were chosen for further tests. These alloys are able to be heat treated to higher nominal hardness values. Samples were laser textured with pulse separations between 12.5µm and 100µm prior to heat treatment, with nominal hardness values between 55HRC (~600HV) and 66HRC (~860HV). Resulting friction values obtained for these samples are presented in Figure 5.18.

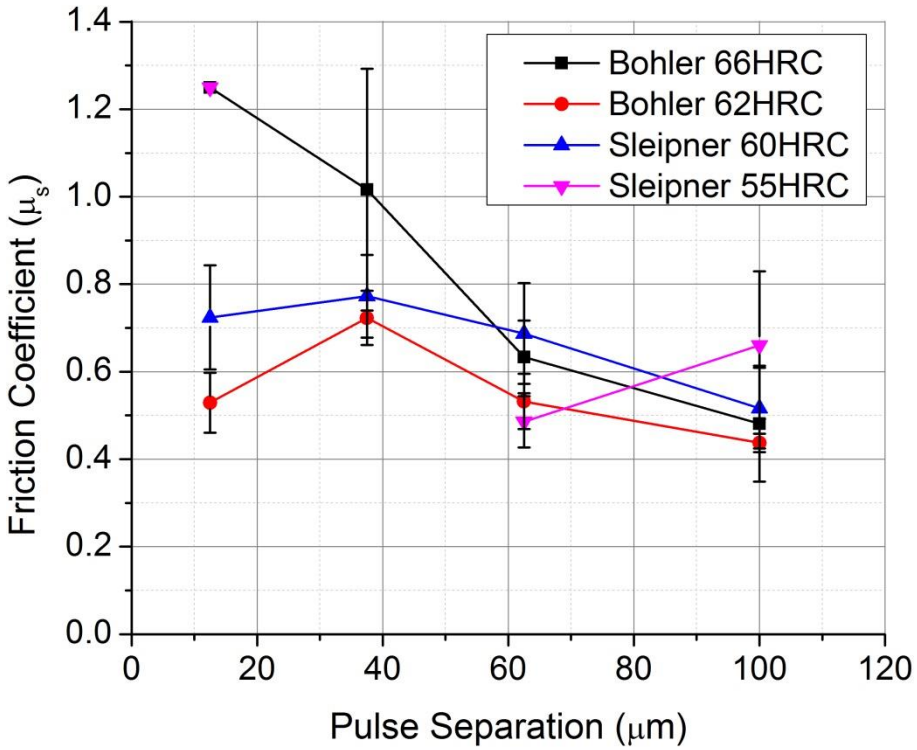

Figure 5.18. Friction coefficient as a function of pulse separation for two tool steel alloys, each heat treated to two different nominal hardness values; texturing performed with 20W EP-S with 0.71mJ, 220ns pulses at 20kHz PRF

As with the results of the Impax tool steel, the results shown in Figure 5.18 are somewhat mixed and unexpected. Whilst the nominally hardest samples (Böhler 66HRC) give the highest friction coefficients, particularly at low pulse separation, there

is no evidence of lower nominal hardness samples resulting in lower friction coefficients. Böhler samples heat treated to 62HRC, for example, consistently gave low friction coefficients whilst the two, nominally lower hardness, Sleipner sample batches typically varied between these two extremes. It should be noted that the Sleipner 55HRC samples textured with 37.5µm pulse separation did not exhibit a sharp slipping point in the load-extension curves and were therefore omitted from the results presented.

5.4.2.1 Hardness Dependence

As with the Impax samples, macro-hardness measurements were performed on each of the different sample textures. The friction coefficients previously obtained are plotted against the results of these measurements in Figure 5.19.

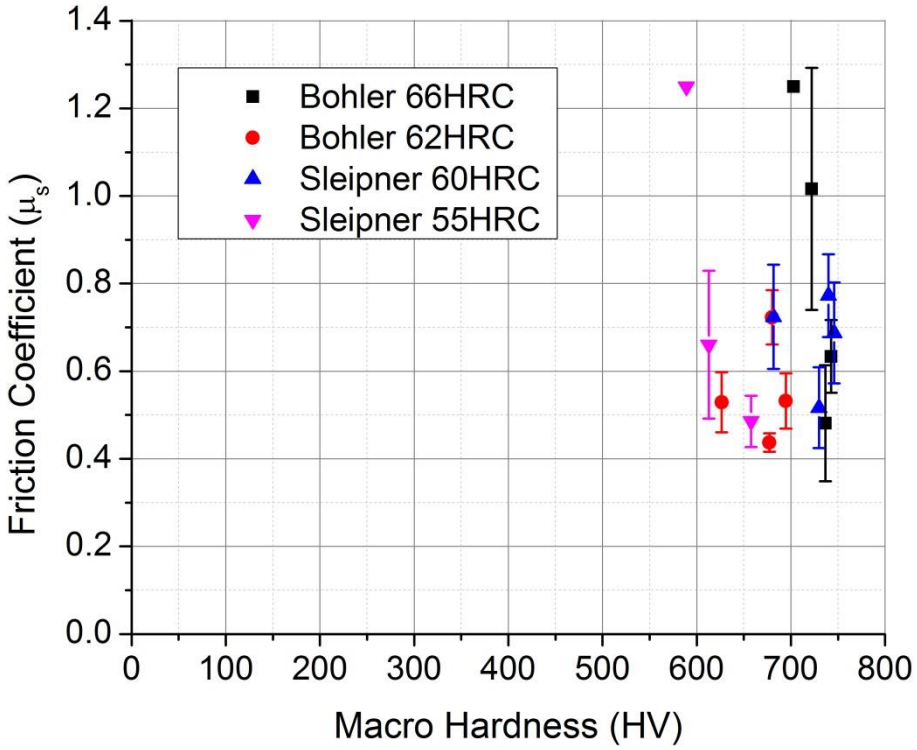

Figure 5.19. Friction coefficient as a function of macro-hardness for two tool steel alloys, each heat treated to two different nominal hardness values

The results of the tests on the Böhler and Sleipner steel samples, presented in Figure 5.19, show no direct correlation between friction and hardness. This is similar to the results obtained for the plasma nitrided samples, discussed in Section 5.3.4, and again suggests that high hardness alone is not enough to generate a high friction surface.

5.4.2.2 Roughness Dependence

Following the hardness results, surface roughness measurements were taken for each sample texture-hardness combination. The previously obtained friction coefficients are plotted against these roughness measurements in Figure 5.20.

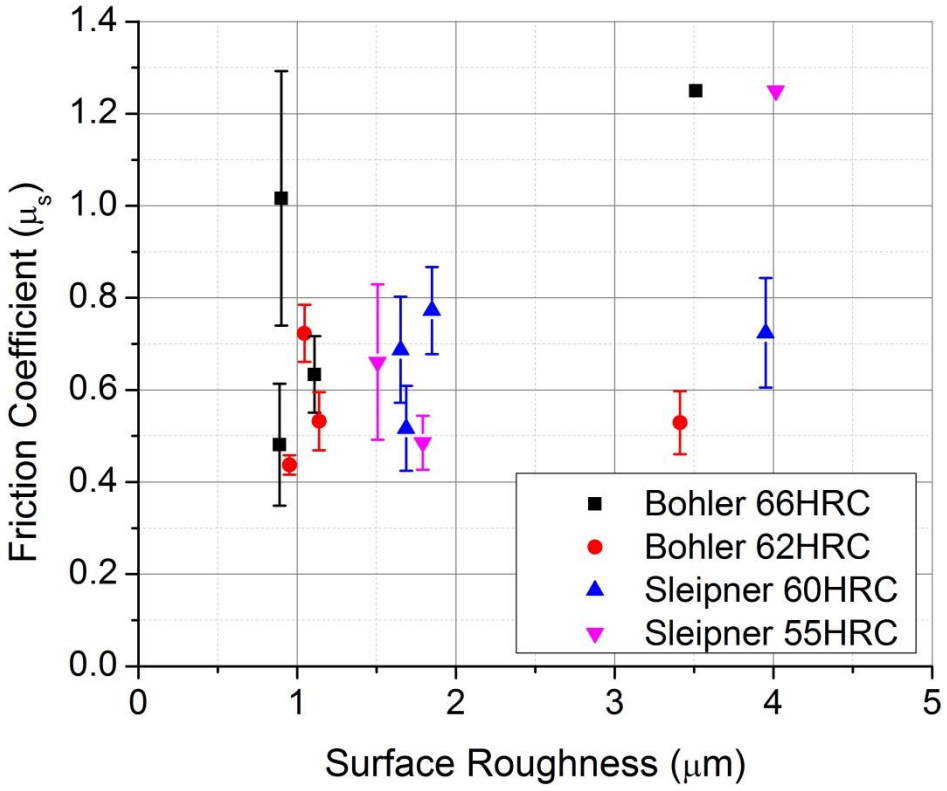

Figure 5.20. Friction coefficient as a function of surface roughness (S_a) for two tool steel alloys, each heat treated to two different nominal hardness values

With the exception of two data points, the general trend observed in Figure 5.20 indicates that higher surface roughness results in higher friction coefficients, as was observed for the nitrided samples in Figure 5.15. One possible explanation for these two outlying points is that the surface hardness of these samples was not high enough to facilitate sufficient embedding of the asperities into the counterpart. This could be due to the moderate temperature achieved during tempering being unable to form hard secondary carbides at the surface (as is thought to be the case at higher tempering temperature) and the hardness achieved at the surface directly through the heat treatment process being insufficiently high to enable adequate embedding.

5.5 Applications

Two applications for high friction shims, for which the work presented thus far has concerned, have been proposed by MDT. These applications are found within the main bearing assembly and the piston rod assembly of the MDT marine engines.

5.5.1 MDT Main Bearing Assembly

The main bearing assembly was the primary application considered. Typically, the assembly would rely on mechanical interlocking between the bearing support and the bearing cap to prevent relative movement between the two. However, due to the size of the components (bedplate length of 9-17m depending on the number of cylinders), the accuracy of the machining and the required matching of all bearing supports and caps makes the machining process very expensive and difficult to achieve. As a result, it is easier to machine the mating surfaces flat and use a high friction shim in between to prevent relative lateral movement of the two components. Figure 5.21 shows a schematic of the main bearing assembly with high friction shim.

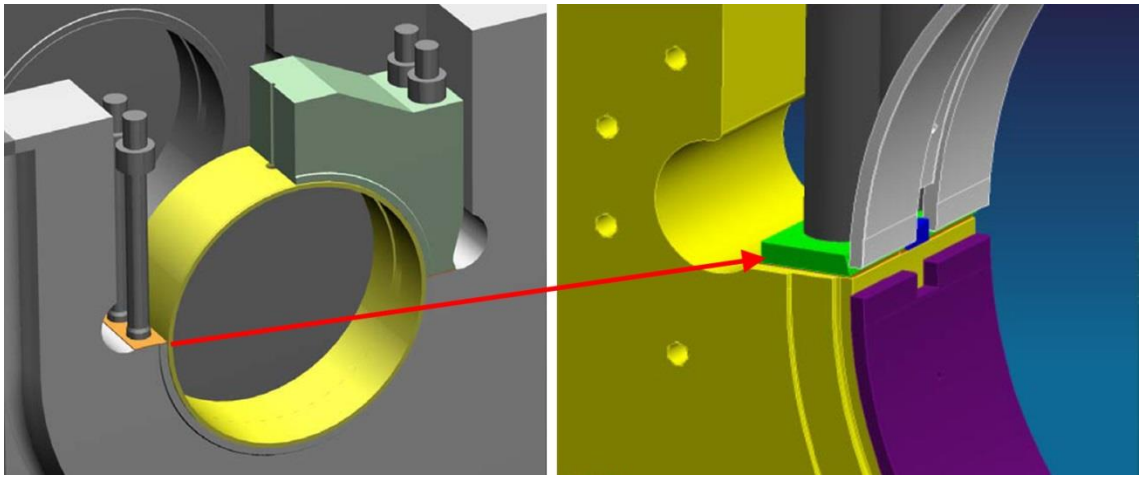

Figure 5.21. Schematic of the main bearing assembly, highlighting the inclusion of a high friction shim

The minimum friction requirement for the shim, shown in green on the right of Figure 5.21, is μ_s=0.6 with higher friction coefficients being preferable. Alternate methods of increasing the friction coefficient of the shims have been considered, such as thermal spraying techniques (HVOF, air plasma spraying (APS), etc.). However, whilst these methods can generate the required friction coefficients, they typically show significant variation and can be considered reproducible only to a certain extent. Thus, a more consistent process like laser texturing would be desirable. Unfortunately, the high friction textures were unable to be tested in this application within the duration of this project.

5.5.2 MDT Piston Rod Assembly (Japan Tests)

In addition to the main bearing assembly application, MDT proposed a second possible application for hardened, textured shims. For this second application, the textured shims were to be mounted between the piston rod and piston crown. Shim discs were proposed to have high friction surfaces in order to prevent fretting wear, observed when no shim is present. Figure 5.22 shows a schematic and photograph of the shim for this application.

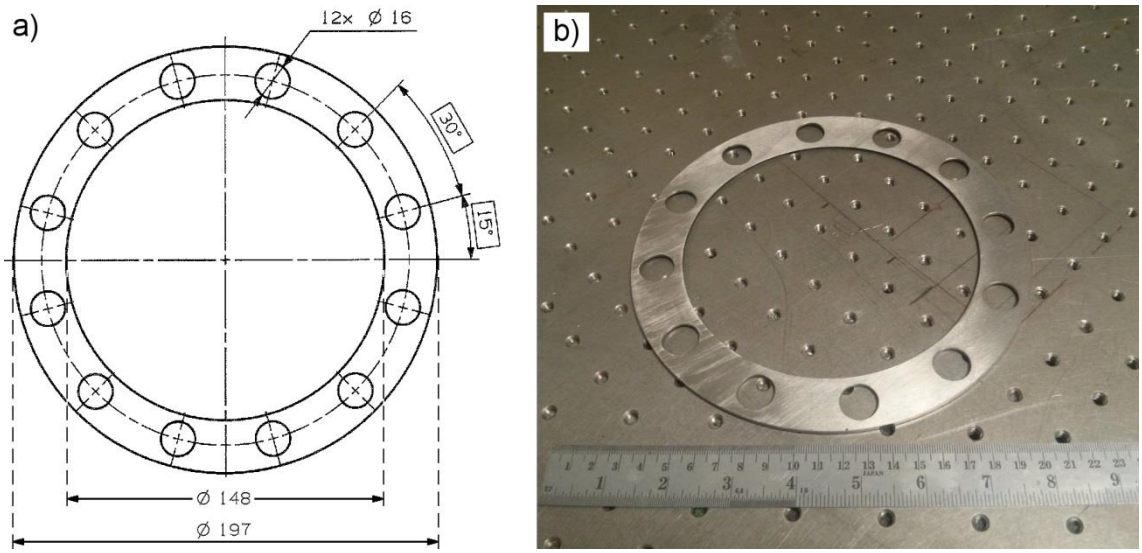

Figure 5.22. High friction disc shim in a) schematic diagram, with units given in mm, and b) photograph of an untextured shim

Nine of the shims, shown in Figure 5.22, were received from MDT and laser textured based on the initial results (Section 5.3.2) rather than the subsequent test results (Section 5.3.4) which had not been observed at the time of texturing. The texturing process was performed by the 20W EP-S laser, with processing parameters of s=25µm, PRF=20kHz, pulse energy of 0.71mJ and pulse duration of 220ns. The shims themselves were made of the nitriding steel alloy and were subsequently nitrided after the laser texturing process.

Also, due to the size of the discs (nearly 200mm outer diameter), it was not possible to use single step laser processing as had been used for all sample texturing. As a result, a step and repeat process was devised in order to cover the full surface area without significant overlap. Figure 5.23 indicates how the step and repeat processing was performed.

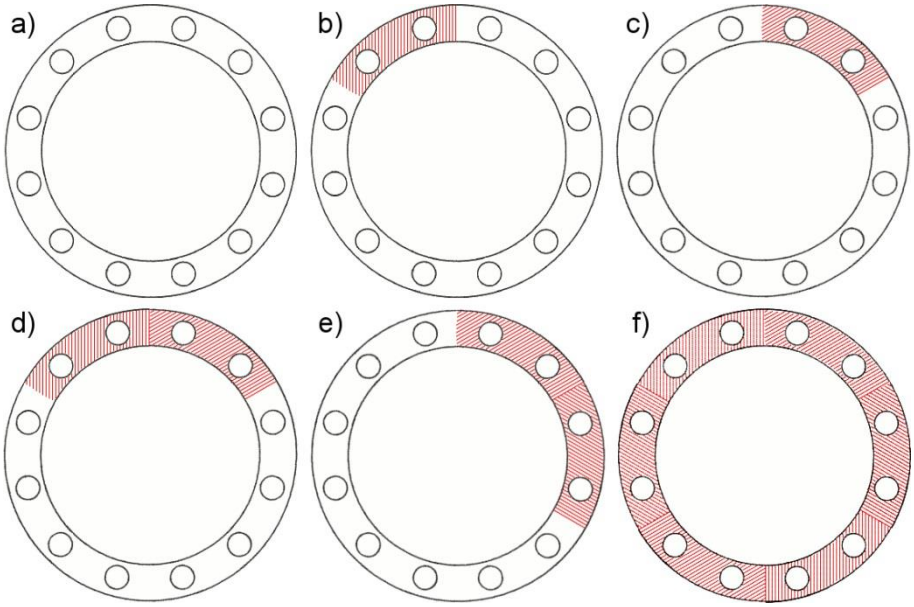

Figure 5.23. Schematic diagram of the step-by-step process of laser texturing a high friction intermediate shim

As depicted in Figure 5.23, the geometry of the shim was utilised in order to texture the full area. In the first step, the area enclosed between the 10 and the 12 on a clock face was textured in the vertical direction, as per Figure 5.23b. The shim was then rotated 60° clockwise, utilising the available holes for alignment, as shown in Figure 5.23c. The same area (relative to the scan head) was then textured (Figure 5.23d) and the process repeated six times until the whole shim was textured, as indicated in Figure 5.23f. Five of the nine shims were textured (with the same processing settings) on both sides whilst four shims were textured on one side only. After texturing the components were plasma nitrided before being sent to Japan for testing within a test engine, as indicated in Figure 5.24.

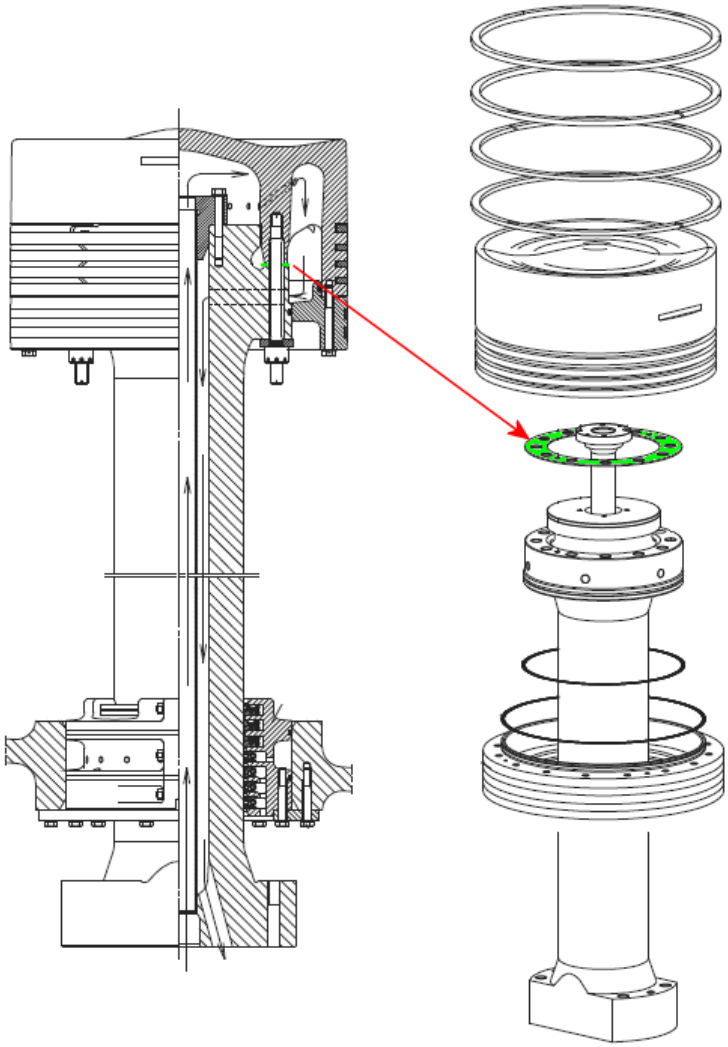

Figure 5.24. Schematic of the piston rod assembly, highlighting the location of the laser textured, high friction shim

5.5.2.1 Results & Outcomes

Testing of the piston assembly was performed with three configurations: no intermediate shim, with an intermediate shim laser textured on one side and with an intermediate shim laser textured on both sides. Images of the piston component after testing can be seen in Figure 5.25.

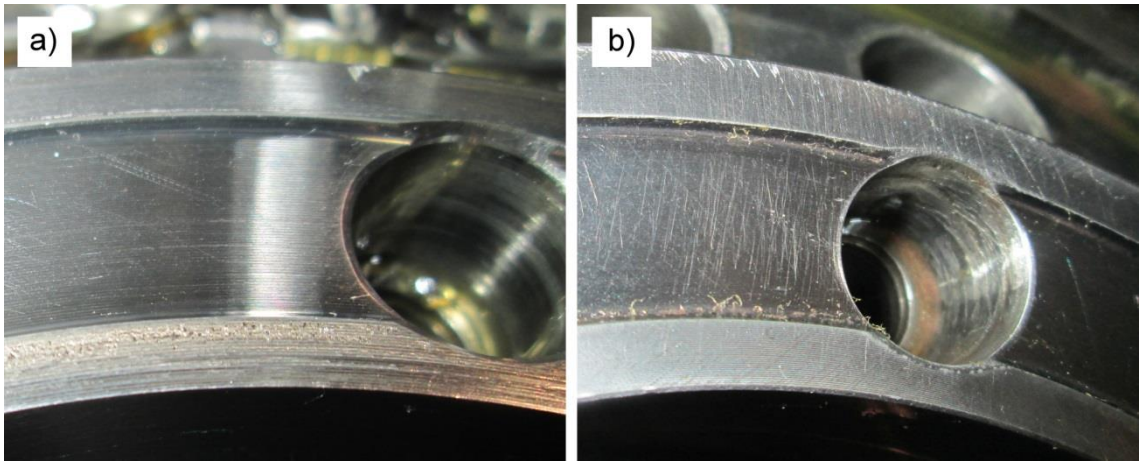

Figure 5.25. Photographic images of a component of the piston rod assembly after testing with a) no intermediate shim and b) an intermediate shim with laser texturing on both sides

Figure 5.25a clearly shows the issue with fretting (high frequency movement causing the severe scratching seen at the bottom of the figure) when no intermediate disc is used in the system. When the laser textured (on both sides) shim is placed in the system, the fretting is no longer observed, as shown in Figure 5.25b. However, the intermediate discs did not prevent the lower frequency scratches associated with thermal expansion and contraction. In addition, the shims textured on a single side exhibited the same results as those textured on both sides, suggesting that a non-textured shim could be sufficient in order to prevent the fretting.

5.6 Summary & Conclusion

Following from the results presented in Chapter 4, this chapter aimed to investigate the friction coefficients achievable with hardened, laser textured surfaces. Three different hardening regimes were considered; hardening through laser texturing only, plasma nitriding and conventional heat treatment, each with varying degrees of success. The hardness possible through laser texturing alone was not expected to be significant enough to noticeably alter the achievable friction coefficients. However, the secondary hardening processes were predicted to enable significant embedding of the asperities of the texture into the counterpart, resulting in higher friction coefficients.

Laser texturing was previously found to provide a small, but not insignificant, increase to the surface hardness, with higher hardness values being obtained for textures with smaller pulse separations. In an attempt to increase the hardness further, lower pulse separations, <12.5µm, were attempted but were found to introduce two issues preventing the textures from achieving high friction coefficients. First, the decreased

pulse separation leads to increased surface roughness, resulting in poorly attached asperities and possibly limiting the contact area. In addition, the high hardness asperities are also brittle, due to the rapid cooling, making them more likely to snap and break when the normal force is applied rather than embedding into the counterpart. As a result, laser texturing alone was deemed insufficient in order to achieve consistently high friction coefficients.

Plasma nitriding was found to greatly increase the surface hardness, from ~300HV30 to ~700HV30. Initial results from sample with plasma nitriding followed by laser texturing showed promising friction results, with average friction results consistently μ_s>0.8 for textures generated with the 50W HS-S laser, independent of the texture used. However, further tests, with laser texturing performed prior to plasma nitriding, gave some inconsistent results and generally lower friction coefficients. Following hardness tests indicated that the plasma nitriding was not as effective in this case, reaching hardness values <450HV30. The martensite and oxide layer generated by the laser texturing process appears to be the cause of this, resulting in reduced diffusion of the nitrogen into the sample. Despite this, laser texturing prior to plasma nitriding was deemed the preferred procedure due to the cleaning effect of the plasma nitriding on the sample, removing any poorly attached debris on sample surface.

Subsequent tests with laser textured-plasma nitrided samples, with more appropriate nitriding achieving hardness values of ~700HV30, resulted in friction coefficients between μ_s=0.3 and μ_s=0.9, depending on the surface texture. Further analysis concluded that the friction in this case was dependent on the surface roughness, with increasing roughness linearly increasing the resulting friction coefficient. Therefore, it is expected that both high hardness (in order to facilitate embedding without deformation of the structure) and high roughness (at least up to S_a~6μm) are necessary in order to achieve consistently high friction coefficients, although further tests with appropriate nitriding are required to prove this conclusively.

Conventional heat treatment, the third technique considered in order to attain high surface hardness, was used on three different tool steel alloys, Uddeholm Impax Supreme, Böhler S600 and Uddeholm Sleipner. Initial results with the Impax alloy, heat treated to three different nominal hardnesses, were found to be somewhat mixed. Measured hardness values ranged between 450HV and 600HV but friction coefficients

were observed to decrease with increasing hardness, contradicting previous results. It is proposed that this is caused by the dissolving of the carbides and formation of martensite during the laser texturing process. During the tempering process, secondary carbides may form in the depleted zone, increasing the surface hardness, whilst decreasing the bulk hardness. In addition, increasing tempering temperature increases the tendency to form the secondary carbides. Therefore, it is possible that the samples with the lowest bulk hardness have the highest surface hardness, explaining the observed friction and macro-hardness results.

Friction tests on the two other tool steel alloys appeared more similar to the final results obtained for the plasma nitrided samples. No obvious dependence on the hardness was evident, but a very general trend of increasing roughness leading to increased hardness was observed, albeit with two outlying points. In conjunction with the results from the plasma nitrided samples, it appears that both high hardness and high roughness are necessary for high friction surfaces, although several issues with the methodology are still required to be solved before the process can become reliable and suitable for use in an industrial setting.

Finally, two possible applications, within the main bearing assembly and piston rod assembly, for high friction shims have been proposed by MDT. Unfortunately, no parts have been textured and tested for the main bearing assembly application as yet. Several tests have been conducted for the piston rod application, however. The inclusion of a shim, with laser texturing performed on both surfaces, within the piston rod assembly was observed to eradicate the signs of fretting wear, which were observable when no shim was present. Low frequency scratches, caused by thermal expansion and contraction, were still visible, however. It should be noted that the same outcome was observed when the shim was textured on only one side was textured as when both sides were textured, raising the possibility that an untextured, hardened shim alone could prevent the fretting wear.

Chapter 6 – Friction Textures – Both Contacting Surfaces

This chapter concerns the generation of high friction contacts where, unlike the previous chapters, both surfaces of the contact are laser textured prior to friction testing with the expectation of generating contacts with significant interlocking. This method of attaining high friction coefficients is not particularly suitable for the main bearing assembly application discussed in Section 5.5, due the sheer size of the components that would require texturing. However, there are other applications where laser texturing of both faces of a contact is viable, one of which is discussed at the end of this chapter. Despite the possible geometric limitations of this processing method, it does benefit from being a one-step process – there is no need for any post-processing in order to change any of the material properties or clean the textured surface. The available parameter space is also increased by laser texturing of both contacting surfaces, possibly enabling fine-tuning of the resulting friction coefficient by tweaking the laser texturing parameters.

All of the textures discussed in this chapter were generated by the 20W EP-S or 50W HS-S (Section 6.5) lasers on SS316 samples and low alloy carbon steel counterparts and no post treatment was performed in order to increase the surface hardness. The resulting friction coefficients discussed are the average of 5-10 tests for each texture. Error bars were calculated as the standard deviation of the measurements taken for each set of tests.

6.1 Friction Measurements

6.1.1 100MPa Normal Pressure

As with the previous friction tests, friction measurements of the contacts with two textured surfaces were performed for a range of pulse separations, from 12.5µm to 200µm. The textures on each sample and CP were identical for each test and generated with 0.71mJ, 220ns pulses at 20kHz PRF, unless stated otherwise. Initial friction tests of these contacts were carried out at 100MPa normal pressure, with a set of typical load-extension curves shown in Figure 6.1.

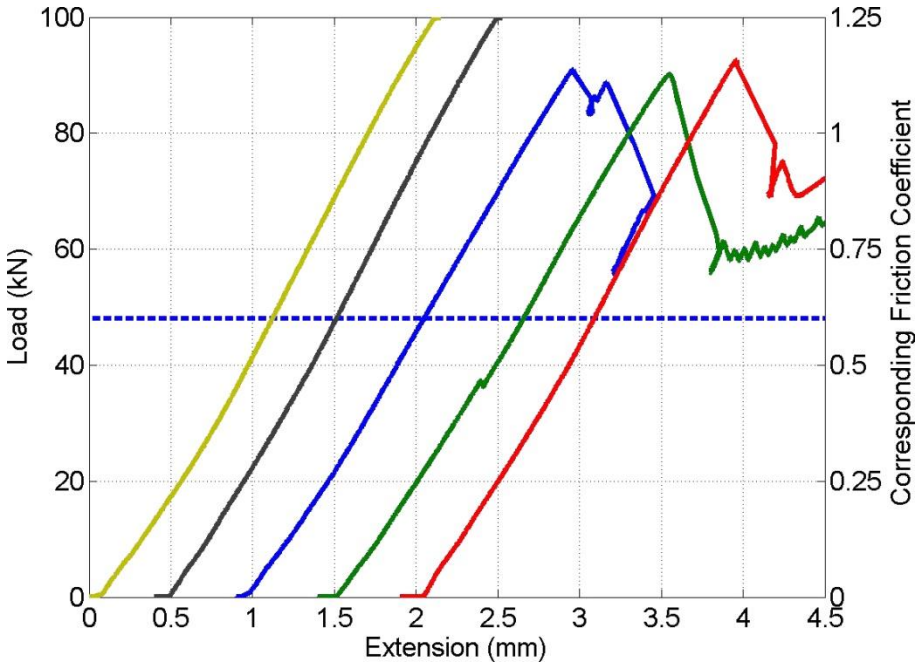

Figure 6.1. A typical load-extension plot; 100MPa normal pressure and 25µm pulse separation on both sample and CP (curves separated for clarity)

As can be observed from Figure 6.1, several of the friction tests do not show the large characteristic slip point below 100kN load force. Since the hydraulic press applying the load is limited to 100kN, the exact slip point, and therefore friction coefficient, for these samples could not be determined. As a result, the minimum possible friction coefficient of μ_s=1.25 was taken for these samples. In addition, the green curve in Figure 6.1 exhibits a very small slip point just below 40kN load. The consequences of these 'micro-slips' are addressed in Section 6.1.1.1.

The friction coefficients were then calculated and averaged for each set of data; both including and excluding the micro-slips. The results of these tests are shown in Figure 6.2.

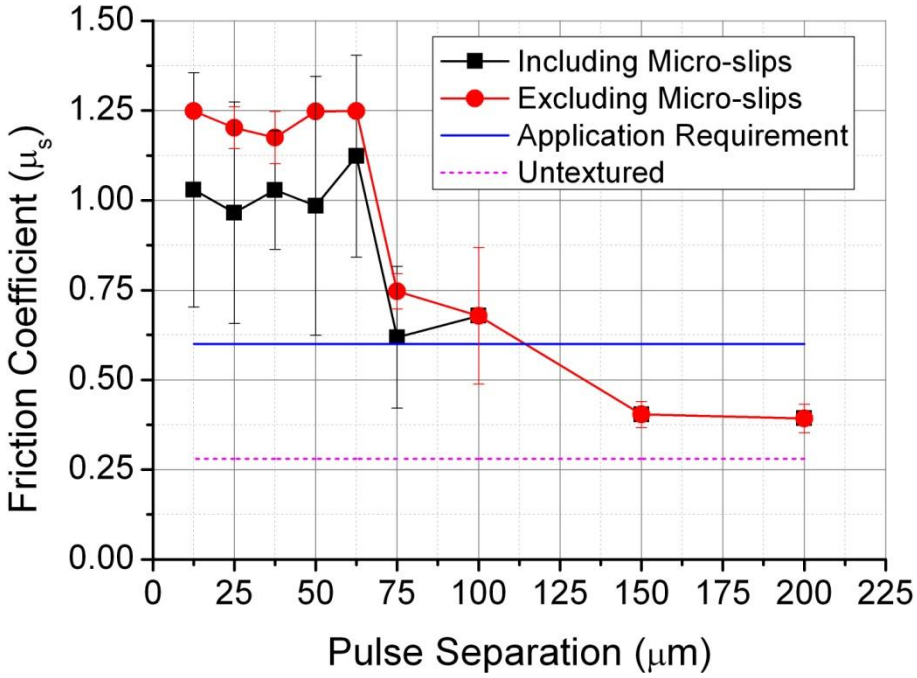

Figure 6.2. Friction coefficient as a function of the texture pulse separation (both sample and counterpart) for friction measurements including and excluding the 'micro-slips'; solid and dotted horizontal lines indicate the minimum desired friction coefficient and the friction coefficient of untextured samples and CP, respectively, for comparison

From the results presented in Figure 6.2, it can be seen that very high static friction coefficients are obtained with moderate-low pulse separation (s<62.5μm, >-35% pulse overlap) textures. In this range, average friction coefficients are consistently ≥1, albeit with significant variance when 'micro-slips' are included when determining the friction coefficient. The friction coefficient plateau observed at these pulse separations when micro-slips are excluded is, as previously discussed in Section 4.5, caused by the limitation of the load force from the hydraulic press.

As pulse separation increases, the observed static friction coefficients decrease dramatically, beginning to converge towards the untextured value at high pulse separation, as expected. The high friction coefficients seen at low pulse separations are assumed to be the product of good interlocking of the two surface textures, facilitated by plastic deformation caused by the substantial normal pressure. As pulse separation is increased, the number of surface features which can securely interlock decreases, giving a surface texture which is similar to an untextured surface, resulting in lower friction coefficients. These assumptions are in agreement with the optical micrographs of the laser textured surfaces, as shown in Figure 6.3.

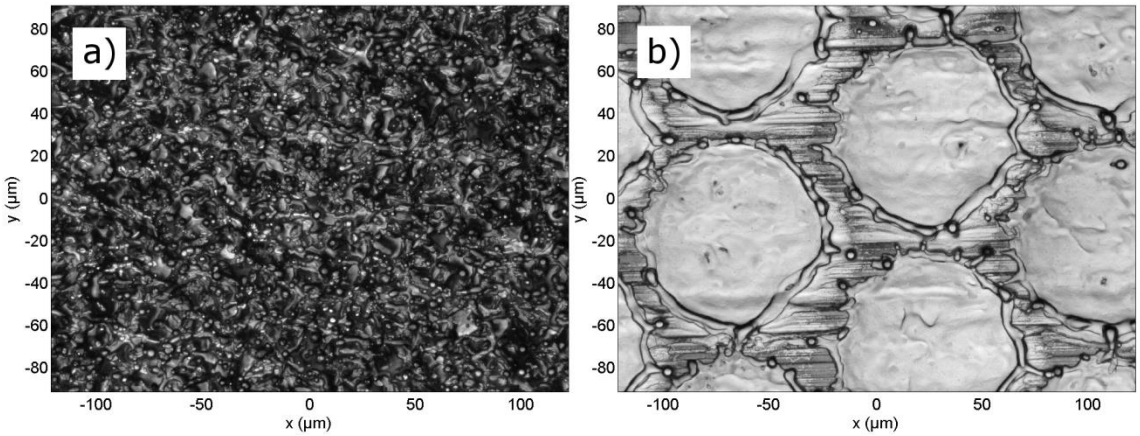

Figure 6.3. Optical micrographs of laser textured surfaces with a) 25µm pulse separation and b) 100µm pulse separation

A micrograph of a typical low pulse separation (25µm) texture is shown in Figure 6.3a, with a surface that appears very random and contains a significant number spherical asperities. In comparison, Figure 6.3b shows the surface topography of a sample with high pulse separation, 100µm in this case. Here the hexagonal structure is clearly visible whilst the number of asperities available for possible interlocking is considerably reduced. Even in this case where the two structures are very dissimilar, the S_a (arithmetic average) roughness values are comparable, as shown in Table 6.1.

Pulse Separation (µm)	Static Friction Coefficient	S_a Roughness (µm)	Peak-Trough Depth (µm)
12.5	>1.25	3.68	32.75
25	>1.20	1.00	10.05
50	>1.25	0.99	7.14
100	0.68	0.95	8.84
200	0.39	0.57	11.61

Table 6.1. Comparison of friction coefficients and roughness measures (obtained from the Alicona profiler) for five laser textures, with the two shown in Figure 6.3 highlighted

As pulse separation is decreased, the roughness values (measured over an area of 1.238x1.244mm) tend to increase. However, typical roughness measurements do not directly correspond to the observed difference in friction coefficients. Analysis using optical microscopy was also performed on several of the tested samples, particularly those which did not slip during testing, such as that shown in Figure 6.4.

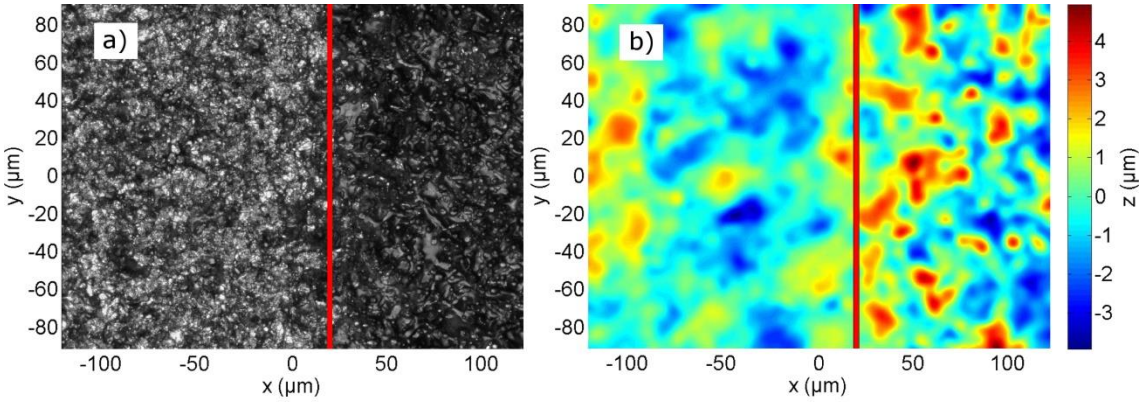

Figure 6.4. Optical micrograph (a) and z-profile (b) of a sample (37.5µm pulse separation) after friction testing, with no slipping – tested area on the left of the vertical line and untested on the right

From Figure 6.4a, a significant change in the surface morphology between the region of the texture which has been friction tested (left) and the untested region (right) can clearly be seen. It was expected that the large normal pressure would cause deformations on the surface of the textured sample – likely reducing the surface roughness in this area. This is clearly visualised in Figure 6.4b, where we see a significant decrease in the height of the peaks on the left hand side compared to the right (peak height of ~2.5µm vs ~5µm). Area roughness measurements of the two distinct areas were also found to agree with this conclusion, with S_a=0.71µm calculated for the tested region compared to S_a=1.25µm for the untested region. Further to the top-down microscopy analysis, cross-sections of the samples after application of the normal load, but prior to friction testing, were also analysed, as shown in Figure 6.5.

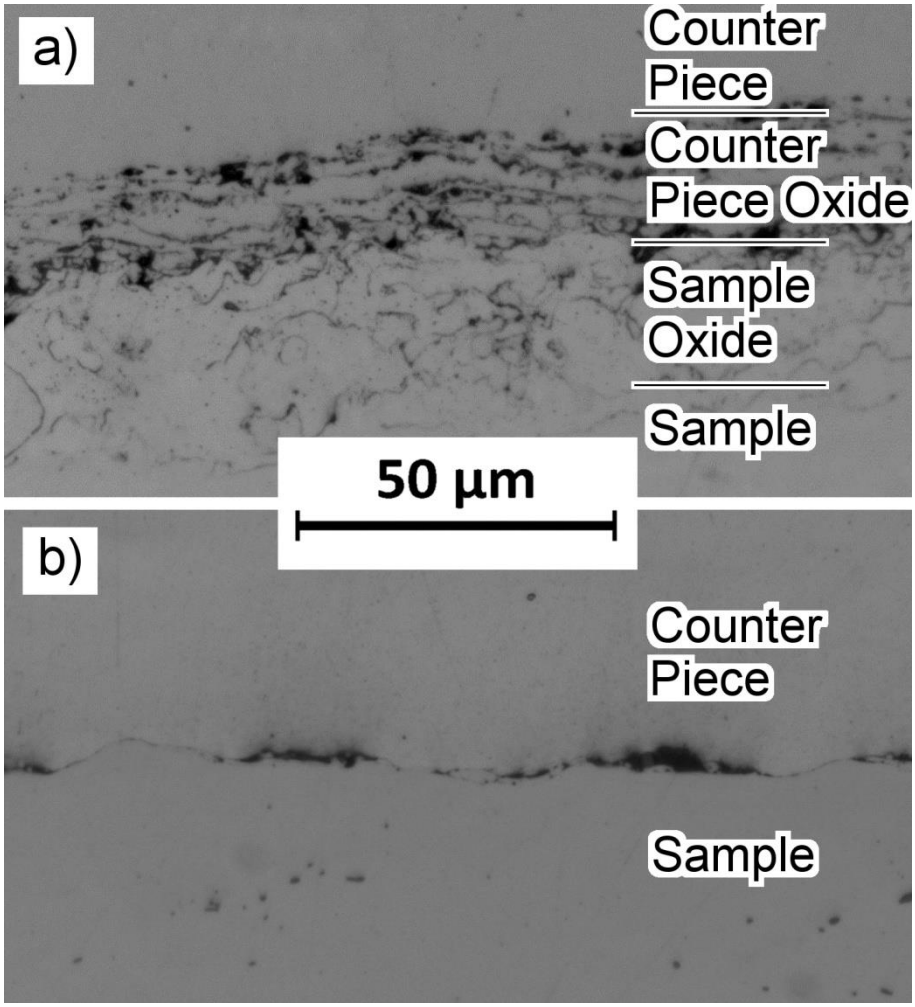

Figure 6.5. Cross-sections of two different textures, with (a) 12.5µm pulse separation and (b) 50µm pulse separation, after application of ~100MPa normal pressure but without friction testing

At 12.5µm pulse separation, shown in Figure 6.5a, the two, thick oxide layers generated by the laser texturing process are deformed significantly by the large normal pressure, resulting in consistent contact along the interface with very dense contacting and interlocking points. The dark spots observable here are small voids generated by the laser texturing process. For the larger pulse separation in Figure 6.5b, several deformations are still present however the oxide layers are very thin (as the total energy input to the surface is significantly lower) and the contact is less consistent (with the presence of observable gaps) in addition to more sparse interlocking points. Despite both of these textures exhibiting high friction coefficients, it is clear that as pulse separation is increased the interlocking becomes weaker. As a result, the lower coefficients observed at larger pulse separations in Figure 6.2 are easily interpreted.

6.1.1.1 Micro-slips

As noted in Section 6.1.1, several of the load-extension curves, such those shown in Figure 6.1, exhibit micro-slips. The cause of these slips and the effect they have on the static friction coefficient was initially unclear. As a result, additional tests and observations were made on these samples. Figure 6.6 highlights the appearance of the micro-slips in the load-extension curves and gives a good indication of the scale at which the slip takes place.

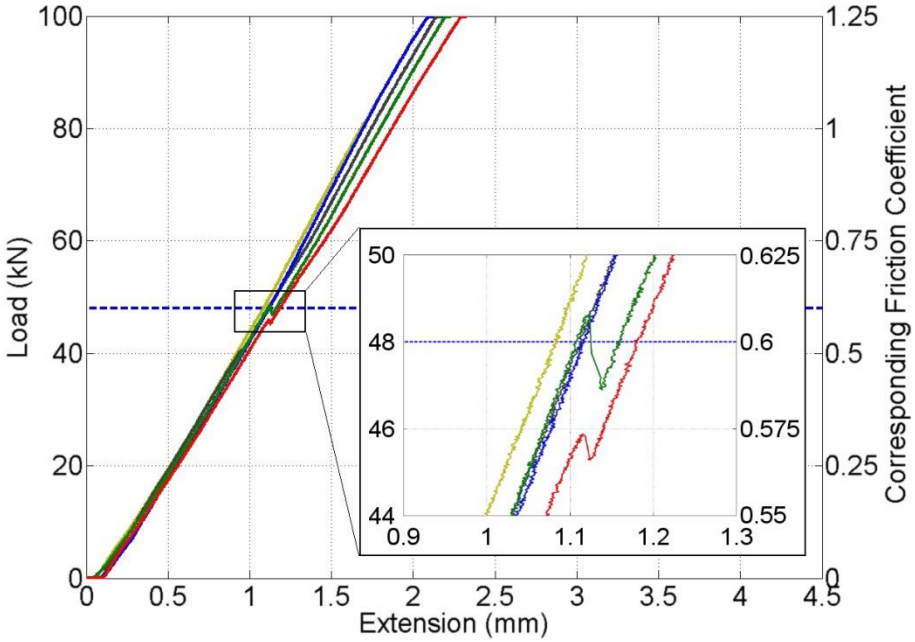

Figure 6.6. Load-extension curve for textures with 50µm pulse separation, with inset highlighting the observed micro-slips

The measurements plotted in Figure 6.6 show that even after micro-slipping, the load can continue to be increased on some samples without exhibiting any further slippage. Following this, the load was removed entirely from several of these samples and then reapplied as in the original friction test. The resulting load-extension curve from these tests showed a straight line as the applied load increased linearly without any slippages, as shown in Figure 6.7.

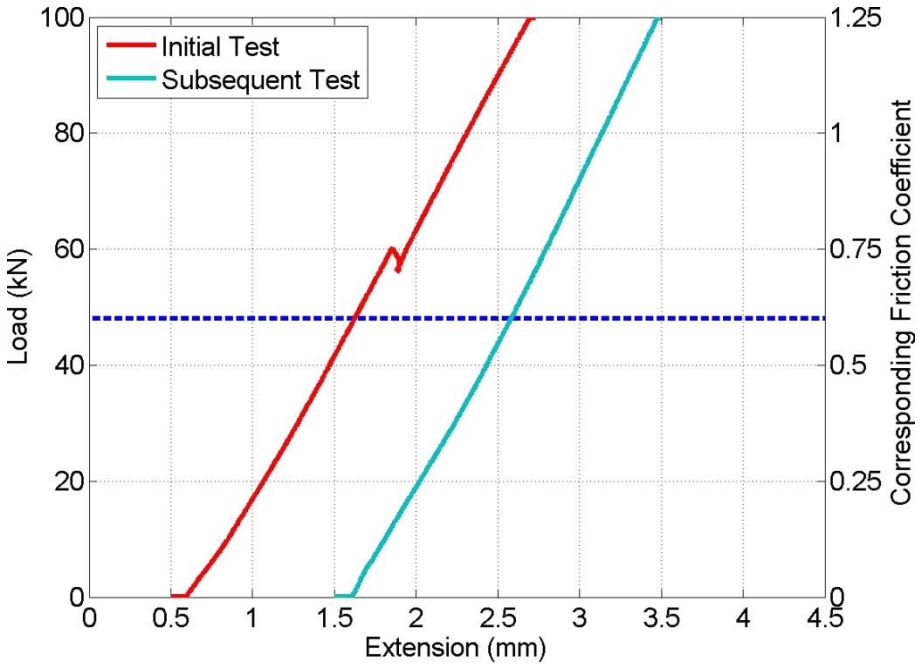

Figure 6.7. Load-extension curves showing difference between initial friction test and subsequent tests for a sample exhibiting a micro-slip (37.5µm pulse separation texture)

Given this observation, and the small movement of the samples during these micro-slips (<50µm), it is reasonable to assume that these micro-slips are not representative of the static friction coefficient but, rather, are actually very small realignments of the structures, facilitating even better interlocking between the surfaces. Although it is understood that such movements may not be tolerable for every application, micro-slips are excluded for the friction coefficient calculations in all of the following measurements.

6.1.2 Friction Measurements at 50MPa

Since a significant number of friction tests performed with 100MPa normal pressure exceeded the measurement capabilities of the hydraulic press, textures of the same design were then tested with a lower normal pressure of 50MPa, thus allowing the determination of friction coefficient values of up to 2.5 with the same testing set-up and equipment. Figure 6.8 shows the friction dependence on the pulse separation using 50MPa normal pressure.

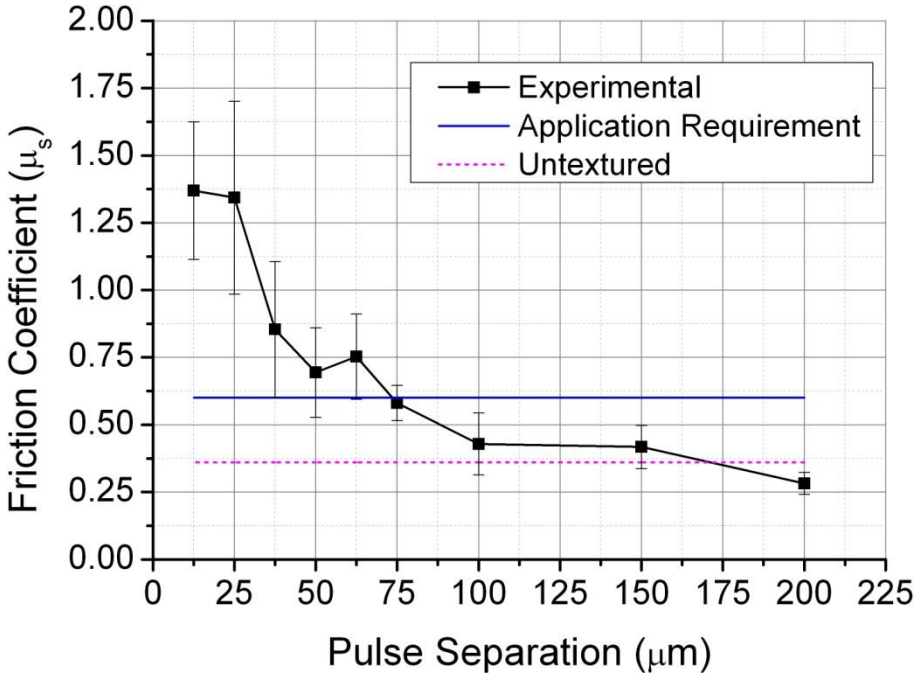

Figure 6.8. Friction coefficient as a function of the texture pulse separation for samples tested at 50MPa normal pressure; solid and dotted horizontal lines indicate the minimum desired friction coefficient and the untextured friction coefficient respectively for comparison

As in Figure 6.2, the friction coefficients observed in Figure 6.8 are very high, above 1.3 on average with individual measurements as high as 1.9 at low pulse separations (≤25μm). These values decrease sharply as pulse separation is increased and converge towards the untextured baseline value (μ_s=0.36±0.04) at around 175μm pulse separation.

Given that the results plotted in Figure 6.2 and Figure 6.8 used identical laser texturing parameters, the measurements can be directly compared as in Figure 6.9.

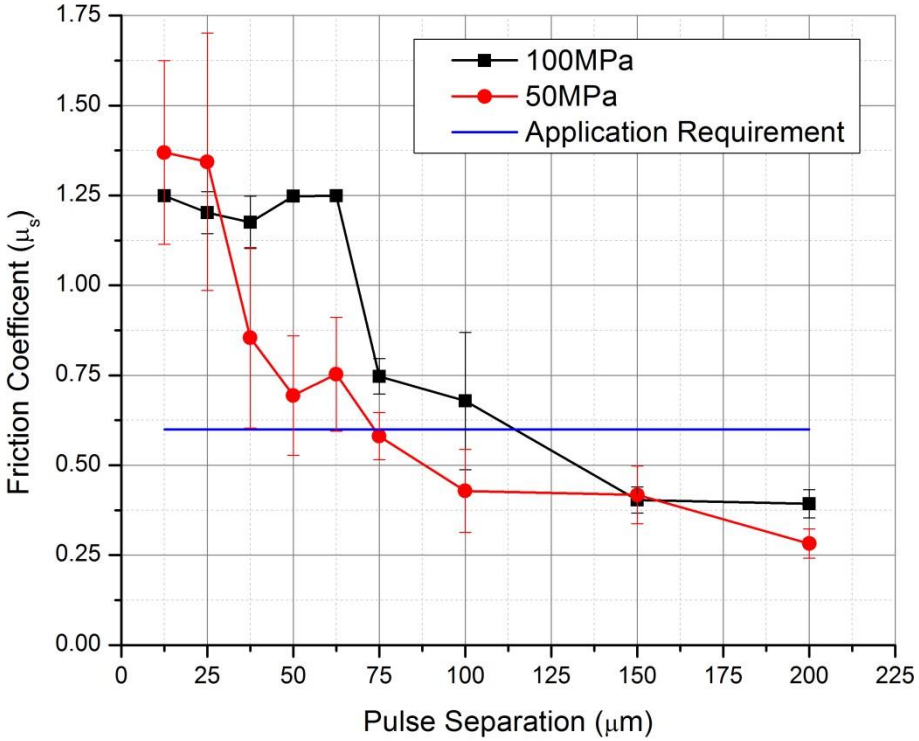

Figure 6.9. Comparison of the dependence of static friction coefficients on laser pulse separation for the two applied normal pressures

As noted previously, the overall trends of the curves are very similar for both normal pressures. However, in the range of pulse separation range where the friction coefficients can be resolved at 100MPa pressure (s>75μm), the samples tested at 100MPa consistently give higher friction coefficients than those tested at 50MPa. This implies that the larger normal force causes more plastic deformations of the textured surfaces, allowing better contact and interlocking of the two textures and therefore increased friction coefficients.

6.1.3 Overloading

Given the observed dependence of the static friction coefficient on the applied normal pressure, it was assumed that even higher static friction coefficients could be achieved by 'overloading' the sample to a very high normal pressure prior to testing at a lower normal pressure. In order to test this, another set of samples were processed with the same textures and then subjected to a normal pressure of 150MPa (design pressure of testing rig) which was then decreased to 50MPa before testing, without realigning the sample. Figure 6.10 shows the results of these tests in comparison to those already presented in Section 6.1.2.

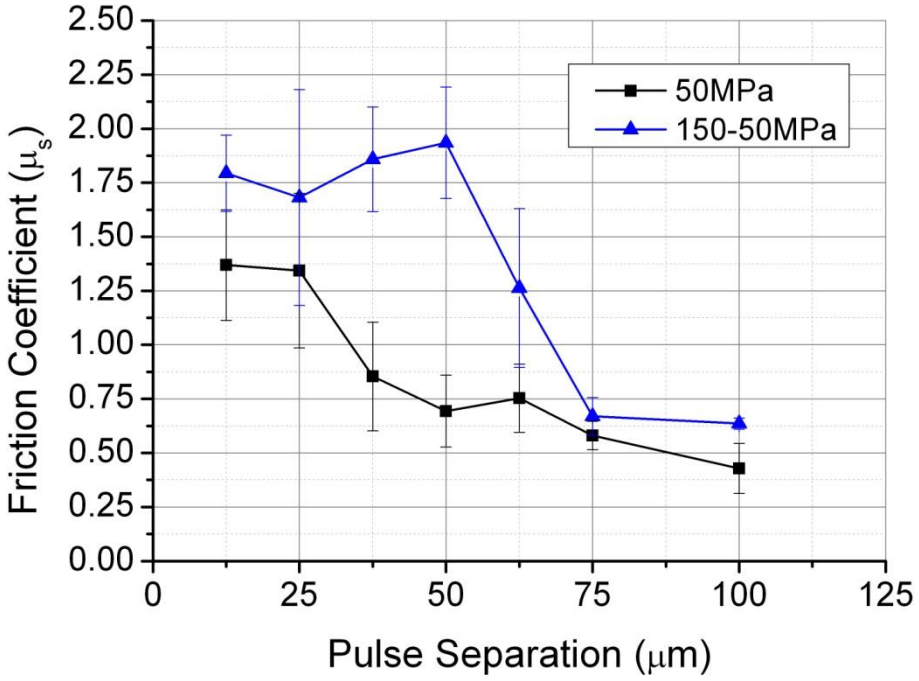

Figure 6.10. Comparison of the static friction coefficients obtained at 50MPa and those loaded to 150MPa then decreased to 50MPa prior to friction testing

The measurements shown in Figure 6.10 clearly show that by initially applying a very large normal pressure of 150MPa, extremely high friction coefficients (μ_s>1.5) can be obtained at lower pulse separations even when testing at much lower normal pressures of 50MPa. The initial normal pressure of 150MPa plastically deforms the contacting surfaces significantly more than when only 50MPa is applied. As a result, even though the pressure is reduced to 50MPa, there is substantially more interlocking of the two textures than when only 50MPa is applied, resulting in extremely high static friction coefficients. As discussed in Section 6.1.1, increasing the pulse separation reduces the ability of the two textures to interlock, due to the low density of features available. Therefore, less plastic deformation takes place and the effectiveness of the high initial normal pressure is reduced. These results are in good agreement with the previous assumptions, based on the original findings, and all but confirm that the high friction coefficients obtained are the result of very good interlocking of the contacting surfaces.

6.2 Friction Measurements of Polished Surfaces

Despite the strong indication that the observed friction coefficients were due to interlocking, the effect of real contact area was investigated (as deformation/interlocking also increases the real contact area). By using a rotation polishing machine (Struers LaboPol-5 with LaboForce-3) and a range of polishing discs/suspensions down to 3μm diamond suspension, the sample and counterpart

surfaces were prepared with a final surface roughness of S_a<50nm. Therefore the real contact area between the surfaces during friction testing is expected to be slightly lower than that obtained with deformed interlocking but significantly higher than that of the standard ground surface (S_a~0.4µm). The load-extension curves of the tests carried out with these samples are shown in Figure 6.11.

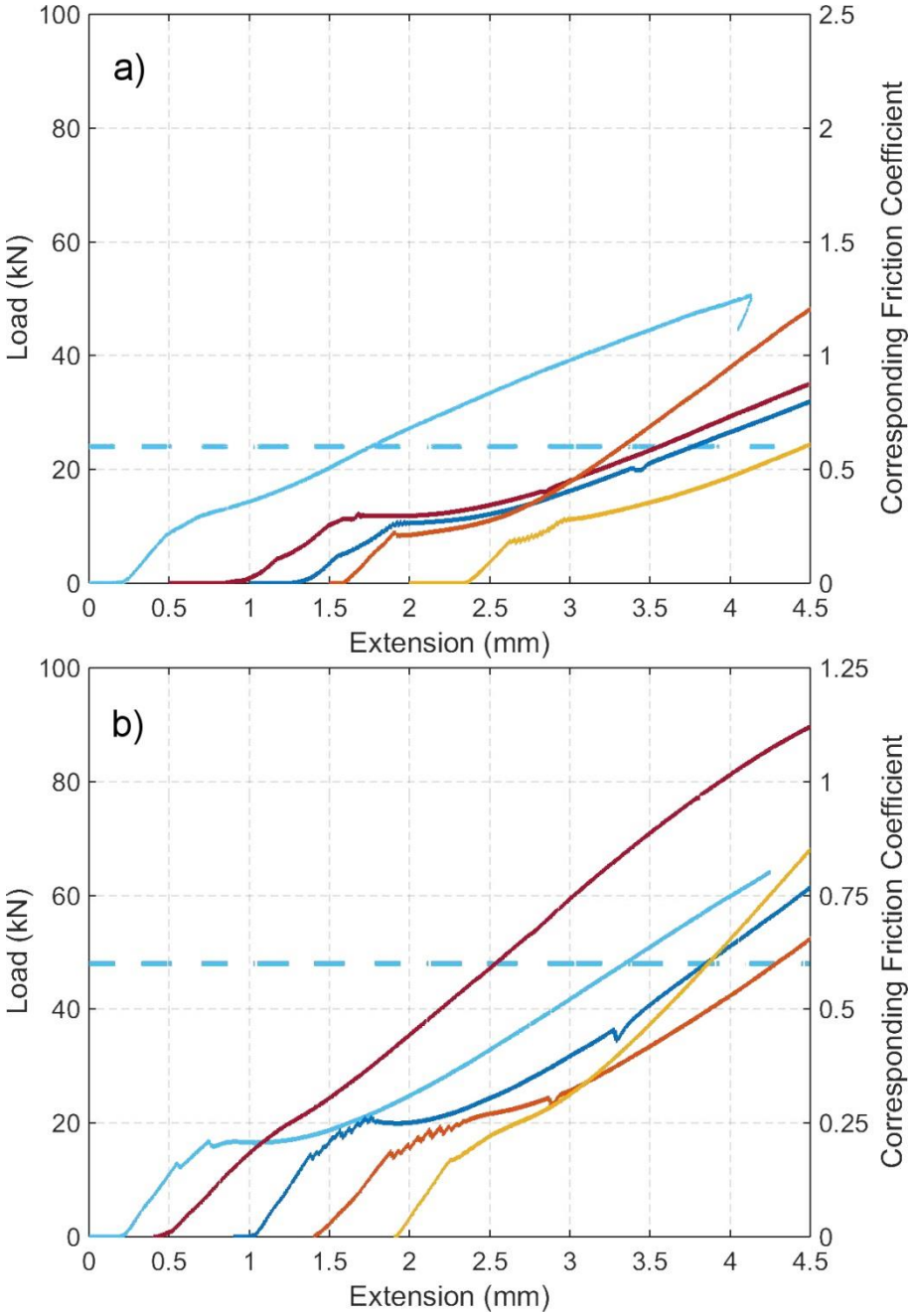

Figure 6.11. Load-extension curves for 5 tests performed on polished samples and counterparts at 50MPa (a) and 100MPa (b) normal pressure

Unlike the typical curves shown in Figure 6.1, the results presented here do not exhibit the sharp slip point of static friction. Rather, the curves in Figure 6.11 show small slip

points or continuous sliding, indicative of an adhesion based friction regime for which the static friction coefficient is difficult to determine precisely. However, by considering the change in gradients observed in the load-extension curves in Figure 6.11, it is clear that the static friction coefficients are consistently very low (μ_s<0.4) for both normal pressures. Therefore, the high friction coefficients obtained with the LST samples are evidently obtained by the interlocking features, and associated shearing required for lateral movement, rather than purely increased real contact area.

6.3 Static Counterpart Texture

Following the high friction coefficients obtained for textures with low pulse separations, which clearly require more time to generate than those with high pulse separations, other approaches were considered with the thought of increasing the processing rate for the texturing whilst maintaining the high friction coefficients. As a result, the texture used on the counterparts was fixed at 25µm pulse separation (single surface processing rate ~0.11cm^2/s) while the texture on the sample was varied between 12.5µm and 200µm (single surface processing rates between 0.03cm^2/s and 6.93cm^2/s) pulse separation, as before.

6.3.1 100MPa Normal Pressure

The friction coefficients obtained from using this texturing technique and testing at 100MPa normal pressure are shown in Figure 6.12, along with the previous results from Section 6.1.1 for comparison.

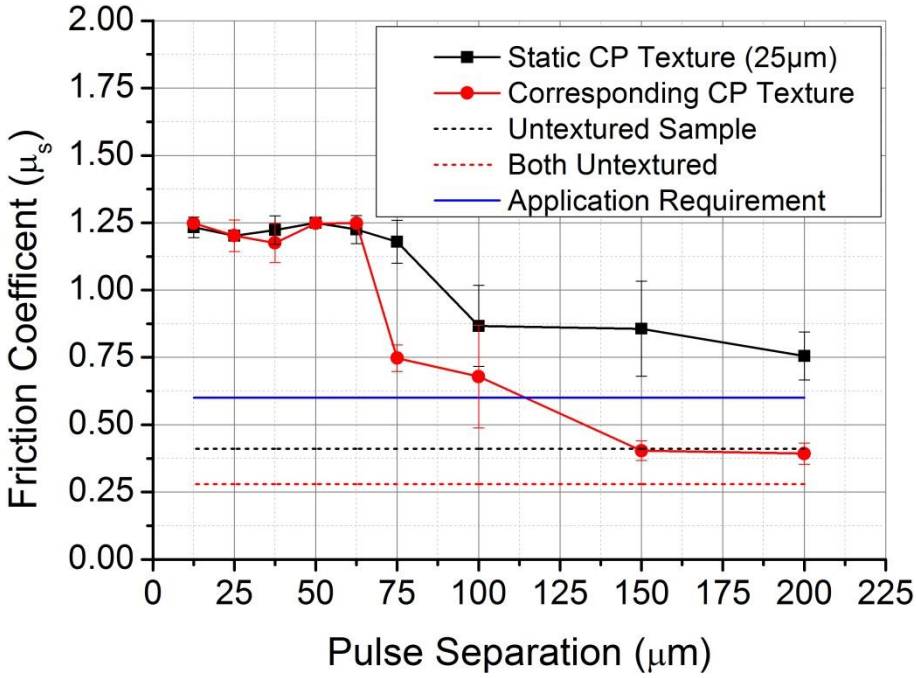

Figure 6.12. Comparison of friction coefficients for samples tested at 100MPa with a constant counterpart texture of 25µm pulse separation (Static CP Texture) and counterpart textures identical to the sample (Corresponding CP Texture) as a function of sample texture pulse separation; dashed horizontal lines indicate the baseline coefficients for untextured sample with 25µm textured counterpart and both components untextured. The solid horizontal line indicates the application requirement of μ_s>0.6

The general trend observed for the tests with the static counterpart texture was found to be the same as the trend observed for the tests with the corresponding counterpart texture, as shown in Figure 6.12. At low pulse separations, the friction coefficient is high, exceeding the measurement limit of μ_s=1.25 at this normal pressure. As the pulse separation increases, a sharp drop in friction coefficient is observed before the coefficients begin to level out. Compared to the results of the tests with the identical counterpart and sample textures, the sharp drop off for the static 25µm counterpart texture tests occurs at larger sample pulse separation – 75-100µm pulse separation compared to ~62.5µm pulse separation. This, along with the much higher coefficients at larger pulse separations, indicates that the dependence of the friction coefficient on the sample texture is reduced in this set up. This is in line with the previous conclusion of interlocking surface features. As the counterpart is processed with the 25µm pulse separation texture, there is a high density of features and asperities available for interlocking with the sample texture. As a result, the dependence on the sample texture for interlocking is decreased, facilitating high friction coefficients, μ_s>0.75, even at pulse separations as large as 200µm for the sample texture.

6.3.2 50MPa Normal Pressure

Friction tests on the same textures were then performed at the lower normal pressure of 50MPa, with the results shown in Figure 6.13 along with the results from Section 6.1.2 for comparison.

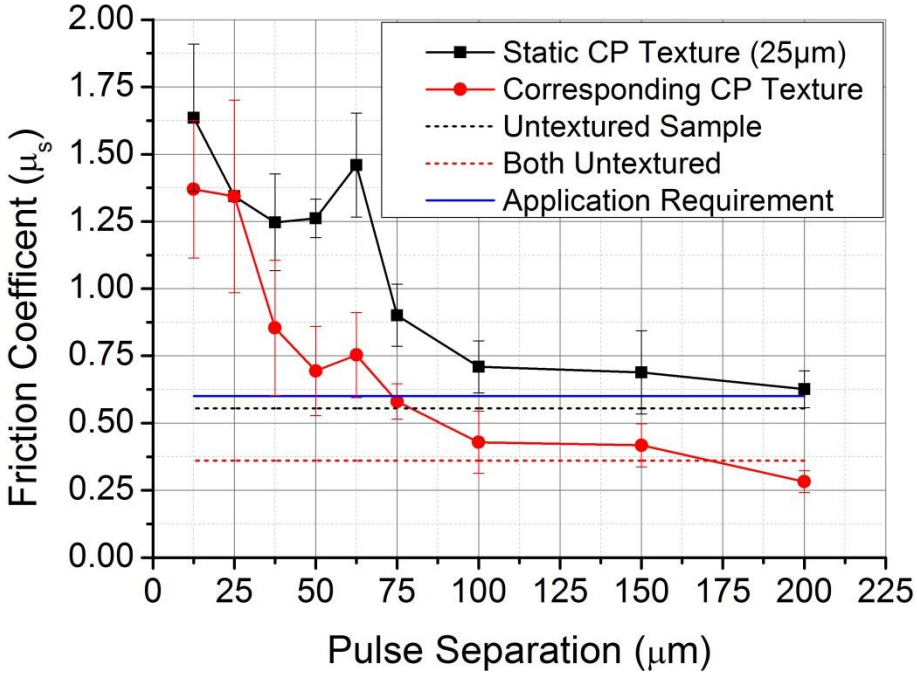

Figure 6.13. Comparison of friction coefficients for samples tested at 50MPa with a constant counterpart texture of 25µm pulse separation (Static CP Texture) and counterpart textures identical to the sample (Corresponding CP Texture) as a function of sample texture pulse separation; dashed horizontal lines indicate the baseline coefficients for untextured sample with 25µm textured counterpart and both components untextured. The solid horizontal line indicates the application requirement of μ_s>0.6

The results obtained at 50MPa, shown in Figure 6.13, were as expected following the results from the tests at 100MPa in Section 6.3.1 and the theory of interlocking asperities and features. At sample pulse separations <62.5µm, very high average friction coefficients (μ_s>1.25) are observed, followed by a sharp decline in friction coefficients as the pulse separation is increased above 62.5µm, as witnessed for 100MPa normal pressure. Despite the sharp decrease in friction coefficient at large pulse separations, the average friction values are still significantly higher (by ~0.2-0.3) with the static counterpart texture than those obtained with the corresponding counterpart texture. As a result, the average friction coefficients are still above the application requirement of μ_s>0.6 at sample pulse separations as high as 200µm, despite the reduced normal pressure of 50MPa.

It should also be noted that there is a small, but not insignificant, peak at ~62.5µm pulse separation (which is also visible in Figure 6.9) in both cases (static and corresponding CP textures), which approximately corresponds to the diameter of the crater generated by a single pulse (~60-65µm - Figure 3.12). Given this, it is clear that increased pulse separation results in discrete craters moving towards the untextured regime. For pulse separations slightly lower than the crater diameter, adjacent pulses will melt/ablate the material forming the ridge of previous craters, resulting in a slightly smoother surface in this region before the increased density of pulses becomes dominant and increases the roughness further. This is highlighted by the surface measurements taken with the Alicona surface profiler.

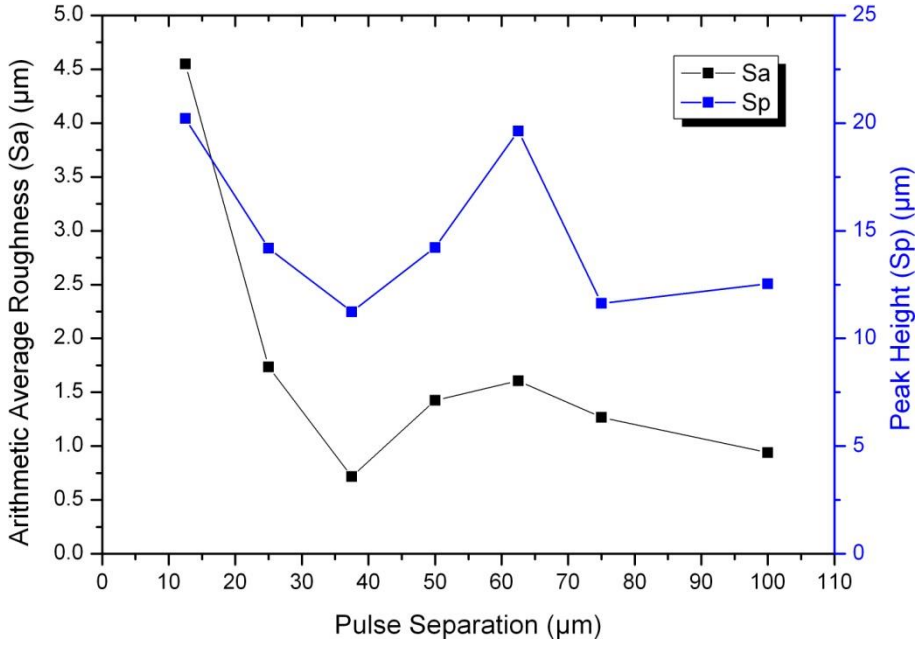

Figure 6.14. Arithmetic average roughness (S_a) and peak height (S_p) as functions of pulse separation for textures generated on SS316 at 20kHz with 220ns pulses

The surface profile measurements presented in Figure 6.14 show a spike in peak height, as well as a small peak in the average roughness value, at *s*=62.5µm in agreement with the previous assumptions for the friction peaks.

6.3.3 Processing Rate

As previously mentioned, the reasoning for maintaining a constant texture on the counterpart was to attempt to achieve high friction coefficients whilst reducing the overall processing time, in order to make the laser texturing process more appealing for industrial applications. Figure 6.15 shows the friction coefficient as a function

processing rate for the results of the friction tests performed with constant and corresponding CP textures at both 100MPa and 50MPa.

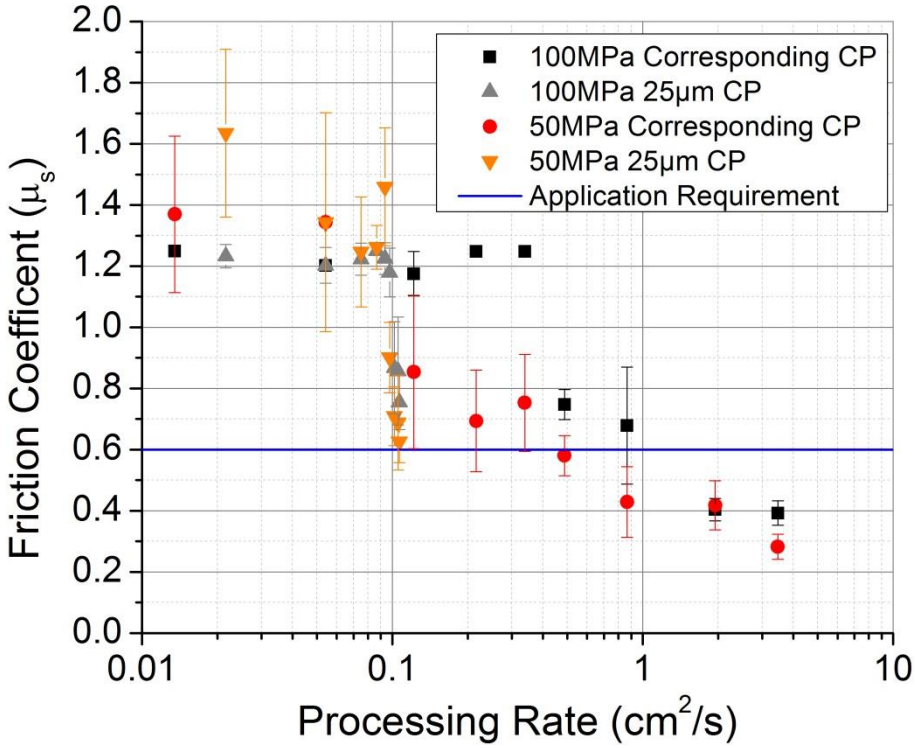

Figure 6.15. Friction coefficient as a function of processing rate (for both sample and counterpart) at 20kHz repetition rate

For the tests with constant counterpart texture, a pulse separation of 25µm was chosen in order to ensure high friction coefficients were achieved. However, from the friction results, it appears that larger pulse separation, up to 50-60µm, could be used to decrease processing time further whilst maintaining μ_s>0.6. The results presented in Figure 6.15 indicate that, in order to reliably obtain static friction coefficients above the application requirement of μ_s>0.6, processing rates of up to 0.1cm^2/s are required for 50MPa normal pressures and up to 0.35cm^2/s for 100MPa (depending on the tolerance required). These values are not improved by using a fixed texture with 25µm pulse separation on one of the surfaces. It should be noted that the quoted speeds are calculated based on a single interface (two textured surfaces) with texturing performed sequentially at a PRF of 20kHz. Figure 6.16 shows a comparison of the theoretical processing rates for various texturing strategies using a PRF of 20kHz.

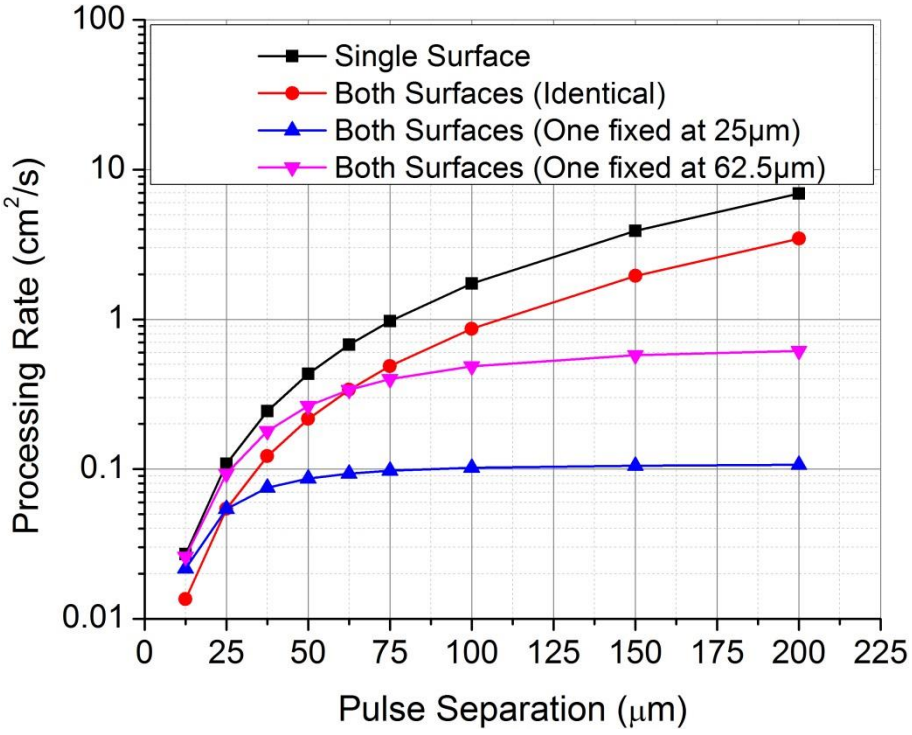

Figure 6.16. Theoretical processing rate as a function of pulse separation of the laser texturing process for four different cases with PRF=20kHz; single surface texturing, texturing of both surfaces with identical textures and texturing of both surfaces with one surface having a fixed texture (25µm and 62.5µm pulse separation)

From the curves shown in Figure 6.16, it is clear that by fixing one of the textures at 25µm pulse separation, the overall processing rate is limited to ≲0.1cm^2/s regardless of the second texture parameters. Therefore, despite the consistently high friction coefficients obtained by using this this constant texture, it does not outperform the results obtained using identical textures. However, by using a constant texture with 62.5µm pulse separation the processing limit is increased considerably to ~0.6cm^2/s, possibly allowing high friction coefficients to be achieved with improved processing rates.

Therefore, there are three clear opportunities for the processing times to be reduced: processing both surfaces in parallel (up to 50% processing time reduction), increasing the pulse separation of the constant texture to 50-60µm and increasing the repetition rate of the laser during the texturing process. The latter two of these three possibilities are explored in Sections 6.4 and 6.5, respectively.

6.4 Static Sample Texture

The effect of maintaining a constant texture on the sample whilst varying the texture of the counterpart was then investigated. As discussed in Section 6.3, improvements to the overall processing rate were speculated with a constant pulse separation of ~50-65µm for one texture. As a result, the sample texture for these tests was fixed with 62.5µm pulse separation, approximately matching the crater diameter of ~60µm.

6.4.1 100MPa Normal Pressure

As before, the pulse separation of the alternate surface texture was varied between 12.5µm and 200µm. The results of the tests performed at 100MPa normal pressure are shown in Figure 6.17.

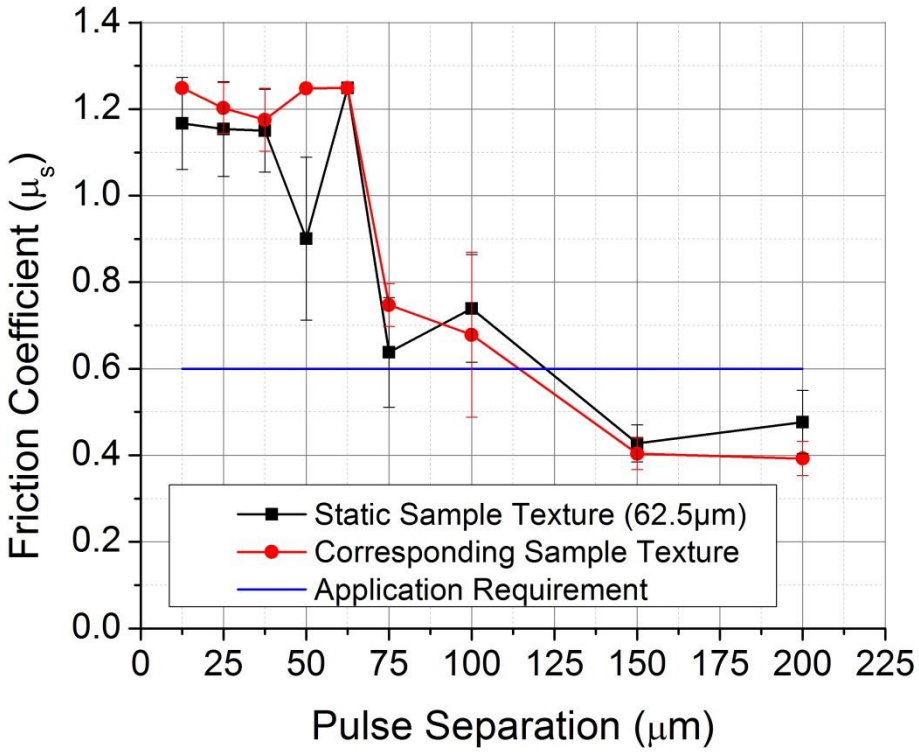

Figure 6.17. Comparison of friction coefficients for samples tested at 100MPa with a constant sample texture of 62.5µm pulse separation and sample textures identical to the counterpart as a function of counterpart texture pulse separation; the solid horizontal line indicates the application requirement of μ_s>0.6

The results presented in Figure 6.17 show typically higher friction coefficients ($\Delta\mu_s$~0.05) when the pulse separation of the counterpart texture was increased, due to the increased number of features available for interlocking compared to the tests with the corresponding sample texture. At lower pulse separations, the reverse is true. In this case, the constant sample texture reduces the number of features available for

interlocking compared to the tests with the corresponding sample texture, resulting in reduced friction coefficients. The limited resolution of the original results (corresponding sample) prevents the quantification of this effect at 100MPa normal pressure, however.

6.4.2 50MPa Normal Pressure

The same textures were then tested at the lower normal pressure of 50MPa, with the results shown in Figure 6.18.

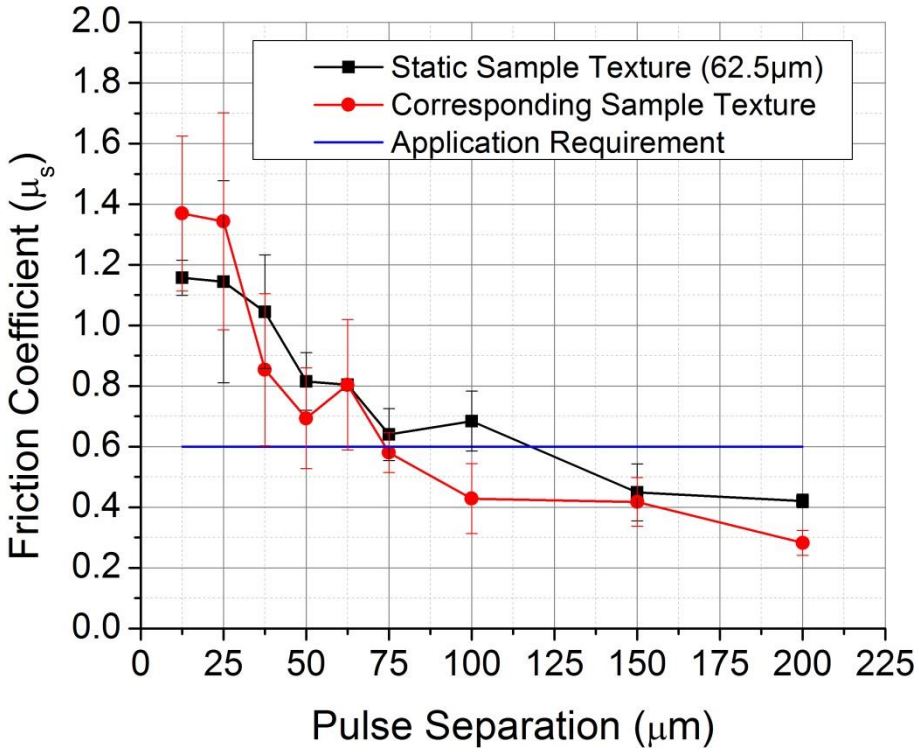

Figure 6.18. Comparison of friction coefficients for samples tested at 50MPa with a constant sample texture of 62.5µm pulse separation and sample textures identical to the counterpart as a function of counterpart texture pulse separation; the solid horizontal line indicates the application requirement of μ_s>0.6

The general trends observed in Figure 6.18 are the same as those discussed in Section 6.4.1 for Figure 6.17; when the constant 62.5µm sample texture is compared to the corresponding sample texture, higher friction coefficients are observed for high pulse separation while lower friction coefficients are observed at low pulse separations. In this case, there is a little more variation around 50µm pulse separation, possibly due to poorer interlocking as a result of the mismatched texture dimensions and limited pressure for deformation. It should also be noted that there is little difference in the friction coefficients, up to $\Delta\mu_s$~0.2, between the static and corresponding sample

textures across the full range of tested pulse separations. This is typically of the order of, or less than, the associated error for the measurements.

6.4.3 Processing Rate

The effect of using a constant texture, for either sample or counterpart, on the overall processing rate and the resulting friction coefficients at 50MPa is shown in Figure 6.19.

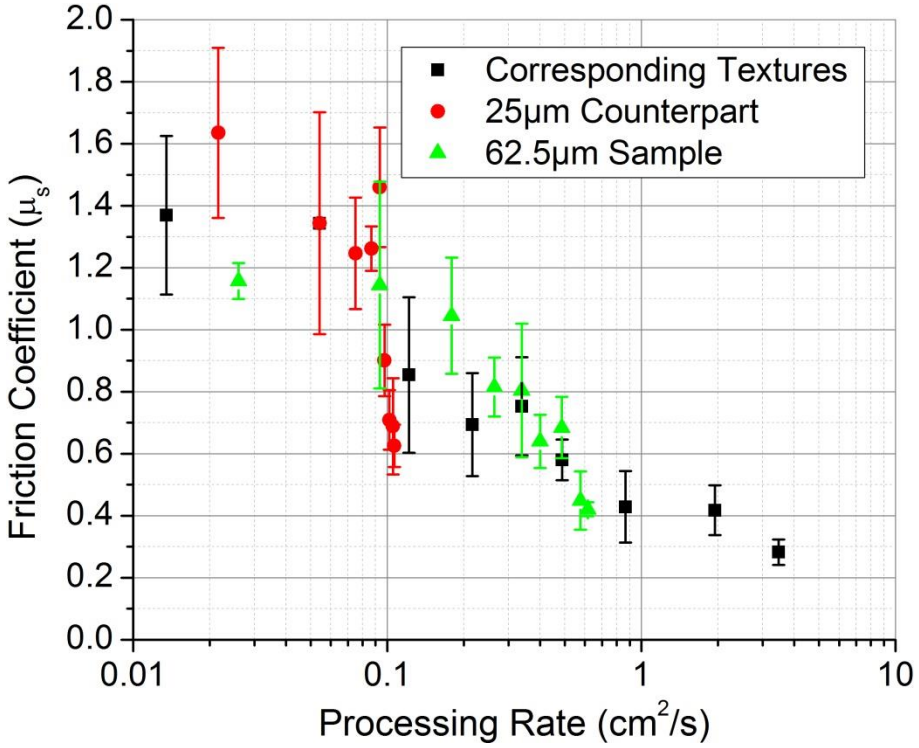

Figure 6.19. Friction coefficient as a function of processing rate for the range of samples tested at 50MPa normal pressure

As a result of the negligible friction improvement, even with the moderate increase in overall processing rate at low pulse separations, the use of a constant sample texture was not found to give the benefits hoped for, as highlighted by Figure 6.19. Therefore, to reduce the complexity of the texturing process, the same texture was generated on both sample and counterpart for all of the following tests. Alternate methods of increasing the processing rate were also considered, with texturing at higher repetition rate examined first, with results presented in Section 6.5.

6.5 Processing Repetition Rate

In order to test the texturing of both surfaces at increased repetition rate, the laser set-up was reverted back to the 50W HS-S. As the optical and pulse properties are nominally

equivalent to those of the 20W EP-S (nominally the same beam quality, spot size and pulse energy/duration), it is reasonable to directly compare the results with the 50W HS-S at 70kHz repetition frequency to the 20W EP-S at 20kHz repetition frequency (14W average power output).

6.5.1 70kHz vs 20kHz at 50MPa Normal Pressure

As a result of increasing the repetition frequency from 20kHz to 70kHz, the laser scan speeds were increased by 3.5× such that the resulting textures maintained the same pulse separation for comparison. Due to limitations with the galvo scan head (max. scan speed ~10,000mm/s), only textures with pulse separations up to 100µm (corresponding to 7,000mm/s) were processed. The results of the friction tests involving these textures are shown in Figure 6.20.

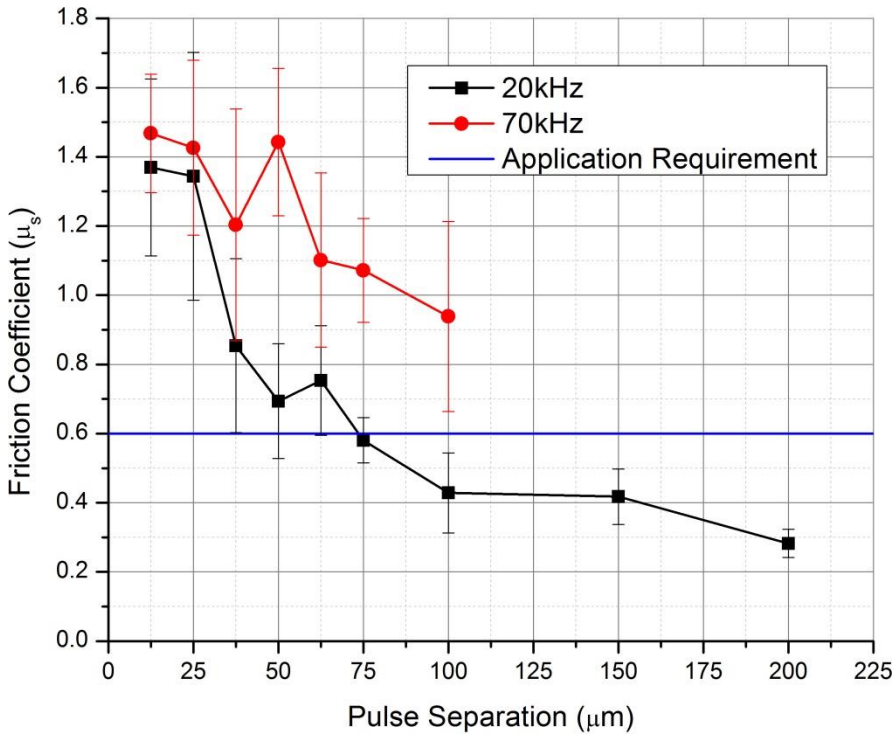

Figure 6.20. Comparison of friction coefficients for samples tested at 50MPa with textures generated with 20kHz and 70kHz repetition frequencies. The solid horizontal line indicates the application requirement of μ_s>0.6

Contrary to the results presented in Section 4.7.5, where the increased repetition frequency was found to have a (slightly) detrimental effect on the friction coefficient, here the increased PRF increased the friction coefficient as well as the processing rate, as shown in Figure 6.20. At the increased PRF of 70kHz, average friction coefficients only fell below 1 at *s*=100µm, with several textures consistently above μ_s>1.2 at 50MPa

normal pressure. This result was somewhat unexpected – the increased PRF was expected to have little effect on the resulting friction coefficient, due to the change in friction mechanism (interlocking vs. embedding in Section 4.7.5). It is possible that the change in laser and optics also changed some of the optical properties of the system (such as spot/crater size; Φ~90µm) and some material properties (hardness, roughness, etc.), causing the observed increase in friction coefficient. However, it is clear that the increased repetition rate does not impact the friction coefficient negatively whilst increasing the processing rate by 250%.

6.5.2 Processing Rate

Following this result, the friction coefficients were then plotted against the processing rate, as shown in Figure 6.21.

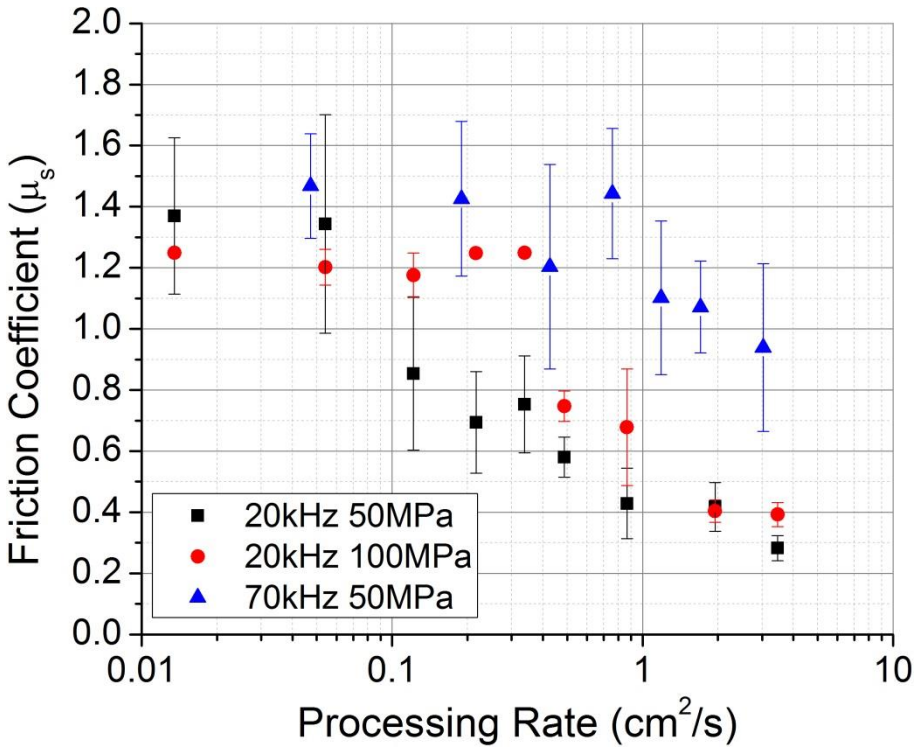

Figure 6.21. Friction coefficient as a function of processing rate for textures fabricated with 20kHz and 70kHz repetition frequencies using identical textures on sample and counterpart

From the results shown in Figure 6.21, it is clear that high friction coefficients (μ_s>0.8) are consistently achievable at moderate processing rates of greater than 1cm^2/s (>0.36m^2/hour). It should be noted that the speeds quoted here are theoretical and do not account for the time required to move between lines or move samples (for larger parts). However, it is possible to increase this processing rate further by texturing both surfaces of the interface in parallel (a two-fold speed increase) and using an even higher

PRF of 100kHz or more (different laser/optic set-up required) in order to utilise the maximum scanner speed of 10,000mm/s (a further 43% speed increase). As a result, it is expected that process speeds of at least 2.85cm^2/s (>1m^2/hour) while maintaining friction coefficients above 0.8, or 8.5cm^2/s (>3m^2/hour) while maintaining friction coefficients above 0.6 are achievable without complicating the texturing process significantly. For further improvements to the processing rate, it may be possible to use multiple lasers/beams in order generate different sections of each texture in parallel.

6.6 Pulse Duration Comparison

The effect of varying pulse duration was also studied. Using the maximum pulse energy available from the 20W EP-S laser, identical texture designs were processed with two different pulse durations at 20kHz PRF. The resulting textures were friction tested at two normal pressures, 100MPa and 50MPa, and analysed using optical microscopy.

6.6.1 100MPa Normal Pressure

Figure 6.22 shows the friction results for a range of textures generated with both 490ns and 220ns pulses (the two extremes available whilst maintaining the maximum pulse energy of 0.71mJ) and tested at 100MPa normal pressure.

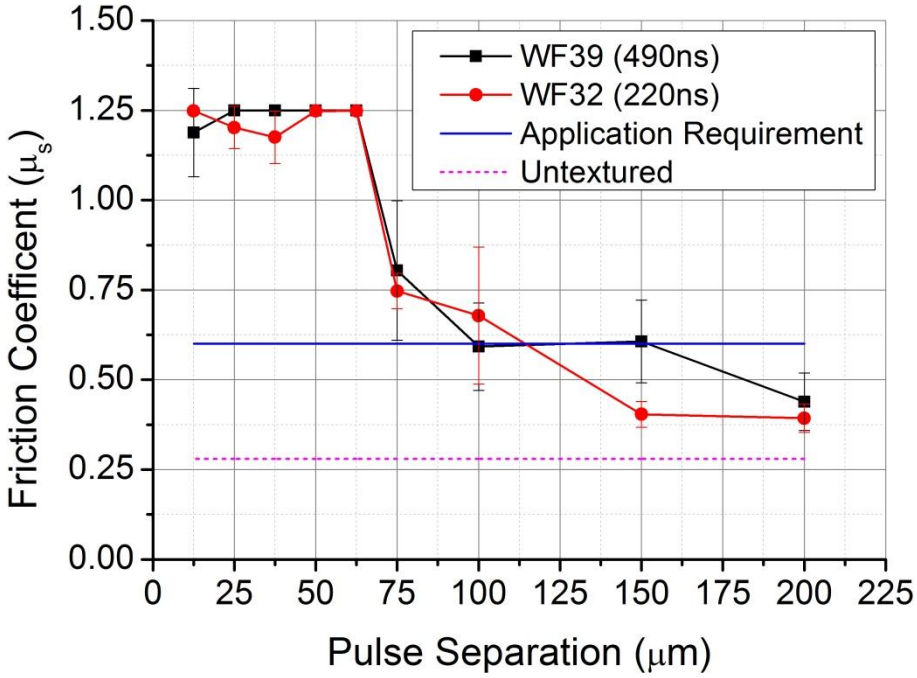

Figure 6.22. Comparison of friction coefficients for samples tested at 100MPa with textures generated with pulse durations of 490ns and 220ns. The solid horizontal line indicates the application requirement of μ_s>0.6, the dotted horizontal line indicates the friction coefficient of the untextured samples

The comparison between textures generated using 490ns and 220ns pulses, shown in Figure 6.22, indicates that the pulse duration has little impact on the resulting friction coefficient, although the results for pulse separations <75µm are undetermined due to the measurement limit. This is somewhat surprising, given that longer pulse durations were found to give deeper troughs and rougher surfaces in Section 3.4.2 (Figure 3.21 and Figure 3.22) which were expected to increase the friction coefficients in this regime where both surfaces are textured but relatively soft (~300HV30). However, the effect of the increased roughness may be masked due to the measurement limitations (observed at pulse separations <62.5µm) or the high normal pressure greatly deforming the textures, minimising the impact of the longer pulse duration.

6.6.2 50MPa Normal Pressure

In order to eliminate, or at least reduce, these two issues, the same textures as used in Section 6.6.1 were then investigated at the lower normal pressure of 50MPa.

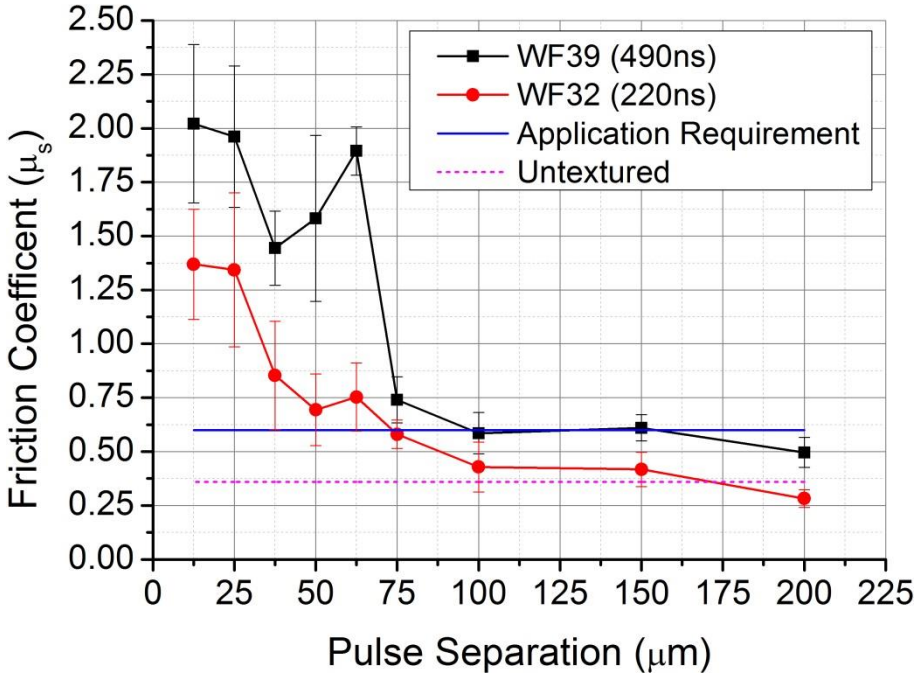

Figure 6.23 Comparison of friction coefficients for samples tested at 50MPa with textures generated with pulse durations of 490ns and 220ns. The solid horizontal line indicates the application requirement of μ_s>0.6

In contrast to those obtained in Section 6.6.1, the results of friction testing at 50MPa normal pressure, shown in Figure 6.23, indicate a significant difference in friction coefficients between the 220ns and 490ns textures. The textures generated with the longer pulses result in significantly higher friction coefficients, especially at low pulse separations ($s \leq 62.5\mu m$) where average friction values are consistently >0.5 higher than those obtained with 220ns pulses, up to $\mu_s \sim 2$. This is a slightly larger increase than was anticipated, however it is more in line with the expectations discussed in Section 6.6.1, with increased surface roughness resulting in increased friction coefficients.

6.7 Roughness Dependence

Following the results obtained with textures generated with 490ns pulses and those at 70kHz repetition rate, the effect of the surface roughness on the resulting friction coefficient was revisited. Only friction tests performed at 50MPa normal pressure were considered (in order to avoid the issue of limited friction resolution at 100MPa). Figure 6.24 shows the friction coefficients as a function of surface roughness (S_a) for each of the sample textures.

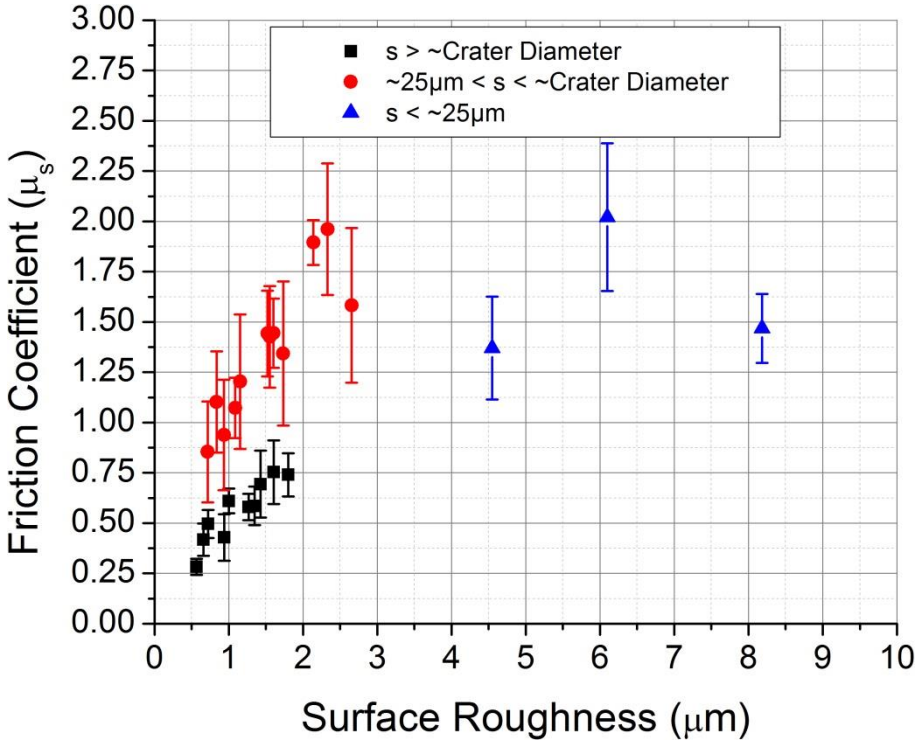

Figure 6.24. Friction coefficients (measured at 50MPa normal pressure) as a function of arithmetic average surface roughness (S_a), with three different regimes highlighted

As shown in Figure 6.24, the dependence of the friction coefficient on the surface roughness can be separated into three different regimes, based on the laser texturing process parameters. For large pulse separations (*s*>crater diameter), roughness is low with a noticeable contribution from the original (S_a~0.4µm) ground surface (surface has large areas which are unaffected by the laser pulses). For these textures, the obtained friction coefficients are low but increase rapidly with increasing roughness (decreasing pulse separation). As the pulse separation decreases to less than the crater diameter (~25µm<*s*<~crater diameter), the surface roughness measures decrease slightly (as seen in Figure 6.14) however there is an increase in the number of features available for interlocking due to the increased number of pulses, and therefore craters, resulting in even higher friction coefficients. As the pulse separation decreases further (*s*<25µm), the surface becomes increasingly rough (S_a>3µm) at which point the roughness begins to have reduced effect on the friction coefficient. This is likely due to reaching the point where the applied normal force is already able to deform the surfaces for near complete contact. Increasing the roughness further (by further decreasing the pulse separation) would be expected to decrease the obtained friction coefficients by limiting the real contact (as previously alluded to in Section 4.7.1, Figure 4.23).

6.8 Low Normal Pressure (25MPa)

In addition to the normal pressures already considered, further reduction of the normal pressure may be beneficial for future applications. This is particularly likely to be the case where components are relatively small and the application of very high normal pressures is not possible. Therefore, tests were carried out using a normal pressure of 25MPa (10kN force) on textures which generated high friction coefficients at 50MPa normal pressure (*s*=25µm, PRF=20kHz, 490ns pulse duration). The resulting load-extension curves for these tests can be seen in Figure 6.25.

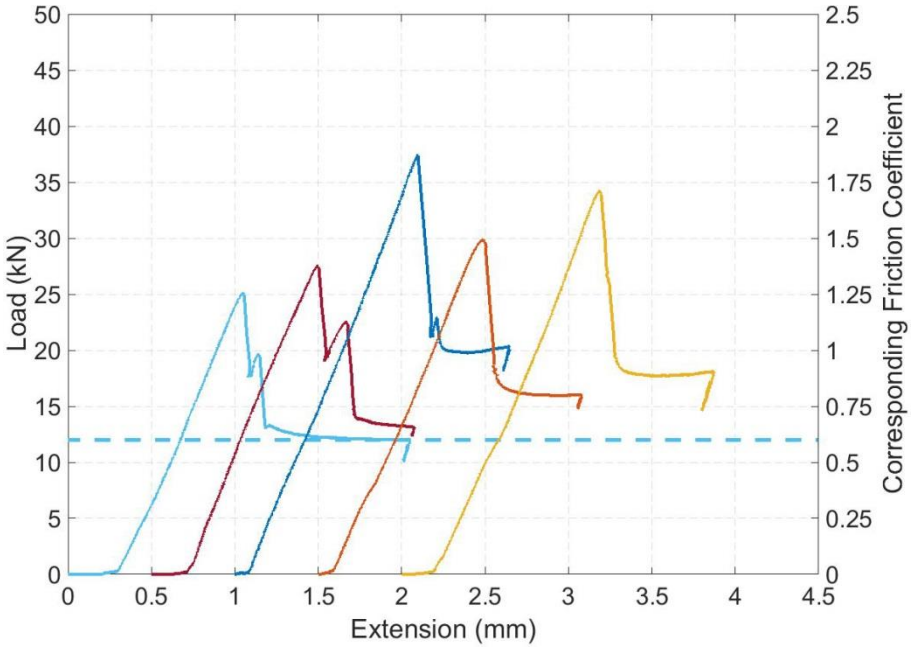

Figure 6.25. Load-extension curves for five samples tested at 25MPa normal pressure; PRF=20kHz, *s*=25µm, 490ns pulse duration

The load-extension curves presented in Figure 6.25 clearly show high friction coefficients with very large, distinct slip points. The average friction coefficient obtained for the five samples tested was calculated as μ_s=1.54 with a standard deviation of σ_μ=0.25, compared to μ_s=1.96±0.33 for samples with identical texturing but tested at 50MPa normal pressure. A decrease in average friction coefficient was expected, due to less deformation of the surfaces. Although the average friction coefficient was found to decrease by ~0.4, the friction coefficient is still very high, suggesting that the surfaces interlock well without significant deformation. Due to limitations with time and the application of the normal pressure (resolution of ±2.5MPa, ±1kN) further tests at even lower normal pressure were not performed, though more testing would be beneficial in

this area in order to determine the minimum pressure required for a given application/friction coefficient.

6.9 Applications

As the technique investigated in this chapter requires direct laser texturing of both mating surfaces, potential applications are somewhat more limited than those discussed in Chapter 5. This is at least the case at this experimental stage where direct laser texturing of large components is not practical; however, one possible application involving a small drive shaft assembly has been proposed by MDT.

6.9.1 MDT Drive Shaft Assembly

In this application, the drive shaft is a safety device which connects a pump to a gear. If the pump generates too much torque, the friction disc is to slip, overloading a shear nut and thus disconnecting the components and relieving the normal pressure. Therefore, the friction coefficient must be high enough such that premature slippage is avoided but not so high that enough torque is transmitted to damage the gear without slippage/failure. This is different from the previously discussed applications where the aim was to achieve as high friction coefficient as possible. It expected that, by choosing appropriate laser textures for both surfaces of the contact, the desired friction coefficient can be achieved without facilitating damage of the assembly by overloading. A schematic of the drive shaft assembly is shown in Figure 6.26.

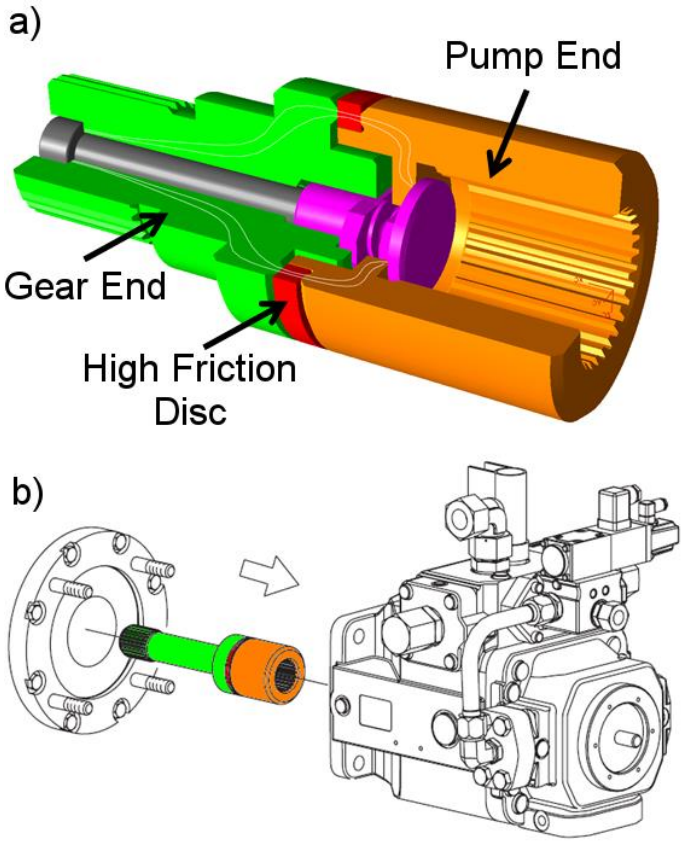

Figure 6.26. (a) Schematic of the driveshaft, highlighting the location of the friction disc in red in relation to the pump and gear ends and (b) the location of the driveshaft assembly within the larger pump housing

6.10 Summary & Conclusion

The tests and results discussed in this chapter were designed to investigate the effect of laser texturing both surfaces of a contact. The change from single surface texturing to the texturing of both contacting surfaces was expected to change the friction regime, from adhesion/embedding to an interlocking regime, resulting in the generation of high friction coefficients without requiring additional hardening processes. As this technique is best suited to contacts without an intermediate shim component, it is expected to be used for applications with smaller and easier to texture contact geometries, however increasing the laser processing rate was still carefully considered.

The initial friction tests with texturing on both contacting surfaces gave very promising high friction coefficients of μ_s>1.25 at 100MPa normal pressure, despite exhibiting several micro-slips in the load-extension curves. Top-down and cross-section microscopy indicate that the high friction coefficients are obtained due to significant plastic deformation, and subsequent interlocking of the surface features, achieved by the high normal pressure. Following further analysis, the micro-slips (<50µm movement) were deemed to be minute realignments of the textures, resulting in improved

interlocking of the surfaces. Undoubtedly, there are applications for which such movements are not tolerable. However, given the minimal slipping and consistent subsequent friction coefficients, such micro-slips were deemed acceptable and excluded from the friction coefficient calculations.

For both normal pressures (100MPa and 50MPa), friction coefficients μ_s>1.25 were obtained at low pulse separation before sharply dropping at *s*~70µm and *s*~30µm respectively. These fall offs are attributed to the decrease in available asperities and features for interlocking with each other, with the effect being more pronounced for the 50MPa tests due to the lack of pressure available to deform the textures. Despite this, average friction coefficients above μ_s>0.6 were obtained at 75µm and 62.5µm pulse separation for 100MPa and 50MPa normal pressures, respectively. Excluding the results limited by the load force supplied by the hydraulic press, friction coefficients were consistently higher for the tests performed at the higher normal pressure, further implying that the friction mechanism is interlocking due to plastic deformation. Tests involving polished surfaces (increasing the real contact area without texturing/interlocking) and the 'overloading' of the normal pressure on textured samples confirmed this to be the case.

Friction tests with mismatched pulse separations on the sample and counterpart textures further consolidate the idea of deformation and interlocking, and indicate that high friction coefficients can be obtained given that at least one of the contacting surfaces provides enough surface features and asperities for interlocking. In this way, the speed of the texturing process can be increased in certain cases, in comparison to the corresponding texturing, by allowing one texture to have high pulse separation (sparse features, quick to texture) whilst the other has low pulse separation (dense features, slower to texture). However, this strategy was found to be of limited use as at least one surface was required to be textured with a low pulse separation (relatively slow). Use of the same texture on both mating surfaces was therefore deemed the most effective method for generating high friction surfaces in the shortest time.

Unexpectedly, increasing the PRF from 20kHz to 70kHz was found to increase the friction coefficient by a modest amount for pulse separations >25µm; possibly due to the change in laser processing set-up (50W HS-S compared to 20W EP-S) rather than the repetition frequency itself. Regardless, the increase in PRF clearly did not have a

detrimental effect on the friction coefficient in this case, unlike in Section 4.7.5. Therefore, process scaling through increased laser pulse repetition frequency is feasible, making the texturing of both contacting surfaces more attractive for industrial applications.

In addition to this, the duration of the pulses used for the laser texturing process was found to have a significant impact on the resulting friction coefficient. Whilst indistinguishable at the higher normal pressure of 100MPa (due to the hydraulic press limitations), at the lower normal pressure of 50MPa, the longer (490ns) pulses were found to greatly increase the friction coefficient, up to μ_s~2 at low pulse separation, and consistently >0.5 greater than the shorter (220ns) pulses across all tested pulse separations. This is assumed to be due to the increased roughness obtained with the longer pulses, as discussed in Section 3.4.2.2, providing more features for interlocking, thus increasing the static friction coefficient.

With the intention of opening up this method of generating high friction textures to a wider range of applications, preliminary tests were performed on samples at low normal pressure of 25MPa. Despite a modest decrease in friction coefficient from μ_s=1.96 at 50MPa to μ_s=1.54 at 25MPa, consistently high friction coefficients were still obtained, implying that the normal pressure can be reduced further whilst maintaining friction coefficients >0.6. However, further work must be carried out in this area in order to confirm how low the normal pressure can be dropped.

Following the results presented in this chapter, it is evident that laser texturing of both contacting surfaces is an excellent technique for increasing the static friction coefficient of an interface at normal pressures up to 100MPa. With the selection of appropriate texturing parameters, friction coefficients of $\mu_s \geq 2$ are achievable, albeit at low processing rates (<0.06cm^2/s for the parameters/set-up used). For industrial applications, where high processing rate is important, static friction coefficients of μ_s~1 with processing rates of >1cm^2/s have been shown and μ_s>0.6 consistently obtained with speeds of >3.5cm^2/s. Furthermore, it is expected that additional improvements to the friction coefficient and processing rate can be obtained by the following:

a) Further increasing the laser pulse repetition frequency and pulse energy (currently limited by the laser power/desired pulse energy)

b) Using long/longer pulse durations to maximise the number of features available for interlocking for a given pulse separation (limited to 490ns by the laser)
c) Optimising the pulse separation (and spot size) of the two textures and possibly increasing the pulse separation in combination with the changes listed above (currently limited to ~140µm at 70kHz due to maximum scanner speed of ~10,000mm/s)
d) Using two (or more) lasers for simultaneous texturing of both surfaces or different parts of each texture with a different laser (currently one laser is used to texture both components in series)

Based on the results presented in this chapter and assuming that the repetition frequency can be increased to 100kHz (43% increase in process speed) and that two lasers are used in parallel for each surface (100% increase in process speed), friction coefficients μ_s>0.6 are expected to be achievable at industrially relevant processing rates of ~10cm^2/s prior to optimising pulse separations and pulse durations.

In order to make the process even more attractive for industrial applications, an obvious first step for future work following these results would be an investigation into the four points mentioned in this summary (a-d). However, as implied in Section 6.8, an investigation into the friction at lower normal pressures could also yield important and relevant results.

Chapter 7 – Laser Beam Shaping

This chapter concerns the use of custom beam shaping optics for the modification of the spatial intensity of the laser beam for use in surface processing applications. In collaboration with PowerPhotonic, the integration of two different types of fused silica beam shaping optics into a typical commercial/industrial laser processing system was investigated. Finally, attempts were made at machining and polishing with the modified laser beam with some comparisons to the unmodified Gaussian beam profile.

7.1 Rationale for Laser Beam Shaping

Beam shaping techniques attempt to generate arbitrary laser intensity profiles and they can be used to facilitate possible improvements in laser processes and process efficiency. Such profiles typically deviate significantly from the standard Gaussian profile, e.g. square and circular flat top profiles or even more complex shapes such as donut shaped intensity profiles. As a result, the laser-material interaction can change substantially depending on the intensity profile [124, 125]. In particular, laser polishing is expected to benefit from using a top hat profile compared to a Gaussian profile by eliminating the majority of the melt flow effects caused by the temperature induced surface tension gradients [38] and minimising evaporation pressure associated with non-uniform intensity beams.

Two different optical beam shaping systems were incorporated into the SPI laser processing workstation discussed in Section 3.1 and tested separately, with further details presented in Sections 7.3 and 7.4. Both of these systems are referred to as 'field mappers', which refract the beam into the desired intensity profile. The performance of such beam shapers can be estimated by the calculation of the (dimensionless) beta factor:

$$\beta = \frac{2\sqrt{2\pi} \cdot r_{beam} \cdot r_{spot}}{f \cdot \lambda} \quad (7\text{-}1)$$

where r_{beam} and r_{spot} are the radius' of the collimated beam and focal spot respectively, f is the focal length of the focussing lens and λ is the laser wavelength [126]. The resulting beta value gives an indication of the beam shaper performance according to the following table:

Beta Value	Resulting combined flat-top performance
$\beta < 4$	Unusably poor performance
$4 < \beta < 16$	Diffraction effects present (ripple, intensity peaks at ridge)
$\beta > 16$	Excellent performance

Table 7.1. Combined flat-top performance of field mapped beam shaper for various beta values [126]

As can be seen from Table 7.1 and Figure 7.1 higher beta values result in higher performance beam shaping. The optical elements which perform the beam shaping are fabricated from UV-fused silica, by pulsed CO_2 laser ablation prior to polishing by cw remelting [127], facilitating the shaping of high power beams.

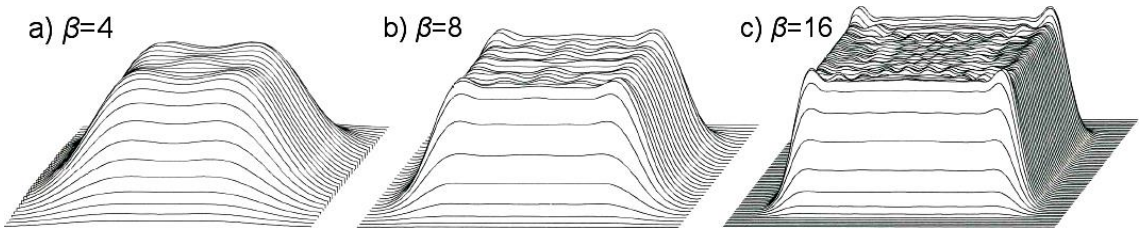

Figure 7.1. Simulated flat-top square beam shapes for a) β=4, b) β=8 and c) β=16 [128, 129]

The beam shapers used in this project were designed for a Gaussian input beam profile with 8mm diameter. Therefore, the 20W EP-S laser was used in conjunction with the 75mm BEC for testing of the beam shaping optics. All beam profiles were measured directly using a CCD camera (iDS imaging uEye SE with Fire-i software) with 1.6µm square pixels after the galvo scanner and F-theta focussing lens. Neutral density filters were used to attenuate the beam in order to protect the CCD from damage.

7.2 Unmodified Gaussian Beam

Prior to inserting the beam shaping optics into the set-up, several measurements were taken with the raw, unmodified Gaussian input beam around focus. Figure 7.2 shows the unmodified beam as measured in the focal plane.

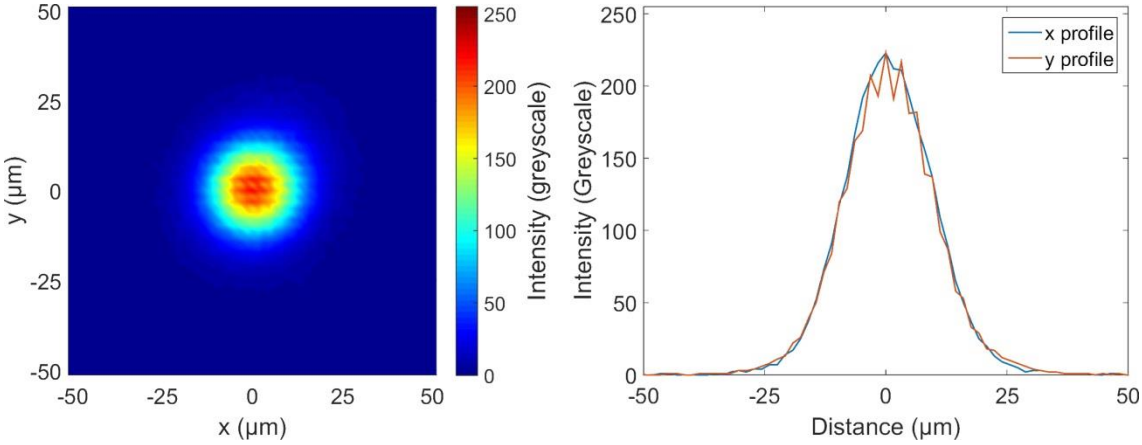

Figure 7.2. Matlab plot of (a) CCD image data and (b) linear profiles through the centre of the beam in x and y for the unmodified Gaussian beam in focal plane

As highlighted by Figure 7.2, the unmodified beam has a Gaussian profile in both x and y directions, with no asymmetry present in the focal plane. The $1/e^2$ beam diameter was measured as ~36µm, slightly larger than the nominal ~30µm expected for a beam with M^2=1.1, but in line with a slightly higher M^2 value of ~1.3. It should be noted that the beam was found to be slightly elliptical when outside of focus.

7.3 Single Optic Beam Shaper

Initial tests with beam shaping were conducted with a single, uncoated optic beam shaper which was inserted into the collimated beam path, as shown in Figure 7.3.

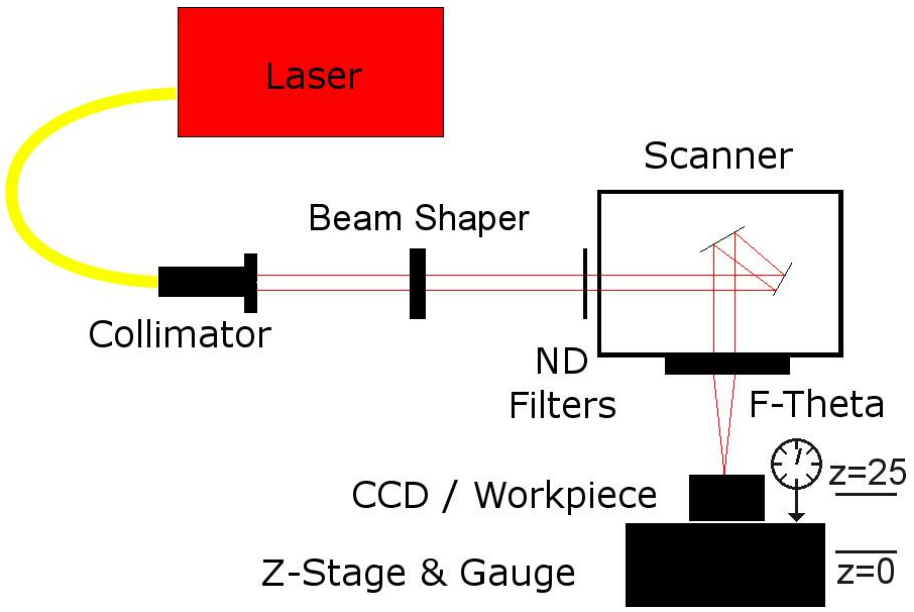

Figure 7.3. Schematic of laser processing set-up with integrated single optic beam shaper

The single optic beam shaper was designed to image a circular flat top beam with a diameter of 2mm (β~235) at the focal plane of the unmodified beam. The evolution of

the output beam profile with varying distance from the nominal focal plane (imaging plane) is shown in Figure 7.4.

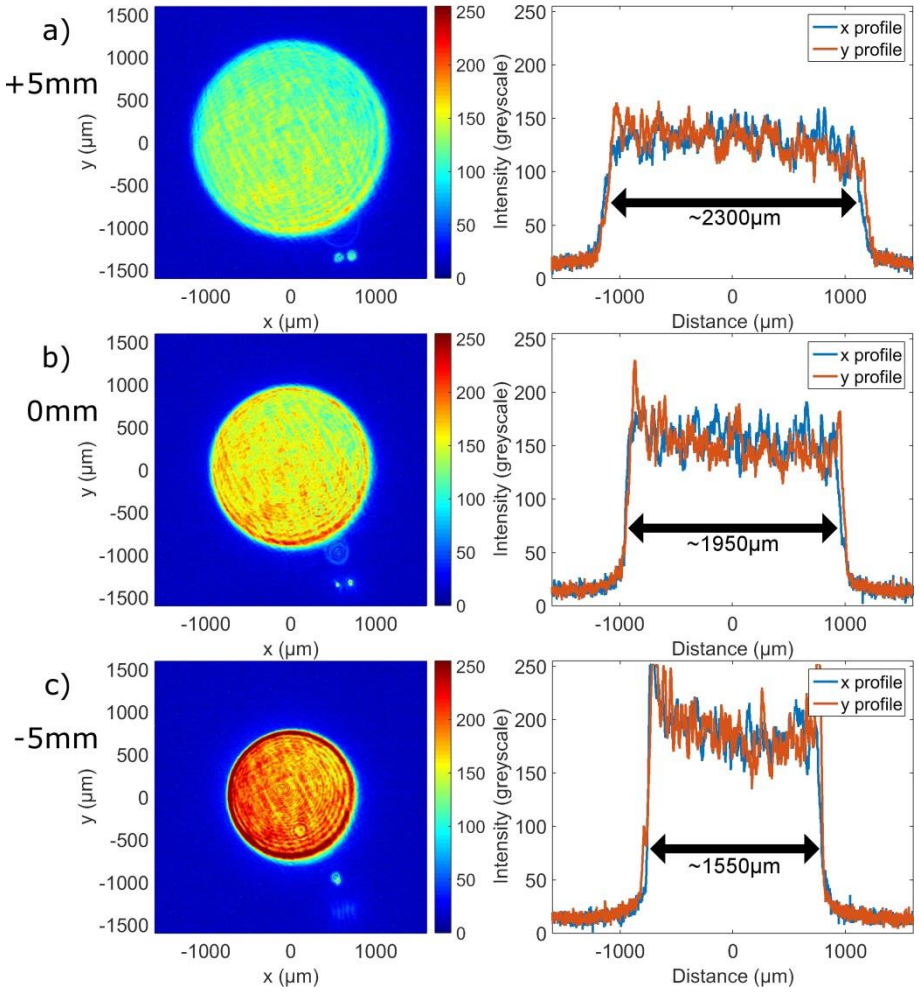

Figure 7.4. Full (left) and cross-section, through (0,0), (right) beam profiles after single optic beam shaper as observed (a) 5mm before the imaging plane, (b) at the nominal imaging plane and (c) 5mm after the imaging plane

As shown in Figure 7.4, the single optic beam shaper generates a very circular, flat-top beam profile with a diameter of ~2mm at the nominal imaging plane. As the beam moves away from the imaging plane, the beam profile remains circular although the diameter varies significantly (~75µm/mm) and the profile becomes less 'flat-top'. Despite this, due to the size of the beam, the depth of field is quite large. The small spots observed at the bottom of the beam profiles are the result of multiple reflections from the neutral density (ND) filters used to attenuate the beam prior to focussing on the CCD camera. No further tests were performed with the single optic beam shaper due to the very limited energy density available (~20mJ/cm^2) with this spot size and laser.

7.4 Two-Optic Beam Shaper

Following the positive initial results with the single optic beam shaper, a second beam shaper containing two optical elements was fabricated to provide a smaller beam suitable for laser processing. This was designed to generate a square, flat top beam with 110µm (β~13) sides at the nominal focal plane. The two optics were placed in the workstation as shown in Figure 7.5.

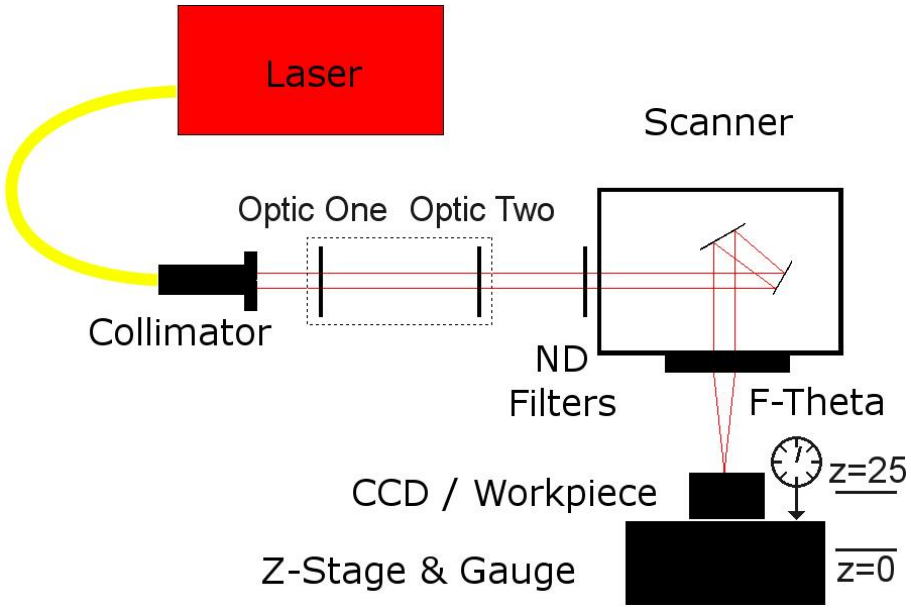

Figure 7.5. Schematic of laser processing set-up with integrated two-optic beam shaper

As with the single optic beam shaper, the beam shaping optics were placed in the collimated beam path, prior to the galvo scanner. Initially, optic one was placed into the system and aligned in x and y directions (see Figure 7.6) such that the measured profile was observed to be symmetrical, indicating that optic one was centred on the collimated laser beam. Optic one was also rotated (manually) at this stage in order to align the square shape with the CCD/workpiece.

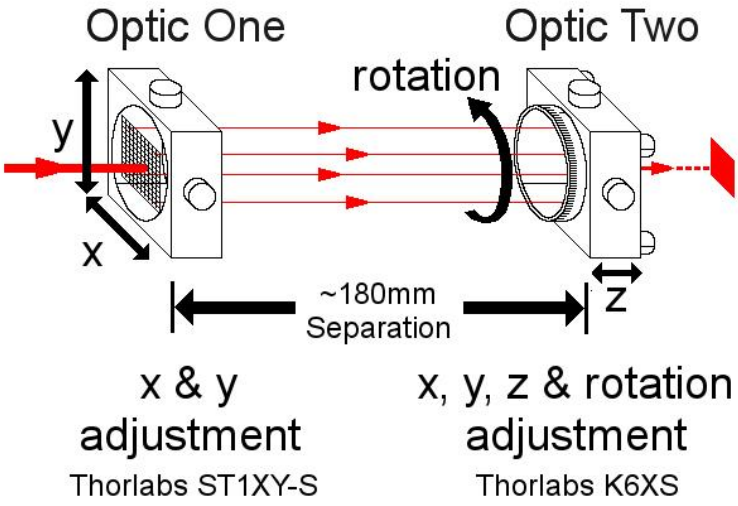

Figure 7.6. Schematic of the alignment of the two beam shaping optics with axes of movement highlighted and labelled

The second optic was then placed into the system, approximately 180mm from optic one. Optic two was then aligned in x, y and rotation until a square, flat top beam was observed. It should be noted that the two beam shaping optics were placed into the system such that the non-flat surface from each optic face each other.

7.4.1 Optic One Only

Two images of the profile resulting from the use of optic one only were taken after the scan head and F-theta lens, with 10mm z separation. The observed profiles are shown in Figure 7.7.

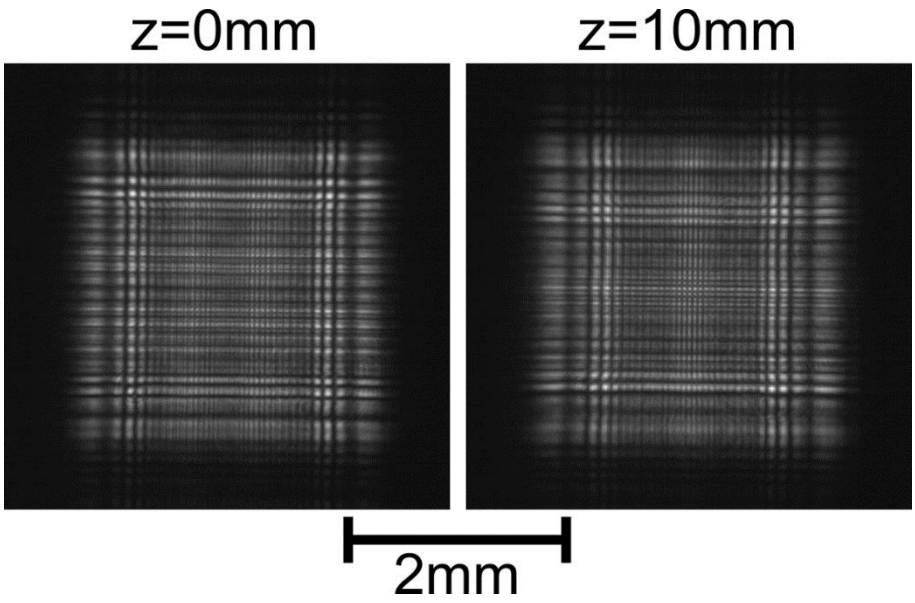

Figure 7.7. Beam profiles for optic one only imaged after scanner and F-theta at two z positions

Both beam profiles presented in Figure 7.7 show a highly symmetrical intensity distribution within a generally square shape, indicating that optic one is well aligned to the collimated beam.

7.4.2 Both Optics

After the second optic was integrated into the system, the x, y and rotational alignment was modified until a nominally square flat top beam was observed. The (somewhat noisy) raw data and cross-sections of the best observed square flat top beam are shown in Figure 7.8.

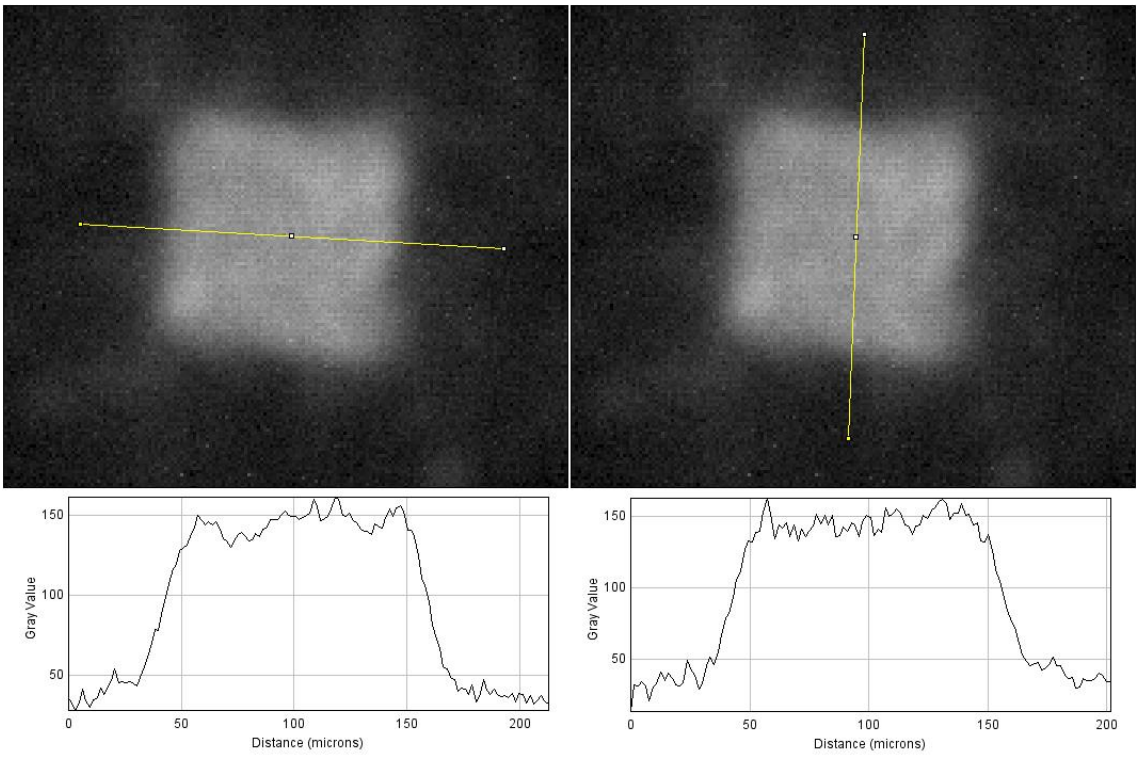

Figure 7.8. Raw data and x and y cross sections for initial square flat top beam profile observed using the two optic beam shaper

Despite the noise in the data, it is clear from Figure 7.8 that a flat top square shape beam is observed with the use of both beam shaping optics. The size of the square profile was measured to be ~120µm, slightly larger than the designed size. The profiles and cross-sections plotted were obtained from the analysis performed with Fiji image processing software. It was noted, however, that this profile was observed several millimetres from the nominal focus of the unmodified Gaussian beam (the expected location of the square flat top) and that the square shape was rotated significantly

compared to optic one alone. Despite this, further tests were performed in order to characterise the system.

7.4.2.1 Depth of Focus

The beam profile was measured over a range of z positions in order to determine the depth of focus. A relatively square flat top beam shape was observed over a range of ±0.3mm, as shown in Figure 7.9.

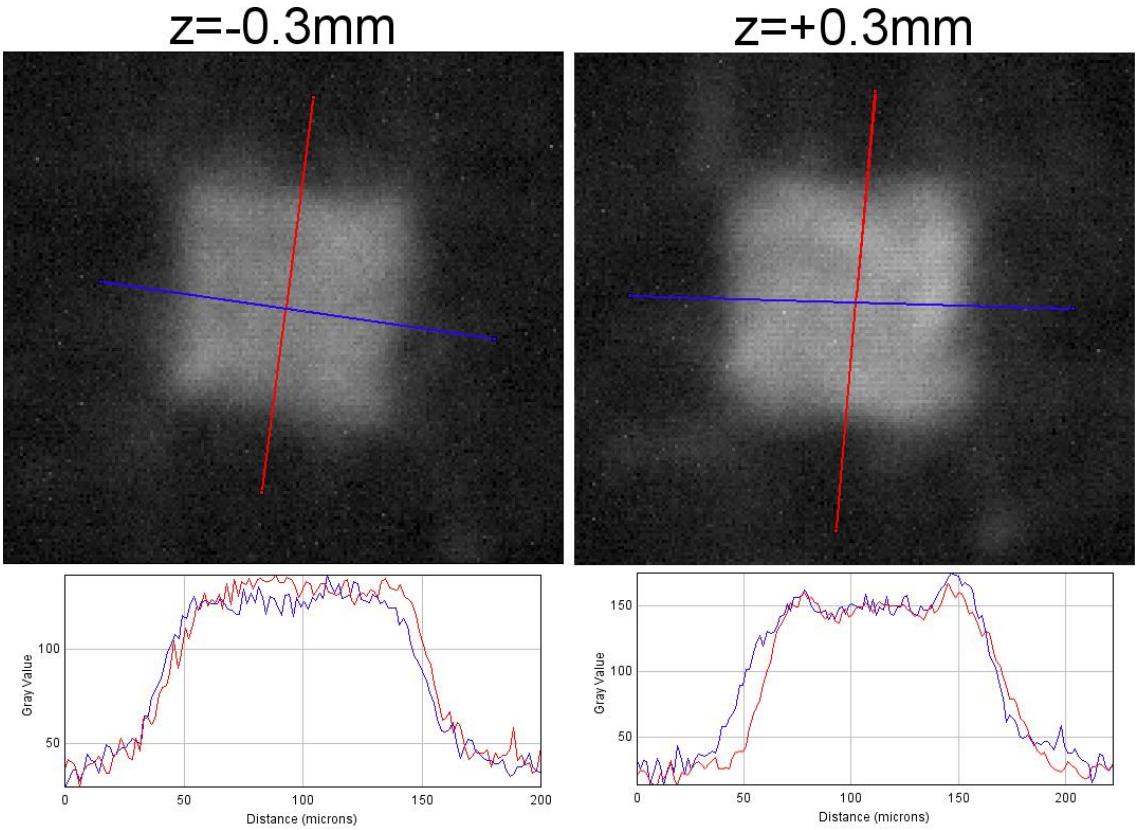

Figure 7.9. Raw data and cross sections for square flat top beam 0.3mm below (left) and above (right) nominal focus

Compared to the beam profile at nominal focus, the profiles observed at z=±0.3mm maintain a reasonable square flat top shape, as shown in Figure 7.9. For comparison, the Rayleigh range (propagation distance over which the beam diameter increases by a factor of $\sqrt{2}$) of the Gaussian beam was calculated to be ~0.7mm. However, for further defocus, the beam profile quickly becomes unrecognisable, losing both the square shape and flat top intensity profile.

7.4.2.2 Power Losses

Power losses in the beam shaping system were then examined, with the power measured after the scanner and F-theta lens both with and without the two beam shaping optics. The measurements obtained from the thermopile power meter (Ophir FL-250A-LP1-SH-V1) are plotted in Figure 7.10.

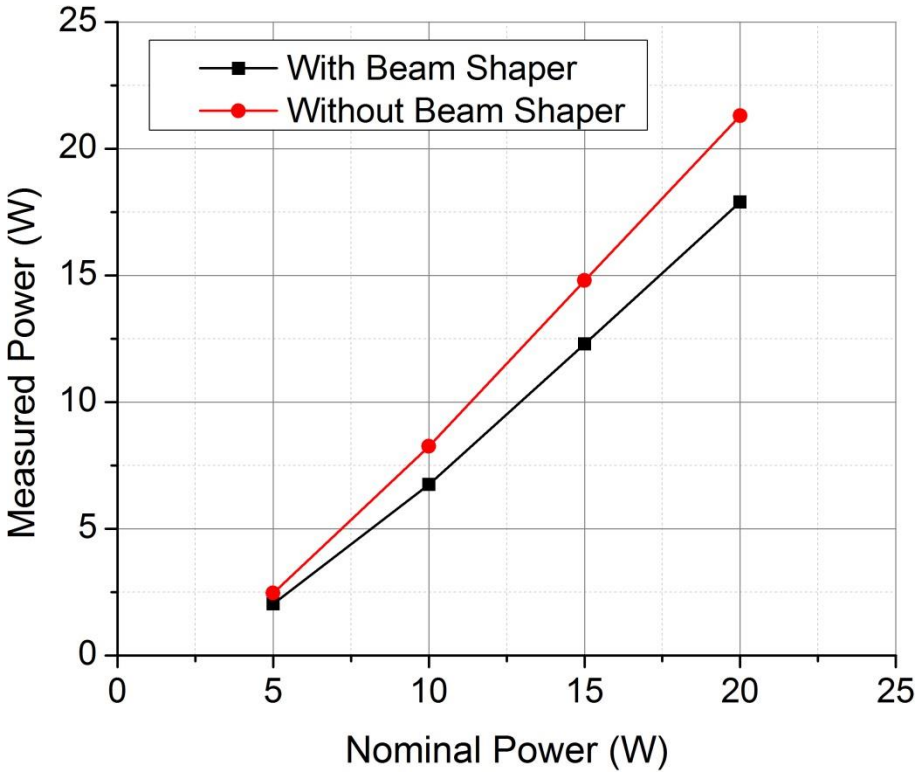

Figure 7.10. Measured power after scan head and F-theta both with and without the two optic beam shaper

The inclusion of the two beam shaping optics results in a significant power loss of 15-20%, depending on the nominal power chosen. A power loss of this magnitude was expected as the optics were not anti-reflection coated. From the Fresnel equations based on air-glass interfaces with normal incidence:

$$R_1 = \left|\frac{n_a - n_g}{n_a + n_g}\right|^2 \tag{7-2}$$

where R_1 is the reflectance from a single interface, n_a is the refractive index of air (~1) and n_g is the refractive index of the glass (~1.5). This gives a reflection of 4% for a single interface. Therefore, the transmission can be calculated as:

$$T = (1 - R_1)^m \tag{7-3}$$

where *m* is the number of optical interfaces. For the two-optic beam shaper, there are four such interfaces and therefore the total theoretical transmission through the system is ~85% (absorption is assumed to be negligible in this case). As a result, the maximum pulse energy calculated to be obtained from the beam shaper was approximately 0.6mJ, giving an energy density of ~5J/cm^2 for an 110µm square spot. In addition to the interface losses, some power is also lost from the main beam into the non-zero diffraction orders and intensity wings, as shown in Figure 7.11.

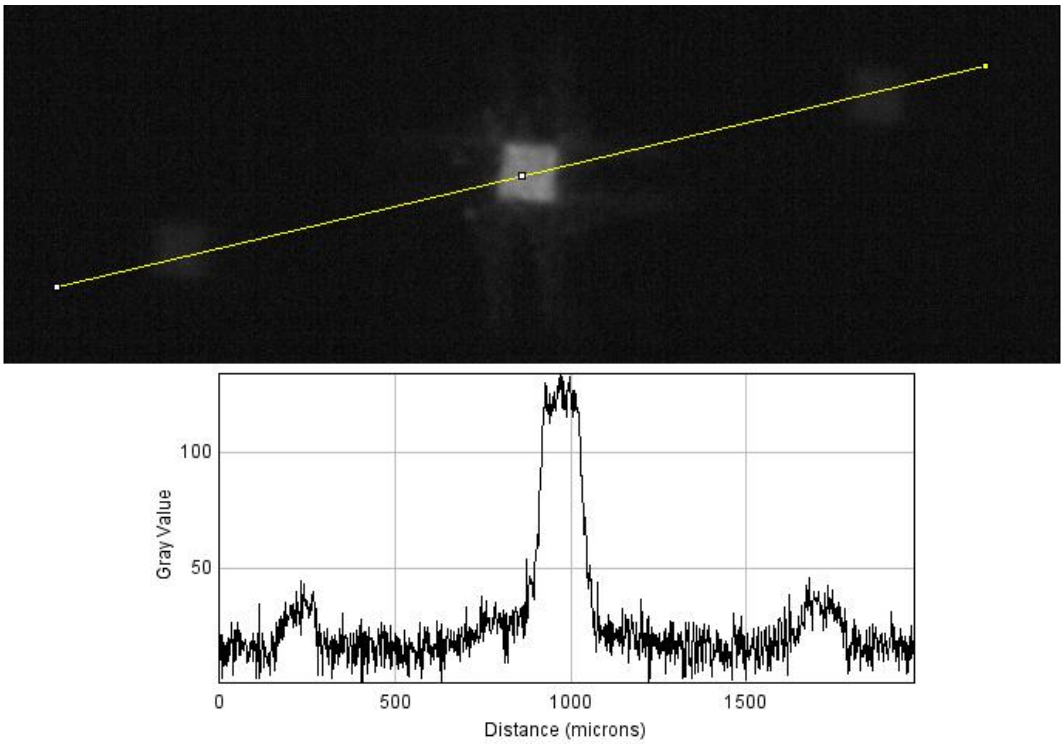

Figure 7.11. Raw profile showing intensity wings around the square beam and highlighting the ±1 diffraction orders

The ±1 diffraction orders, shown in Figure 7.11, were not excluded from the previous power measurement. Therefore, due to these additional losses, the central beam can be expected to have less than 0.6mJ pulse energy (approximately 4-5J/cm^2).

7.4.2.3 Lateral Alignment Sensitivity

Data capture was optimised, including changing CCD and laser settings, in order to improve the poor noise levels observed in the previous results prior to quantifying the alignment sensitivity of the beam shaping system.

First, the alignment sensitivity of optic two in x and y directions was investigated. The beam shaper optics were aligned and the CCD camera moved into the nominal focal

position. The position of optic two was then moved in the x and y directions via the two micrometre thumbscrews on the optical mount (Thorlabs K6XS). Based on the supplier specification of this unit, rotating the thumbscrew by ~10° was calculated to result in a translation of the optic by 7µm. Therefore, the beam profile was measured at the nominal alignment, 7µm and 14µm in both x and y directions, with the measured profiles presented in Figure 7.12.

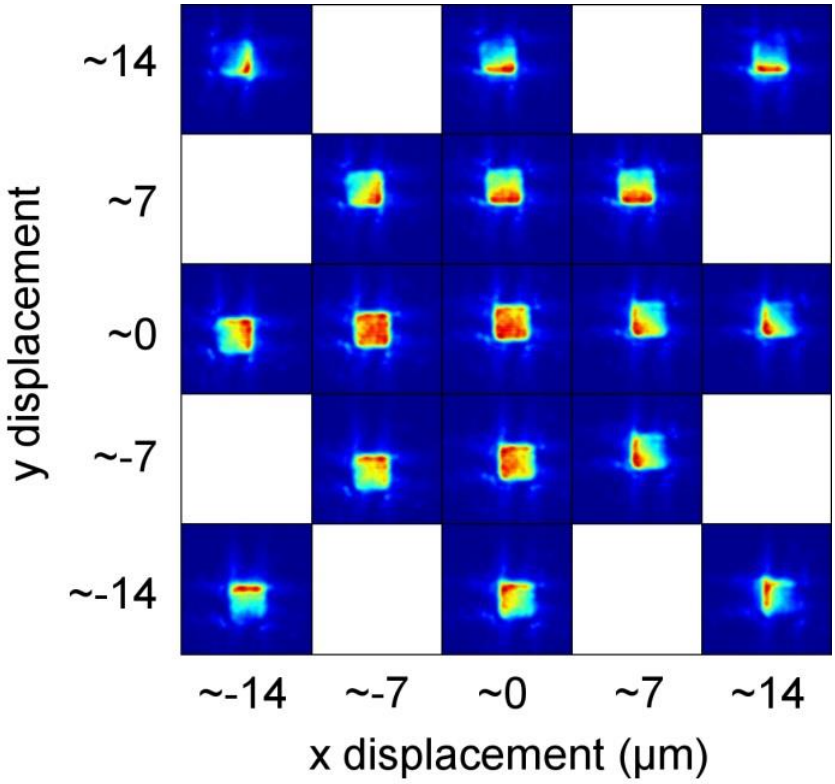

Figure 7.12. Beam profile with varying misalignment of optic two in the x and y directions

From the profiles shown in Figure 7.12, it is clear that the shape of the resulting beam is highly sensitive to the lateral position of the second optic. Displacement of just 7µm can change the intensity distribution from a fairly uniform flat top to a highly skewed intensity distribution. A displacement of ~14µm can result in a complete change of beam shape in addition to further distortion of the intensity profile. Figure 7.12 also indicates that displacement of the optic in the x axis can also affect the resulting profile in the y axis. This is purely due to the scan head, which partially rotates the beam as it is deflected off the two mirrors. Therefore, the x and y axes, denoted for the optic mount (Figure 7.6), are not the same orientation as the normal x and y axes of the CCD images. Finally, as thumbscrews were used to induce the displacement, the absolute value of the displacement for each image is not known accurately due to backlash

within the mount. However, it is still easy to interpret the approximate sensitivity of the beam shape on the lateral position of the second optic from these results.

7.4.2.4 Rotational Alignment Sensitivity

The rotational sensitivity of optic two was also investigated. During previous alignments and measurements, the intensity distribution of the main beam was observed to rotate when the CCD was moved through z, indicating that the two beam shaping optics were not perfectly aligned in rotation. Therefore, after alignment in x and y, the second optic was turned until no rotation of the intensity profile was observed when the z position of the CCD was altered, as shown in Figure 7.13.

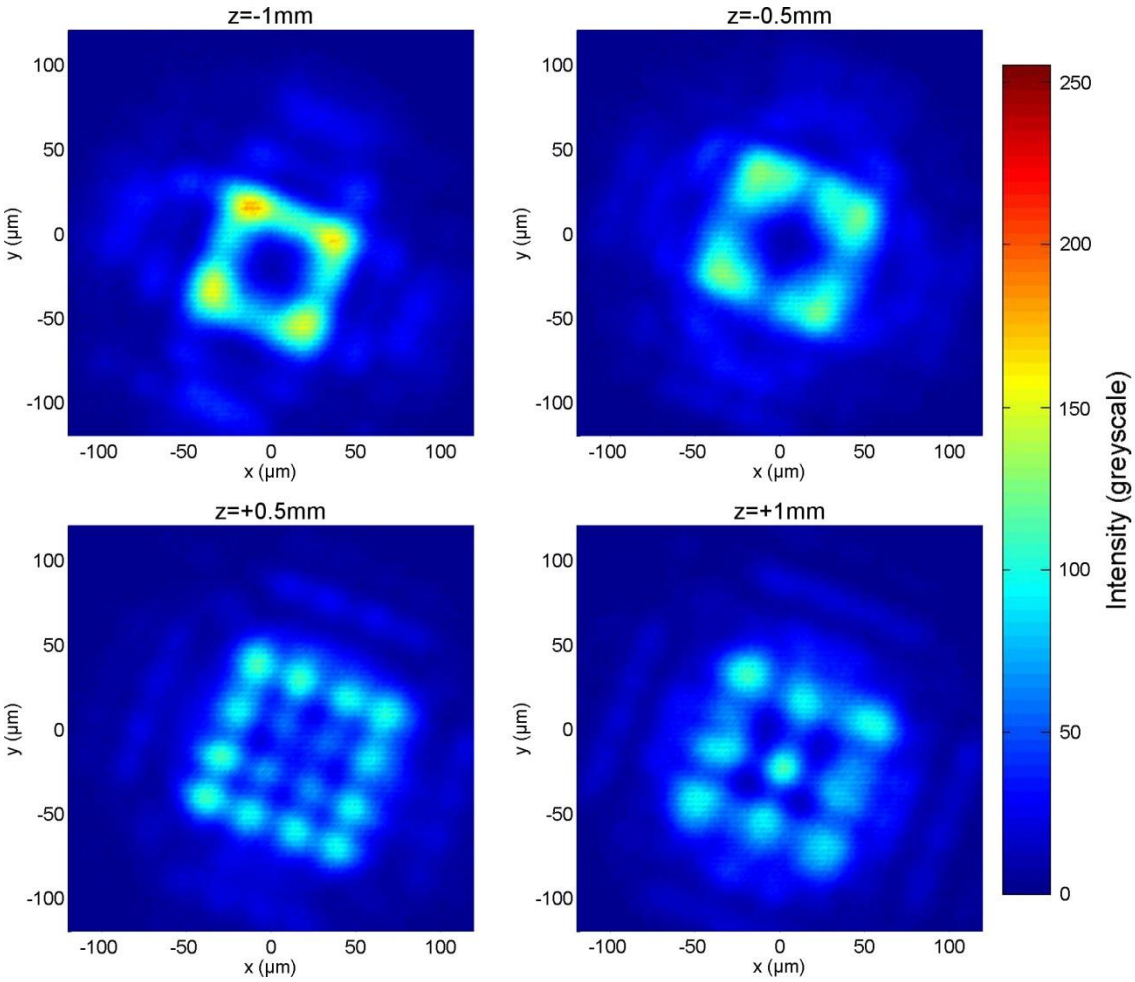

Figure 7.13. Beam profiles at various z positions after alignment in x, y and rotation

In addition to the profiles presented in Figure 7.13, the intensity distribution was observed to maintain symmetry through a wide range of z positions (~25mm scan range). Given that the optics were well aligned, the best square flat top profile was expected to be obtained at the focal plane of the unmodified Gaussian beam.

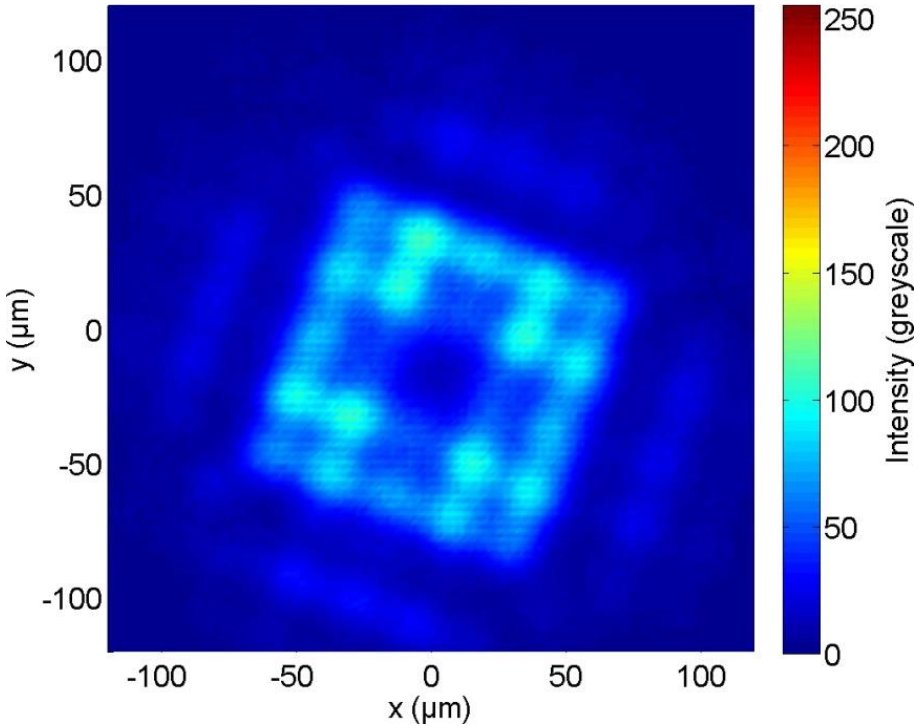

Figure 7.14. Beam shape in expected focal plane (focal plane of unmodified Gaussian beam) after x, y and rotational alignment

However, as can be seen from Figure 7.14, a flat top beam profile was not obtained at this position. As the two optics were well aligned in x, y and rotation, it is believed that this result is due to poor alignment in z, i.e. the two optics were only nominally placed 180mm apart. Given the sensitivity of the optics in the x and y directions, it is highly probable that this is the cause. However, due to a lack of time and poor control over the z-separation in the set-up used, this theory was not investigated. Despite this, the sensitivity of the optics to rotational alignment was studied, with the results plotted in Figure 7.15.

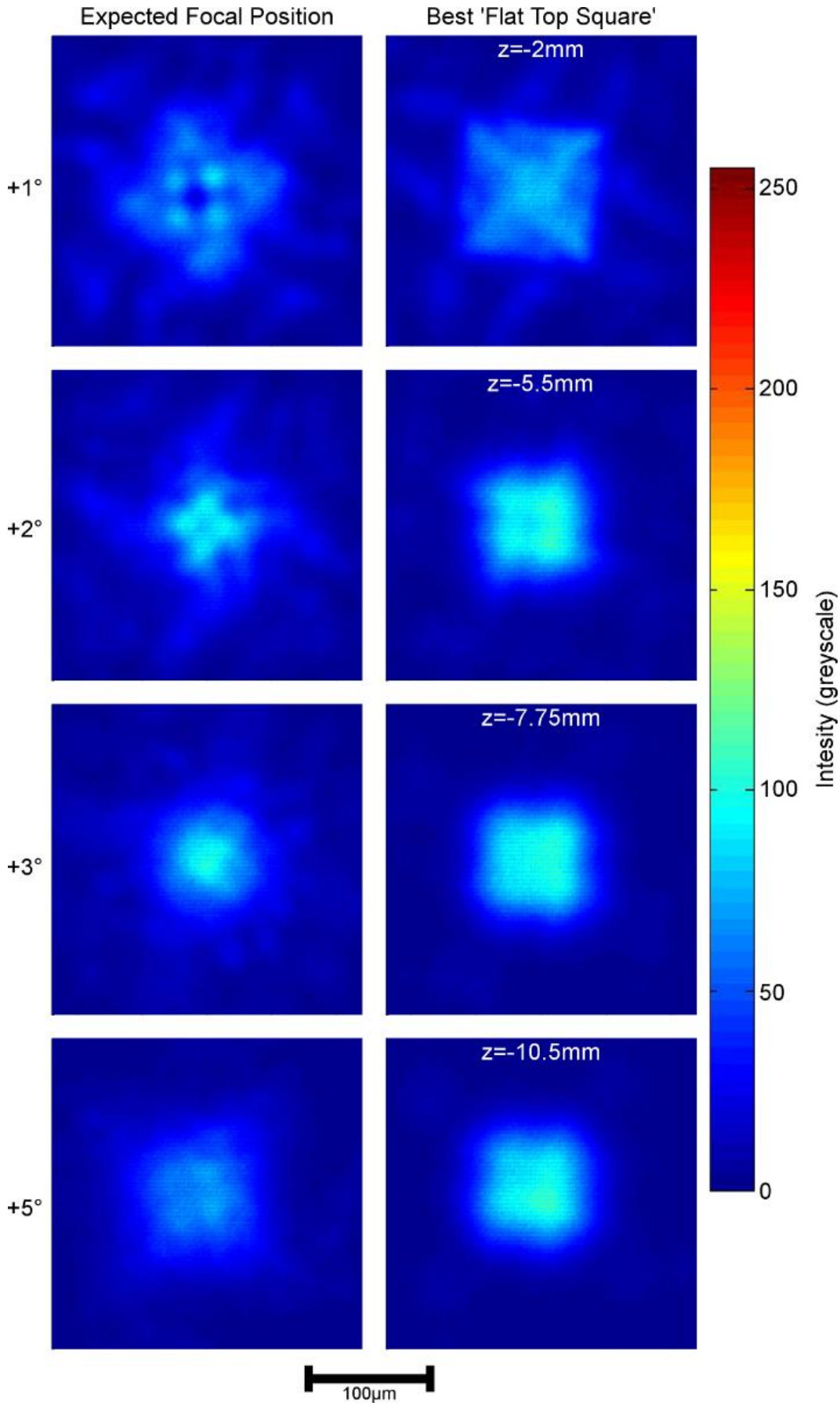

Figure 7.15. Beam intensity profiles for various misalignment angles of optic two (1°, 2°, 3° and 5°) in the expected focal plane (unmodified Gaussian focal plane) and the plane exhibiting the best 'flat top square'

The results shown in Figure 7.15 show that a flat top square profile is not obtained in the expected focal plane, regardless of the rotation of optic two. However, by scanning through z positions after the expected focal plane (below in the experimental set-up, Figure 7.5), more square flat top profiles were observed. This implies that, although not ideal, it is possible to compensate for inaccurate z-separations of the two optics by deliberately rotating optic two relative to the aligned position. A rotation angle of 3-5° was observed to result in the best square shape at a z-position 7.75-10.5mm after the expected focal plane. Following the rotation measurements, a misalignment of 5° was chosen and realigned in x and y before performing further tests.

7.4.2.5 Scan Head Deflection Sensitivity

If a shaped beam is to be used for industrial processes, it is important that it can be translated over a large area without significant distortion. Therefore, using the same set-up shown in Figure 7.5, the beam was deflected by the scan head for a range of x and y displacements. Although the scanner company quotes a working area of ~110mm square for the optics used, typically only the central 80-90% is used in order to avoid undesirable edge effects (defocus, elongation, etc.). As a result, the square flat top beam was measured over an area covering 100mm of the working area, with the profiles shown in Figure 7.16.

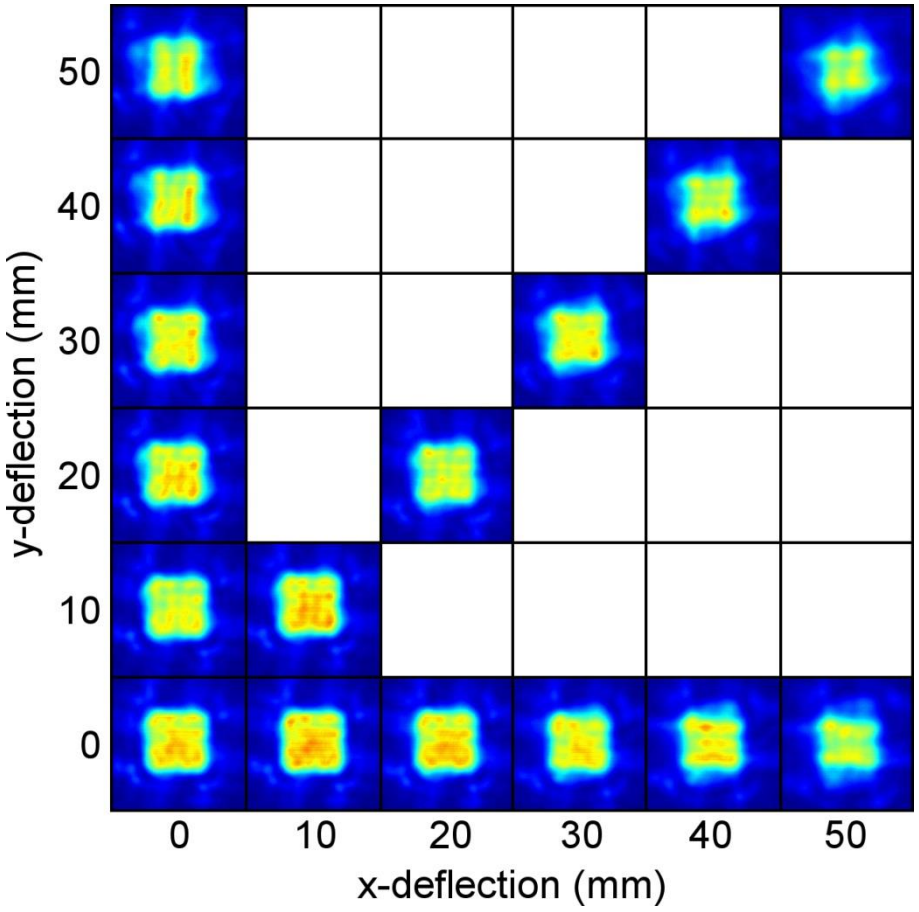

Figure 7.16. Beam profiles of the square flat top after varying x and y deflections by the scan head; deflection values are values set in the SCAPS scan head control software

A good square flat top beam was observed near the centre of the scan field (no deflection) and became more distorted as the beam was deflected towards the edge of the scan field, as shown in Figure 7.16. A square beam with a relatively flat top intensity profile was observed at deflections of up to 30mm in both x and y directions, resulting in a total usable scan area of ~60mm×60mm. Beyond 30mm deflection in either x or y, the shape of the beam became stretched (in the respective direction), giving a rectangular beam shape. When both x and y deflections exceed 30mm the resulting beam remains relatively square although the intensity profile of the beam was clearly no longer flat.

7.4.3 Machining Trials

Machining trials were performed with the square flat top beam on two different materials. First, a glass substrate coated with a thin (~250nm) chromium layer was machined in order to determine the quality of the machining that was possible with the shaped beam. This was followed by machining of stainless steel (grade 304) substrates. It should be noted that the machining trials were performed before the square beam was

aligned to the CCD/scan head axes and, as a result, the square shape is angled in the following micrographs.

7.4.3.1 Chrome Plated Glass

Initial trials with the chrome plated glass showed that the thin chromium layer was easily ablated by the shaped beam. Optimisation of the process enabled the ablation of a square area of chromium with a single laser pulse. In order to determine the defocus required in order to obtain an approximately equivalent spot size with the Gaussian beam, beam parameters were calculated assuming a near-Gaussian beam. First, the minimum beam diameter for the optical system was calculated as:

$$d_0 = \frac{4 \cdot M^2 \cdot \lambda \cdot f}{\pi \cdot D} \tag{7-4}$$

where M^2 is the beam quality factor (nominally ~1.1 for the 20W EP-S laser), λ is the laser wavelength (1064nm), f is the focal length of the focussing laser (160mm) and D is the diameter of the collimated input beam to the focussing lens (8mm) [130]. The beam diameter at a given distance, z, from the focal plane can then be calculated as:

$$d_z = d_0 \cdot \left(1 + \left(\frac{z}{z_R}\right)^2\right)^{\frac{1}{2}} \tag{7-5}$$

where z_R is the Rayleigh range, the distance from the beam waist at which the diameter has increased by a factor of $\sqrt{2}$ [130]. The Rayleigh range can be calculated as:

$$z_R = \frac{\pi \cdot d_0}{4 \cdot \lambda}. \tag{7-6}$$

By combining and rearranging these three equations, the defocus required (z) in order to obtain a spot size of 110µm was determined to be ~2.35mm. Micrographs of the optimised machining are shown in Figure 7.17, along with defocussed Gaussian machining for comparison.

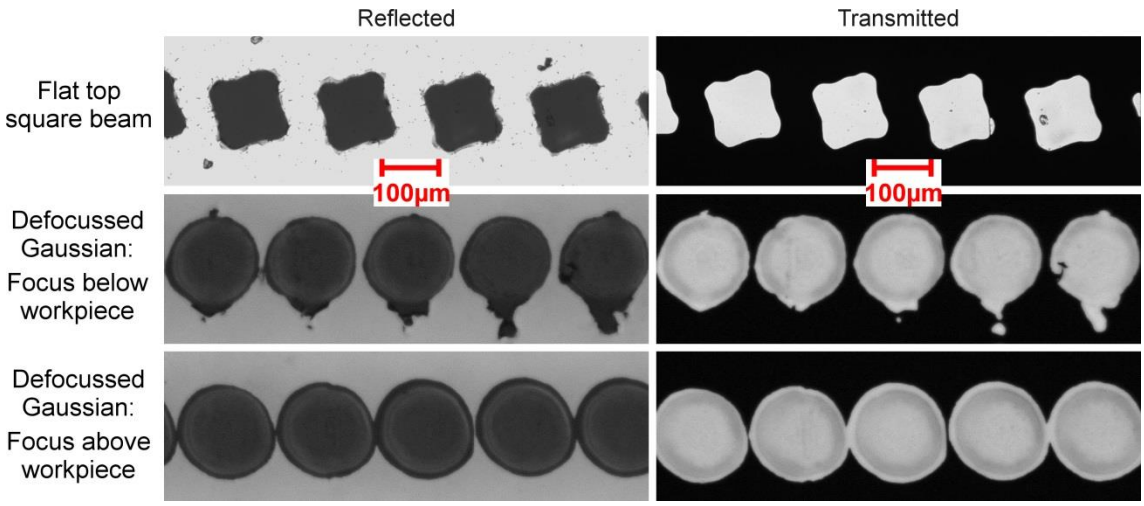

Figure 7.17. Reflection and transmission micrographs of the chrome plated glass with several machining marks for the square flat top beam and the Gaussian beam defocussed both above and below the workpiece

Each mark shown in Figure 7.17 was machined with a single laser pulse using 10W (nominal) power, 220ns pulses (WF32) with a PRF of 28kHz. Uniform, square marks are observed for the square flat top beam, with little debris surrounding the marks. For the defocussed Gaussian beam, several irregularities were observed in the shape of the mark when the focus was below the workpiece (possibly relating to further absorption within the glass closer to focus). When focussed above the workpiece, very regular circular marks were observed, albeit slightly larger than the marks obtained with the square beam shape and Gaussian beam focussed below the workpiece.

7.4.3.2 Stainless Steel (SS304)

Following the positive results on the chrome plated glass, machining trials were performed on stainless steel grade 304. These tests were carried out using the maximum and pulse energy available from the laser, 20W nominal power, WF32 (220ns) and 28kHz repetition frequency. A micrograph showing a set of results for various numbers of laser pulses is shown in Figure 7.18.

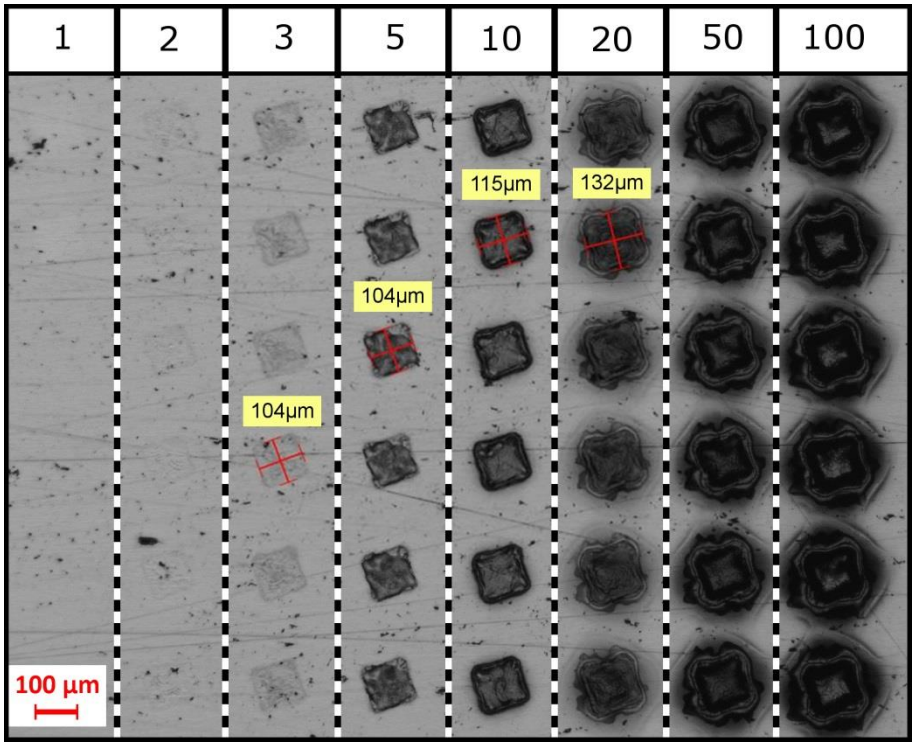

Figure 7.18. Optical micrograph showing the effect of number of pulses (1-100) and consistency of machining on a stainless steel 304 substrate with the square flat top shaped beam

For these trials, the laser was programmed to pulse a set number of times (between one and 100) in a given location before moving to the next location (similar to percussion drilling). The micrograph in Figure 7.18 shows that very little machining/marking is observed for 1-2 pulses, indicating that the energy density of a single pulse is not high enough to enable noticeable melting of the steel surface. The shaped beam energy density (fluence) was calculated as <4.2J/cm^2 (based on a 120µm square beam with 0.6mJ energy). In comparison, melting was observed with a single pulse in Section 3.2.1 at a fluence of ~3J/cm^2 (0.16mJ nominal, 0.06mJ measured, with a ~50µm 1/e^2 diameter near-Gaussian beam). However, as there are additional power losses in the shaped beam (±1 diffraction orders and intensity wings) and the intensity distribution is uniform (as opposed to Gaussian which peaks higher than the average fluence in the centre of the beam), it is not too surprising that the steel surface is unmodified after just one or two pulses.

As the number of pulses increases, however, square marks can clearly be observed on the surface; particularly when between 3 and 10 pulses are used. This is due to the effect of thermal accumulation caused by the short time between consecutive pulses (~36µs) and the low thermal conductivity of the steel substrate (~16W/m·K). When the number of pulses is increased further, the shape of the mark becomes distorted, likely

due to increased thermal accumulation and the intensity wings of the beam beginning to mark the surface. Therefore, the optimal number of pulses required to generate a uniform square mark lies between 5 and 10. This also corresponds to the number of pulses required to make a mark of 110µm sides.

7.5 Laser Polishing

Based on these results, it is also evident that ablation of steel is not possible using this beam shaper with the 20W EP-S laser system due to a lack of fluence at the workpiece. However, as melting is clearly possible with just a few pulses, attempts were made to use the shaped beam for laser polishing of steel.

By aligning the shaped beam to the scan head axes, lines were processed on the steel surface with varying pulse overlap (20W, 28kHz, WF32, varying scan speed). Due to the number of pulses required to attain significant melt on the surface, the optimal scan speeds were found to be very low, <10mm/s. As a result, a large amount of heat was built up in the steel substrate, leading to significant oxidation of the melted surface.

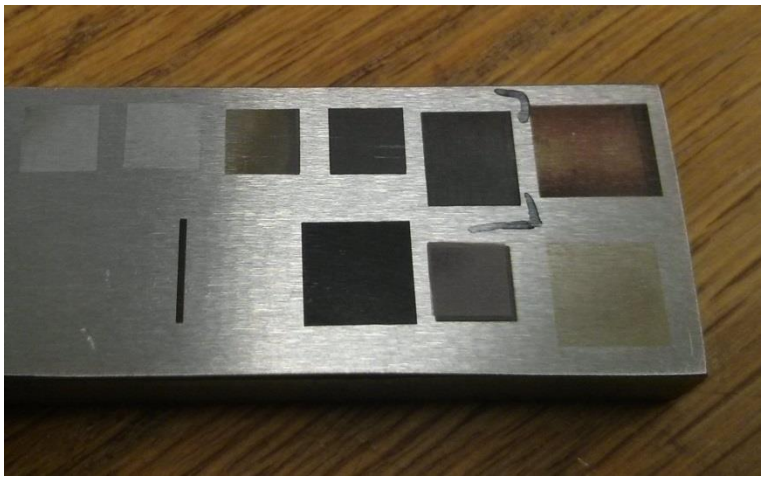

Figure 7.19. Stainless steel 316 sample with various polishing marks showing clear signs of oxidation

Such oxidation generates a dark black mark on the surface, as shown in Figure 7.19, and is therefore highly undesirable for polishing applications, despite a small but noticeable improvement in roughness (from S_a~1µm to S_a~0.8µm). The oxidation process is also exothermic, increasing the temperature and therefore absorption at the surface, assisting the low energy density pulses to smooth the surface.

Attempts were made to overcome this issue of oxidation by processing in an inert atmosphere. This was achieved by placing the sample in an enclosure with a glass lid which was subsequently flooded with argon before and during laser processing. Unfortunately, due to the addition of the glass window and the cooling effect of the flowing argon over the sample, it was not possible to even melt the steel surface in this arrangement. As no other laser sources were available with higher pulse energy and the required beam profile, no further results were achieved on the use of beam shaping for polishing applications.

7.6 Summary & Conclusion

The results presented in this chapter have shown that the integration of beam shaping optics into a standard, commercially available laser processing workstation can easily be achieved with little modification.

After the initial set-up, a relatively square, flat top beam was observed after the scan head and F-theta lens, albeit several millimetres from the expected focal position was expected. The shape of the output beam was found to be highly sensitive to the alignment of the beam shaping optics in x, y and rotation. Misalignments of just ~7µm in x or y were found to distort the intensity profile of the resulting beam, with ~14µm misalignment making the profile almost unrecognisable. Rotation of the optics was found to distort the shape of the beam, rather than altering the homogeneity of the intensity distribution, with misalignments of just 1° having a significant impact. From the sensitivity tests performed, it was concluded that the z-separation is also highly sensitive but not well defined in this set-up. However, it has been shown that this can be mostly compensated by deliberately misaligning the rotation of the optics, resulting in a fairly well defined square, flat top beam. This beam was found to be slightly larger than the design beam size (~120µm vs 110µm) and a distance away from the expected focal plane (depending on the misalignment angle).

With the best observed square, flat top profile, scan head deflection measurements indicate that the beam remains relatively distortion free for deflections of up to 30mm. For larger deflections, the beam was observed to elongate and distort. Despite this, an effective scan field of 60mm×60mm is suitable for many laser processing applications.

Machining trials with the shaped beam showed that clean, sharp ablation can be achieved on 250nm thick chrome plated glass with a single laser pulse, comparable to that of the Gaussian beam defocussed with the focal plane above the workpiece. For the stainless steel substrate, multiple pulses at maximum power were required to melt the surface, due to the large spot and reduced pulse energy caused by the uncoated beam shaping optics (15-20%). Despite this, a homogeneous square mark was observed when 5-10 pulses were used, with mark dimensions of ~110µm. Attempts to use the beam for polishing required very high pulse overlap in order to achieve sufficient melting, resulting in significant oxidation of the surface. Efforts to overcome the oxidation proved to introduce further power losses, resulting in the inability to even melt the surface.

It is still expected that use of a shaped beam profile may provide benefits to various laser surface and laser micro-machining processes, although a smaller spot size (~50-60µm) would be better suited for use with this particular laser system. This should be easily achieved by altering the design of the beam shaping optics and increasing the diameter of the collimated beam while maintaining the same quality of flat top beam (β~13). In addition, the set-up should also be modified in order to enable accurate positioning of the two optics in the z-axis (as well as the alignment controls already available).

Chapter 8 – Final Conclusions & Future Work

8.1 General Discussion

The work presented in this thesis aimed to develop and understand the processes which allow the friction properties of a surface to be modified in a controlled manner, primarily through the application of high power fibre lasers. Two successful methods of achieving high static friction surfaces by the use of laser surface texturing (LST) – the generation of rough, hard surface features which can embed into a softer counterpart and the generation of two roughened surfaces whose features can then interlock with each other – have been presented and discussed. Despite a significant number of publications on the use of LST for reducing the friction of contacts, very little research has been performed on increasing friction, especially using LST. The absence of knowledge and research in this area highlights the novelty of both the application and the method.

Initial results concerning the investigation of the laser-material interaction confirmed that commercially available pulsed fibre lasers operating at a wavelength of 1064nm are more than suitable for LST applications with steel substrates. It was observed that near independent control over the crater width and depth was possible by selecting a particular pulse energy and number of pulses for the desired crater dimensions. This was due to the crater diameter being dependent on the area of the beam for which the laser fluence exceeded the ablation threshold while the crater depth was significantly smaller than the Rayleigh range of the beam, thus enabling a consistent volume of material removal with each pulse. These observed trends, for both SS316 and SS304 substrates, were found to agree with results presented in the literature.

The overlapping of pulses in order to generate lines, or troughs, also showed similar trends. The line width was found to vary with pulse energy whilst being independent of the pulse overlap. The average trough depth, however, was found to increase linearly with number of pulses per distance, with some influence from pulse energy. The generation of various surface textures, containing craters arranged in a square or hexagonal pattern, was considered. The square design was found to introduce undesirable periodic structures. As a result, all friction textures were generated using the hexagonal pulse layout.

Initial test results, performed at 150MPa normal pressure, revealed that high friction coefficients of μ_s>0.83 can be achieved, providing reason and motivation for continued investigation into this application. Friction tests were then performed across a wide range of the laser processing parameter space in order to indicate the optimal regime for the generation of high friction surface textures.

Surface hardness was found to have the largest impact on the resulting friction coefficient of these tests, surpassing even the impact of the surface roughness. Increasing pulse overlap was observed to increase the surface hardness, a fact likely due to the generation of hard oxides at the surface of the texture. In particular, very hard oxides such as chromium oxide and aluminium oxide were observed via EDX analysis of the samples textured with high pulse overlap.

Of the parameters considered, laser spot size, processing atmosphere, pulse repetition frequency and substrate material were observed to have a noticeable impact on the resulting friction coefficient. Despite the limited number of tests for each case, the following were typically found to result in the highest static friction coefficients:

- Maximum pulse energy available from the laser (typically 0.7-1mJ)
- Low repetition rate, 20-25kHz, regardless of the laser PRF0
- Use of a small focus spot size (typically ~25-35µm)
- Processing in air atmosphere
- Hardened material surface (after laser processing)

The use of higher PRF values was considered in detail, due to the implications for speeding up the process for industrial applications. Thermal accumulation from the use of higher repetition rates was found to be detrimental to the observed friction coefficients, possibly by altering the surface chemistry leading to an adhesion based friction contact. Several alternate texturing strategies were proposed in order to overcome the thermal accumulation, including the interlacing of laser pulses, thus allowing the substrate to cool down between adjacent pulses. The resulting friction coefficients were reduced further, however, possibly as a result of the change in surface and subsurface structures.

Friction tests of samples subject to laser texturing in addition to external hardening processes, including plasma nitriding and conventional heat treatment, were found to result in high but somewhat inconsistent friction coefficients. Samples plasma nitrided prior to laser texturing achieved consistently high friction coefficients of μ_s>0.8. Unfortunately, poor/inconsistent plasma nitriding limited the number of samples tested in this regime. For the second batch of successfully nitrided material, friction coefficients varied between 0.3 and 0.9 depending on the surface texture. Further analysis concluded that the friction in this case was dependent on the surface roughness, with increasing roughness linearly increasing the resulting friction coefficient. It is therefore assumed that both high hardness and high roughness are required in order to achieve a contact with a high friction coefficient. This is expected to be due to the embedding of the hardened asperities into the comparatively soft counterpart, significantly increasing the force required to shear the contacting asperities. Test results of samples hardened by conventional heat treatment exhibited a similar trend. However, limited samples and several outlying points cast doubt upon this conclusion. Therefore further testing is required to confirm this definitively.

Texturing of both contacting surfaces facilitated the generation of even higher friction coefficients. Coefficients consistently greater than μ_s>1.25 were achieved for low pulse separation (<25µm) at both 100MPa and 50MPa normal pressure. The coefficients obtained decreased rapidly with increasing pulse separation, although average values above 0.6 were obtained at 75µm and 62.5µm pulse separation for 100MPa and 50MPa normal pressures, respectively. Subsequent analysis showed that these values were achieved by significant interlocking of features, partially facilitated by the large normal pressure. The interlocking of the asperities acts in a similar manner to the embedding of the hard asperities discussed previously by increasing the tangential force required in order to shear the contacting asperities. In this case, the interlocking asperities are higher density and thus result in higher friction coefficients. This interlocking theory was confirmed by overloading tests which enabled meaningful interlocking via plastic deformation before friction testing at much lower normal pressure (150MPa → 50MPa). Attempts to improve the processing rate by altering the pulse separation of one of the textures were unsuccessful, although the results did prove insightful, further consolidating the theory of interlocking. Increasing the pulse duration, however, did prove beneficial to the friction coefficient, likely by generating larger surface features

for interlocking due to the increased melt duration. In addition, high friction coefficients (μ_s=1.54) were achieved at an even lower normal pressure of 25MPa. In contrast to the case of single-surface texturing, increasing the pulse repetition frequency did not reduce the friction coefficient, thus providing a very straightforward method of increasing the processing rate in this regime. Following this, static friction coefficients of μ_s~1 with processing rates of >1cm^2/s have been shown with μ_s>0.6 consistently obtained with rates of >3.5cm^2/s. Based on the results achieved, it is assumed that friction coefficients of μ_s>0.6 should be possible at processing rates of ~10cm^2/s with optimisation of the process and equipment by using two lasers to texture the two surfaces simultaneously at a PRF of 100kHz .

The feasibility of integrating custom beam shaping optics into a typical commercial/industrial laser processing workstation without significant modification has also been demonstrated. The two different beam shapers from PowerPhotonic (one optic and two optic beam shapers) were characterised within the system and found to generate high quality flat top beams with a respectable depth of field (~±0.3mm). The two-optic beam shaper was observed to be highly sensitive to misalignments in x, y and rotation, with displacements of just ~7µm or 1° significantly distorting the resulting beam profile. When aligned, however, the beam was robust to deflections by the galvo scanner, resulting in a usable working area of 60mm×60mm. Unfortunately, due to the spot size, limited laser pulse energy and losses at the uncoated beam shaping optics, the possibilities for machining trials were limited. However, ablation of a thin (250nm) chromium layer on a glass substrate was achieved by a single laser pulse, highlighting the square shape and sharp edges of the beam. With a smaller spot size, which should be fairly straightforward to achieve, it is expected that the flat top beam would provide benefits for use in laser polishing and other surface engineering applications.

8.2 Key Conclusions

From the results obtained and presented in this thesis, several key conclusions can be taken for each of the areas investigated, including:

High friction by laser texturing only a single surface:

- High friction coefficients (μ_s>0.8) can be obtained by laser texturing alone, although high pulse overlap (>50%) and a high normal pressure (150MPa) was required in order to achieve this

- At reduced normal pressure (100MPa) much lower friction coefficients were observed (typically μ_s<0.6) and surface hardness was found to play an important role in the resulting friction coefficients obtained

High friction by laser texturing and hardening a single surface:

- Samples plasma nitrided after laser texturing were found to achieve high friction coefficients (up to μ_s~0.9) at 100MPa normal pressure, depending on the laser texturing parameters used. For samples with approximately the same hardness, friction coefficients were found to increase approximately linearly with surface roughness, indicating an embedding friction regime

- Samples laser textured followed by conventional heat treatment hardening processes showed some similarities to those obtained with the plasma nitrided samples. However, the results from these tests were less conclusive

High friction by laser texturing of both contacting surfaces:

- Extremely high friction coefficients of up to μ_s~2 were obtained by laser texturing of both surfaces of the contact. Cross-section microscopy indicates that these coefficients are facilitated by significant deformation and interlocking of the surface features generated by the laser texturing

- Use of longer pulse durations and higher repetition rates were found to increase the friction coefficients and processing speed, respectively. As a result, friction coefficients of μ_s>0.6 are expected to be obtainable at processing speeds of ~10cm^2/s with minimal alterations to the laser texturing set-up

Incorporation of beam shaping optics into commercial laser processing workstations:

- Two custom designed beam shaping optic systems (Gaussian to circular and square flat-tops) were easily incorporated into the laser processing workstation. Both flat top beams were observed to exhibit a relatively large depth of field (>1.5mm) through the galvo scanner/F-theta lens. Although the beam shape was found to be very sensitive to alignment of the optics in x, y, z and rotation, once aligned the resulting beam profile was mostly preserved for galvo deflections of up to ~30mm in x and y, resulting in a in a usable working area of ~60mm×60mm

8.3 Future Work

The work presented in this thesis has generated many interesting results, whilst also leaving several opportunities for further investigation.

With regards to laser texturing with hardening for high friction surfaces, areas of interest for future work include:

i. Further tests in order to confirm requirement of hardness and surface roughness in order to achieve high friction coefficients.

ii. Determine any minimum limits (in either hardness or roughness) for achieving a specific friction coefficient (e.g. μ_s>0.6).

iii. Optimisation of the laser texturing and hardening process parameters for industrial applications, including process scalability.

iv. Combining of the laser texturing and hardening process by nitriding the surface during laser texturing. (High power processing of alumina with high pressure nitrogen assisting gas has already shown promise in improving wettability properties [131].)

With regards to laser texturing of both contacts for high friction:

i. Perform further tests at lower normal pressures (<25MPa), possibly enabling more applications where such high pressures are not feasible, and determine if there is a minimum limit for high friction at low pressure in this regime.

ii. Perform tests on components for real applications, such as the drive shaft assembly. Texturing of parts for this has already taken place, as shown in Figure 8.1, although measurements and analysis of these parts has yet to take place.

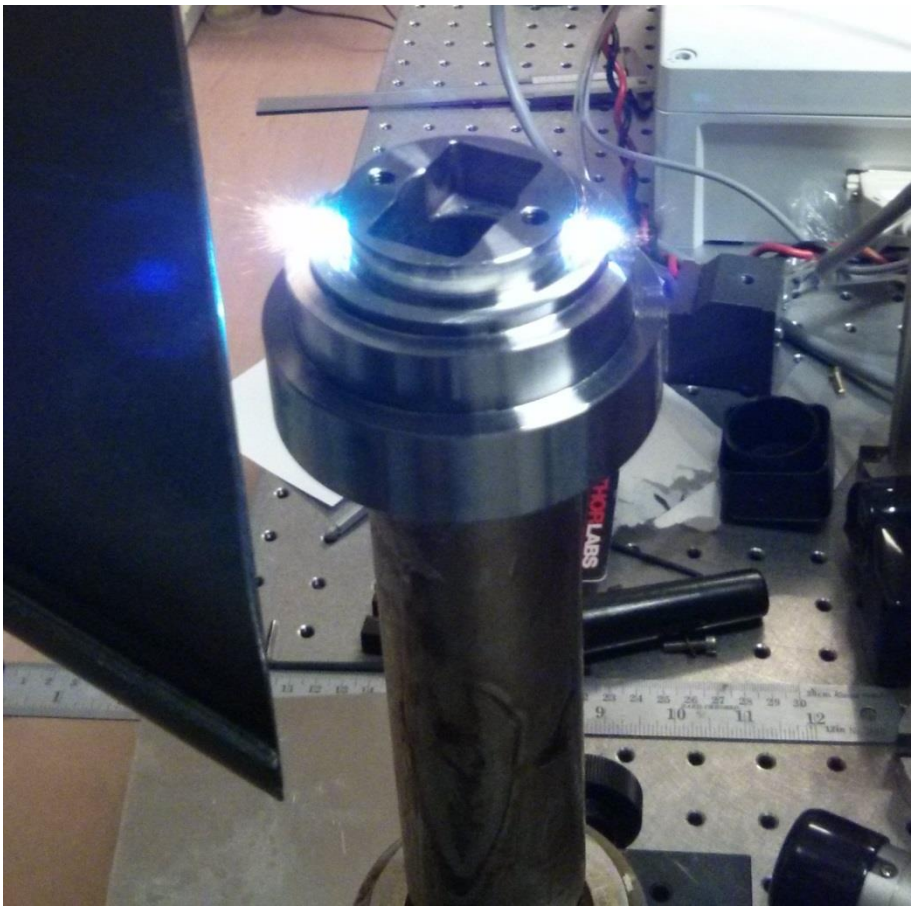

Figure 8.1. Photograph of the gear end of the drive shaft during the laser texturing process (bright blue sparks are the result of laser ablation of the material surface). Only a small ring (53mm outer diameter, 41mm inner diameter) was textured on each component, with both surfaces of the intermediate disc being textured

iii. Optimise the processing rate by using longer pulses at higher pulse repetition rates. Possibly incorporate multiple lasers/beams if the application requires large area texturing or extremely high processing rate.

iv. Generate unidirectional friction coefficients by deliberately generating periodic linear structures, as shown in Figure 8.2, facilitating a tongue and groove style interlocking in one direction. In this case, the regime is more like mechanical interlocking than friction as has been previously discussed; however, it can be achieved by a similar process and will result in high resistance to lateral movement of the two surfaces.

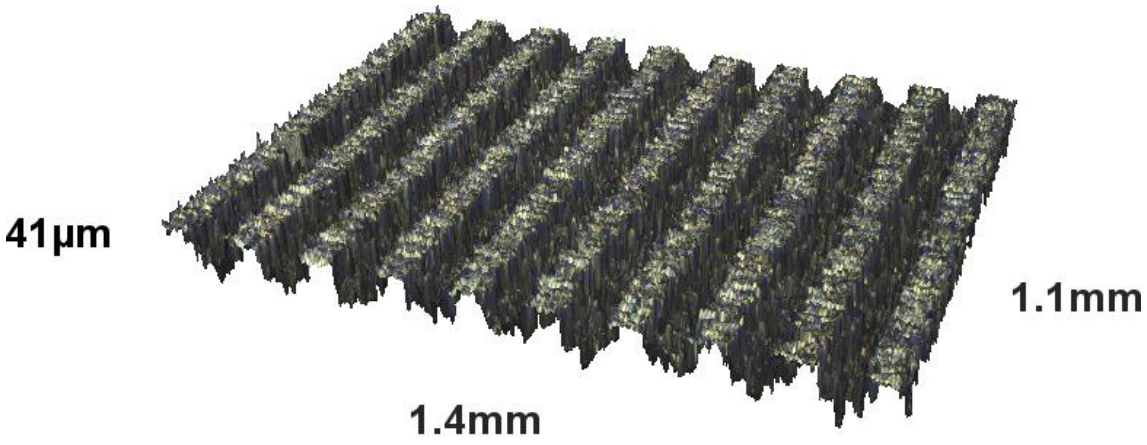

Figure 8.2. Example of a possible texture for generating a unidirectional friction coefficient, whereby the counterpart would be textured with an identical structure enabling substantial interlocking in one direction; profile obtained from the Alicona profilometer

With regards to beam shaping:

i. Generate smaller spot size for use with current laser system or use higher pulse energy laser system with current beam shaper.

ii. Optimise machining/polishing performance of the shaped beam (top hat, donut, etc.) and compare to a Gaussian beam of similar properties.

In addition, a fully developed model of the laser-material interaction, including melt flow, would also be beneficial. This could enable the optimal surface morphology to be designed prior to laser texturing, whilst also possibly estimating material properties, therefore reducing the number of tests required for each application. This may also be included into a friction contact model, possibly providing estimates of the resulting friction coefficients for a set of given laser texturing parameters, reducing the requirement for a large number of experimental tests to determine the effectiveness of a given surface topography.

Appendix A – SPI Laser Waveform Tables

A.1 SPI 20W HS-L

Waveform (#)	Approx. Electrical Duration (ns)	PRF0 (kHz)	E_{max} (mJ)
0	200	25	0.8
1	65	65	0.31
2	30	125	0.16
3	15	250	0.08
4	12	375	0.053
5	9	500	0.04
6-10	Duplicate of waveform 5		
11	200	25	0.8
12	190	26	0.77
13	180	27	0.74
14	170	28	0.71
15	160	29	0.69
16	150	30.5	0.66
17	140	32	0.63
18	130	33.5	0.6
19	120	35.5	0.56
20	110	38	0.53
21	100	41	0.49
22	90	45	0.44
23	80	50	0.4
24	70	57	0.35
25	60	66	0.3
26	50	78	0.26
27	40	97	0.21
28	30	135	0.15
29	20	250	0.08
30+	Duplicate of waveform 29		

A.2 SPI 50W HS-S

Waveform (#)	Approx. Electrical Duration (ns)	PRF0 (kHz)	E_{max} (mJ)
0	220	70	0.71
1	120	110	0.45
2	55	180	0.28
3	25	340	0.15
4	18	540	0.09
5	15	580	0.09
6-10	Duplicate of waveform 5		
11	220	70	0.71
12	205	74	0.68
13	200	78	0.64
14	190	88	0.57
15	160	96	0.52
16	140	102	0.49
17	120	110	0.45
18	100	120	0.42
19	95	126	0.40
20	85	136	0.37
21	75	148	0.34
22	65	160	0.31
23	55	180	0.28
24	45	210	0.24
25	35	250	0.20
26	25	340	0.15
27	18	540	0.09
28	15	590	0.08
29+	Duplicate of waveform 28		

A.3 SPI 20W EP-S

Waveform (#)	Approx. Electrical Duration (ns)	PRF0 (kHz)	E_{max} (mJ)
0	241	33	0.61
1	221	35	0.57
2	202	38	0.53
3	177	40	0.50
4	161	42	0.48
5	144	44	0.45
6	131	47	0.43
7	118	50	0.40
8	113	52	0.38
9	103	54	0.37
10	100	57	0.35
11	90	60	0.33
12	80	63	0.32
13	65	67	0.30
14	58	71	0.28
15	60	75	0.27
16	55	80	0.25
17	50	85	0.24
18	45	90	0.22
19	40	98	0.20
20	36	110	0.18
21	33	115	0.17
22	30	125	0.16
23	26	140	0.14
24	23	150	0.13
25	20	175	0.11
26	16	220	0.09
27	13	300	0.07
28	10	400	0.05
29	7	500	0.04
30	5	700	0.03
31	3	1000	0.02
32	220	28	0.71
33	245	28	0.71
34	270	28	0.71
35	320	28	0.71
36	350	28	0.71
37	390	28	0.71
38	440	28	0.71
39	490	28	0.71

A.4 SPI 70W RM-Z

Waveform (#)	Approx. Electrical Duration (ns)	PRF0 (kHz)	E_{max} (mJ)
0	260	70	1
1	40	330	0.21

A.5 SPI 20W EP-Z

Waveform (#)	Approx. Electrical Duration (ns)	PRF0 (kHz)	E_{max} (mJ)
0	241	23	0.87
1	221	25	0.8
2	202	27	0.74
3	177	29	0.7
4	161	30	0.67
5	144	32	0.63
6	131	34	0.6
7	118	36	0.56
8	113	37	0.54
9	103	39	0.52
10	100	41	0.49
11	90	43	0.47
12	80	45	0.44
13	65	48	0.42
14	58	51	0.39
15	60	54	0.37
16	55	57	0.35
17	50	61	0.33
18	45	65	0.31
19	40	70	0.29
20	36	76	0.26
21	33	83	0.24
22	30	90	0.22
23	26	100	0.2
24	23	107	0.19
25	20	123	0.16
26	16	157	0.13
27	13	215	0.09
28	10	290	0.07
29	7	395	0.05
30	5	500	0.04
31	3	715	0.03
32	220	20	1
33	245	20	1
34	270	20	1
35	320	20	1
36	350	20	1
37	390	20	1
38	440	20	1
39	490	20	1

Appendix B – Material Compositions & Selected Properties

B.1 Grade 316 Stainless Steel 1.4401 (SS316) [132]

Chemical Element	Percentage (%)
Carbon (C)	0.0-0.07
Chromium (Cr)	16.50-18.50
Molybdenum (Mo)	2.00-2.50
Silicon (Si)	0.0-1.00
Phosphorous (P)	0.0-0.05
Sulphur (S)	0.0-0.03
Nickel (Ni)	10.0-13.0
Manganese (Mn)	0.0-2.0
Nitrogen (N)	0.0-0.11
Iron (Fe)	Balance

Property	Value	Unit
Density	8000	Kg/m^3
Melting Point	1400	°C
Thermal Expansion	15.9×10^{-6}	/K
Thermal Conductivity	16.3	W/m·K
Tensile Strength	500-700	MPa
Hardness (Brinell)	<215	HB

B.2 Grade 304 Stainless Steel 1.4301 (SS304) [133]

Chemical Element	Percentage (%)
Carbon (C)	<0.07
Chromium (Cr)	17.5-19.5
Silicon (Si)	<1
Phosphorous (P)	<0.05
Sulphur (S)	<0.03
Nickel (Ni)	8-10.5
Manganese (Mn)	<2
Nitrogen (N)	<0.11
Iron (Fe)	Balance

Property	Value	Unit
Density	8000	Kg/m^3
Melting Point	1450	°C
Thermal Expansion	17.2×10^{-6}	/K
Thermal Conductivity	16.2	W/m·K
Tensile Strength	500-700	MPa
Hardness (Brinell)	<215	HB

B.3 S20R Hot Rolled Carbon Steel (Low Alloy)

Chemical Element	Percentage (%)
Carbon (C)	0.2
Silicon (Si)	0.25
Phosphorous (P)	<0.05
Sulphur (S)	<0.05
Manganese (Mn)	0.5
Iron (Fe)	Balance

Property	Value	Unit
Hardness (Brinell)	115-215	HB

B.4 Cr-Mo-Al Low Alloy Steel (Nitriding Steel)

Chemical Element	Percentage (%)
Carbon (C)	0.34
Chromium (Cr)	1.1
Molybdenum (Mo)	0.2
Silicon (Si)	0.3
Phosphorous (P)	<0.03
Sulphur (S)	<0.035
Aluminium (Al)	0.85-1.2
Manganese (Mn)	0.6
Iron (Fe)	Balance

Property	Value	Unit
Hardness (Brinell) Pre-nitriding	235-280	HB
Hardness (Vickers) Post-nitriding	900-1100	HV

B.5 Uddeholm Impax Supreme Tool Steel (Impax) [134]

Chemical Element	Percentage (%)
Carbon (C)	0.37
Chromium (Cr)	2
Molybdenum (Mo)	0.2
Silicon (Si)	0.3
Nickel (Ni)	1
Manganese (Mn)	1.4
Iron (Fe)	Balance

Property	Value	Unit
Density	7800	Kg/m^3
Thermal Expansion	12.7×10^{-6}	/K
Thermal Conductivity	28	W/m·K
Specific Heat	460	J/kg·K
Hardness (Brinell) Delivery Condition	290-330	HB

B.6 Böhler S600 Tool Steel (Böhler) [135]

Chemical Element	Percentage (%)
Carbon (C)	0.9
Chromium (Cr)	4.1
Molybdenum (Mo)	5
Vanadium (V)	1.8
Tungsten (W)	6.2
Iron (Fe)	Balance

Property	Value	Unit
Density	8100	Kg/m^3
Thermal Expansion	$11.5\text{-}12.9\times10^{-6}$	/K
Thermal Conductivity	22	W/m·K
Specific Heat	433	J/kg·K
Hardness (Brinell) Delivery Condition	<280	HB

B.7 Sleipner Tool Steel (Sleipner) [136]

Chemical Element	Percentage (%)
Carbon (C)	0.9
Chromium (Cr)	7.8
Molybdenum (Mo)	2.5
Silicon (Si)	0.9
Vanadium (V)	0.5
Manganese (Mn)	0.5
Iron (Fe)	Balance

Property	Value	Unit
Density	7730	Kg/m^3
Thermal Expansion	$11.6\text{-}12.7\times10^{-6}$	/K
Thermal Conductivity	20-25	W/m·K
Specific Heat	460	J/kg·K
Hardness (Brinell) Delivery Condition	235	HB

Appendix C – Finite Element Model of Laser-Material Interaction

In conjunction with the experimental tests and analysis, a relatively basic finite element model was written and developed in an attempt to provide some further insight into the laser-material interaction for the generation of individual craters and lines, with the possibility of expanding into modelling the generation of 2D textures.

C.1 Model & Approximations

The model was written in Matlab and based on the heat equation for thermal diffusion in two dimensions (but extendable to 3D if required):

$$\frac{\partial T}{\partial t} = \alpha \nabla^2 T \tag{C-1}$$

where T is the temperature in space (x and z dimensions in this case), ∇ is the Laplace operator and α is the thermal diffusion coefficient, which is defined as:

$$\alpha = \frac{k}{c_p \rho} \tag{C-2}$$

where k is the thermal conductivity, C_p is the specific heat capacity and ρ is the density. Typical values for the properties mentioned above for stainless steel were used in the model, along with values for latent heat (L) of both fusion and vaporisation, the boiling and melting temperatures and the optical absorption. The values used are shown in Table C.1 [75, 137].

Property (Symbol)	Value	Units
Thermal Conductivity (k)	16.3	W/m/K
Specific Heat Capacity (C_p)	460	J/kg/K
Density (ρ)	8000	kg/m^3
Latent Heat of Fusion (L_f)	300	kJ/kg
Latent Heat of Vaporisation (L_v)	5500-7600	kJ/kg
Melting Point (T_m)	1700	K
Boiling Point (T_B)	3000	K

Table C.1. Table of material properties of stainless steel used in the finite element model

In order to keep the simulation relatively simple and fast, all of the properties in Table C.1 were assumed to be constant with temperature. The optical absorption, however, was made temperature dependent based on the experimental findings of Kwon et al., shown in Figure C.1 [138].

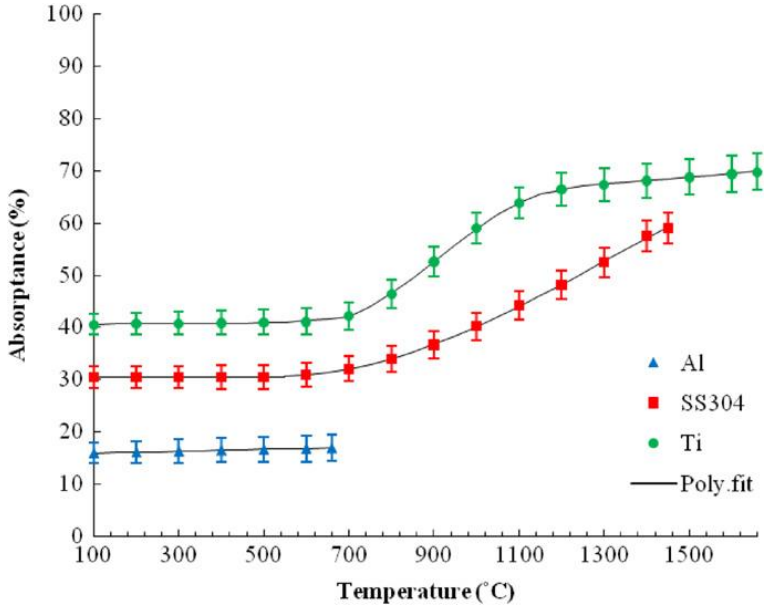

Figure C.1. Absorptance of metals for 1.07µm beam with temperature up to melting point [138]

In addition to the constant material properties, the following assumptions and approximations were made in the model:

1. Upon the temperature/energy increasing beyond boiling point, material is removed immediately
2. Whilst the liquid phase was included in model (through latent heat) it behaves identically to solid material (no melt flow etc.)
3. Samples are assumed to be fully thermally insulated – only energy loss mechanism is the ablated material removal
4. Spatial pulse distribution is assumed to be a perfect Gaussian, temporal pulse shape is approximately 20W HS-L WF0 shape (based on FPD measurements presented in Section 3.4.1).

C.2 Model Results

C.2.1 Individual Craters - Depth

First, the model was used to simulate the generation of individual craters, with varying pulse energies and number of pulses. The laser and pulse characteristics were based on

those of the 20W EP-S laser using WF32 (20W HS-L WF0 and 20W EP-S temporal pulse shapes are similar, temporal duration scaled accordingly) in order to provide results comparable to experimental measurements of crater depth and diameter. The crater depth as a function of number of pulses, for both experimental and simulation results, is shown in Figure C.2.

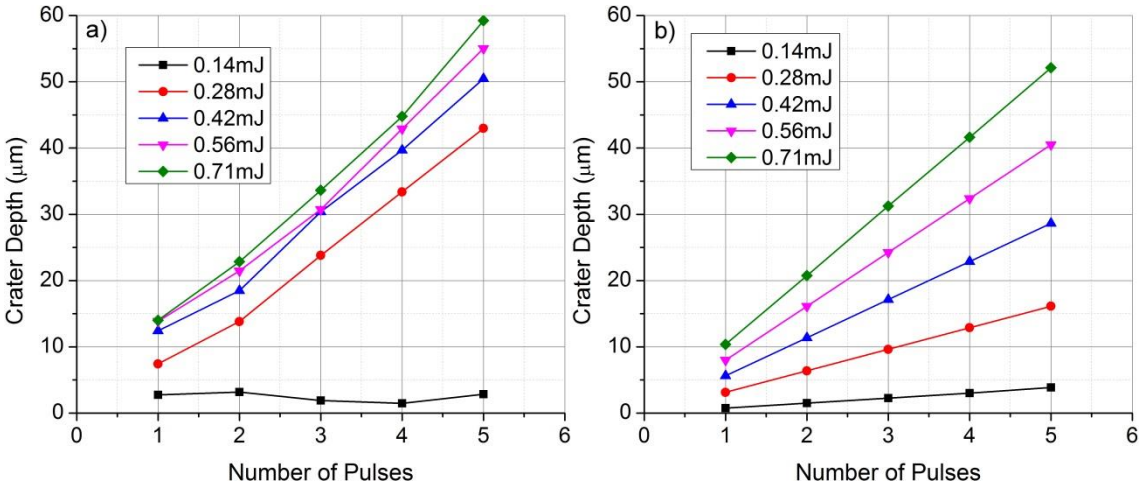

Figure C.2. Crater depth as a function of number of laser pulses using 20kHz repetition rate for a) experimental results and b) simulation results. Quoted pulse energies are nominal values; actual values obtained from results shown in Section 3.3 were used in the simulation

The experimental results, shown in Figure C.2a, indicate that when the pulse energy is increased above the ablation threshold (~0.2mJ, ~20J/cm^2) then the crater depth increases linearly with number of pulses but with little dependence on pulse energy, up to ~60μm at 0.71mJ for 5 pulses. The simulation results, shown in Figure C.2b, also indicate a linear trend with number of pulses as expected, but with a clear dependence on the pulse energy – with increasing pulse energy resulting in deeper craters. This is likely due to the lack of melt flow within the simulation. Experimentally, the vaporisation of material exerts a pressure on the surrounding molten material, causing it to flow out of the crater [75], thus increasing the crater depth compared to an ablation only process as modelled in the simulation. Due to the temporal pulse shape, increasing the pulse energy is not likely to greatly change the depth of the melt pool (given that the pulse duration is constant at ~220ns) prior to the material vaporisation, therefore it has little effect on the experimental crater depths. The effect of pulse energy can be seen more clearly in Figure C.3.

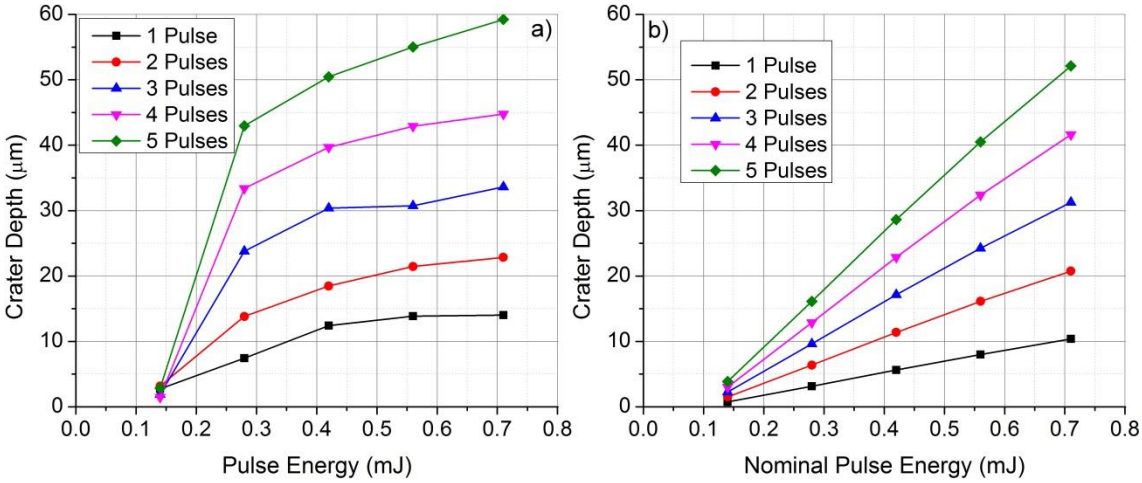

Figure C.3. Crater depth as a function of pulse energy using 20kHz repetition rate for a) experimental results and b) simulation results. Quoted pulse energies are nominal values; actual values obtained from results shown in Section 3.3 were used in the simulation

Figure C.3a clearly shows that the crater depth does not change significantly with pulse energy (when above the ablation threshold). As described previously, this is likely due to the limited melt depth achieved prior to vaporisation and the subsequent melt expulsion. The ejected material (plume), both vapour and molten, is also likely to interfere with the remaining duration of the incoming beam, limiting the effectiveness of the increased energy. The simulation results, presented in Figure C.3b, show a linear trend between crater depth and pulse energy. This is most likely due to lack of both melt expulsion and beam interference within the simulation. It should be noted that the depth achieved at maximum pulse energy (0.71mJ) is similar for both experimental and simulation results despite the approximations made (likely due to the lack of melt expulsion and plume-beam interaction cancelling each other out at this point).

C.2.2 Individual Craters – Width

The width of the craters was also measured in the simulations and compared to the experimental measurements (manually determined from optical micrographs). Figure C.4 shows the measured widths as a function of number of pulses.

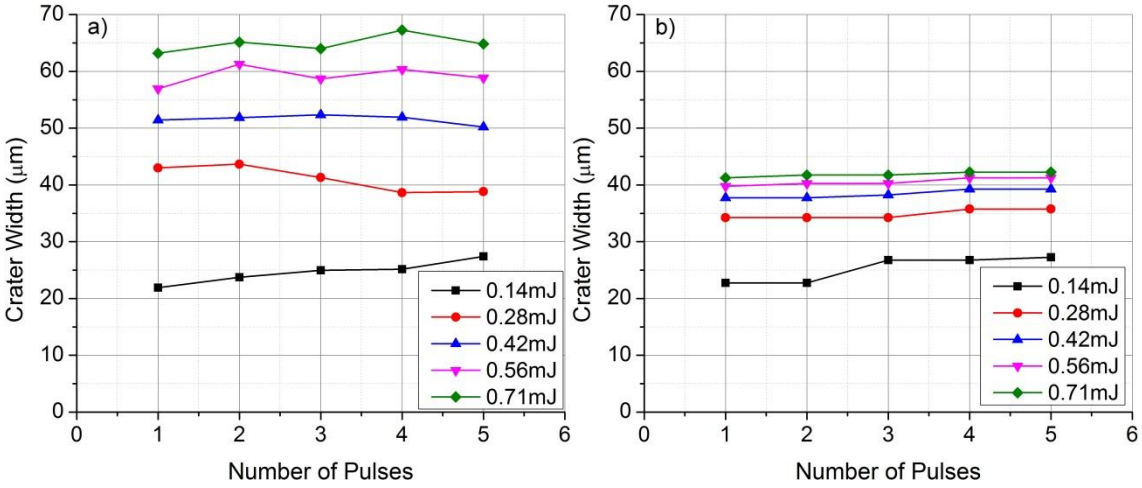

Figure C.4. Crater width as a function of number of laser pulses using 20kHz repetition rate for a) experimental results and b) simulation results. Quoted pulse energies are nominal values; actual values obtained from results shown in Section 3.3 were used in the simulation

Experimentally, Figure C.4a, the number of pulses was found to have little or no impact on width of the laser induced craters as the area with pulse energy above the melting and ablation thresholds remains constant, regardless of the number of pulses. This trend is replicated with the simulation results, shown in Figure C.4b, as expected, albeit the widths are much narrower at increased pulse energy. This discrepancy is highlighted further in Figure C.5.

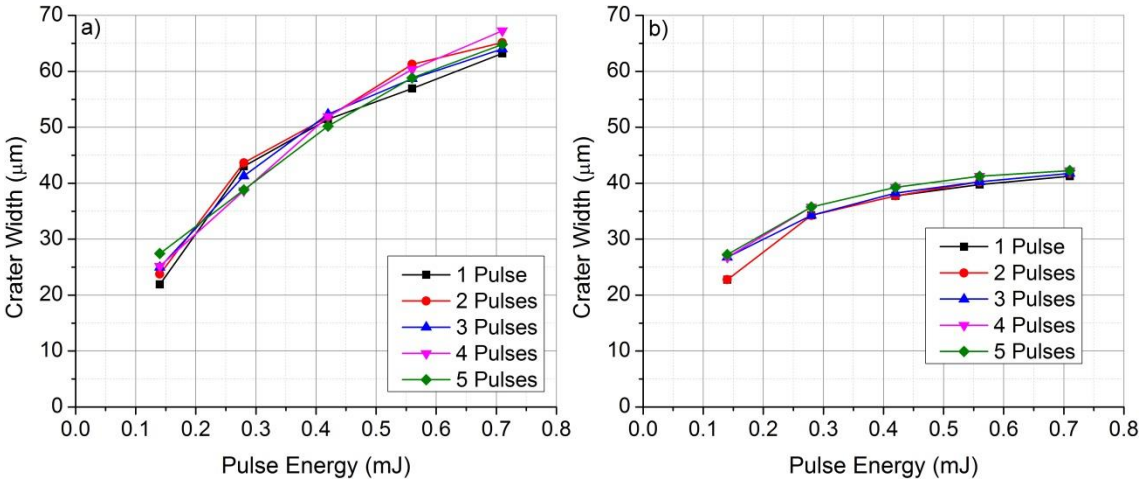

Figure C.5. Crater width as a function of pulse energy using 20kHz repetition rate for a) experimental results and b) simulation results. Quoted pulse energies are nominal values; actual values obtained from results shown in Section 3.3 were used in the simulation

Experimentally, Figure C.5a, the crater width was found to increase with pulse energy, at least up to 0.71mJ, whereas the simulation results, Figure C.5b, predict the crater width to plateau at pulse energies above ~0.4mJ. Again, this discrepancy is due to the

melt ejection, widening the crater further than would be expected from ablation only material removal.

C.2.3 Line Depth (Overlapping Pulses)

Following from the simulations on individual craters (drilling), the processing of lines was simulated using the same laser and material parameters but with varying pulse separation. In order to compare the simulation results with the experimental observations, the average depth of the trough for each line was calculated, as shown in Figure C.6.

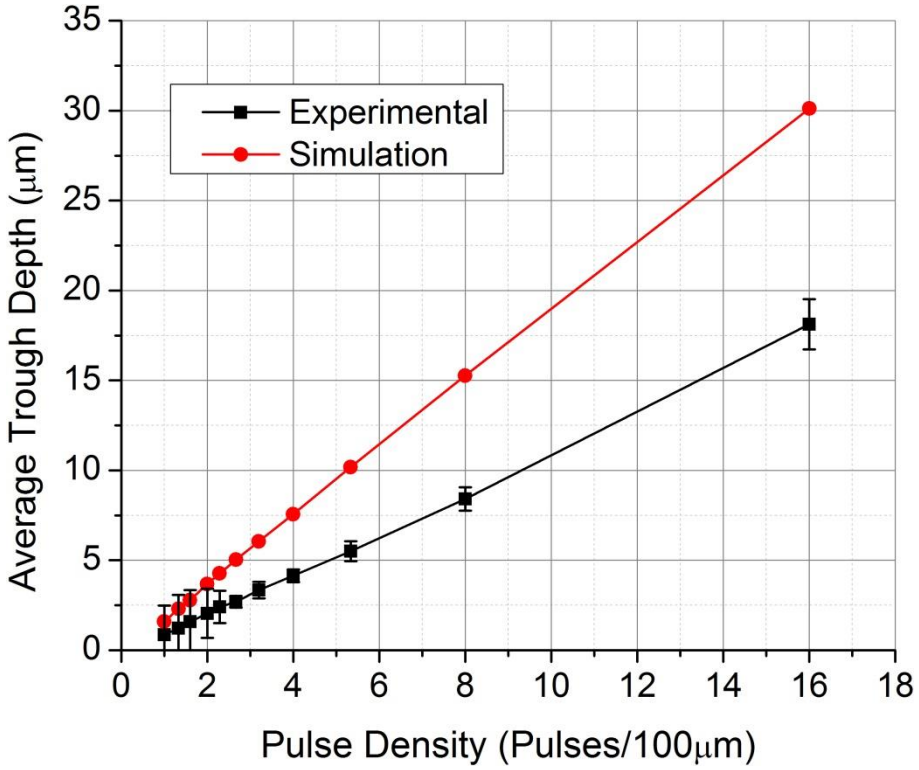

Figure C.6. Average trough depth as a function of linear pulse density (pulses per 100μm) for both experimental and simulation measurements

The pulse separation was varied between 100μm and 6.25μm (1-16 pulses/100μm) for both experimental and simulation results, shown in Figure C.6. Both sets of data show a clear linear trend between the average depth and pulse density. However, unlike the previous results concerning individual craters (drilling), here the depth of the simulated troughs exceeds the experimental measurements. Despite leading to increased depth when considering individual craters, melt ejection results in a shallower trough when generating lines as each consecutive pulse moves molten material both back into the previously created part of the trough, partially refilling it, and onto the substrate surface where the next pulse in the line will interact, increasing the volume of material requiring

removal to reach the same depth. The combination of these two mechanisms results in the experimental depth being significantly shallower than the simulated depth at high pulse densities. This highlights the limitation of the thermal diffusion model again; general trends may be predicted but, without serious consideration of the molten material, particularly melt flow and ejection, accurate values for the size and shape of the resulting surface features cannot be predicted.

C.2.4 Investigation of the Thermal Accumulation Effect

The model was also used in an attempt confirm the understanding of the changes in material properties and morphologies observed after laser texturing at different pulse repetition frequencies. Figure C.7 shows the results of a simulation considering the surface temperature at various distances from a single, low energy, 500ns laser pulse.

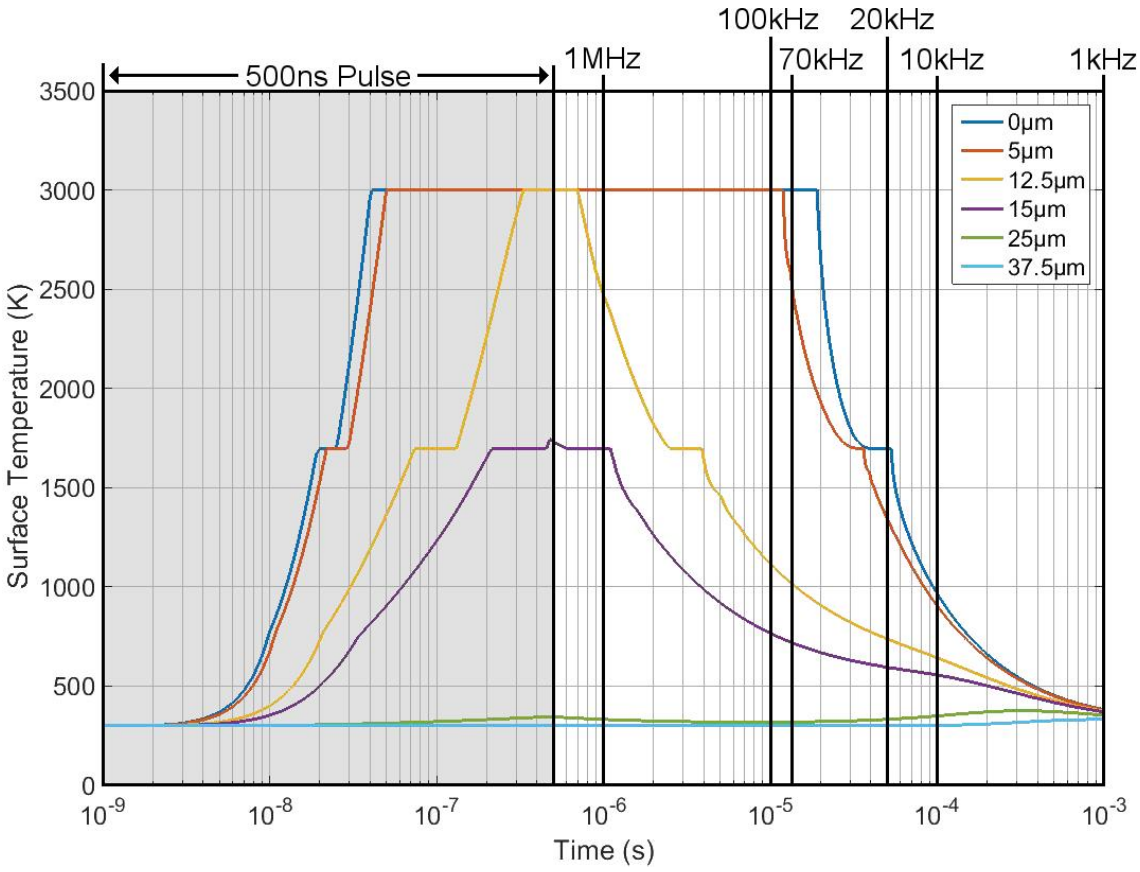

Figure C.7. Simulation results of surface temperature as a function of time at various distances from the centre of a low energy pulse, with times corresponding to the temporal spacing of various PRFs noted and the 500ns pulse duration highlighted

It is clear from the curves plotted in Figure C.7 that the extra time between pulses at 20kHz compared to 70kHz can have a significant impact on the surface temperature, depending on the distance from the initial pulse location. At 12.5µm separation, for

example, the temperature at the time corresponding to 70kHz was ~1000K but decreased to ~740K at the time corresponding to 20kHz. As anticipated, this effect was more pronounced closer to the centre of the pulse where the energy input is highest. Also, in order to minimise the number of variables to consider in this simulation, the laser pulse energy was minimised such that no material was ablated. As a result, larger temperature variations between 20kHz and 70kHz can be expected at higher pulse energy. The simulation also shows that, given a large enough separation between consecutive pulses, thermal accumulation effects can be avoided entirely. For the low energy pulse simulated, this corresponds to ~25µm separation. For higher energy pulses, this would be expected to be in the range of 50-60µm or more.

C.3 Finite Element Model Summary & Conclusion

The thermal diffusion model, written and developed in Matlab, was designed to simulate the laser material interaction and, as a result, predict trends related to the laser processing parameters. Ultimately, the aim was to simulate and predict the resulting surface geometry following a given laser process.

Despite the significant approximations made, several trends, including the linear increase of crater depth with number of pulses and constant crater width with number of pulses, were successfully predicted by the model. However, other trends, such as the crater depth levelling off with increasing pulse energy and change in crater width with pulse energy, were not accurately predicted.

The primary cause of these inaccuracies is assumed to be the lack of melt flow and ejection processes within the simulation. As observed in Chapter 3, melt flow and ejection processes are significant in the long nanosecond processing regime of metals, having a substantial effect on the resulting surface topography. As a result, in order to improve the value of this finite element model of the laser-material interaction, melt flow and ejection must be included. As the simulation was primarily intended to support the main experimental project, continued development of the model into melt flow was not undertaken, due to the time and resource requirement for such a task.

As speculated, simulation results show also that increasing pulse repetition frequency will result in higher surface temperature, although, as with the other model results,

accurate values were not obtained. However, the change in surface temperature is likely to be significant enough to alter the surface chemistry during and after processing. Given that these chemistry changes likely to cause modifications to the surface properties which are relevant for friction surfaces and other surface engineering applications, thermal accumulation will require further investigation in order to use PRF scaling to increase laser processing rates for industrial applications.

Given the modest results obtained with the model in its current form, the inclusion of detailed melt flow calculations would be expected to greatly improve the accuracy of the simulation, facilitating accurate predictions of the resulting surface topographies. Therefore, it would be worthwhile, and a natural continuation of the work presented, to extend the model into this area.

References

1. Thyagarajan, K. and A. Ghatak, *Lasers: Fundamentals and Applications*. 2010: Springer US.
2. Demtröder, W., *Laser Spectroscopy: Vol. 1: Basic Principles*. 2008: Springer Berlin Heidelberg.
3. Miziolek, A.W., Vincenzo Palleschi, and e. Israel Schechter, *Laser Induced Breakdown Spectroscopy*. 2006: Cambridge University Press.
4. Vandenabeele, P., *Practical Raman Spectroscopy: An Introduction*. 2013: Wiley.
5. Weitkamp, C., *Lidar: Range-Resolved Optical Remote Sensing of the Atmosphere*. 2006: Springer New York.
6. Rand, S.C., *Raman laser cooling of solids.* Journal of Luminescence, 2013. **133**: p. 10-14.
7. Braun, M., P. Gilch, and W. Zinth, *Ultrashort Laser Pulses in Biology and Medicine*. 2008: Springer.
8. Nouri, K., *Lasers in Dermatology and Medicine*. 2011: Springer.
9. Wlodarczyk, K.L., et al., *Picosecond laser cutting and drilling of thin flex glass.* Optics and Lasers in Engineering, 2016. **78**: p. 64-74.
10. Steen, W., K.G. Watkins, and J. Mazumder, *Laser Material Processing*. 2010: Springer.
11. Temmler, A., E. Willenborg, and K. Wissenbach, *Design Surfaces by Laser Remelting.* Physics Procedia, 2011. **12**: p. 419-430.
12. Schaaf, P., *Laser Processing of Materials*. Materials Science. 2010: Springer-Verlag.
13. Castillejo, M., P.M. Ossi, and L. Zhigilei, *Lasers in Materials Science*. 2014: Springer.
14. Dahotre, N.B. and S.P. Harimkar, *Laser Fabrication and Machining of Materials*. 2008, New York, USA: Springer.
15. Sugioka, K., M. Meunier, and A. Piqué, *Laser Precision Microfabrication*. 2010: Springer-Verlag.
16. Allmen, M.v. and A. Blatter, *Laser-Beam Interactions with Materials*. Second ed. 1998: Springer.
17. Liu, Q.M., et al., *Ultrafast optical Kerr effect in amorphous Ge10As40S30Se20 film induced by ultrashort laser pulses.* Journal of Optoelectronics and Advanced Materials, 2005. **7**(3): p. 1323-1328.
18. Brown, M.S. and C.B. Arnold, *Fundamentals of Laser-Material Interaction and Application to Multiscale Surface Modification*, in *Laser Precision Microfabrication*. 2010, Springer.
19. Kennedy, E., G. Byrne, and D.N. Collins, *A review of the use of high power diode lasers in surface hardening.* Journal of Materials Processing Technology, 2004. **155-156**: p. 1855-1860.
20. Samant, A.N. and N.B. Dahotre, *Laser machining of structural ceramics—A review.* Journal of the European Ceramic Society, 2009. **29**(6): p. 969-993.
21. Prokhorov, A.M., *Laser Heating of Metals*. 1990: Adam Hilger.
22. Wang, X., *Optimized Nanosecond Pulsed Laser Micromachining of Y-TZP Ceramics.* Journal of the American Ceramic Society, 2007.
23. Liu, H., X. Wang, and H. Ji, *Fabrication of lotus-leaf-like superhydrophobic surfaces via Ni-based nano-composite electro-brush plating.* Applied Surface Science, 2014. **288**: p. 341-348.

24. Chen, T., et al., *Fabrication of low adhesive superhydrophobic surfaces using nano Cu/Al2O3 Ni–Cr composited electro-brush plating.* Applied Surface Science, 2015. **356**: p. 81-90.
25. Chen, X., et al., *Construction of mechanically durable superhydrophobic surfaces by thermal spray deposition and further surface modification.* Applied Surface Science, 2015. **356**: p. 639-644.
26. Amiriyan, M., et al., *Dry sliding wear behavior of Fe3Al and Fe3Al/TiC coatings prepared by HVOF.* Wear, 2015. **342-343**: p. 154-162.
27. Zaki, M.F., W.A. Ghaly, and H.S. El-Bahkiry, *Photoluminescence, optical band gap and surface wettability of some polymeric track detectors modified by electron beam.* Surface and Coatings Technology, 2015. **275**: p. 363-368.
28. Lenivtseva, O.G., et al., *Structure and properties of titanium surface layers after electron beam alloying with powder mixtures containing carbon.* Applied Surface Science, 2015. **355**: p. 320-326.
29. Huang, Y., D.K. Sarkar, and X. Grant Chen, *Superhydrophobic aluminum alloy surfaces prepared by chemical etching process and their corrosion resistance properties.* Applied Surface Science, 2015. **356**: p. 1012-1024.
30. Harcuba, P., et al., *Surface treatment by electric discharge machining of Ti-6Al-4V alloy for potential application in orthopaedics.* J Mech Behav Biomed Mater, 2012. **7**: p. 96-105.
31. Pramanik, A., et al., *Electrical discharge machining of 6061 aluminium alloy.* Transactions of Nonferrous Metals Society of China, 2015. **25**(9): p. 2866-2874.
32. Strnad, G. and N. Chirila, *Corrosion Rate of Sand Blasted and Acid Etched Ti6Al4V for Dental Implants.* Procedia Technology, 2015. **19**: p. 909-915.
33. Dunn, A., et al., *Nanosecond laser texturing for high friction applications.* Optics and Lasers in Engineering, 2014. **62**: p. 9-16.
34. Duarte, M., et al., *Increasing Lubricant Film Lifetime by Grooving Periodical Patterns Using Laser Interference Metallurgy.* Advanced Engineering Materials, 2008. **10**(6): p. 554-558.
35. Chang, C.-S., et al., *Influence of laser beam fluence on surface quality, microstructure, mechanical properties, and tribological results for laser polishing of SKD61 tool steel.* Journal of Materials Processing Technology, 2016. **229**: p. 22-35.
36. Marimuthu, S., et al., *Laser polishing of selective laser melted components.* International Journal of Machine Tools and Manufacture, 2015. **95**: p. 97-104.
37. Pfefferkorn, F.E., et al., *Improving surface finish in pulsed laser micro polishing using thermocapillary flow.* CIRP Annals - Manufacturing Technology, 2013. **62**(1): p. 203-206.
38. Nüsser, C., I. Wehrmann, and E. Willenborg, *Influence of Intensity Distribution and Pulse Duration on Laser Micro Polishing.* Physics Procedia, 2011. **12**: p. 462-471.
39. Gao, Y., et al., *A two-step nanosecond laser surface texturing process with smooth surface finish.* Applied Surface Science, 2011. **257**(23): p. 9960-9967.
40. Olakanmi, E.O., R.F. Cochrane, and K.W. Dalgarno, *A review on selective laser sintering/melting (SLS/SLM) of aluminium alloy powders: Processing, microstructure, and properties.* Progress in Materials Science, 2015. **74**: p. 401-477.
41. Zhou, Y., et al., *A novel titanium alloy manufactured by selective laser melting: Microstructure, high temperature oxidation resistance.* Materials & Design, 2015.

42. Jia, Q. and D. Gu, *Selective laser melting additive manufactured Inconel 718 superalloy parts: High-temperature oxidation property and its mechanisms.* Optics & Laser Technology, 2014. **62**: p. 161-171.
43. Hanzl, P., et al., *The Influence of Processing Parameters on the Mechanical Properties of SLM Parts.* Procedia Engineering, 2015. **100**: p. 1405-1413.
44. Emmelmann, C., et al., *Laser Additive Manufacturing of Modified Implant Surfaces with Osseointegrative Characteristics.* Physics Procedia, 2011. **12**: p. 375-384.
45. Jagdheesh, R., J.J. García-Ballesteros, and J.L. Ocaña, *One-step fabrication of near superhydrophobic aluminum surface by nanosecond laser ablation.* Applied Surface Science, 2015.
46. Choubey, A., et al., *Studies on pulsed Nd:YAG laser cutting of thick stainless steel in dry air and underwater environment for dismantling applications.* Optics & Laser Technology, 2015. **71**: p. 6-15.
47. Leone, C., et al., *An Investigation on Nd:YAG Laser Cutting of Al 6061 T6 Alloy Sheet.* Procedia CIRP, 2015. **28**: p. 64-69.
48. Dubey, A.K. and V. Yadava, *Experimental study of Nd:YAG laser beam machining—An overview.* Journal of Materials Processing Technology, 2008. **195**(1-3): p. 15-26.
49. Leone, C., et al., *Experimental investigation on laser milling of aluminium oxide using a 30W Q-switched Yb:YAG fiber laser.* Optics & Laser Technology, 2016. **76**: p. 127-137.
50. Diaci, J., et al., *Rapid and flexible laser marking and engraving of tilted and curved surfaces.* Optics and Lasers in Engineering, 2011. **49**(2): p. 195-199.
51. Stephen, A., et al., *High Speed Laser Micro Drilling for Aerospace Applications.* Procedia CIRP, 2014. **24**: p. 130-133.
52. Ng, G.K.L. and L. Li, *Repeatability characteristics of laser percussion drilling of stainless-steel sheets.* Optics and Lasers in Engineering, 2003. **39**(1): p. 25-33.
53. Man, H.C., K.Y. Chiu, and X. Guo, *Laser surface micro-drilling and texturing of metals for improvement of adhesion joint strength.* Applied Surface Science, 2010. **256**(10): p. 3166-3169.
54. Nath, S., S. Pityana, and J. Dutta Majumdar, *Laser surface alloying of aluminium with WC+Co+NiCr for improved wear resistance.* Surface and Coatings Technology, 2012. **206**(15): p. 3333-3341.
55. Singh, A. and S.P. Harimkar, *Laser Surface Engineering of Magnesium Alloys: A Review.* Jom, 2012. **64**(6): p. 716-733.
56. Hammersley, G., L.A. Hackel, and F. Harris, *Surface prestressing to improve fatigue strength of components by laser shot peening.* Optics and Lasers in Engineering, 2000. **34**(4-6): p. 327-337.
57. Qiao, H., J. Zhao, and Y. Gao, *Experimental investigation of laser peening on TiAl alloy microstructure and properties.* Chinese Journal of Aeronautics, 2015. **28**(2): p. 609-616.
58. Ta, D.V., et al., *Nanosecond laser textured superhydrophobic metallic surfaces and their chemical sensing applications.* Applied Surface Science, 2015. **357**: p. 248-254.
59. Hao, L. and J. Lawrence, *Effects of Nd:YAG laser treatment on the wettability characteristics of a zirconia-based bioceramic.* Optics and Lasers in Engineering, 2006. **44**(8): p. 803-814.

60. Bizi-Bandoki, P., et al., *Modifications of roughness and wettability properties of metals induced by femtosecond laser treatment.* Applied Surface Science, 2011. **257**(12): p. 5213-5218.
61. Kietzig, A.M., S.G. Hatzikiriakos, and P. Englezos, *Patterned superhydrophobic metallic surfaces.* Langmuir, 2009. **25**(8): p. 4821-7.
62. Moradi, S., et al., *Femtosecond laser irradiation of metallic surfaces: effects of laser parameters on superhydrophobicity.* Nanotechnology, 2013. **24**(41): p. 415302.
63. Wu, B., et al., *Superhydrophobic surfaces fabricated by microstructuring of stainless steel using a femtosecond laser.* Applied Surface Science, 2009. **256**(1): p. 61-66.
64. Martínez-Calderon, M., et al., *Femtosecond laser fabrication of highly hydrophobic stainless steel surface with hierarchical structures fabricated by combining ordered microstructures and LIPSS.* Applied Surface Science, 2015.
65. Chang, F.-M., et al., *Superhydrophilicity to superhydrophobicity transition of CuO nanowire films.* Applied Physics Letters, 2010. **96**(11): p. 114101.
66. Chen, M.-F., et al., *Laser coding on the eggshell using pulsed-laser marking system.* Journal of Materials Processing Technology, 2009. **209**(2): p. 737-744.
67. O'Hana, S., et al., *Laser surface colouring of titanium for contemporary jewellery.* Surface Engineering, 2008. **24**(2): p. 147-153.
68. Yao, J., et al., *Selective appearance of several laser-induced periodic surface structure patterns on a metal surface using structural colors produced by femtosecond laser pulses.* Applied Surface Science, 2012. **258**(19): p. 7625-7632.
69. Fasasi, A.Y., et al., *Nano-second UV laser processed micro-grooves on Ti6Al4V for biomedical applications.* Materials Science and Engineering: C, 2009. **29**(1): p. 5-13.
70. Zheng, H.Y., D. Rosseinsky, and G.C. Lim, *Laser-evoked coloration in polymers.* Applied Surface Science, 2005. **245**(1-4): p. 191-195.
71. Marx, C., et al., *Investigations on laser marking of plants and fruits.* Biosystems Engineering, 2013. **116**(4): p. 436-446.
72. Ahsan, M.S., et al., *Colorizing stainless steel surface by femtosecond laser induced micro/nano-structures.* Applied Surface Science, 2011. **257**(17): p. 7771-7777.
73. Dusser, B., *Controlled nanostructrures formation by ultrafast laser pulses for color marking.* Optics Express, 2010.
74. Antończak, A.J., et al., *Laser-induced colour marking—Sensitivity scaling for a stainless steel.* Applied Surface Science, 2013. **264**: p. 229-236.
75. Wlodarczyk, K.L., et al., *Laser microsculpting for the generation of robust diffractive security markings on the surface of metals.* Journal of Materials Processing Technology, 2015. **222**: p. 206-218.
76. Ukar, E., et al., *Laser Polishing of GGG70L Cast Iron with 2D Scan-head.* Procedia Engineering, 2013. **63**: p. 53-59.
77. Hafiz, A.M.K., E.V. Bordatchev, and R.O. Tutunea-Fatan, *Influence of overlap between the laser beam tracks on surface quality in laser polishing of AISI H13 tool steel.* Journal of Manufacturing Processes, 2012. **14**(4): p. 425-434.
78. Nüsser, C., H. Sändker, and E. Willenborg, *Pulsed Laser Micro Polishing of Metals using Dual-beam Technology.* Physics Procedia, 2013. **41**: p. 346-355.
79. Erdogan, M., et al., *Texturing of titanium (Ti6Al4V) medical implant surfaces with MHz-repetition-rate femtosecond and picosecond Yb-doped fiber lasers.* Opt Express, 2011. **19**(11): p. 10986-96.

80. Zimmermann, S., et al., *Improved adhesion at titanium surfaces via laser-induced surface oxidation and roughening.* Materials Science and Engineering: A, 2012. **558**: p. 755-760.
81. Man, H.C., Q. Wang, and X. Guo, *Laser surface microdrilling of Ti and laser gas nitrided Ti for enhancing fixation of dental implants.* Optics and Lasers in Engineering, 2010. **48**(5): p. 583-588.
82. Resnick, R., D. Halliday, and K.S. Krane, *Physics*. 5th ed. 2001: John Wiley & Sons, Incorporated.
83. Popov, V., *Contact Mechanics and Friction: Physical Principles and Applications*. 2010: Springer Berlin Heidelberg.
84. Blau, P.J., *The significance and use of the friction coefficient.* Tribology International, 2001. **34**(9): p. 585-591.
85. Ben-David, O. and J. Fineberg, *Static Friction Coefficient Is Not a Material Constant.* Physical Review Letters, 2011. **106**(25).
86. Liu, Z., A. Neville, and R.L. Reuben, *Static Friction Modeling in the Presence of Soft Thin Metallic Films.* Journal of Tribology, 2002. **124**(1): p. 27.
87. Cohen, D., Y. Kligerman, and I. Etsion, *A Model for Contact and Static Friction of Nominally Flat Rough Surfaces Under Full Stick Contact Condition.* Journal of Tribology, 2008. **130**(3): p. 031401.
88. Hulikal, S., K. Bhattacharya, and N. Lapusta, *Collective behavior of viscoelastic asperities as a model for static and kinetic friction.* Journal of the Mechanics and Physics of Solids, 2015. **76**: p. 144-161.
89. Waghmare, A.K. and P. Sahoo, *A Study of Elastic-plastic Contact of Rough Surfaces Using N-point Asperity Model.* Procedia Materials Science, 2014. **5**: p. 1716-1725.
90. Mulvihill, D.M., et al., *An elastic–plastic asperity interaction model for sliding friction.* Tribology International, 2011. **44**(12): p. 1679-1694.
91. Shoukat Choudhury, M.A.A., M. Jain, and S.L. Shah, *Stiction – definition, modelling, detection and quantification.* Journal of Process Control, 2008. **18**(3-4): p. 232-243.
92. de Souza L. Cuadros, M.A., C.J. Munaro, and S. Munareto, *Improved stiction compensation in pneumatic control valves.* Computers & Chemical Engineering, 2012. **38**: p. 106-114.
93. Zaghloul, U., et al., *On the reliability of electrostatic NEMS/MEMS devices: Review of present knowledge on the dielectric charging and stiction failure mechanisms and novel characterization methodologies.* Microelectronics Reliability, 2011. **51**(9-11): p. 1810-1818.
94. Iannacci, J., *Reliability of MEMS: A perspective on failure mechanisms, improvement solutions and best practices at development level.* Displays, 2015. **37**: p. 62-71.
95. Podgornik, B., et al., *Effectiveness and design of surface texturing for different lubrication regimes.* Meccanica, 2012. **47**(7): p. 1613-1622.
96. Ibatan, T., M.S. Uddin, and M.A.K. Chowdhury, *Recent development on surface texturing in enhancing tribological performance of bearing sliders.* Surface and Coatings Technology, 2015. **272**: p. 102-120.
97. Kovalchenko, A., et al., *Friction and wear behavior of laser textured surface under lubricated initial point contact.* Wear, 2011. **271**(9-10): p. 1719-1725.
98. Huang, W., S. Liao, and X. Wang, *Wettability and friction coefficient of micro-magnet arrayed surface.* Applied Surface Science, 2012. **258**(7): p. 3062-3067.
99. Wu, Z., et al., *Effect of surface texturing on friction properties of WC/Co cemented carbide.* Materials & Design, 2012. **41**: p. 142-149.

100. Xing, Y., et al., *Effect of laser surface texturing on Si3N4/TiC ceramic sliding against steel under dry friction.* Materials & Design, 2013. **52**: p. 234-245.
101. Scaraggi, M., et al., *Minimize friction of lubricated laser-microtextured-surfaces by tuning microholes depth.* Tribology International, 2014. **75**: p. 123-127.
102. Braun, D., et al., *Efficiency of laser surface texturing in the reduction of friction under mixed lubrication.* Tribology International, 2014. **77**: p. 142-147.
103. Li, J., et al., *Effect of surface laser texture on friction properties of nickel-based composite.* Tribology International, 2010. **43**(5-6): p. 1193-1199.
104. Voevodin, A.A. and J.S. Zabinski, *Laser surface texturing for adaptive solid lubrication.* Wear, 2006. **261**(11-12): p. 1285-1292.
105. Etsion, I., *Improving tribological performance of mechanical components by laser surface texturing.* Tribology Letters, 2004. **17**(4): p. 733-737.
106. Zenebe Segu, D. and P. Hwang, *Friction control by multi-shape textured surface under pin-on-disc test.* Tribology International, 2015. **91**: p. 111-117.
107. Amanov, A., et al., *The influence of bulges produced by laser surface texturing on the sliding friction and wear behavior.* Tribology International, 2013. **60**: p. 216-223.
108. Olofinjana, B., et al., *Effect of laser surface texturing (LST) on tribochemical films dynamics and friction and wear performance.* Wear, 2015. **332-333**: p. 1225-1230.
109. Hoppermann, A. and M. Kordt, *Tribological optimisation using laser-structured contact surfaces.* O+P Oelhydraulik und Pneumatik, 2002.
110. Weman, K., *Welding Processes Handbook*. 2nd ed. 2012: Woodhead Publishing Limited.
111. Bolelli, G., et al., *Tribology of HVOF- and HVAF-sprayed WC–10Co4Cr hardmetal coatings: A comparative assessment.* Surface and Coatings Technology, 2015. **265**: p. 125-144.
112. Fang, W., et al., *Processing optimization, surface properties and wear behavior of HVOF spraying WC–CrC–Ni coating.* Journal of Materials Processing Technology, 2009. **209**(7): p. 3561-3567.
113. Kang, M., et al., *Micro- and nanoscale surface texturing effects on surface friction.* Applied Surface Science, 2015. **345**: p. 344-348.
114. Hammerström, L. and S. Jacobson, *Designed high-friction surfaces—Influence of roughness and deformation of the counter surface.* Wear, 2008. **264**(9-10): p. 807-814.
115. Vilhena, L.M., et al., *Surface texturing by pulsed Nd:YAG laser*. Tribology International, 2009. **42**(10): p. 1496-1504.
116. Varenberg, M., G. Halperin, and I. Etsion, *Different aspects of the role of wear debris in fretting wear.* Wear, 2002. **252**(11-12): p. 902-910.
117. Schille, J., et al. *Experimental Study on Laser Surface Texturing for Friction Coefficient Enhancement*. in *International Symposium on Laser Precision Microfabrication*. 2014. Vilnius, Lithuania.
118. Gabzdyl, J. and E.B. Hansen, *Surface Texturing with ns pulse fiber lasers*, in *NOLAMP*. 2011: Norwegian University of Science and Technology, Norway.
119. Sun, Q., et al., *Dry sliding wear behavior of TC11 alloy at 500°C: Influence of laser surface texturing.* Tribology International, 2015. **92**: p. 136-145.
120. Xie, W., E.C. De Meter, and M.W. Trethewey, *An experimental evaluation of coefficients of static friction of common workpiece-fixture element pairs.* International Journal of Machine Tools & Manufacture, 2000. **40**(4): p. 467-488.
121. BOC, *Nitriding and Nitrocarburising*. 2013, BOC Online.

122. Conci, M.D., A.C. Bozzi, and A.R.F. Jr., *Effect of plasma nitriding potential on tribological behaviour of AISI D2 cold-worked tool steel.* Wear, 2014. **317**(1-2): p. 188-193.
123. Kurelo, B.C.E.S., et al., *Plasma nitriding of HP13Cr supermartensitic stainless steel.* Applied Surface Science, 2015. **349**: p. 403-414.
124. Wellburn, D., et al., *Variable beam intensity profile shaping for layer uniformity control in laser hardening applications.* International Journal of Heat and Mass Transfer, 2014. **79**: p. 189-200.
125. Funck, K., R. Nett, and A. Ostendorf, *Tailored Beam Shaping for Laser Spot Joining of Highly Conductive Thin Foils.* Physics Procedia, 2014. **56**: p. 750-758.
126. Currie, M., *White Paper: Laser Beamshaping for Industrial Applications*. 1v0 ed. 2014: Powerphotonic. 12.
127. Baker, H.J., et al., *Beam shapers for high power lasers, fabricated by laser micro-machining*, in *Conference on Lasers and Electro-Optics*. 2009, IEEE: Baltimore, Maryland USA.
128. Dickey, F.M., *Laser Beam Shaping: Theory and Techniques, Second Edition*. 2014: Taylor & Francis.
129. Dickey, F.M., et al., *Laser Beam Shaping Applications*. 2005: CRC Press.
130. Svelto, O., *Principles of lasers*. 5 ed. 2010: Springer.
131. Yilbas, B.S., et al., *Laser texturing of alumina surface for improved hydrophobicity.* Applied Surface Science, 2013. **286**: p. 161-170.
132. Limited, A.M. *Stainless Steel 1.4401 Sheet and Plate*. 2015 02/09/2015 [cited 2015 12th November]; Available from: http://www.aalco.co.uk/datasheets/Aalco-Metals-Ltd_Stainless-Steel-14401-Sheet-and-Plate_345.pdf.ashx.
133. Limited, A.M. *Stainless Steel 1.4301 Sheet and Plate*. 2015 02/09/2015 [cited 2015 12th November]; Available from: http://www.aalco.co.uk/datasheets/Aalco-Metals-Ltd_Stainless-Steel-14301-Sheet-and-Plate_343.pdf.ashx.
134. Uddeholm. *Uddeholm Impax Supreme*. 2011 09/2011 [cited 2015 12th November]; Available from: http://www.uddeholm.com/files/PB_impax_supreme_english.pdf.
135. Böhler. *Böhler Edelstahl S600 High Speed Steel*. 2007 10/2007 [cited 2015 12th November]; Available from: http://www.bohler-edelstahl.com/files/S600DE.pdf.
136. Uddeholm. *Uddeholm Sleipner*. 03/2011 [cited 2015 12th November]; Available from: http://www.uddeholm.com/files/PB_Uddeholm_sleipner_english.pdf.
137. Balasubramanian, K.R., et al., *Numerical and experimental investigation of laser beam welding of AISI 304 stainless steel sheet.* Advances in Production Engineering & Management, 2008.
138. Kwon, H., et al., *Temperature-dependent absorptance of painted aluminum, stainless steel 304, and titanium for 1.07μm and 10.6μm laser beams.* Optics and Lasers in Engineering, 2012. **50**(2): p. 114-121.